Structure-based design of P2X receptor small molecule modulators

A thesis submitted in accordance with the conditions governing candidates for the degree of Philosophiae Doctor in Cardiff University

By Gaia Pasqualetto

September 2018

School of Biosciences
Cardiff University

LIFE SCIENCES RESEARCH NETWORK WALES
RHWYDWAITH GWYDDORAU BYWYD CYMRU

To my parents for their unconditional love,

To Mark for the immense moral support

ACKNOWLEDGMENTS

Firstly, I would like to express my gratitude to my supervisors Dr Mark Young and Prof Andrea Brancale for giving me the opportunity to work on this project, for their guidance, their scientific insight and their inspiring outlook. Their extreme patience with me and the treasurable moral support - especially during the last few months - have been very helpful and empowering. I would also like to thank both for offering me a positive and motivating research environment where I could explore and learn. I have greatly enjoyed and I will cherish this research experience (although the 'write up' might not be my favorite part). Additionally, I would like to acknowledge Dr Marta Radwan for teaching me most molecular biology techniques I know and Dr Wynand Van der Goes van Naters and Dr Mark Young for the fascinating and inspiring scientific conversations. I apologize for not naming everyone but I would also want to thank all the PIs that allowed me to use their equipment to conduct my work.

I am also grateful to Dr Marcella Bassetto for her support and understanding while I have been juggling with the 'write up'. I would like to extend my thanks to all the past and present members of the three labs for their help, friendship and for bearing with my personality. Moreover, I feel very lucky and grateful for meeting members of 'neighboring' labs, including Emily C. and Claire, who have become very good friends of mine and an incredible source of positive moral support. I am also thankful to Kath for trying to teach me some self-kindness and stress management.

Huge thanks go to my parents for their unconditional love and understanding and for their ability to support me and for being always present although geographically quite distant.

Finally I would like to thank Life Science Research Network Wales for providing the funding for the project and all the people who have supported me during the course of this work directly or indirectly.

SUMMARY

P2X4 and P2X7 receptors have gained increasing significance as drug targets for their involvement in neurotransmission, pain, cancer, inflammation and immunity. To date, numerous P2X7 antagonists have been developed, yet relatively few P2X4 antagonists have been reported, and no data is available regarding their binding sites on the receptor. Using *in silico* techniques, we attempted to identify novel P2X4 and P2X7 modulators, and combined experimental and structural data to explore allosteric pockets with future potential for drug design. Two virtual screenings of commercially available drug-like compounds performed in the human P2X4 homology model led to the selection, purchase and biological evaluation *via* calcium influx assay of 42 compounds. While no compound with significant antagonist activity at human P2X4 was found, multiple compounds abolished ATP-induced YO-PRO dye uptake at human P2X7, including Compound 25 (IC_{50} value of 8 μM). Further 27 structural analogues to Compound 25 were purchased and assayed, expanding the number of active antagonists and offering an insight in the structure-activity relationship. In parallel, a mutagenesis study of human and rat P2X4 receptors based on (i) species-specific pharmacology and (ii) the recently published panda P2X7 crystal structures led us to identify the allosteric binding site for the P2X4-selective antagonist BX-430. The pocket was then used to perform a new virtual screen, identifying 20 potential 'hit' candidates for future biological evaluation. Finally, we performed docking simulations of the positive P2X4 allosteric modulator ivermectin and the partially selective P2X7 agonist 2'(3')-4-O-benzoylbenzoyl ATP (BzATP), with good correlation between binding conformations and previously published pharmacological data. In conclusion, although no novel human P2X4 antagonist has been identified, this work led to (i) the discovery of an allosteric site not previously described in human P2X4, (ii) the identification of a novel P2X7 antagonist with micromolar potency and (iii) and increased understanding of the molecular basis for subtype-specific modulator potency at P2X4 and P2X7 receptors.

TABLE OF CONTENTS

LIST OF FIGURES

LIST OF TABLES

GENERAL ABBREVIATIONS

2-APB	2-Aminoethoxydiphenyl borate
2-meSATP	2-Methylthioadenosine-5‘-O-triphosphate
5-BDBD	5-(3-Bromophenyl)-1,3-dihydro-2H-benzofuro[3,2-e]-1,4-diazepin- 2-one
A	Adenine
A-438079	3-((5-(2,3-dichlorophenyl)-1H-tetrazol-1-yl)methyl)pyridine
A740003	N-(1-{[(cyanoimino)(5-quinolinylamino) methyl] amino}-2,2-dimethylpropyl)-2-(3,4-dimethoxyphenyl)acetamide
A804598	N-cyano-N'-[(1R)-1-phenylethyl]-N''-quinolin-5-ylguanidine
ACO	Artificial ant colony optimization
ADMET	Absorption, Distribution, Metabolism, Excretion and Toxicity
ADP	Adenosine 5‘-diphosphate
AF-219	5-(2,4-diamino-pyrimidin-5-yloxy)-4-isopropyl-2-methoxy-benzenesulfonamide (also known as MK-7264 or gefapixant)
ALP	allopregnanolone
AMD	Age-related macular degeneration
AMP	Adenosine 5‘-monophosphate
AMPA	α-Amino-3-hydroxy-5-methyl-4-isoxazolepropionic acid
Ap4P	Diadenosine Tetraphosphate
ASC	Adapter protein apoptosis associated speck-like protein
ATP	Adenosine-5‘-triphosphate
AZ116453743	3-[1-[4-(3-nitrophenyl)phenoxy]-4-pyridin-4-ylbutan-2-yl]-1,3-thiazolidine-2,4-dione
AZD-9056	N-(1-adamantylmethyl)-2-chloro-5-[3-(3-hydroxypropylamino) propyl]benzamide
BBB	Blood brain barrier

BBG	Brilliant Blue G
BDNF	Brain-derived neurotrophic factor
BDNF	Brain-derived neurotrophic factor
BX-430	N-[2,6-Dibromo-4-(1-methylethyl)phenyl]-N'-(3-pyridinyl)urea
BzATP	2‘(3‘)-O-(4-Benzoylbenzoyl)adenosine-t‘-triphosphate
C	Cytosine
Ca2+	Calcium ions
CCL21	Chemokine C-C motif ligand 21
CCL3	Chemokine (C-C motif) ligand 3
CCR2	C-C chemokine receptor type 2
cDNA	Complementary deoxyribonucleic acid
CE-224,535	2-chloro-N-[(1-hydroxycycloheptyl)methyl]-5-[4-[(2R)-2-hydroxy-3-methoxypropyl]-3,5-dioxo-1,2,4-triazin-2-yl]benzamide
CNS	Central nervous system
CO	Carbon monoxide
COPD	Chronic obstructive pulmonary disease
CORM-2	Carbon monoxide-releasing molecule; Tricarbonyldichlororuthenium(II) dimer
COX	Cyclooxygenase
cryo-EM	Cryo-Electron microscopy
CSF1	Colony stimulating factor 1
Csf1	Colony stimulating factor 1 gene
CSF1R	Colony stimulating factor 1 receptor
CTD	C-Terminal domain
CTP	Cytidine triphosphate
CVD	Cardiovascular disease
DdP2XA-E	*Dictyostelium discoideum P2X receptor subtypes A-E*

DICER1	Micro-RNA processing enzyme
DMEM	Dulbecco's modified Eagle medium
DMSO	Dimethyl sulfoxide
DORN1	Kinase-like purinergic receptor found in green plants (also referred as P2K1)
E-NTPDase	Ectonucleoside triphosphate diphosphohydrolase
EC_{50}	Concentration of half-maximal receptor activation
EDTA	Ethylenediaminetetraacetic acid
eNOS	Endothelial nitric oxide synthase
ER	Endoplasmic reticulum
EVT-401	2-(3-fluoro-4-(trifluoromethyl)phenyl)-N-(2-(1-hydroxypropan-2-yl)-6-methyl-1-oxo-1,2-dihydroisoquinolin-5-yl)acetamide
FACE	Fusion-activated calcium entry
FBS	Foetal bovine serum
FDA	Food and Drug Administration
Fluo-4 AM	Fluo-4 acetoxymethyl ester
G	Guanine
G34	Cell line expressing human P2X4 (initially named WB34)
G418	Geneticin
GABA	γ-Aminobutyric acid
GluCls	Glutamate-activated chloride channels
GPCR	G protein-coupled receptor
GSK1482160	(2S)-N-[[2-chloro-3-(trifluoromethyl)phenyl]methyl]-1-methyl-5-oxopyrrolidine-2-carboxamide
GW791343	2-(3,4-difluoroanilino)-N-[2-methyl-5-(piperazin-1-ylmethyl)phenyl]acetamide
HdP2X	*Hypsibius dujardini P2X receptor*
HEK-293	Human embryonic kidney cells
HEPES	4-(2-Hydroxyethyl)-1-piperazineethanesulfonic acid

HIV	Human immune deficiency virus
hP2X4	Human (*Homo sapiens*) P2X4
hP2X7	Human (*Homo sapiens*) P2X7
HTS	High-throughput screening
HTVS	High throughput screening
HUVEC	Human Umbilical Vein Endothelial Cells
IBD	Inflammatory bowel disease
IC_{50}	Concentration of half-maximal receptor inhibition
IL-18	Interleukin 18
IL-1ß	Interleukin 1 beta
IRF5	Interferon regulatory factor 5
IRF8	Interferon regulatory factor 8
IVM	Ivermectin
JNJ-54175446	(R)-(2-chloro-3-(trifluoromethyl)phenyl)(1-(5-fluoropyrimidin-2-yl)-4-methyl-1,4,6,7-tetrahydro-5H-[1,2,3]triazolo[4,5-c]pyridin-5-yl)methanone
JNJ-55308942	S)-(3-fluoro-2-(trifluoromethyl)pyridin-4-yl)(1-(5-fluoropyrimidin-2-yl)-6-methyl-1,4,6,7-tetrahydro-5H-[1,2,3]triazolo[4,5-c]pyridin-5-yl)methanone
JNJ-64413739	(S)-(3-fluoro-2-(trifluoromethyl)pyridin-4-yl)(6-methyl-1-(pyrimidin-2-yl)-1,4,6,7-tetrahydro-5H-[1,2,3]triazolo[4,5-c]pyridin-5-yl)methanone
JNK-1/2	c-Jun N-terminal kinases 1/2
K+	Potassium ions
KCC2	Chloride channel
KO	Knock out
LPS	Lipopolysaccharide
MAPK	Mitogen-activated protein kinases
max.	Maximal
MM	Molecular Mechanics

mRNA	Messenger RNA
n. c.	No convergence
n. d.	Not determined
Na+	Sodium ions
nACh	Nicotinic acetylcholine receptor
NC 2600	P2X4 allosteric modulator (undisclosed structure)
nfP2X7	Non-pore functional P2X7
NF-kB	Nuclear factor kappa-light-chain-enhancer of activated B cells
NF023	8,8'-[Carbonyl-bis(imino-3,1-phen-ylenecarbonylimino)]bis-1,3,5- naphthalene-trisulfonic acid
NF279	8,8'-[Carbonyl-bis(imino-4,1-phenylenecarbonylimino-4,1-pheylene-carbonyl-imino)]bis-1,3,5-naphthalene trisulfonic acid
NHS	National Health Service
NLR	NOD-like receptor
NLRP3	inflammasome
NMDA	N-methyl-D-aspartate
NMDAR	N-methyl-D-aspartate receptor
NMR	Nuclear magnetic resonance
NO	Nitric oxide
NOS	Nitric Oxide Synthase
NP-1815-PX	(5-[3-(5-thioxo-4H-[1,2,4]oxadiazol-3-yl)phenyl]-1H-naphtho[1, 2-b][1,4]diazepine-2,4(3H,5H)-dione)
NRTI	Nucleotiside Reverse Transcriptase Inhibitor
NRTI	Nucleoside reverse transcriptase inhibitors
NSAID	Non-steroidal anti-inflammatory drug
p	Probability value
P2K1	kinase-like purinergic receptor found in green plants (also refered as DORN1)

P2RX1	Gene coding for P2X1
P2RX2	Gene coding for P2X2
P2RX3	Gene coding for P2X3
P2RX4	Gene coding for P2X4
P2RX7	Gene coding for P2X7
p38	P38 mitogen-activated protein kinases
PCP	Phencyclidine
PDB	Protein Data Bank
pEC_{50}	Negative decadic logarithm of EC50 value
PET	Positron emission tomography
pH	Negative decadic logarithm of H+ concentration
pIC_{50}	Negative decadic logarithm of IC50 value
PLIF	Protein-Ligand Interaction Fingerprint
PNP	Purine nucleoside phosphorylase
PPADS	Pyridoxalphosphate-6-azophenyl-2‘-4‘-disulfonic acid
PPARα	Peroxisome proliferator-activated receptor α
PSB-12054	N-(benzyloxycarbonyl)phenoxazine
PSB-12062	N-(p-methylphenylsulfonyl)phenoxazine
QM	Quantum Mechanics
RB-2	Reactive Blue-2
RMSD	Root Mean Square Deviation
RNA	Ribonucleic acid
ROS	Reactive oxygen species
rP2X4	Rat (Rattus norvegicus) P2X4
rP2X7	Rat (Rattus norvegicus) P2X7
RPE	Retinal pigment epithelial cells
rs208294	Polymorphism responsible for gain-of-function mutation

	(Y155H) in human P2X7
rs25644	Missense single nucleotide polymorphism responsible for the S242G mutation in human P2X4
rs3751143	Polymorphism responsible for loss-of-function mutation (E496A) in human P2X7
rs7958311	Polymorphism responsible for hypo-function mutation (R270H) in human P2X7
RT	Room temperature
SchP2X	*Schistosoma mansoni P2X receptor*
SDH	Spinal dorsal horn
SEM	Standard error of the mean
SH3	Src homology 3
siRNA	Small (or short) interfering RNA
SNP	Single nucleotide polymorphism
SP	Standard Precision
STAT3	Signal transducer and activator of transcription 3
T	Thymine
TCA	Tricyclic antidepressant
THDOC	Tetrahydrodeoxycorticosterone; 3α,21-dihydroxy-5α-pregnan-20-one
TLR	Toll-like receptors
TM	Transmembrane domain
TNFR	Tumor necrosis factor receptor
TNFR1	tumor necrosis factor receptor 1
TNFα	Tumor necrosis factor alpha
TNP-ATP	2‘-3‘-O-(2, 4,6-Trinitrophenyl)adenosine-5‘-triphosphate
TRIS	Tris(hydroxymethyl)aminomethane
TrkB	Tropomyosin receptor kinase B
UDP	Uridine 5‘-diphosphate

UTP	Uridine 5‘-triphosphate
VEGF	Vascular endothelial growth factor
WB34	Cell line expressing human P2X4 (also named G34)
XP	Extra precision
zfP2X4	Zebrafish P2X4 receptor
α,ß-MeATP	α,ß-Methylene-adenosine 5‘-triphosphate

AMINO ACID ABBREVIATIONS

Ala (A)	Alanine
Asn (N)	Asparagine
Asp (D)	Aspartic acid
Arg (R)	Arginine
Cys (C)	Cysteine
Glu (E)	Glutamic acid
Gln (Q)	Glutamine
Gly (G)	Glycine
His (H)	Histidine
Ile (I)	Isoleucine
Leu (L)	Leucine
Lys (K)	Lysine
Met (M)	Methionine
Phe (F)	Phenylalanine
Pro (P)	Proline
Ser (S)	Serine
Thr (T)	Threonine
Trp (W)	Tryptophan
Tyr (Y)	Tyrosine
Val (V)	Valine

Chapter 1:

General Introduction

1 INTRODUCTION

Intracellular adenosine triphosphate (ATP) is important as an energy source and second messenger in signal transduction. In the extracellular compartment – where the concentration of purines and pyrimidines is usually several fold lower (around nanomolar concentration) (Di Virgilio 2012; Gorodeski 2012) – ATP plays a pivotal role in the purinergic signalling system. Following cell damage, release through hemichannels or from presynaptic neurons, ATP binds both metabotropic (P2Y) and ionotropic (P2X) purinergic receptors (North 2002). While P2X receptors display a strong selectivity to ATP, P2Y is activated also by uridine triphosphate (UTP), uridine diphosphate and adenosine diphosphate (ADP); the latter is a product of degradation of ATP by ectonucleotidases, which are capable of catalysing the breakage of the phosphoesteric bond (Abbracchio et al. 2009). Further degradation leads to adenosine and adenine, also involved in intercellular signalling (Thimm et al. 2015) (**Figure 1-1**)

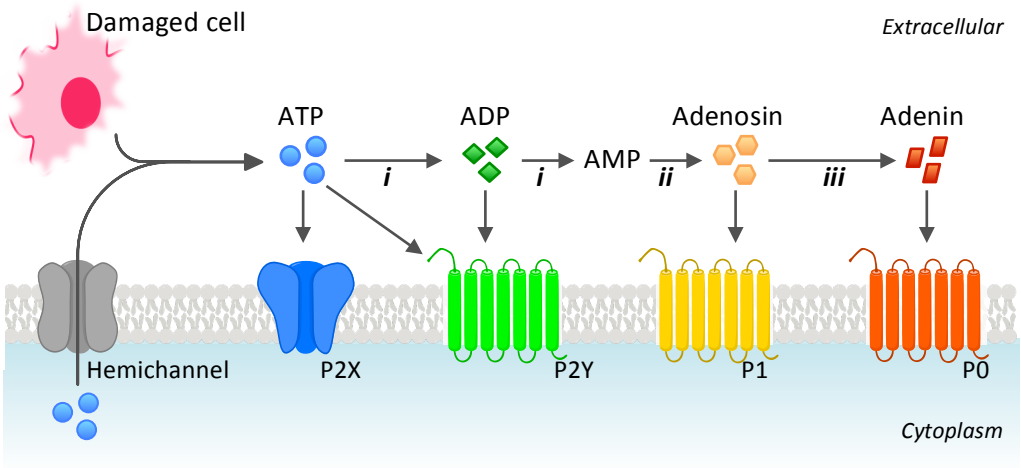

Figure 1-1: Extracellular purines involved in purinergic signalling. ATP is released in the extracellular compartment through hemichannels (pannexins and connexins), from synapsis or after cell damage and where it interacts with P2X and P2Y receptors. ATP is also readily converted in ADP, adenosine and Adenine through the action of ectonucleotidases such as ectonucleoside triphosphate diphosphohydrolases (E-NTPDases; ***i***), ecto-5'-nucleotidase (***ii***) and purine nucleoside phosphorylase (PNP; ***iii***).

1.1 The P2X receptor family

1.1.1 Phylogeny of P2X receptors

ATP signalling *via* ionotropic receptors is thought to have been one of the first intercellular systems to develop and is widely present in eukaryotes. P2X receptors have been experimentally identified in numerous invertebrates and primitive organisms such as basal fungi (Cai 2012), trematodes (*Schistosoma mansoni,* SchP2X) (Agboh et al. 2004), amoebas (*Dictyostelium discoideum,* DdP2XA-E) (Fountain et al. 2007), algae (*Ostreococcus tauri*) (Fountain et al. 2008), choanoflagellates (*Monosiga brevicollis*) (Cai 2006), tardigrades (*Hypsibius dujardini,* HdP2X) (Bavan et al. 2009), molluscs (e.g. *Lymnea stagnalis*) (Bavan et al. 2012) and arthropods (*Boophilus microplus)* and the Gulf Coast tick *Ambylomma maculatum*) (Bavan et al. 2011; Kasuya et al. 2016). Interestingly some model organisms such as *C. elegans* and *Drosophila melanogaster* and green plants do not show evidence for the presence of P2X receptors in their genomes, suggesting that the gene was lost in some major lineages; nevertheless there is no doubt that ATP maintains an important signalling role in those organisms (e.g. the DORN1 kinase-type receptor in *Arabidopsis thaliana* and *Camelina sativa*, named P2K1) (Cao et al. 2014; Cho et al. 2017; Li et al. 2016). The increasing availability of genome data is a source for further future identification of P2X receptor homologues in other organisms aiming at a more comprehensive understanding of structure and function of P2X receptors.

1.1.2 General structure of P2X receptors

1.1.2.1 Main conserved features

P2X receptors are a family of ATP-gated trimeric cation channels. Each subunit comprises an intracellular N- and C-terminal cytoplasmic domain connected to an approximately 280-amino-acid extracellular domain through two transmembrane α-helices (TM). Trimers contain three ATP-binding sites, each located at the extracellular interface of two adjacent subunits and the residues directly interacting with the ATP are highly conserved (Jiang et al. 2000b; Newbolt et al. 1998; Roberts and Evans 2004; Young 2010). The orthosteric pocket will be

described in greater details in **Section 1.5.3.1**. The extracellular domain also bears the interacting sites for ions (Acuña – Castillo et al. 2007; Liu et al. 2008) and at least one allosteric binding site as shown by crystal structure data (see **Section 1.5.3.2**). The receptors undergo post-translational modifications that include the formation of disulfide bonds and N-glycosylation. All the subtypes bear 10 cysteine residues in the extracellular domain (also conserved across different species), which greatly contribute to the tertiary structure by pairing into 5 disulfide bonds (Clyne et al. 2002; Ennion and Evans 2002). N-glycosylation at the consensus sequence *Asn-X-Ser/Thr* in the extracellular domain is critical in receptor trafficking and cell surface expression. Although glycosylation sites varies from 2 to 6 across subtypes, receptors that present at least two or three glycosylated sites are expressed on the plasma membrane and appear to be functional whereas, receptors that were treated with tunicamycin or bear mutations leaving one or no glycosylated site are not functional (Newbolt et al. 1998; Torres et al. 1998). In contrast, the cytoplasmic C-terminal domains of the receptors show little conservation among different subtypes and significantly vary in length ranging from 29 residues in human P2X4 to 240 residues in human P2X7 (North 2002).

1.1.2.2 Trimeric assembly: homotrimers and heterotrimers

Physiologically relevant receptors may be formed by three identical subunits – therefore called homo-trimers – or by different subunits (hetero-trimers) (Antonio et al. 2014; Guo et al. 2007; Lewis et al. 1995). The possible organization and combinations are widely reviewed in (Saul et al. 2013) and shown in **Table 1.1**. The first identified and most largely characterized heterotrimer was P2X2/3, initially identified through co-immunoprecipitation after co-expression in a insect cell host expression system (Radford et al. 1997) and subsequently confirmed for human receptors (Hausmann et al. 2012). A later study showed that engineered cysteine residues in P2X3 and P2X2 were able to form functional receptors that showed intermediate functional characteristics between P2X2 and P2X3 (Jiang et al. 2003). Furthermore, the same study demonstrated the stoichiometry of the functional unit (P2X2/3(2)) by taking advantage of cysteine mutagenesis and subtype-specific pharmacological properties of the competitive P2X3 and P2X2/3 agonist αß-meATP. In native tissues the P2X2/3 assembly is found in rodents in

sensory and autonomic ganglia neurons, in the nerve fibers of the bladder and in taste buds (Cockayne et al. 2005) (Bo et al. 1999). The applicability of this data to humans is not clear, as human dorsal root ganglia neurons do not express P2X2 transcripts (Serrano et al. 2012). The formation of heterotrimers between P2X4 and P2X7 subtypes had been cause of debate. An initial report showed the presence of natively co-expressed P2X4/7 heterotrimers in numerous epithelial and immune cell types (Guo et al. 2007). Subsequent works in mouse lung epithelial cells (Weinhold et al. 2010) and when P2X4 and P2X7 were co-expressed in oocytes suggested an interaction between homomers rather than the presence of an heterotrimeric receptor type with a distinct electrophysiological or pharmacological phenotype (Schneider et al. 2017).

	P2X1	**P2X2**	**P2X3**	**P2X4**	**P2X5**	**P2X6**	**P2X7**
Functional hetero-trimers	P2X2[a] P2X4[b] P2X5[c]	P2X1[a] P2X3[d] P2X4[f] P2X5[e] P2X6[f]	P2X2[d]	P2X1[b] P2X2[f] P2X5[g] P2X6[f] P2X7[h]	P2X1[c] P2X2[e] P2X4[g]	P2X2[f] P2X4[f]	P2X4[h]

[a](Brown, Townsend-Nicholson, Jacobson, Burnstock, & King, 2002); [b](Nicke, Kerschensteiner, & Soto, 2005); [c](Annmarie Surprenant, Schneider, Wilson, Galligan, & North, 2000); [d](Radford et al., 1997) (Hausmann et al., 2012) (Jiang et al., 2003); [e](Compan et al., 2012); [f](Ligia S Antonio et al., 2014); [g](Torres, Egan, & Voigt, 1999); [h](Guo et al., 2007).

Table 1.1: List of proposed heterotrimeric P2X receptor assemblies.

1.1.3 Receptor activation

In functional trimers, the binding of ATP causes receptor activation and the opening of the pore resulting in non-selective cation flux (Ca^{2+}, Na^{+} influx and K^{+} efflux). This leads to depolarisation and consequent activation of signalling pathways. Concentration-response curved derived from the measurement of ion current recordings following receptor activation usually show a Hill Coefficient greater than 1, implying a cooperative effect of ATP binding. According to the mathematical models of Yan *et al.* and Kandra *et al.*, the binding of one molecule of ATP to P2X7 is not sufficient to activate the receptor but it is necessary for the receptor to be more susceptible to the binding of a second molecule of ATP in the

adjacent subunit, which is then sufficient to cause receptor activation (Khadra et al. 2013; Yan et al. 2010). Channel gating may be described in 3 phases: activation, desensitization and deactivation (North 2002). A rapid increase in ion currents is observed after activation by ATP. Desensitization happens with current decay when the agonist is still bound, and this is followed by deactivation when the current rapidly stops after the ATP leaves the binding site. Different receptor subtypes show different desensitization kinetics. P2X1 and P2X3 show fast desensitization kinetics whereas P2X2 and P2X4 show slow desensitization after application of ATP (North 2002). The gating of the receptor has been studied through biophysical-mathematical models (Khadra et al. 2013) and recently has been captured through a series of crystal structures of human P2X3 (Mansoor et al. 2016) that will be further described in **Section 1.5.3.1**.

1.1.4 P2X receptor involvement in physiological and patho-physiological processes

There are 7 subtypes of P2X receptors in humans, widely distributed in many different tissues, which play roles in inflammation (Lister et al. 2007), neuronal modulation (North 2002), immune system activation (Trautmann 2009) and smooth muscle and cardiac contraction (Yamamoto et al. 2006). Due to the recent growing interest in P2X receptors for their involvement in diseases, numerous experiments have been carried out using knock-out mice, as well as extensive analysis of receptor polymorphisms in humans (Roberts et al. 2006a) (see **Table 1.2** and **Table 1.3**). P2X1 knock-out mice reveal roles for P2X1 in male infertility (Mulryan et al. 2000), kidney function (Inscho et al. 2004) and arterial thrombosisis (Hechler et al. 2003). In humans, a 3-nucleotide in-frame deletion in the *P2RX1* gene (corresponding to Leu-351, Leu-352 or Leu-353) is associated with deficiency in platelet aggregation (Oury et al. 2000).

In the *P2RX2* gene, a non-synonymous single nucleotide polymorphism (SNP) results in the expression of a loss-of-function mutant (V60L) in humans linked to hereditary hearing loss in Chinese individuals characterised by noise-induced progressive loss of sensitivity (Yan et al. 2013). A different polymorphism (1057G>C) responsible for the expression of G353R mutant has been found in members of an Italian family with hereditary hearing loss (Faletra et al. 2014).

The link between P2X2 loss-of-function mutants and hearing loss is further supported P2X2 knockout mice (Yan et al. 2013). Mice lacking P2X2 also show reduced inflammatory pain sensation, decreased bladder reflex and motility and reduced taste sensation (Cockayne et al. 2005). P2X2 is also involved in tuning the ventilatory response to hypoxia (Rong et al. 2003). P2X3 has been associated with decreased pain, lower bladder reflex and loss of visceral mechanosensory transduction (Cockayne et al. 2005) and cough reflex. Recently a P2X3 antagonist (AF-219) has been advanced to the phase II of clinical trial as treatment for cough (Abdulqawi et al. 2015). P2X2/P2X3 heterotrimers are natively expressed in sympathetic and sensory neurons and when generating P2X2/P2X3 double knock-out mice by breeding single knock-outs, the majority of the double-knockout mice (approximately 90%) died before weaning, showing numerous phenotype abnormalities, while a normal phenotype was observed for the ones that reached adulthood, perhaps due to compensation (Cockayne et al. 2005). The P2X2 and P2X3 single knock out showed only modest lost of taste compared to the double KO - where taste sensation was completely abolished (Eddy et al. 2009; Finger and Kinnamon 2013) - implying that the heteromeric P2X2/3 receptor is involved in gustatory signaling.

P2X4 has been primarily associated with pain signaling and hypertension while P2X7 is mainly expressed in immune cells and play a role in inflammation and cell survival (a more detailed description of P2X4 and P2X7 involvement in diseases is described in **Section 1.2** and **Section 1.4**). P2X5 is mainly non-active in humans due to alternative splicing and only 10-15% of humans produce the full-length receptor (Kotnis et al. 2010). In fact, in the African American population a single nucleotide mutation gives rise to splice variants, which may include or exclude exon 10. In contrast, samples from people of American Caucasian, Chinese and Middle Eastern backgrounds showed only the allele that gives rise to the espression of P2X5 lacking exon 10, which is deprived of a portion of the ATP binding site and part of the transmembrane domain and is not functional (Kotnis et al. 2010). The function of P2X5 in individuals carrying the receptor containing exon 10 has not yet been elucidated. Similarly, P2X6 is widespread in many tissues; its role is unclear, although it appears to function only in heterotrimers (see **Table 1.1**). In fact, when expressed in oocytes P2X6 appeared to form oligomers - mainly tetramers - that were retained in the ER, leading to the

hypothesis that P2X6 is unable to homo-oligomerize to form a functional receptor (Aschrafi et al. 2004).

Receptor Subtype	Localization	Main functions
P2X1	Platelets, smooth muscle, CNS	Promoting platelet aggregation, involved in kidney function, male fertility (infertility in KO rodents)
P2X2	Autonomic ganglia, sensory ganglia, smooth muscle, CNS, pancreas	Inflammatory pain transduction, role in sensory transduction (taste and hearing loss in KO rodents)
P2X3	Nociceptive neurons, sympathetic neurons, sensory neurons, CNS	Pain transduction, sensory transduction (taste and temperature), bladder reflex and intestinal motility
P2X4	Microglia, endothelial cells, CNS,	Inflammatory and neuropathic pain transduction, vasodilation, cardio-protection and increased heart function
P2X5	Skeletal muscle, epithelial cells, skin	-
P2X6	Peripheral nerves, CNS	-
P2X7	Immune cells, macrophages, microglia, pancreas	Inflammation, pain transduction, fluid secretion, normal skeletal functions

Table 1.2: Main localization and function of P2X receptor subtypes. P2X5 is prominently non-functional in humans due to a splice variant polymorphism. P2X6 is unable to from homotrimers and is found only as subunit forming heterotrimers.

Receptor subtype	Chromosome location	Polymorphism, mutation	Implicated condition, Reference
P2X1	17p13.2	L351, L352 or L353 in-frame deletion	Platelet aggregation defect (Oury et al. 2000)
P2X2	12q24.33	178G>T; V60L (loss-of-function receptor)	Hearing loss (Yan et al. 2013)
		1057G>C; G353R	Hearing loss (Faletra et al. 2014)
P2X3	11q12.1	-	-
P2X4	12q24.32	1248A>G; T315C; *rs28360472*	High pulse pressure (Stokes et al. 2011) age-related macular degeneration (Gu et al. 2013)
		S242G; rs25644	Increased lumbar bone mineral density (Wesselius et al. 2013b)
P2X5	17p13.2	328-349 amino acid deletion (loss-of-function receptor)	n/a (Kotnis et al. 2010)
P2X6	22q11.21	-	-
P2X7	12q24.31	370T>V; A76V; *rs17525809*	Multiple sclerosis (Oyanguren-Desez et al. 2011)
		474G>A; G150R; *rs28360447*	Osteoporosis (Husted et al. 2013; Wesselius et al. 2013a)
		489C>T; H155Y; *rs208294*	Multiple sclerosis (Oyanguren-Desez et al. 2011), sepsis (Geistlinger et al. 2012), chronic pain (Sorge et al. 2012)
		835G>A; R270H; *rs7958311*	Chronic pain (Sorge et al. 2012)
		946G>A; R307Q; *rs28360457*	Osteoporosis (Gartland et al. 2012; Jørgensen et al. 2012)
		1068G>A; A348T (gain of function); *rs1718119*	Osteoporosis (Husted et al. 2013; Jørgensen et al. 2012; Varley et al. 2016; Wesselius et al. 2013a), anxiety disorder (Erhardt et al. 2007), toxoplasmosis (Jamieson et al. 2010)
		1096C>G; T357S; *rs2230911*	Osteoporosis (Gartland et al. 2012)
		1405A>G; Q460R; *rs2230912*	Osteoporosis (Gartland et al. 2012; Husted et al. 2013; Jørgensen et al. 2012; Wesselius et al. 2013a),

			Multiple sclerosis, sepsis (Geistlinger et al. 2012), mood disorders (Barden et al. 2006) (Hejjas et al. 2009; Lucae et al. 2006; McQuillin et al. 2009) but not confirmed by (Green et al. 2009; Grigoroiu‐Serbanescu et al. 2009)
		1513A>C; E496A; *rs3751143*	Osteoporosis (Gartland et al. 2012; Husted et al. 2013; Jørgensen et al. 2012; Ohlendorff et al. 2007; Varley et al. 2016; Wesselius et al. 2013a), tuberculosis (Fernando et al. 2007; Niño‐Moreno et al. 2007; Tekin et al. 2010) but not seen in Chinese population (Xiao et al. 2009)
		1729T>A; I568N; *rs1653624*	Osteoporosis (Gartland et al. 2012; Jørgensen et al. 2012; Ohlendorff et al. 2007)

Table 1.3: Summary of the most reported single polymorphisms and P2X variants and their association with pathological conditions in humans. Table modified from (Caseley et al. 2014).

1.2 P2X4 as a drug target

1.2.1 P2X4 distribution and main physiological functions

P2X4 is characterized by a wide tissue distribution being mainly expressed in the central nervous system, in glandular tissues, lungs, immune cells, testis and epithelial cells (North 2002; Suurväli et al. 2017). P2X4 was initially cloned in rat brain and found in rat spinal cord and non-neuronal organs (Bo et al. 1995; Buell et al. 1996; Soto et al. 1996) and later shown to be strongly expressed in activated microglial cells where it plays a pivotal role in pain neurotransmission (see **Section 1.2.3.3**). P2X4 is also expressed in salivary glands (Tenneti et al. 1998) and endocrine glandular tissues (Stojilkovic and Zemkova 2013) such as the hypothalamus (Vavra et al. 2011), adrenal glands (Tanaka et al. 1996), thymus (Glass et al. 2000; Tanaka et al. 1996), pancreas (Coutinho-Silva et al. 2001), testis (Antonio et al. 2009) and placenta (Roberts et al. 2006b) where purinergic signalling is involved in hormonal regulation and release (Burnstock 2014). P2X4 receptors are present in in HUVEC (Human Umbellical Vein Endothelial Cells) (Yamamoto et al. 2000b) and in capillaries, in arteries and arterioles where they also localize at the level of the endothelium, playing a role in smooth muscle tone (Yamamoto et al. 2006) (see **Section 1.2.3.3** for further details). Furthermore, P2X4 is expressed in lymphocytes (being the most abundant P2X present), monocytes and in CD34+ stem and progenitor cells (Wang et al. 2004) suggesting a role in immune system regulation. Notably, the P2X4 receptor displays a peculiar preferential subcellular localization at the level of early endosomes and lysosomes (Bobanovic et al. 2002; Qureshi et al. 2007) and undergoes fast dynamin-dependent internalization from the membrane after activation and before being recycled and trafficked back to the plasma membrane (Qureshi et al. 2007). It has been shown that N-glycosylation confers stability to P2X4 in the proteolytic lysosomal enviorment, preserving its function and preventing protein degradation (Qureshi et al. 2007). Indeed, lysosomal P2X4 is dually regulated by intraluminal ATP concentration and pH, which at resting condition (lysosomal pH~4.5-5.0) inhibits ATP-induced Ca^{2+} efflux from the lysosome (Huang et al. 2014) as previously shown by multiple research groups who observed that P2X4 activity is pH-dependent (Stoop et al. 1997) (Clarke et al. 2000) and identified His-286 as the amino acid residue responsible for pH-sensitivity (Clarke et al. 2000). In alveolar

type II cells, P2X4 is located in the lamellar bodies (a cellular compartment with many similarities to lysosomes) and is critically important in the secretion and activation of the pulmonary surfactant in the alveoli by promoting fusion pore opening and fusion-activated Ca^{2+} entry (FACE) (Miklavc et al. 2011; Miklavc et al. 2013; Thompson et al. 2013). Very recently, Fois *et al.* showed that the source of ATP required to activate the P2X4 is the lamellar bodies themselves, finely tuning the fusion events process and the localised increase of Ca^{2+} (Fois et al. 2017). The localised increase of Ca^{2+} to which P2X4 contributes stimulates the reabsorption of liquids from the alveolar lumen and the secretion of the lipophilic pulmonary surfactant at the gas-liquid interface (**Figure 1-2**). This process is crucial for the correct gas-liquid exchange in the alveoli during respiration (Fois et al. 2017).

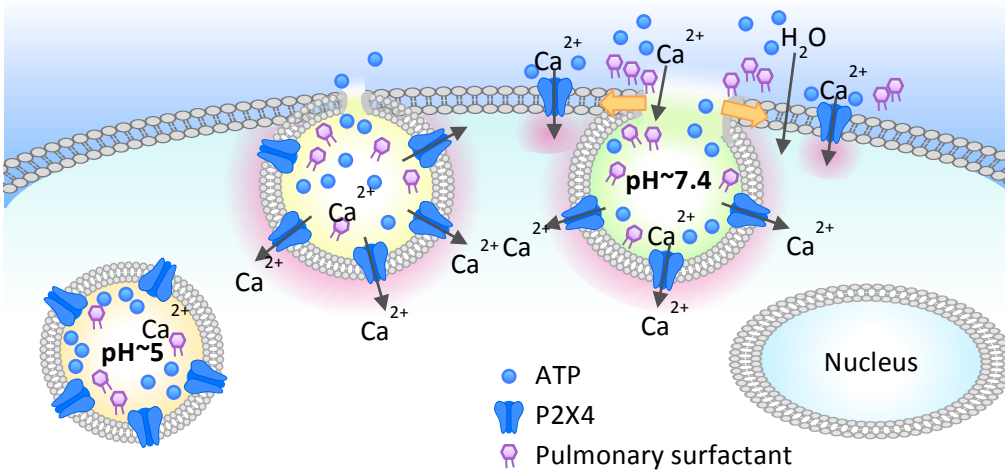

Figure 1-2: P2X4 modulation of pulmonary surfactant secretion in alveolar type II cells. Lamellar bodies are large vacuolar intracellular organelles expressing P2X4 and characterized by acidic pH in the lumen in resting conditions. Under these conditions P2X4 is inhibited. Upon exocytosis, P2X4 becomes part of the plasma membrane and under more alkalinized condition is activated by extracellular ATP resulting in localized increased of Ca^{2+}. The local increase in Ca^{2+} around the fused vesicle promotes the fusion of the lamellar body. Reabsorption of fluid is also promoted assisting the release of surfactant. Figure adapted from (Miklavc et al. 2013).

1.2.2 P2X4 isoforms, polymorphisms and disease susceptibility

Three different isoforms have been identified for human P2X4 (Carpenter et al. 1999; Dhulipala et al. 1998) and interestingly one of these shows a portion of a heat shock protein substituting for TM1, although it is not clear what are the pathophysiological implications of the expression of such isoform and no further study has been conducted on this P2X4 variant. Multiple naturally occurring variants have also been observed for P2X4, some of which are linked to medical conditions or pathologies (see **Figure 1-3** for the location of the most common disease-related and non-disease related point mutations and **Table 1.3**), such as the missense single nucleotide polymorphism (SNP) responsible for the S242G mutation (*rs25644*) which has been linked to increased lumbar bone mineral density (Wesselius et al. 2013b). The same study identified a significant correlation between Y315C – of which the function is impaired – and increased risk of osteoporosis. Multiple studies associated the same polymorphism with increased risk of age-related macular degeneration (AMD) (Gu et al. 2013), increased risk of multiple sclerosis (Sadovnick et al. 2017), increased pulse pressure (Stokes et al. 2011) highlighting the potential involvement of P2X4 in various and highly dissimilar pathologies.

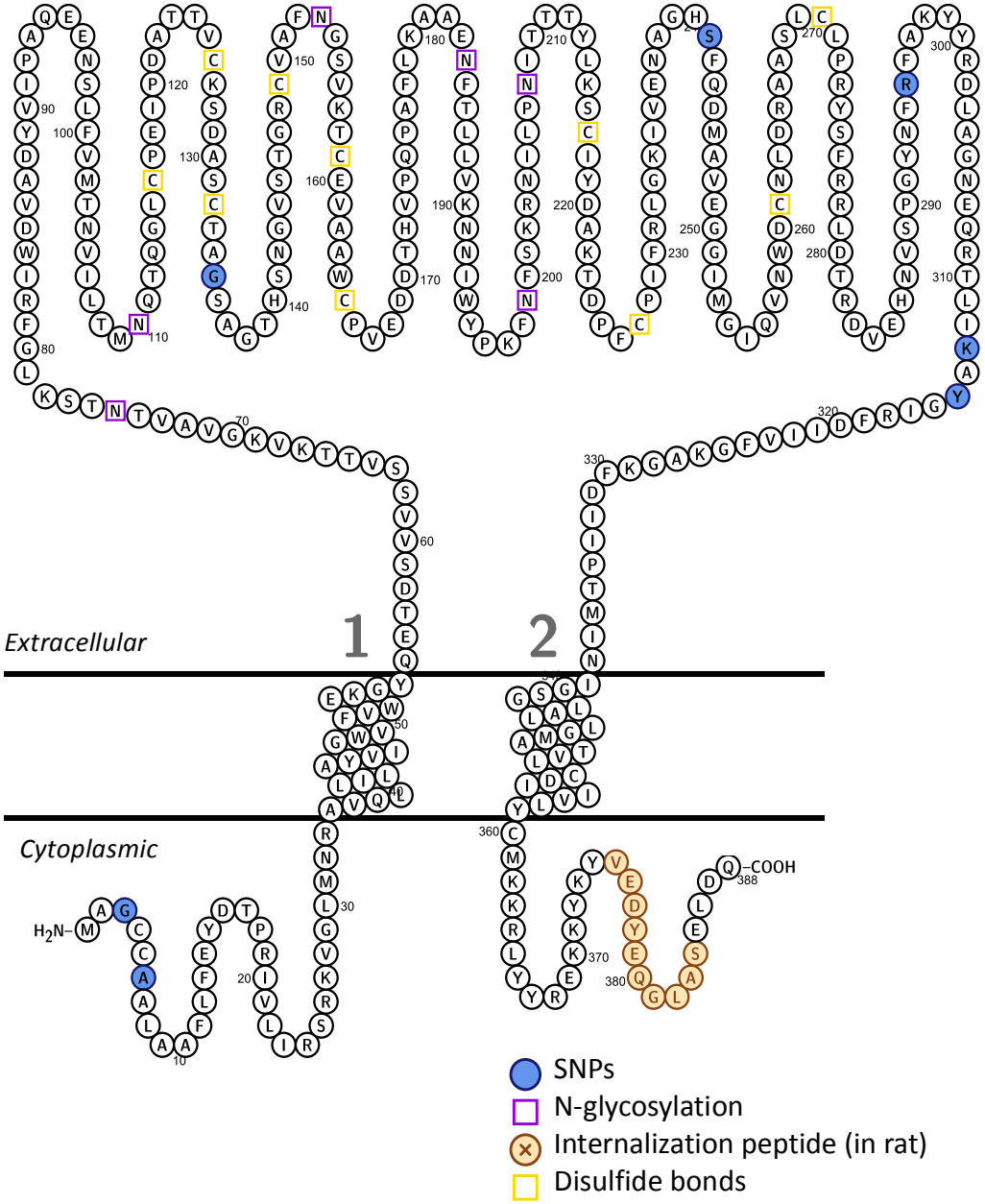

Figure 1-3: Bubble diagram of human P2X4 sequence representing general receptor features and the most-studied single nucleotide polymorphisms (SNPs). Image created using Protter 1.0 (http://wlab.ethz.ch/protter/)

1.2.3 P2X4 involvement in pathological conditions

1.2.3.1 Cardiovascular diseases

P2X4 has been found in the heart where it shows a positive cardio-protective role when overexpressed, while on the contrary a deletion of P2X4 in a rodent model of heart failure has been linked to lower myocyte contractile performance (Hu et al. 2002; Shen et al. 2006; Shen et al. 2009). P2X4 expression was also detected in smooth muscle cells of human mammary artery isolated from patients undergoing coronary bypass (Wang et al. 2002) although the expression was significantly lower than P2X1, the most abundant (Vial and Evans 2002; Wang et al. 2002). The highest expression of P2X4 in the circulatory system is in endothelium, the inner cell monolayer in direct contact with blood. The endothelial cells are capable of sensing the shear stress on the walls of the vessel, which is correlated to an increase of cytosolic Ca^{2+} (Ando et al. 1993). Yamamoto *et al*. demonstrated that P2X4 is responsible for the shear stress-induced Ca^{2+} influx, observing that the activation of P2X4 expressed in HUVEC cells happens in response to increased flow shear-stress combined with low levels of ATP (<250 nmol/L) and is sufficient to induce Ca^{2+} influx (Yamamoto et al. 2000a). The increase of cytosolic Ca^{2+} triggers the activation of the nitric oxide synthase (NOS) and the production of nitric oxide (NO) that has a vasodilatation action on the smooth muscles of the blood vessels (Bredt et al. 1992; Zhao et al. 2015) (see **Figure 1-4**). The discovery of Yamamoto *et al*. has important consequences for our understanding of the physiological mechanism of blood pressure control and was later supported by the observation of increased pulse pressure in humans who have the P2X4 loss-of-function polymorphism Y315C (Stokes et al., 2011). Increased pulse pressure is one of the best-known risk factors contributing in the rise of cardiovascular pathologies. According to the World Health Organization (WHO), approximately 17.7 million (31% of all the deaths) people died worldwide in 2015 due to cardiovascular diseases (CVDs) ranking CVDs as first cause of mortality (World Health Organization (WHO) 2017). If the low-functional P2X4 contributes to increased pulse pressure, then selective P2X4 agonists or allosteric activators might aid in the treatment of hypertension.

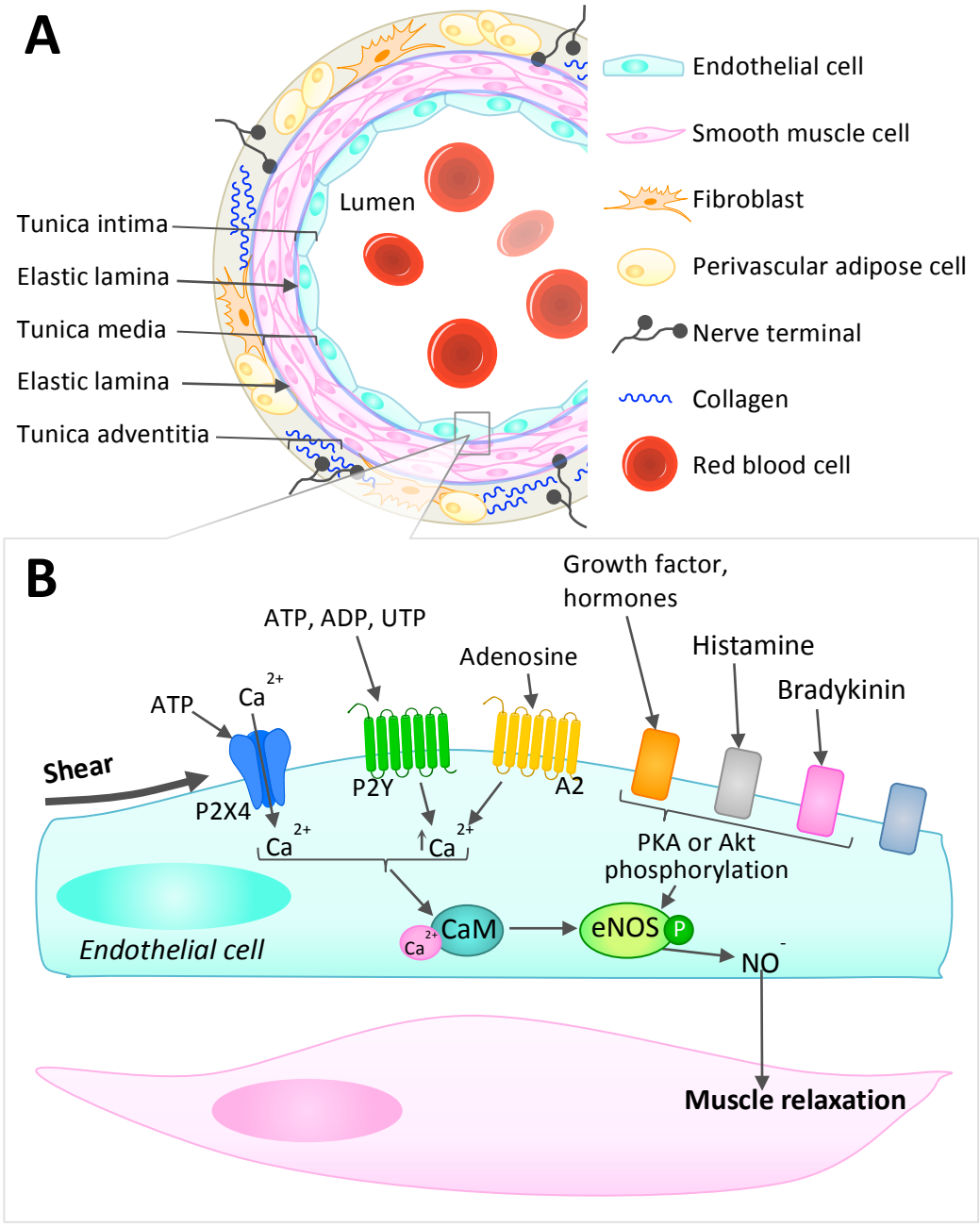

Figure 1-4: Mechanism of shear stress-induced smooth muscle relaxation in blood vessels through activation of P2X4 on endothelial cells. (**A**) Schematic representation of the layers forming blood vessels. Arterioles and arteries differ from veins for a thicker tunica media formed by smooth muscle cells and the presence of an additional elastic membrane between the tunica media and tunica adventitia (outer tunica), not present in veins. (**B**) Mechanism of nitric oxide production in endothelial cells. Nitric oxide is one of the most important physiological mechanisms that controls vasodilation under physiological and pathological conditions.

1.2.3.2 P2X4 in the central nervous system

P2X4 is expressed in the central nervous system and might be involved in the mediation of the glutamatergic and GABAergic signalling. In P2X4 knock-out mice, social interactions are compromised, in addition to the mice displaying as enhanced perception to sensory stimuli (Wyatt et al. 2013). Furthermore, the function of GABAergic and glutamatergic receptor signalling is altered (Du et al. 2012; Duncan 2005), leading to a phenotype that present similarities with rodent models of autism-spectrum disorder (Wyatt et al. 2013). In studies conducted primarily by Professor Davies group, ethanol has shown allosteric modulation at P2X4 (Davies et al. 2002b) and the positive modulation of P2X4 seemed to counteract alcohol dependency behaviour in rodent models (Franklin et al. 2014) (Khoja et al. 2018). The correlation between P2X4 and alcohol dependency remains unproven in humans; a pilot study aiming to test the effect of ivermectin administration on alcohol dependency behaviour in human volunteers failed to show a decrease in alcohol-craving behaviour (Roche et al. 2016).

1.2.3.3 Neuropathic Pain

P2X4 is expressed in microglial cells that are found in brain and spinal cord and represent the prominent form of innate immunity in the central nervous system (CNS). The development of neuropathic pain after nerve damage is an extremely complex mechanism that involves multiple pathways and is characterized by pain hypersensitivity and allodynia (pain caused by otherwise normally innocuous stimuli). After nerve damage, the proliferation of microglia cells in the spinal dorsal horn (SDH) has been observed (referred as microgliosis) (Gilmore and Skinner 1979) and the blockage of this phenomenon avoids the development of pain hypersensitivity (Gu et al. 2016). During microgliosis but not in inflammatory pain, the expression of colony stimulating factor 1 (CSF1) is rapidly increased and the silencing of *Csf1* gene or inhibition of CSF1 receptor reduces migrogliosis and pain hypersensitivity (Masuda et al. 2012). CSF1 is also responsible for the up-regulation of multiple factors and genes including the interferon regulatory factor 8 (IRF8), which in turn induces IRF5 production and localization in the cytoplasm (Masuda et al. 2014; Masuda et al. 2012). Upon stimulation by fibronectin, IRF5 translocates to the nucleus and promotes P2X4 expression (Masuda et al. 2014; Tsuda et al. 2008). Activation of P2X4 results in the release of brain-derived

neurotrophic factor (BDNF). BDNF increases Cl^- levels in neurons by down-regulating the KCC2 chloride channel *via* the TrkB receptor. This intracellular increase in intracellular Cl^- strengthens glutamatergic responses (via NMDA receptors) (Hildebrand et al. 2016) and switches inhibitory GABAergic signalling to excitatory (Coull et al. 2005). This imbalance towards hyper-excitation in neurons is at the base of mechanical allodynia and neuropathic pain (see **Figure 1-5**). In a rodent model of neuropathic pain, P2X4 expression is up-regulated in microglia after peripheral nerve damage (Tsuda et al. 2003; Ulmann et al. 2008). In P2X4 knock-out mice *via* siRNA-silencing, and in pharmacological P2X4 blockade, pain hypersensitivity to innocuous stimuli was abolished after nerve injury (Tsuda et al. 2003). In multiple studies the administration of P2X4 antagonists decreases allodynia and pain hypersensitivity after nerve injury (Matsumura et al. 2016; Nagata et al. 2009). Furthermore the intracranial injection of activated microglial cells (P2X4-stimulated cultured cells) in non-injured rats was sufficient to attain allodyinic responses (Tsuda et al. 2003). Taken together these evidences strongly suggest that the development of selective and potent P2X4 antagonists could be a substantial step for effective treatments towards neuropathic pain treatment, which is still an unmet medical need. In fact, approximately 20% of people suffer from chronic pain worldwide (Treede et al. 2015), and 6-10% of those individuals suffer from neuropathic pain (Bouhassira et al. 2008; van Hecke et al. 2014), a disabling condition due to nerve damage that poorly responds to usual pain-killer treatment options (Kamerman et al. 2015).

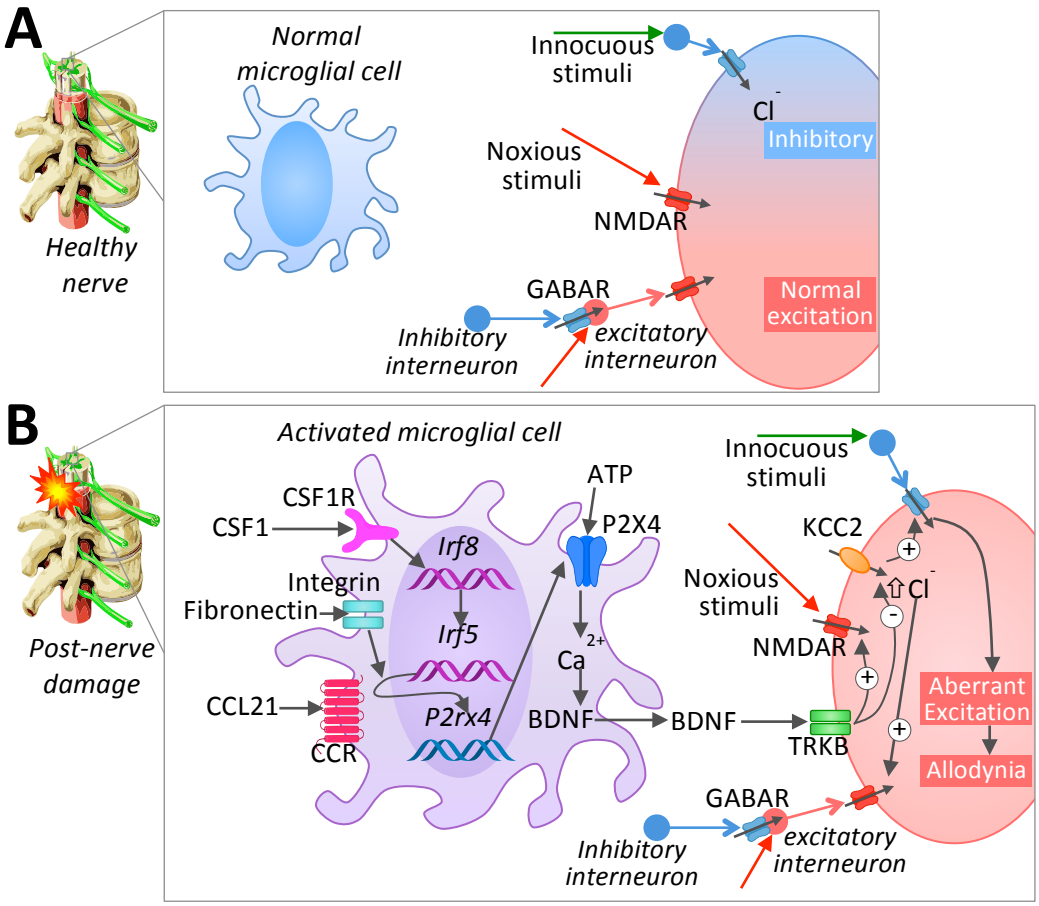

Figure 1-5: Mechanism of pain transduction in individuals without nerve injury (**A**) and after peripheral nerve injury (**B**).

1.2.3.4 P2X4 and airway diseases

Very recently, the role of P2X4 in alveolar type II cells has been investigated and a crucial role in surfactant exocytosis has been observed (see **Section 1.2.1**) (Fois et al. 2017; Miklavc et al. 2011; Miklavc et al. 2013; Thompson et al. 2013). This raises the prospect of targeting a deregulated surfactant secretion system to provide beneficial effects in multiple airway pathological conditions including respiratory distress syndrome in the premature infant, asthma, lung infections, Chronic obstructive pulmonary disease and emphysema and pneumonia (Frerking et al. 2001).

1.3 P2X4 ligands: state of the art

1.3.1 P2X4 antagonists

As yet — despite the rising interest in P2X receptors as drug targets — for most subtypes, relatively few agonists or antagonists have been developed (with scarce subtype-selectivity) and, even in the case of P2X7, where several potent and selective compounds have been described, none have yet successfully passed clinical trials (Gunosewoyo and Kassiou 2010).

In the case of P2X4, few modulators have been described. TNP-ATP, Brilliant Blue G (BBG) and PPADS (see **Table 1.4** for detailed IC_{50} and **Figure 1-6** for chemical structures) are well-known and frequently used as comparative controls in activity assays until recently but none of them display significant subtype selectivity.

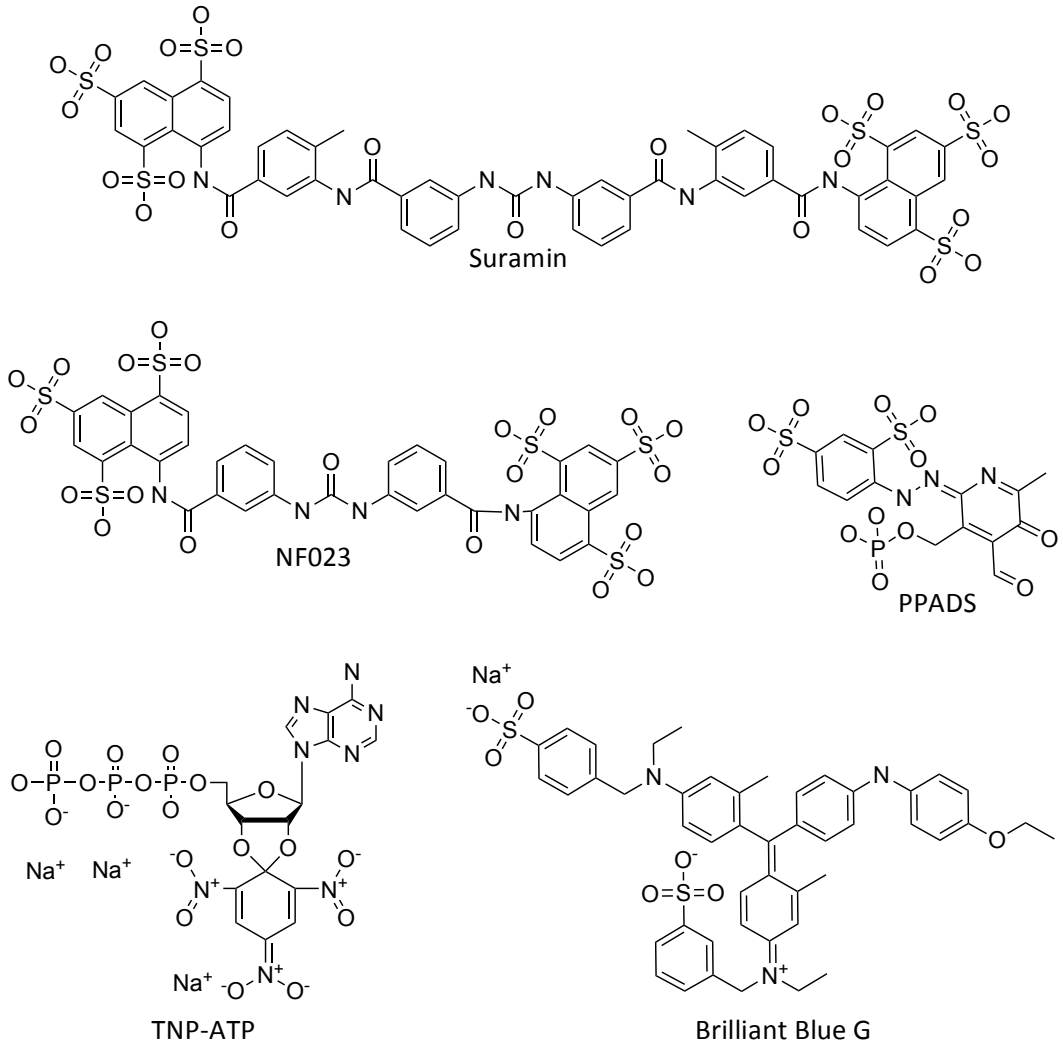

Figure 1-6: Structures of the first generation of unselective antagonists at P2X4

To date, the compound PSB-12054 is one of the most potent allosteric antagonists described in a scientific journal (IC_{50} of 0.189 μM, see **Table 1.4** and **Figure 1-7**), with 35-fold higher selectivity at hP2X4 compared to other human P2X receptors (Hernandez-Olmos et al. 2012). A structurally similar compound, PSB-12062 (discovered by the same research group), also displayed a relatively high potency (IC_{50} of 0.928–1.76 μM), but a lower species-selectivity (among rat, mouse and human) (Hernandez-Olmos et al. 2012). Both compounds present some structural similarities with tricyclic antidepressants, some of which (but not all) display activity at P2X receptors (Hempel et al. 2013; Nagata et al. 2009; Sim and North 2010). Antidepressants such Paroxetine and Fluoxetine show activity at P2X4 and P2X7 but their mechanism of action is slightly controversial in the case of P2X4, where they appear to affect receptor trafficking (Toulme et al. 2010). This effect seems to be subtype-dependent as there is evidence for the two antidepressants acting directly on P2X7 activation (Dao-Ung et al. 2015). In 2014 a new group of compounds was developed from the scaffold of Carbamazepine, another CNS active molecule. Compound 34 was identified as partially selective against human P2X4 displaying an IC_{50} of 3.44 μM (Tian et al. 2014). A patented allosteric antagonist, 5-BDBD, was reported to have a significant potency (IC_{50}= 0.5 μM) and acceptable P2X4-selectivity but the full activity profile was not described in the patent (Fischer et al. 2004), and later characterisation displayed inconsistent results with previous studies (Balázs et al. 2013). Further analogues of 5-BDBD (in addition to the original patent) among whose some N-methylated compounds have been synthesized and their activity is reported to be comparable with 5-BDBD (Wang et al. 2017a). A substantial advance in P2X4-selective compound development occurred in 2015 when a new allosteric antagonist, BX430, was described as potent and selective with IC_{50} of 0.55 μM and approximately 100-fold higher potency compared to human P2X7 (although the data regarding to selectivity were not shown in the publication (Ase et al. 2015)). Very recently the group led by Professor Tsuda published the structure of NP-1815-PX, a potent and selective allosteric modulator (IC_{50} of 0.26 μM) with anti-allodynic effect in a rodent model of herpetic pain becoming one of the first P2X4 compounds active in an animal model reported in literature (Matsumura et al. 2016). NP-1815-PX is poorly permeable to the blood brain barrier (BBB) but NC 2600, a compound developed by the same collaboration between Kyushu University and Nippon Chemipharm with better ADMET profile, has advanced to Phase I of clinical trial

(Inoue and Tsuda 2018). Some antagonists are only reported in patents, an example worth remembering is the structure herein called Compound 30 (see **Figure 1-7** and **Table 1.4**), which showed a very high potency in cell based assay with a reported IC_{50} lower than 0.1 μM (Newcom and Spear 2015).

P2X4 activation (in contrast to most of the other receptor subtypes) is sensitive to pH, which has important implications in physiological conditions (see **Section 1.2.1**).

Intriguingly, ethanol has been demonstrated to act as a P2X4 antagonist in rodent models, with an IC_{50} of approximately 50 mM in rat (Xiong et al. 2000). Despite a much lower potency compared to other antagonists, the action of ethanol on P2X4 receptors (known to be expressed in the central nervous system) has opened a new perspective in the development of animal models of alcohol dependency. Since the inhibitory effect of ethanol is antagonized by ivermectin (Asatryan et al. 2010), the use of ivermectin has been explored and proposed to treat alcohol dependency behaviour (see **Section 1.2.3.2**). Although, a recent pilot study in human volunteers failed to show a decrease in alcohol-craving behaviour (Roche et al. 2016).

Compound	IC_{50} (μM)	Methods	References
Antagonists and negative allosteric modulator			
Suramin	>300	two-electrode voltage-clamp	(Soto et al. 1996)
NF023; 8,8'-[carbonylbis(imino-3,1-phenylenecarbonylimino)]bis-1,3,5-naphthalene-trisulphonic acid	>100	two-electrode voltage-clamp	(Soto et al. 1999)
PPADS; 4-[2-[4-formyl-6-methyl-5-oxo-3-(phosphonooxymethyl) pyridin-2-ylidene] hydrazinyl] benzene-1,3-disulfonic acid	>300	two-electrode voltage-clamp	(Soto et al. 1996)
BBG; Brilliant Blue G; sodium;3-[[4-[(E)-[4-(4-ethoxyanilino)phenyl]-[4-[ethyl-[(3-sulfonatophenyl)methyl]azaniumylidene]-2-methylcyclohexa-2,5-dien-1-ylidene]methyl]-N-ethyl-3-methylanilino]methyl]benzenesulfonate	3–100	whole-cell patch clamp	(Jiang et al. 2000a)
TNP-ATP, 2',3'-O-(2,4,6-Tri-nitrophenyl)adenosine-5'-triphosphate	15	whole-cell patch clamp	(Virginio et al. 1998)
5-BDBD; 5-(3-Bromophenyl)-1,3-dihydro-2H-benzofuro[3,2-e]-1,4-diazepin-2-one	0.5	Ca^{2+} influx assay	(Fischer et al. 2004)
Paroxetin	1.87	whole-cell patch clamp; Ca^{2+} imaging assay	(Nagata et al. 2009)
Compound 34; N,N-diisopropyl-5H-dibenz[b,f]aze- pine-5-carboxamide	3.44	Ca^{2+} influx assay	(Tian et al. 2014)
BX-430; N-[2,6-Dibromo-4-(1-methylethyl)phenyl]-N'-(3-pyridinyl)urea	0.5	Ca^{2+} influx assay; whole-cell patch clamp	(Ase et al., 2015
PSB-12054	0.189	Ca^{2+} influx assay	(Hernandez-Olmos et al. 2012)
PSB-12062	0.9-1.7	Ca^{2+} influx assay	(Hernandez-Olmos et al. 2012)

NP-1815-PX; (5-[3-(5-thioxo-4H-[1,2,4]oxadiazol-3-yl)phenyl]-1H-naphtho[1, 2-b][1,4]diazepine-2,4(3H,5H)-dione)	0.26	Ca^{2+} imaging assay; hot plate and tail flick in mice models	(Matsumura et al. 2016)
NC 2600 (unknown structure)	n/a	n/a	(Inoue and Tsuda 2018)
Compound 30 (WO 2015088564 A1); 3-acetyl-8-chloro-4-(pyridin-3-yl)-1,5-dihydro-2H-pyrido[3,2-b]indol-2-one; (as representative of the class)	<0.1	Ca^{2+} influx assay	(Newcom and Spear 2015)
H^+	pKa ~ 7.0	whole-cell patch clamp	(Stoop et al. 1997)
Cu^{2+}	10	whole-cell patch clamp	(Coddou et al. 2007)
Hg^{2+}	10	whole-cell patch clamp	(Coddou et al. 2005)
CO	Not determined	whole-cell patch clamp	(Wilkinson et al. 2009)
CORM-2	36.6	whole-cell patch clamp	(Wilkinson and Kemp 2011)
Ethanol	50000-60000	whole-cell patch clamp	(Xiong et al. 2000; Davies et al. 2002a)

Table 1.4: P2X4 antagonists and allosteric modulators.

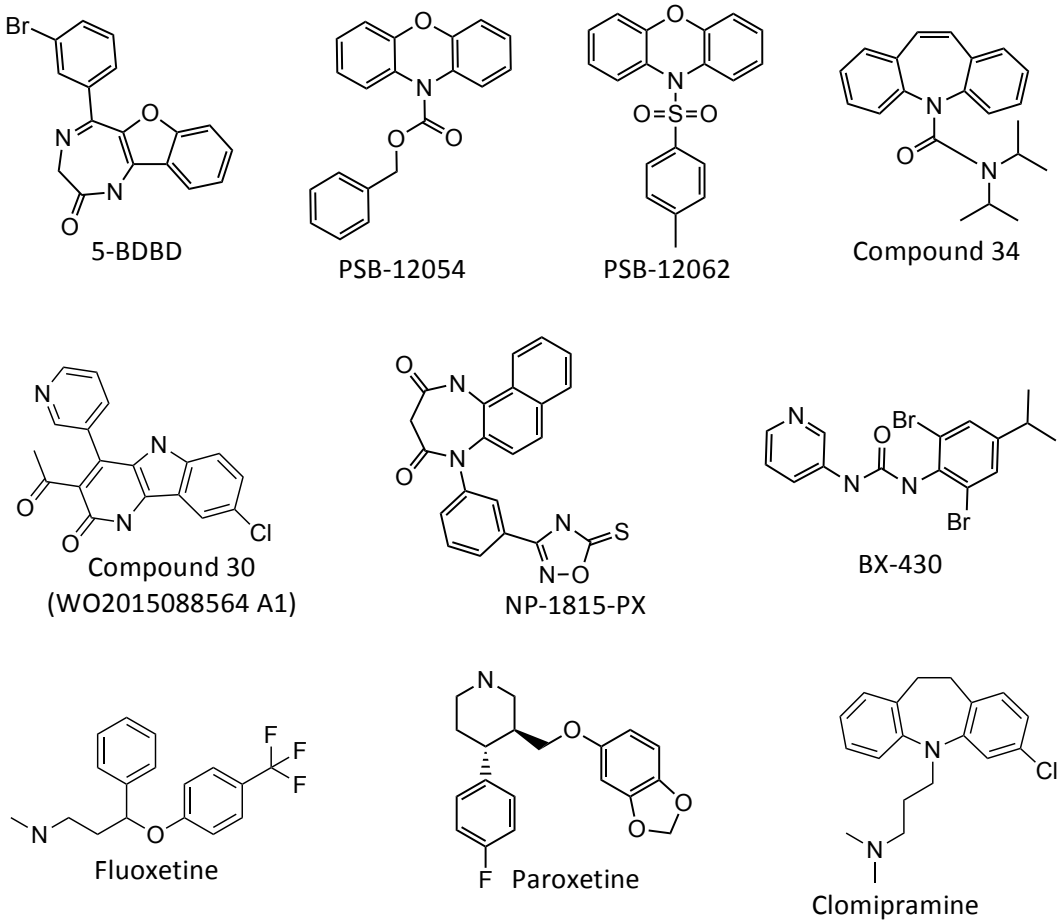

Figure 1-7: Structures of recent P2X4 antagonists and antidepressants with reported activity at P2X4 or at receptor trafficking.

1.3.2 P2X4 agonists and positive allosteric modulators

Compared to other P2X receptor subtypes, P2X4 has a distinctive sensitivity profile towards agonist molecules; it is only partially activated by 2meSATP and BzATP (EC_{50}=10-100 μM and EC_{50}=3-10 μM respectively, see **Figure 1-8**), and poorly activated by either αßmeATP or other ATP analogues (see **Table 1.5** for a comprehensive list of modulators and the corresponding potencies). **Figure 1-8** and **Figure 1-10** report the structures of P2X4 modulators (selection).

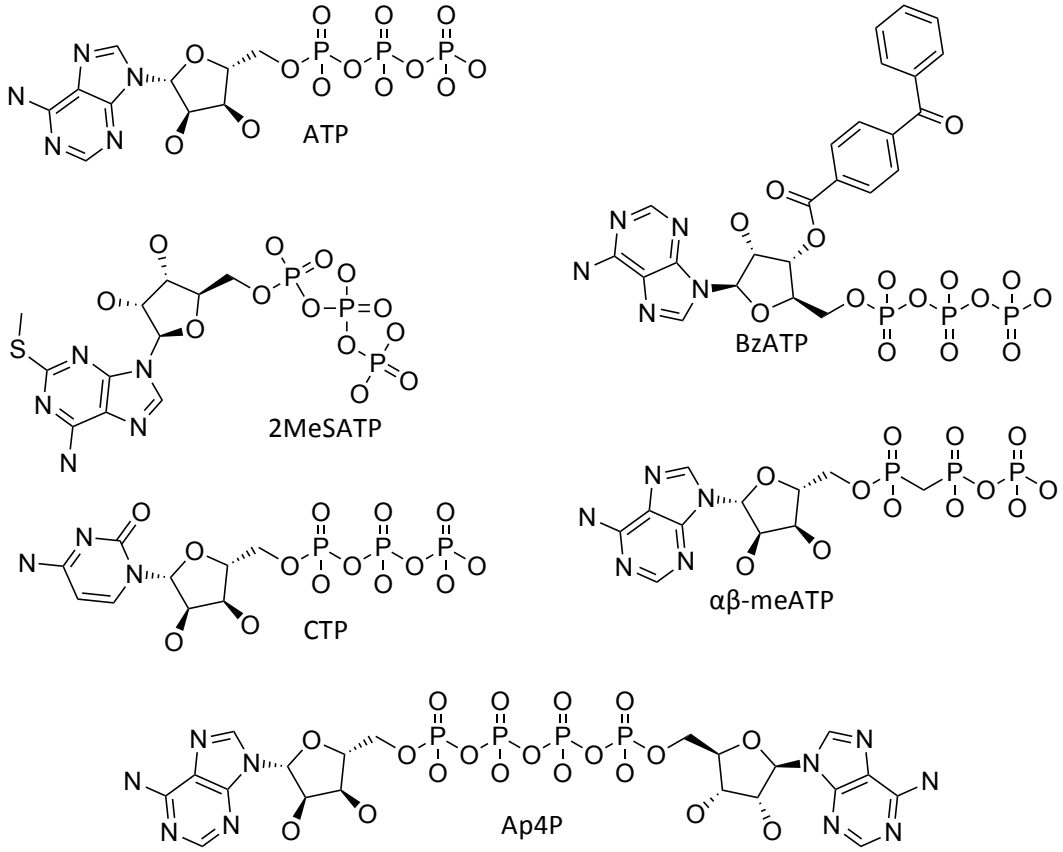

Figure 1-8: Structures of agonist and partial agonists at P2X4 receptor.

Ivermectin (IVM) is an anti-parasitic macrolide drug whose primary mode of action is the positive allosteric modulation of GluCls (glutamate-activated chloride channels) (Hibbs and Gouaux 2011), which causes paralysis in invertebrates. Ivermectin is an non-selective allosteric modulator at numerous receptors such as glutamate-sensitive Cl^- channel, alpha-glycine receptor (Du et al. 2015; Huang et al. 2017; Shan et al. 2001), nicotinic acetylcholine receptor α7 (Krause et al. 1998) and GABA receptor (Menez et al. 2012). Ivermectin also modulates P2X4 and has been demonstrated to both prolong and increase the ATP-response at P2X4 in an allosteric manner (Priel and Silberberg 2004). Although its mechanism of action at P2X4 has not been elucidated, mutagenesis studies (Jelínkova et al. 2008; Jelínková et al. 2006; Silberberg et al. 2007), biophysical-mathematical (Mackay et al. 2017) and molecular modelling studies (Latapiat et al. 2017; Pasqualetto et al. 2018) and two ivermectin-bound crystal structures of three different ionotropic receptors (GluCls, α1-glycine receptor and α3-glycine receptor, PDB ID entries: 3RI5, 3JAF and 5VDH respectively. 3RI5 and 3JAF are compared in **Figure 1-9**) strongly suggest that the drug might insert at the level of the phospholipid bilayer, between transmembrane domains at the subunit interface, preventing closure of the ion channel. Ivermectin is a valid tool for the study of P2X receptor pharmacology but caution needs to be taken when investigating ivermectin in drug repurposing due the non-selective profile and its ability to interact with a great variety of receptors present in the nervous system.

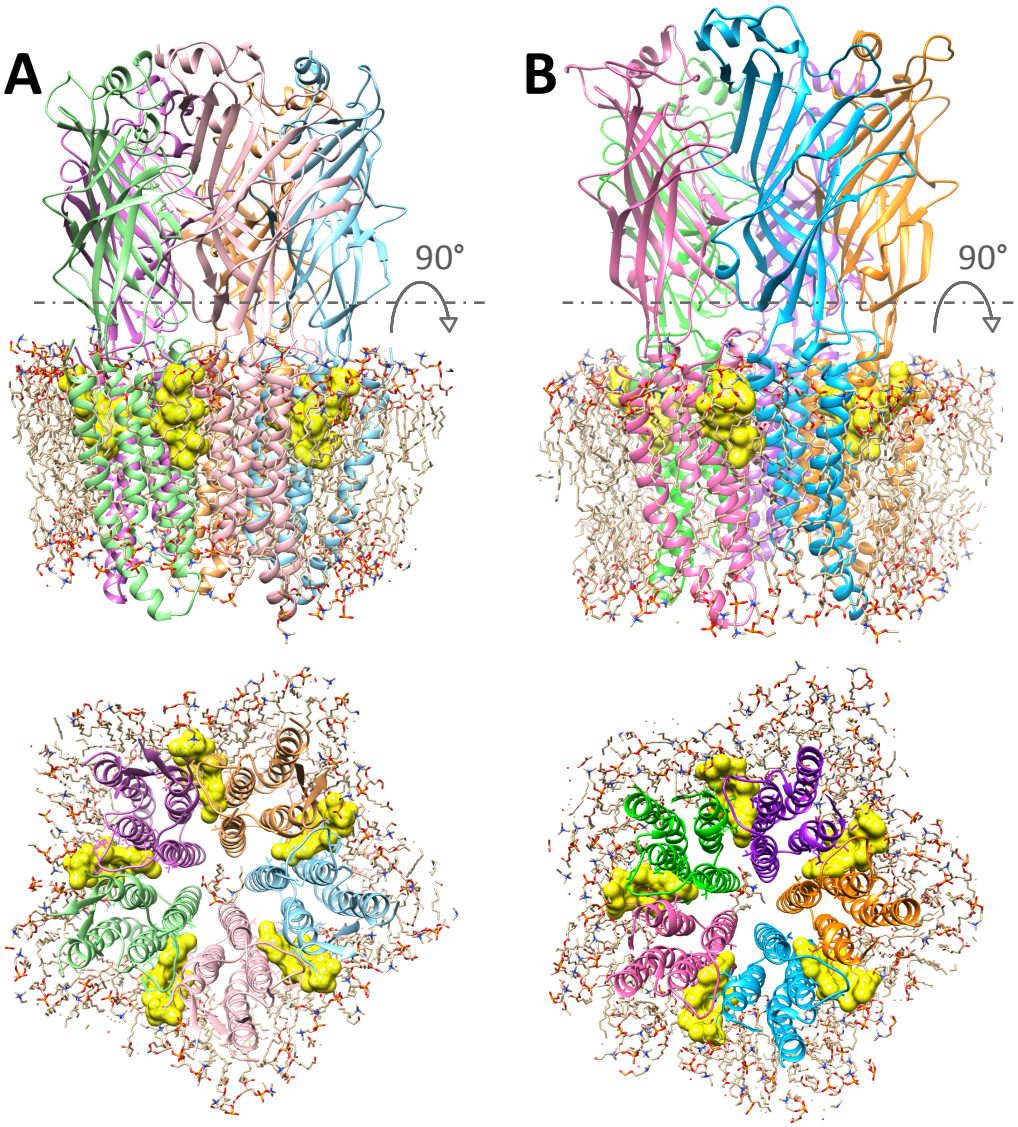

Figure 1-9: Crystal structure of glutamate-sensitive Cl channel (A, PDB ID: 3RI5) (Hibbs and Gouaux 2011) and of the alpha-glycine receptor (**B**, PDB ID: 3JAF) (Du et al. 2015) in complex with ivermectin. Structures embedded in the lipid bilayer were obtained from MemProtMD database (http://memprotmd.bioch.ox.ac.uk).

An allosteric positive modulation in the low nanomolar range was also seen for group of neuroactive steroids (see **Table 1.5**) including alphaxalone (EC_{50}=0.3-1 nM (Codocedo et al. 2009)). It is unclear whether the modulatory effect is due to a specific binding-site interaction or to the interplay with the membrane surrounding the receptor: specific stereo-selective steroid effects were not investigated on P2X4. However, the aforementioned neurosteroids are not

receptor-selective, being also $GABA_A$ blockers (alphaxalone IC_{50}=0.9 μM in the presence of GABA and IC_{50}=90 μM in its absence) with general anaesthetic properties (alphaxalone is approved for veterinary use), therefore causing major and potentially dangerous side-effects.

Compound	EC_{50} (µM)	Methods	References
Full agonists			
ATP; Adenosine triphosphate	1–10	two-electrode	(Soto et al. 1996)
		whole-cell patch clamp	(Jones et al. 2000; Stokes et al. 2011)
Partial agonists			
BzATP; 3'-O-(4-Benzoylbenzoyl)ATP (**Note:** usually sold as isomer mixture with 2'-O-(4-Benzoyl)benzoyl ATP)	9.4	whole-cell patch clamp	(Stokes et al. 2011)
2-meSATP	4–300	two-electrode voltage-clamp	(Soto et al. 1996)
		whole-cell patch clamp	(Jones et al. 2000)
αβ-meATP	>300-	two electrode voltage-clamp	(Soto et al. 1996)
CTP	200	two-electrode voltage-clamp	(Soto et al. 1996)
	564	two-electrode voltage-clamp	(Kasuya et al. 2016)
Ap4P; Diadenosine Tetraphosphate	2-10	two-electrode voltage-clamp	(Wildman et al. 1999)
		whole-cell patch clamp	(Jones et al. 2000)
Positive Modulators			
Ca^{2+}	1000	whole-cell patch clamp	(Khakh et al. 1999)
Zn^{2+}	5	whole-cell patch clamp	(Soto et al. 1996; Coddou et al. 2007)
Cd^{2+}	20	two-electrode voltage-clamp	(Coddou et al. 2005)
IVM	0.250	whole-cell patch clamp	(Khakh et al. 1999)
Alfaxalone	0.4	whole-cell patch clamp	(Codocedo et al. 2009)
ALP; allopregnanolone	0.3	whole-cell patch clamp	(Codocedo et al. 2009)
THDOC; Tetrahydrodeoxycorticosterone; 3α,21-dihydroxy-5α-pregnan-20-one	0.1	whole-cell patch clamp	(Codocedo et al. 2009)

Cibacron blue	>300	whole-cell patch clamp	(Miller et al. 1998)
Propofol	50	whole-cell patch clamp	(Tomioka et al. 2000)

Table 1.5: Potencies of P2X4 agonists and allosteric (positive) modulators.

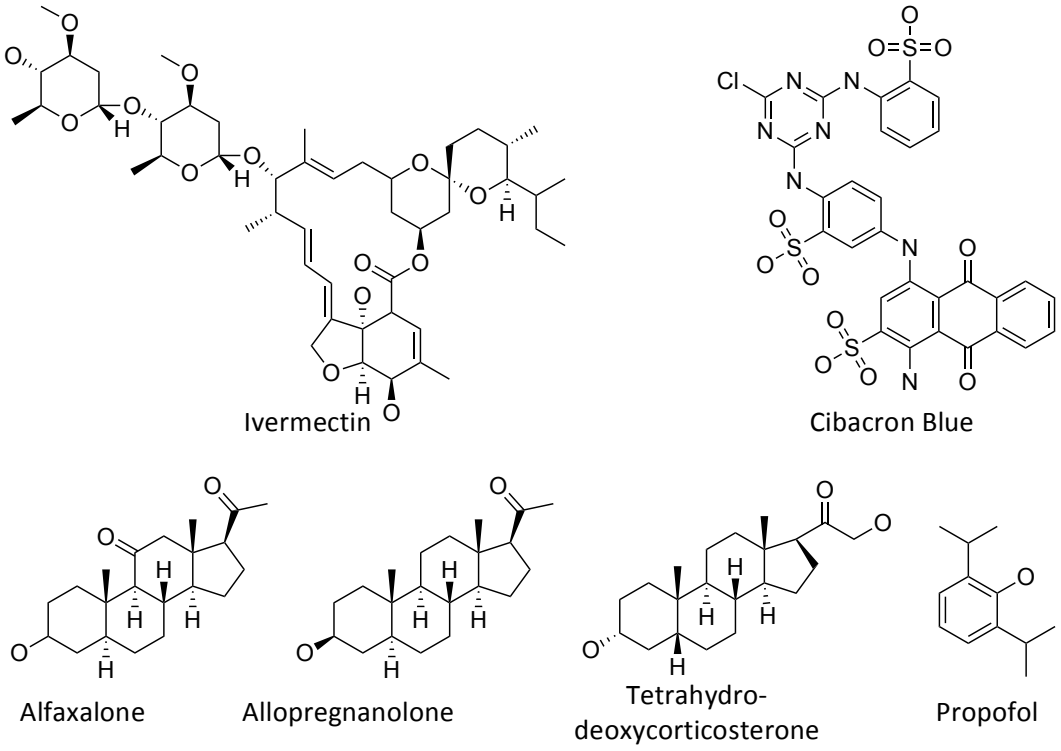

Figure 1-10: Structures of P2X4 positive allosteric modulators

In conclusion, the clear physiological significance of P2X4 receptor together with the lack of available well-characterised, highly potent and selective compounds (IC_{50} values in the low nanomolar range), highlights the need to develop novel selective and potent modulators and any class of molecule (agonist, positive allosteric modulator, competitive or allosteric antagonist) may be of potential therapeutic benefit.

1.4 P2X7 as a drug target

1.4.1 P2X7 C-terminal domain

One distinctive characteristic of P2X7 is its long (240 amino-acid) intracellular C-terminal domain (CTD), which undergoes post-translational modification (palmitoylation) of at least 3 groups of cysteine residues, which presumably anchor the C-terminal domain to the plasma membrane like molecular staples. Mutation of these domains (and consequent lack of palmitoylation) leads to lack of receptor expression and alteration of receptor function (Gonnord et al. 2009; Karasawa et al. 2017). A second distinctive characteristic of P2X7 is its ability to form a large-conductance pore permeable to fluorescent dye molecules following activation, which is thought to require the distal portion of the CTD (amino-acids 582-595) (Smart et al., 2003). Recently, *Karasawa et al.* reconstituted a giant panda P2X7 construct lacking significant portions of both the N- and C-terminal domains into synthetic lipid vesicles, and demonstrated the ability of this construct to form the large-conductance pore, implying that the CTD is not required for pore formation. However, the authors also demonstrated that incorporation of cholesterol into the vesicles markedly attenuated pore formation, suggesting a physiological role for the CTD in binding cholesterol to counteract its inhibitory effect on pore formation (Karasawa et al. 2017). While the 3-dimensional structure of the CTD is not known, multiple protein- and lipid-binding motifs have been identified within it (**Figure 1-11**), which confer exclusive physiological properties to the receptor including its role in inflammation and cell death. Among the identified motifs are the Src homology 3 (SH3) binding domain (441-460, rat numbering) (Denlinger et al. 2001), a tumour necrosis factor receptor 1 (TNFR1) homology region (436-531, rat numbering) identified as a death domain responsible for apoptosis (Denlinger et al. 2001), two regions usually found in cytoskeleton-interacting proteins (389-405; 494-508) and a lipopolysaccharide (LPS)-binding region (573-590) (Denlinger et al. 2001). The presence of multiple motifs led to the hypothesis of multiple interacting proteins (Kim et al. 2001), and a number of interactors have been identified, including cytoskeletal proteins (such as ß-actin, α-actinin 4, laminin α-3) and a variety of cytoplasmic and membrane proteins involved in trafficking and signalling

(http://www.p2x7.co.uk). In the light of the recent crystal structure of human P2X3 (see **Section 1.5.2**) it might also be hypothesized that a portion of the P2X7 CTD may form a cytoplasmic cap when binding ATP (Mansoor et al. 2016).

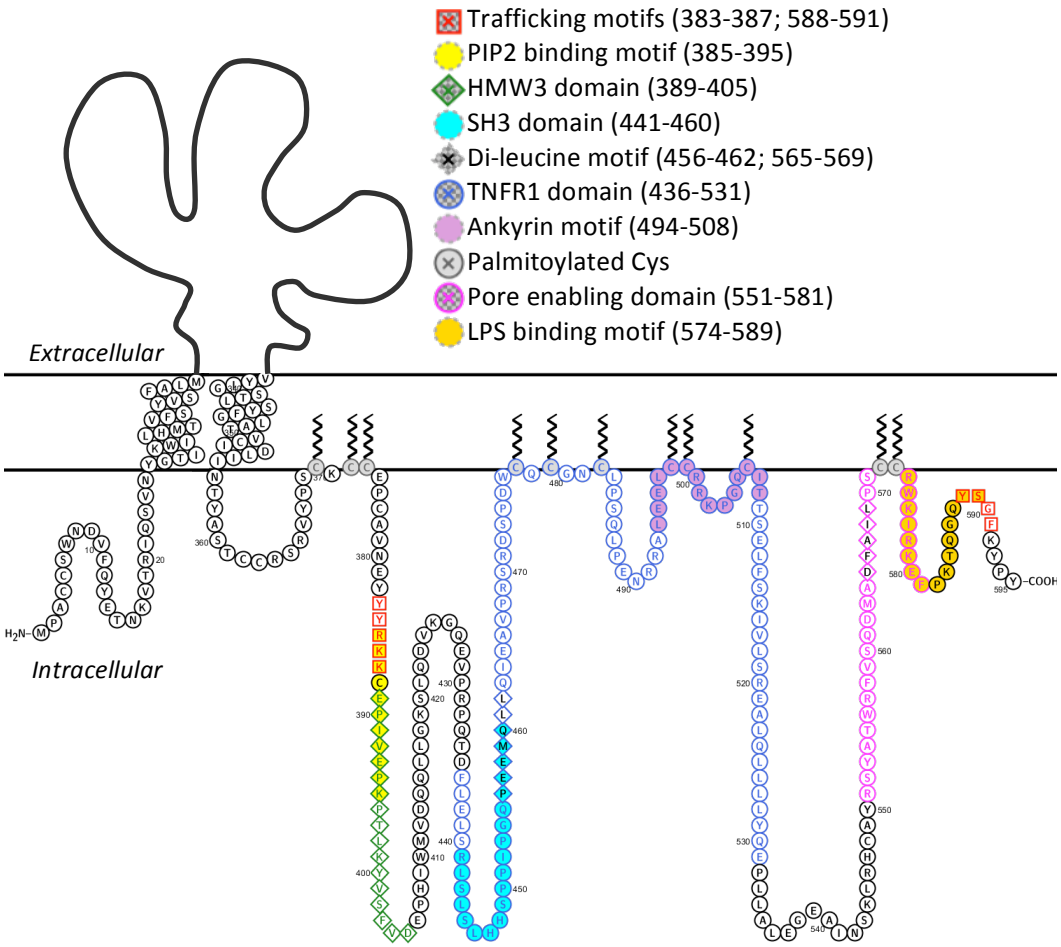

Figure 1-11: C-terminal motifs present in rat P2X7 receptor. The palmitoylation is depicted for all the cysteines found involved in post-translational modification according to Gonnord *et al.* (groups of cysteines that gave approximately 50% of surface expression are also shown anchored to the membrane) (Gonnord et al. 2009).

1.4.2 P2X7 distribution and main physiological functions

P2X7 is mostly expressed in osteoclasts and hematopoietic cells such as macrophages, monocytes, erythrocytes, eosinophils, lymphocytes, natural killer cells, dendritic cells and mast cells (Burnstock and Knight 2004; Gu et al. 2000; Kaczmarek-Hájek et al. 2012). P2X7 is also found in fibroblasts, various endothelial and epithelial tissues, nervous system cells such as microglia, oligodendrocytes, astrocytes and also peripheral nervous system cells (Burnstock and Knight 2004; Gorodeski 2012; Montreekachon et al. 2011; Wilson et al. 2007). Furthermore P2X7 is present in several different cell types in the eye (Sanderson et al. 2014), including the lachrymal gland where it is responsible for triggering protein secretion through an increase in intracellular Ca^{2+} (Hodges et al. 2009), corneal epithelium (also present as splice variant) (Mankus et al. 2011), amacrine cells where it may modulate GABAergic signalling and the outer plexiform layer where P2X7 may control photoreceptor function (Puthussery and Fletcher 2004). In retinal ganglion cells P2X7 stimulation leads to cell death (Hu et al. 2010) while in retinal pigment epithelium P2X7 activation decreases cell turnover and increases lipid oxidation (Guha et al. 2013).

In several cell types (including astrocytes, macrophages and monocytes), the activation of P2X7 leads to activation of JNK-1/2, ERK-1/2 and p38 as part of the MAPK/ERK signalling cascade (Bradford and Soltoff 2002; Potucek et al. 2006). P2X7 activation is involved in numerous pathways; notably it is involved in the release of pro-inflammatory cytokines especially interleukin 1 beta (IL-1ß) and interleukin 18 (IL-18) through NLRP3 inflammasome activation. Inflammasomes are cytosolic assemblies of multiple proteins that act as bio-molecular sensors. NLRP3 in particular is formed by a NOD-like receptor (NLR), adapter protein apoptosis associated speck-like protein (ASC) and procaspase 1 and their oligomerization which in turn leads to proteolysis, caspase 1 activation and subsequent excretion of pro-inflammatory cytokines (Martinon et al. 2009). P2X7 activation has been associated with NRLP3 activation and rapid release of pro-inflammatory cytokines through microvescicle shedding in human THP-1 monocytes – a novel mechanism of secretion for secretory proteins lacking specific secretory motifs (Ferrari et al. 1997; MacKenzie et al. 2001). The mechanism of activation of the inflammasome is still unclear but reactive oxygen species (ROS) production, release of oxidized

mitochondrial DNA (mtDNA) in the cytoplasm and potassium efflux play key roles in its activation, and it has been proposed that P2X7 NLRP3-activation follows a similar cascade of events (**Figure 1-12**) (Dubyak 2012; Kanneganti et al. 2007) (He et al. 2016).

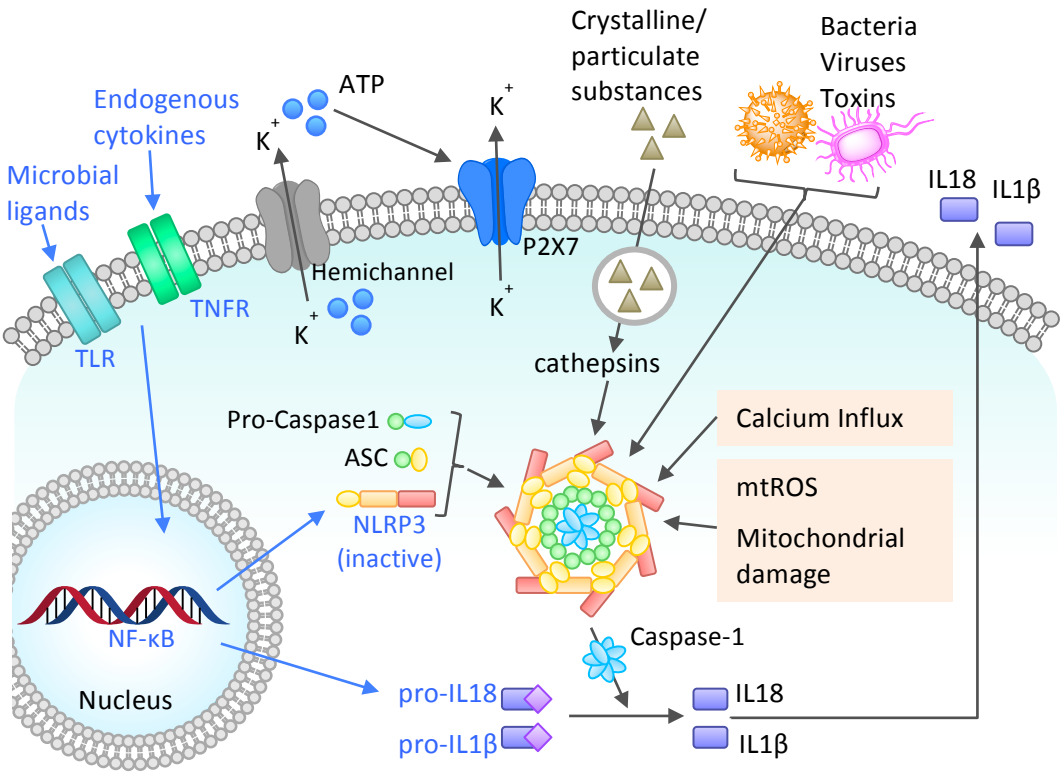

Figure 1-12: Inflammasome NLRP3 activation and pro-inflammatory cytokines release through microvesicle shedding (He et al. 2016). NLRP3 activation may be the results of two different signals: (i) priming (arrows and labels in blue) and (ii) activation (in black). (i) Pro-interleukin-1 beta (pro-IL ß) and NLRP3 (whose levels at rest in macrophages are insufficient for inflammasome activation) are upregulated by exposure to microbial molecules and endogenous cytokines through activation of NF-kB. (ii) Stimuli such as toxins, ATP, K+ efflux activates Caspase-1 converts pro-IL ß in IL ß, which is secreted through microvescicle shedding.

1.4.3 Polymorphisms and isoforms

P2X7 not only has widespread tissue distribution but also a wide number of receptor isoforms. Ten different splice isoforms are present in humans (A-J) of which isoform A is the best characterized and contains 13 exons displaying the canonical 595 amino acids (Cheewatrakoolpong et al. 2005). Among the others, isoforms G and H show an additional exon (N3) giving rise to an alternative starting codon and a receptor which lacks the first transmembrane domain (TM1) (Cheewatrakoolpong et al. 2005), while more than one isoform lacks or presents a shorter CTD (B, E and G). Of particular interest, isoform B is expressed in multiple tissues (spleen, lymph node, thymus tonsil, bone marrow, lung brain, fetal liver) and in higher levels compared to isoform A in lymphoid tissues and lymphocytes (Adinolfi et al. 2010; Cheewatrakoolpong et al. 2005). It has been shown that isoform A and B heterotrimers form functional receptors with increased activity, pore formation and membrane blebbing and their activation leads to increased levels of extracellular ATP and intracellular Ca^{2+} resulting in lymphocyte proliferation via nuclear factor activation (Adinolfi et al. 2010; Cheewatrakoolpong et al. 2005).

P2X7 displays also a high degree of polymorphism with more than 650 recorded single nucleotide polymorphisms (SNPs) (Bradley et al. 2011), of which most are intronic or synonymous. However, among the non-synonymous SNPs, some have been associated with higher risk for pathologies such as age-related macular degeneration (AMD) (together with P2X4), osteoporosis and mood disorders (see **Table 1.3**). The *rs3751143* (E496A) polymorphism is a loss-of-function mutation of the receptor that is highly associated with tuberculosis susceptibility. A SNP responsible for a gain-of-function mutation is associated with increased pain sensitivity following mastectomy or osteoarthritis (*rs208294* (Y155H)), while in contrast, for the hypo-functional mutation caused by SNP *rs7958311* (R270H), lower pain susceptibility has been reported (Sorge et al. 2012).

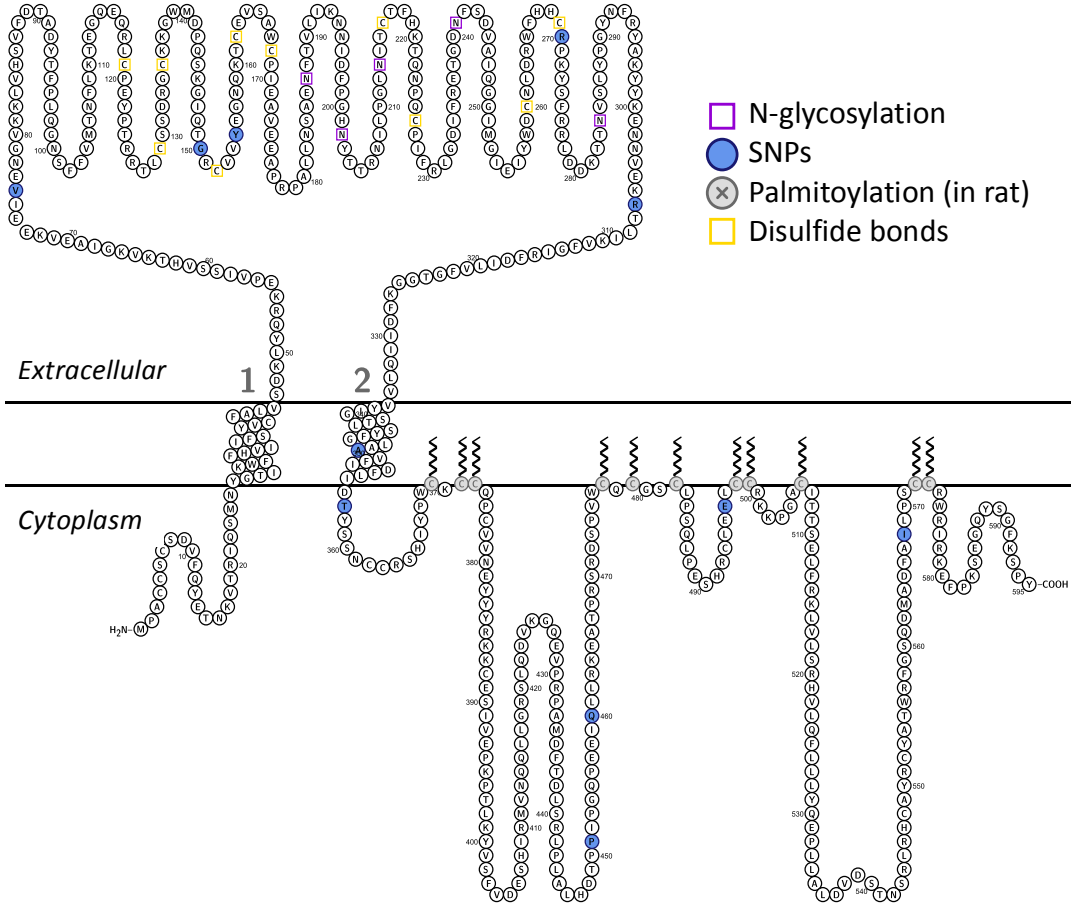

Figure 1-13: Recurrent polymorphisms in human P2X7 sequence.

1.4.4 P2X7 involvement in pathophysiology

1.4.4.1 Inflammation, infection and immunity

Extracellular ATP is a danger-signal molecule that activates inflammatory and immune responses. P2X7 activation in response to ATP released from damaged or infected cells leads to release of pro-inflammatory cytokines, in particular interleukin (IL)-1β, through the NLRP3-inflamasome pathway (Giuliani et al. 2017). This also happens in polarized pro-inflammatory macrophages (M1) but in polarized anti-inflammatory macrophages (M2) the activation of the inflammasome and ROS production appears to be disconnected from P2X7 activation (Pelegrin and Surprenant 2009). The role of P2X7 in innate immunity was further highlighted in animal models of bacterial and parasite infections where hypo-activation of P2X7 (or loss of receptor in knock-out animals) led to a reduced ability to contain the infection. In mice with viral infection, P2X7 activation regulates the acute immune response (Corrêa et al. 2016; Graziano et al. 2015; Morandini et al. 2014; Swartz et al. 2015; Tewari et al. 2015). Inflammation plays a substantial role in many physiological and pathological conditions, therefore it is not a surprise that P2X7 is involved in a variety of diverse diseases. P2X7 involvement has been suggested in allergy, chronic obstructive pulmonary disease (COPD), asthma, cystic fibrosis and airway infection (Zheng et al. 2017), and injury (Lucattelli et al. 2011; Monçao-Ribeiro et al. 2014). It also plays a role in Inflammatory bowel disease (IBD) (Kurashima et al. 2015), in the damaging of kidney in nephritis (Zhao et al. 2013) and in inflammatory skin disorders such as psoriasis, chronic dermatitis as well as wound healing (Geraghty et al. 2016). Strong evidence from animal models implicating P2X7 in osteoarthritis led to the first clinical evaluations of a P2X7 antagonist in rheumatoid arthritis (Keystone et al. 2012b; Stock et al. 2012) and in Crohn's disease (Eser et al. 2015). No efficacy was observed against rheumatoid arthritis (Keystone et al. 2012b; Stock et al. 2012) and in diminishing pro-inflammatory markers in Crohn's diseases (although AZ9056 showed potential in reducing the chronic pain associated with the disease (Eser et al. 2015)) and thus the potential of anti-P2X7 for inflammatory diseases and at which stage of the disease P2X7-signalling blockage is efficacious is still under debate.

1.4.4.2 Age related macular degeneration (AMD)

Age-related macular degeneration (AMD) is an incurable condition characterized by progressive tissue degeneration and cell death leading ultimately to loss of central vision. WHO (World Health Organization) reports AMD as the third prominent cause of blindness worldwide ranking it higher than diabetic retinopathy (World Health Organization (WHO) 2018). Globally, AMD is the first among the non-avoidable causes of visual impairment and in the United Kingdom there are more than 600,000 sufferers according to NHS (National Health Service (NHS) 2018). Two forms of AMD have been classified (wet and dry) according to the presence of abnormal angiogenesis under the macula and currently there are relatively few treatment options for the wet form, mainly surgery or intraocular injection of anti-VEGF antibodies (National Institute for Health and Care Excellence (NICE) 2018), whereas there are no treatment options for the most common type of AMD (the dry form) (National Institute for Health and Care Excellence (NICE) 2018). Disease pathogenesis is complex but the death of retinal pigment epithelial cells (RPE) plays a critical negative role (Datta et al. 2017). As in other cell types, the prolonged activation of NLRP3 inflammasome in RPE causes cell death (Anderson et al. 2013; Gnanaguru et al. 2016). In a DICER-knockout mouse model, and in human subjects with AMD or with geographical atrophy (the advanced dry form of AMD), the dismetabolism of Alu-RNA due to lack or loss-of-function of DICER1 (micro-RNA processing enzyme) leading to Alu-RNA accumulation is cytotoxic for retinal pigment epithelium cells (Kaneko et al. 2011; Tarallo et al. 2012). Alu–RNA was demonstrated to induce NLRP3 activation (Tarallo et al. 2012) through a P2X7-dependent mechanism (Kerur et al. 2013). The combination of P2X7 activation that causes ROS, lipid oxidation (Bartlett et al. 2013) and lysosomal disregulation (Guha et al. 2013) triggers cell death. In 2014 it was observed that the administration of NRTIs (see **Section 1.4.5**) blocked the activation of NLRP3 inflammasome by Alu-RNA acting as antagonists of the P2X7 signalling pathway, reducing RPE cell death (Fowler et al. 2014). These findings highlight the importance of P2X7 as target for slowing down the progression of age-related macular degeneration and other visual impairment conditions such as diabetic retinopathy where chronic inflammation leads to retinal degeneration.

1.4.4.3 Inflammatory pain and neuropathic pain

In animal models of neuropathic pain, not only P2X4, but also P2X7 plays a pivotal role in aberrant pain transduction. P2X7 expression is increased in microglia after peripheral nerve damage and in paclitaxel-treated rodents (P2X7-knockout rodents show decreased chronic inflammatory and neuropathic pain in neuropathic pain models (Alves et al. 2013; Chessell et al. 2005)). Moreover it has been shown that administration of P2X7 antagonists decreases pain hypersensitivity after peripheral nerve damage (Honore et al. 2006) and paclitaxel-induced pain hypersensitivity (Ochi-Ishi et al. 2014) (A740003 and A438079 respectively, see **Section 1.4.5** for further details about antagonist potencies and structures). In the latter study it was proposed that activation of P2X7 results in the release of CCL3, but although CCL3 blockade decreases pain hypersensitivity (Matsushita et al. 2014), the mechanism involving CLL3 in allodynia is still not entirely clear. Release of pro-inflammatory cytokines after P2X7 activation is a well-studied pathway (in particular the release of IL-1β). As both type 1 and type 2 diabetes are inflammatory diseases, the consequently development of diabetic neuropathy and its correlation with P2X7 has been studied. Various polymorphisms are associated to pain sensitivity in diabetic neuropathy (Ursu et al. 2014), and a reduction in P2X7 expression in dorsal root ganglia by administration of long noncoding silencing-RNA helps reducing pain hypersensitivity and release of pro-inflammatory factors (such as TNFα) in a type 2 diabetes rodent model (Liu et al. 2017; Liu et al. 2016).

1.4.4.4 Tumor progression

P2X7 is overexpressed in multiple cancer cells although the role played by P2X7 is contradictory. Numerous studies show an association between increased expression of P2X7 and reduced tumour proliferation (Park et al. 2016); in contrast other evidences suggested that P2X7 increased cancer cell proliferation (Ferrari et al. 2017). These dual conflicting effects might be linked to diverse levels of activation of P2X7, with basal activity leading to proliferation and conversely an overstimulation by extracellular ATP resulting in apoptosis and further activation of the anti-tumour immune system responses (Garg et al. 2017; Savio et al. 2018). The dual effect of P2X7 activation was also observed in mouse embryonic stem where exogenous millimolar concentration of ATP stimulated pro-

apoptotic and pro-necrotic signalling leading to cell death while endogenous low levels of ATP promoted cell survival (Thompson et al. 2012).

Variants of P2X7 unable to form a large pore conductance - in response of agonist stimulation - have also been identified in multiple cancer cells (Ghiringhelli et al. 2009). Gilbert *et al*. recently showed that a molecularly distinct form of non-pore functional P2X7 (nfP2X7) was selectively recognised by a specific antibody (raised against 200-216 amino acid sequence) binding to E200 residue, which conversely is not accessible by the same antibody in P2X7 wild-type (Gilbert et al. 2018). Furthermore, Gilbert et al. demonstrated that cell exposure to high concentration of ATP - mimicking the ATP concentration in the tumor micro-environment – promoted nfP2X7 membrane expression, which in turn promoted cell survival (Gilbert et al. 2018). The role of P2X7 as an anti-tumour target is supported by a clinical study (phase I) for the treatment of basal cell carcinoma where targeting non-pore functional P2X7 (nfP2X7) with topical application of a specific antibody showed a reduction of over 10% of the tumour after a month of ointment application, with a good tolerance and safety profile (Gilbert et al. 2017).

1.4.4.5 Diseases of the SNC: neurodegenerative diseases and mood disorders

P2X7 is believed to be involved in multiple diseases of the central nervous system such as multiple sclerosis where some P2X7 polymorphisms have been linked - together with P2X4 polymorphisms (Sadovnick et al. 2017) - to increase disease susceptibility in humans (Gu et al. 2015). In Alzheimer's disease, P2X7 plays a role in the formation of amyloid plaque during the disease onset and progression, as activation of P2X7 triggers the α-secretase pathway that leads to the processing of the β-amyloid precursor into the amyloid form abundant in the extracellular noxious deposits. The administration of Brilliant Blue G (BBG) in a transgenic mouse model of Alzheimer's disease led to reduced plaque formation (Burnstock 2017; Chen et al. 2014; Miras-Portugal et al. 2015). P2X7 is also involved in Parkinson's disease and research in this field has demonstrated that antagonizing P2X7 might be a potential approach to reduce the synapto-toxicity, neurotoxicity and gliosis seen in the progression of the disease (Carmo et al. 2014; Jorg et al. 2014; Wang et al. 2017b).

An increasingly accredited hypothesis postulates that neuro-inflammation and prolonged (or altered) activation of the innate immune system is accountable for the development of mood disorders. Rodent models with stress-induced depression-like and anxiety-like phenotypes showed high levels of pro-inflammatory cytokines (IL-1β in particular), TNFα and higher expression in NLRP3 and caspase-1 in the hippocampus and pre-frontal cortex, the regions considered important in the development of mood disorders (Iwata et al. 2016). Furthermore *Iwata et al.* observed an improvement in mood disorder phenotypes when the expression of NLRP3 inflammasome was abolished by gene knockout or pharmacological blockade, observing also a consequent reduction in IL-1β levels (Iwata et al. 2016). In multiple clinical studies an alteration of the innate immune system in patients with mood disorders was observed, in particular elevated plasma concentrations of NLRP3, caspase1 and IL-1β showed a positive correlation with the severity of depression (Alcocer-Gómez et al. 2014). The same markers of inflammation were found to be increased after a manic episode in individuals with bipolar disorder (Söderlund et al. 2011). The NRLP3 inflammasome pathway is triggered by P2X7 activation in immune cells (see **Section 1.4.4**); therefore the impact of blockage of P2X7 on mood disorders has been investigated in behavioural studies. Manic-like behaviours induced by amphetamine (as model for bipolar disorder) were greatly reduced in P2X7 knock-out mice compared to wild type controls (Basso et al. 2009; Csölle et al. 2013) and confirmed by pharmacological P2X7 blockade by treatment with P2X7 antagonists such as BBG (Csölle et al. 2013) and A-438079 (Gubert et al. 2016). In parallel, depression-like behaviours were better managed with low doses of imipramine in P2X7 knock-out mice (Basso et al. 2009). However, a significant difference between the knock-out and the wild type was not observed in all the conducted behavioural tests (Basso et al. 2009). Furthermore, in a rodent model of phencyclidine (PCP)-induced schizophrenia, the pharmacological blockade of P2X7 with the blood-brain-barrier permeant compound JNJ-42253432, and the genetic deletion of P2X7, resulted in a significant change in behaviour, including a decrease in stereotypical behaviour, a decrease in hyper-locomotion and improved social behaviours (Lord et al. 2014). A subsequent study confirmed the results obtained for P2X7 knock-out models but did not show an improvement in social behaviour when the receptor was blocked with JNJ-47965567 – another brain-permeant compound (Koványi et al. 2016). Still there is the need to shed light on the degree of involvement of P2X7 in the genesis

and development of mood disorders, as some studies do not show a significant correlation between P2X7 blockade and anti-anxiety and anti-depressant effects. In addition, genetic studies are sometimes conflicting and although most show an association between P2X7 single nucleotide polymorphisms and mood disorders some failed to support the correlation. 1405A>G P2X7 SNP (causing the Q460R mutation) is particularly prominent in patients showing major depression in multiple cohort studies across Europe (Barden et al. 2006; Lucae et al. 2006; McQuillin et al. 2009) (Hejjas et al. 2009; Soronen et al. 2011), although some studies did not observe this correlation (Ferreira et al. 2008; Green et al. 2009). To note, the Q460R mutation leads to the expression of a receptor that shows similar properties to the wild type in ion currents (in electrophysiology experiments) but that alters the function of receptors when forming heteromeric channels with WT subunits (Aprile-Garcia et al. 2016).

1.4.5 P2X7 agonists, antagonists and allosteric modulators

Among the P2X receptor family, P2X7 is one of the most studied subtypes in terms of its pharmacology. Distinct properties of P2X7 are its relatively low sensitivity to ATP (EC_{50}>100 μM), many folds lower than other P2X subtypes, and its high sensitivity to BzATP - usually sold and tested as an isomeric mixture of 2'-O-(4-Benzoylbenzoyl)ATP and 3'-O-(4-Benzoylbenzoyl)ATP - which is approximately 30-fold more potent than ATP at the rat isoform (Surprenant et al. 1996). Notably, the concentration-response relationships of P2X7 agonists are influenced by extracellular divalent cation concentrations (Surprenant et al. 1996). P2X7 is negatively regulated by extracellular divalent cations including Ca^{2+}, Mg^{2+}, Cu^{2+} and Zn^{2+}, and mutagenesis studies have demonstrated a role for multiple histidine residues in the extracellular domain in this modulation (Acuña – Castillo et al. 2007). Furthermore, it has been demonstrated that ginsenosides (compounds isolated from *Panax ginseng* extract, **Figure 1-14**) are positive modulators of P2X7 activity; co-administration with 50 μM ATP led to increased YO-PRO dye uptake, increased Ca^{2+} influx responses and increased ATP-evoked membrane currents at both human and mouse P2X7 (Helliwell et al. 2015).

Compound	EC_{50} (μM)	Methods	References
Full agonists			
ATP; Adenosine triphosphate	~100 (rat)	two-electrode voltage-clamp (extracellular low divalent cation solution)	[a] (Surprenant et al. 1996)
	~130 (rat)[c]; 870 (mouse)[c]; ~300 (human)[e]	two-electrode voltage-clamp (extracellular low divalent cation solution), Yo-pro assay	[b](Khakh et al. 2001) [c](Young et al. 2006) [d](Karasawa and Kawate 2016) [e](Stokes et al. 2006)
BzATP; 3'-O-(4-Benzoylbenzoyl) ATP (**Note:** sold as isomer mixture with 2'-O-(4-Benzoyl) benzoyl ATP, although in early reports the mixture was referend as 3'-O-(4-Benzoylbenzoyl) ATP)	8-20 (rat)[a,c]; 236 (mouse)[c]	voltage-clamp (extracellular low divalent cation or standard solution)	[a](Surprenant et al. 1996) [c](Young et al. 2006)
Positive Modulators			
Ginsenosides (Rb1, Rd, Rh2, CK)	~1	Yo-pro assay, Ca^{2+} influx, patch-clamp	(Helliwell et al. 2015)

Table 1.6: Potencies of P2X7 agonists and positive allosteric modulators

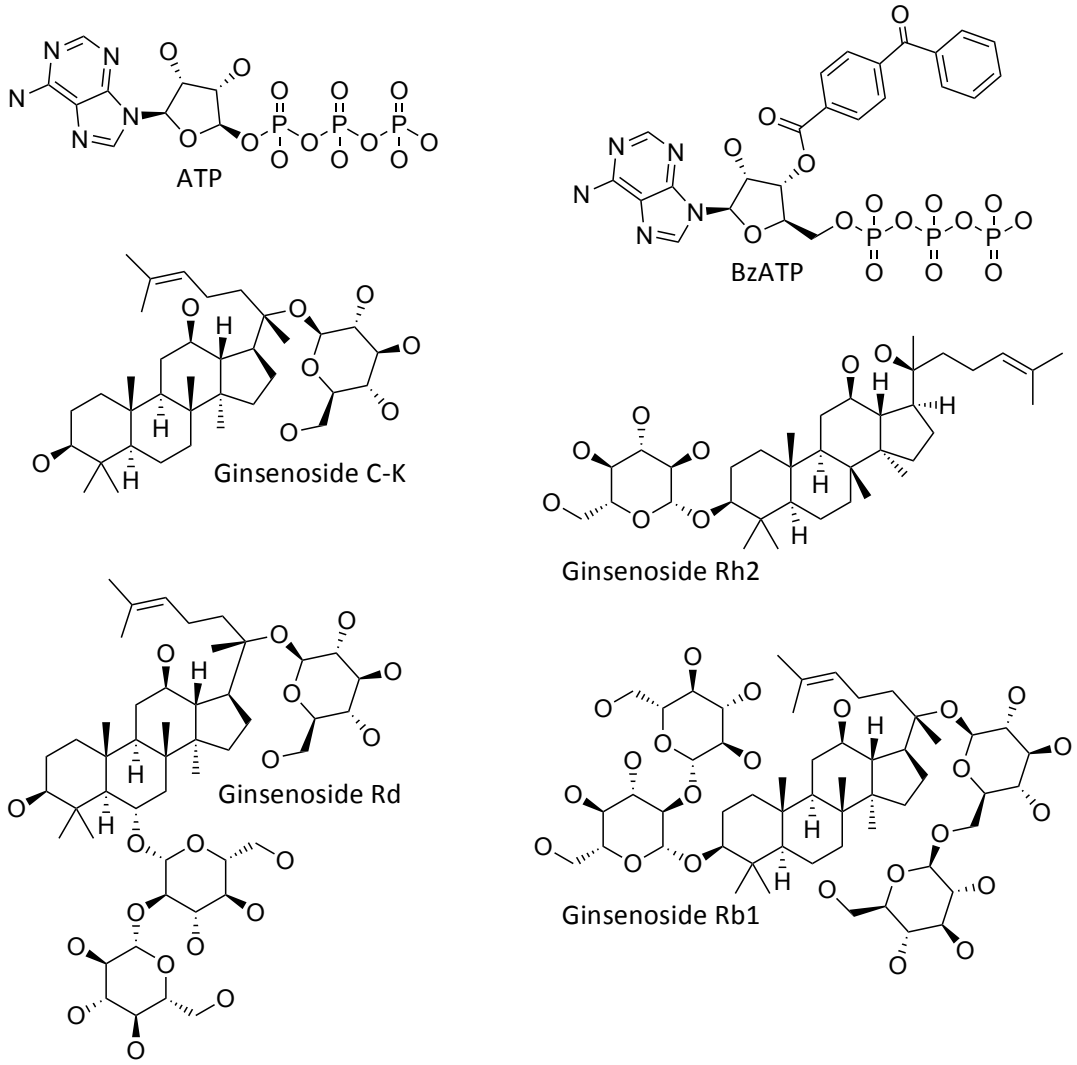

Figure 1-14: Structure of P2X7 competitive agonists and positive allosteric modulators. Note that BzATP is referred to 3'-O-(4-Benzoyl)benzoyladenosine 5'-triphosphate although it is commercially available as mixture of isomers.

In contrast to the low number of small-molecule P2X7 agonists and positive modulators, the number of P2X7 antagonists is by far larger. Historically, most of the compounds identified as P2X7 antagonists are non-selective (see **Table 1.7**) such as PPADS, some dyes such as Brilliant Blue G and Cibacron, and suramin, which is also acts as inhibitor on a wide array of different protein targets including viral proteins (Albulescu et al. 2015; Ferla et al. 2018), transcription factors (Berg and Berg 2017) and channels (Papineni et al. 2002). The first classes of compounds developed as P2X antagonists were suramin or dye analogues with ameliorated selectivity and potency profiles (Carroll et al. 2009). Interestingly some P2X1 antagonists were found to be significant antagonists at P2X7 such as NF279 (Klapperstück et al. 2000) and MRS 2159 (Donnelly – Roberts et al. 2009).

Compound	IC_{50} (μM)	Methods	References
Antagonists (and compounds with unknown binding mode)			
Suramin; 8,8'-((3,3'-((3,3'-(carbonylbis(azanediyl))bis(benzoyl))bis (azanediyl)bis(4-methylbenzoyl)) bis(azanediyl))bis(naphthalene-1,3,5-trisulfonic acid)	78 (rat), 92 (human)	whole-cell patch clamp, yo-pro assay	(Rassendren et al. 1997)
NF279; 8,8'-[Carbonylbis(imino-4,1-phenylenecarbonylimino-4,1-phenylenecarbonylimino)]bis-1,3,5-naphthalenetrisulfonic acid	2.8 (human)	two-electrode voltage-clamp	(Klapperstück et al. 2000)
KN62; [4-[(2S)-2-[isoquinolin-5-ylsulfonyl(methyl)amino]-3-oxo-3-(4-phenylpiperazin-1-yl)propyl]phenyl] isoquinoline-5-sulfonate	0.013 (human)	Ethidium bromide uptake; Ca^{2+} influx assay	(Gargett and Wiley 1997)
Briliant Blue G (BBG); 3-((((1E,4E)-4-((4-((4-ethoxyphenyl)amino)phenyl)(4-(ethyl(4-sulfonatobenzyl)amino)-2-methylphenyl) methylene)-3-methylcyclohexa-2,5-dien-1-ylidene) (ethyl)ammonio)methyl)benzenesulfonate	0.2 (rat)	whole-cell patch clamp, yo-pro assay (single cell imaging)	(Jiang et al. 2000a)
PPADS; (E)-4-(2-(4-formyl-6-methyl-5-oxo-3-((phosphonooxy)methyl)pyridin-2(5H)-ylidene)hydrazineyl)benzene-1,3-disulfonic acid	51 (rat), 62 (human)	whole-cell patch clamp, yo-pro assay	(Rassendren et al. 1997)
MRS 2159; (E)-4-((4-formyl-5-hydroxy-6-methyl-3-((phosphonatooxy)methyl) pyridin-2-yl)diazenyl)benzoate	~0.288-1.73 (human)	Yo-pro assay, two-electrode voltage-clamp	(Donnelly‐Roberts et al. 2009)
Probenecid; 4-(N,N-dipropylsulfamoyl) benzoic acid	203 (human)	whole-cell patch clamp, Ca^{2+} influx	(Bhaskaracharya et al. 2014)
TNP-ATP; 2',3'-O-(2,4,6-Tri-nitrophenyl)adenosine-5'-triphosphate	>30 (human)	whole-cell patch clamp	(Virginio et al. 1998)
Reactive Blue 2; 1-amino-4-((4-((4-chloro-6-((2-sulfonatophenyl)amino)-1,3,5-triazin-2-yl)amino)-3-sulfonatophenyl)amino)-9,10-dioxo-9,10-dihydroanthracene-2-sulfonate	69 (human)	Ca^{2+}influx assay, ethidium bromide uptake	(Wiley et al. 1993)

Table 1.7: List of non-selective, first generation of P2X7 antagonists. Receptor specie in brackets.

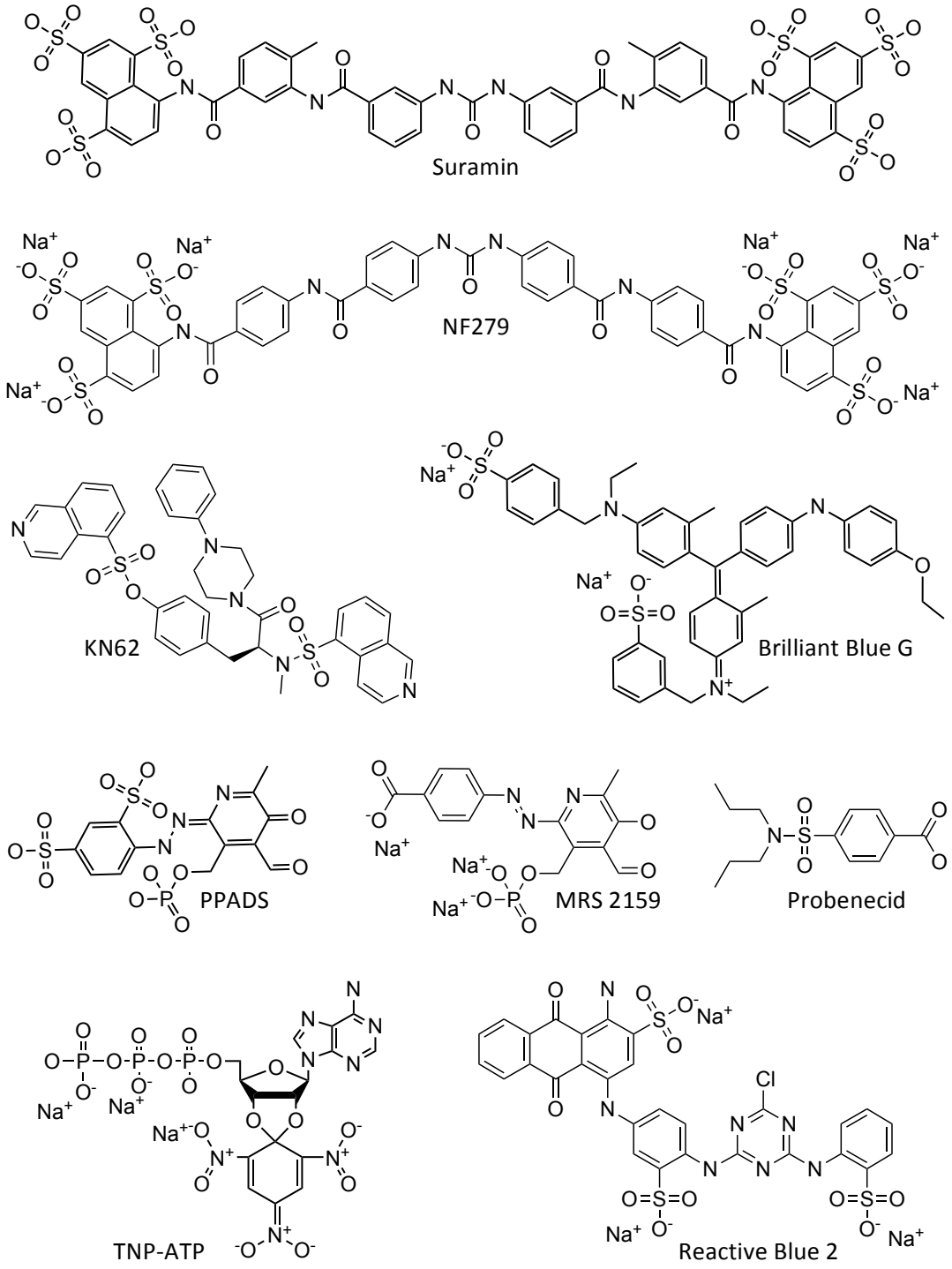

Figure 1-15: Structure of non-selective P2X7 antagonists

In the last two decades following the identification of P2X7 as key role component in inflammatory conditions and its identification as valuable drug target, many efforts were made in the identification of potent and selective P2X7 antagonists leading to the discovery of novel compounds active in the low nanomolar

concentration range (Carroll et al. 2009; Guile et al. 2009; Gunosewoyo and Kassiou 2010), or to the repurposing of well-characterised drugs as anti-P2X7 drugs. Multiple Nucleoside Reverse Transcriptase Inhibitor (NRTI) primarily used as antivirals in the management of HIV - such as stavudine and zidovudine (also known as azidothymidine) (**Table 1.8** and **Figure 1-16**) - showed inhibition at P2X7 *in vitro* and efficacy in rodent models of age-related macula degeneration where P2X7 activation is involved in photoreceptor death (Fowler et al. 2014) (see **Section 1.4.4.2**). Examples of recently discovered novel compounds are listed in **Table 1.8** (see **Figure 1-16** and **Figure 1-17** for structures). Surprisingly, some of the potent antagonists initially believed to be competitive such as A740003 (Honore et al. 2006) and A804598 (Donnelly-Roberts et al. 2009) were later demonstrated to act as allosteric ligands through mutagenesis and crystallographic data (see **Section 1.5**), underlining the need for deep pharmacological characterization of novel compounds. Some recently characterized compounds are also able to cross the blood-brain barrier, and have become of high interest as potential drug candidates in the treatment of CNS disorders (Bhattacharya 2018), among which are A438079 (Nelson et al. 2006), compound 7f developed by Pfizer (Chen et al. 2010), compound 16 (Beswick et al. 2010) compound 18 (Abberley et al. 2010) and GSK-1482160 (Abdi et al. 2010) developed by Glaxo Smith Kline (GSK). Additionally, the brain-penetrant JNJ-422534327 (Letavic et al., 2013)(Lord et al. 2014), JNJ-47965567 (Letavic et al., 2013), JNJ-54175446 (Alcazar-Vaca et al. 2013), JNJ-55308942 (Letavic et al. 2013) and JNJ-64413739 (Kolb et al. 2016) are among the compounds developed by Janssen. The ability of compounds to permeate across the blood-brain barrier has been exploited for the development of compounds as Positron emission tomography (PET) tracers as both (i) potential marker of neuro-inflammation and (ii) to monitor and quantify the occupancy in the CNS of a compound of interest co-administered with the PET tracer (Bhattacharya 2018). In particular one PET tracer, ^{18}F-JNJ-64413739, has been co-administered with JNJ-54175446 (ClinicalTrial.gov identifier: NCT03088644) in Phase I clinical trials involving healthy volunteers to investigate the safety, tolerability and pharmacokinetics of the compounds, although no study results are publicly available. Another Phase I study exploring ^{18}F-JNJ-64413739 and JNJ-55308942 (NCT03437590) is currently recruiting healthy volunteers (see **Table 1.8**, **Table 1.9** and **Figure 1-17**).

Compound	IC_{50} (μM)	Methods	References
Negative allosteric Modulators			
A740003; (Z)-N-(1-(3-cyano-2-(quinolin-5-yl)guanidino)-2,2-dimethylpropyl)-2-(3,4-dimethoxyphenyl)acetamide	0.0693 (panda)	whole-cell patch clamp, yo-pro assay	(Karasawa and Kawate 2016)
A804598; N-cyano-N'-[(1R)-1-phenylethyl]-N''-quinolin-5-ylguanidine	0.0217 (panda)	whole-cell patch clamp, yo-pro assay	(Karasawa and Kawate 2016)
A438079; 3-((5-(2,3-dichlorophenyl)-1H-tetrazol-1-yl)methyl)pyridine	0.1 (human)	IL-1β release, yo-pro assay, Ca^{2+} influx assay	(Nelson et al. 2006)
AZ11645373; 3-[1-[4-(3-nitrophenyl)phenoxy]-4-pyridin-4-ylbutan-2-yl]-1,3-thiazolidine-2,4-dione	0.005-0.09 (human)	IL-1β release, yo-pro assay, Ca^{2+} influx assay, whole-cell patch clamp	(Stokes et al. 2006)
Compound 7f	0.027 (human)	yo-pro assay	(Chen et al. 2010)
Compound 16	0.01	n/a	(Beswick et al. 2010)
Compound 18	0.01	Ethidium bromide uptake	(Abberley et al. 2010)
GW791343; 2-(3,4-difluoroanilino)-N-[2-methyl-5-(piperazin-1-ylmethyl)phenyl]acetamide	0.1 (human), 8.9 (panda)	whole-cell patch clamp, yo-pro assay	(Karasawa and Kawate 2016; Michel et al. 2008)
JNJ-422534327; 2-methyl-N-((1-(4-phenylpiperazin-1-yl)cyclohexyl) methyl)-1,2,3,4-tetrahydroisoquinoline-5-carboxamide	~0.01[a] (human)	n/a	(Letavic et al. 2013; Lord et al. 2014)
JNJ-47965567; 2-(Phenylthio)-N-[[tetrahydro-4-(4-phenyl-1-piperazinyl)-2H-pyran-4-yl]methyl-3-pyridinecarboxamide	~0.01[a] (human); 11.9 (panda)	whole-cell patch clamp, yo-pro assay	(Karasawa and Kawate 2016; Letavic et al. 2013)
AZ10606120; 2-(1-adamantyl)-N-[2-[2-(2-hydroxyethylamino)ethylamino] quinolin-5-yl]acetamide	0.01 (human), 0.231 (panda)	whole-cell patch clamp	(Allsopp et al. 2017; Karasawa and Kawate 2016)
Azidothymidine (Zidovudine); 1-[(2R,4S,5S)-4-azido-5-(hydroxymethyl)oxolan-2-yl]-5-	Not reported	whole-cell patch clamp	(Fowler et al. 2014)

methylpyrimidine-2,4-dione			
Stavudine; 1-[(2R,5S)-5-(hydroxymethyl)-2,5-dihydrofuran-2-yl]-5-methylpyrimidine-2,4-dione	Not reported	whole-cell patch clamp	(Fowler et al. 2014)
Ca^{2+}	Not reported		(Yan et al. 2011)
Mg^{2+}	Not reported		(Acuña – Castillo et al. 2007)
Copper	Not reported		(Acuña – Castillo et al. 2007; Liu et al. 2008)
Zn^{2+}	Not reported		(Liu et al. 2008)

Table 1.8: List of reported selective and potent P2X7 antagonists (selection). Receptor specie in brackets. [a]Inhibition constant (Ki) instead of IC_{50}.

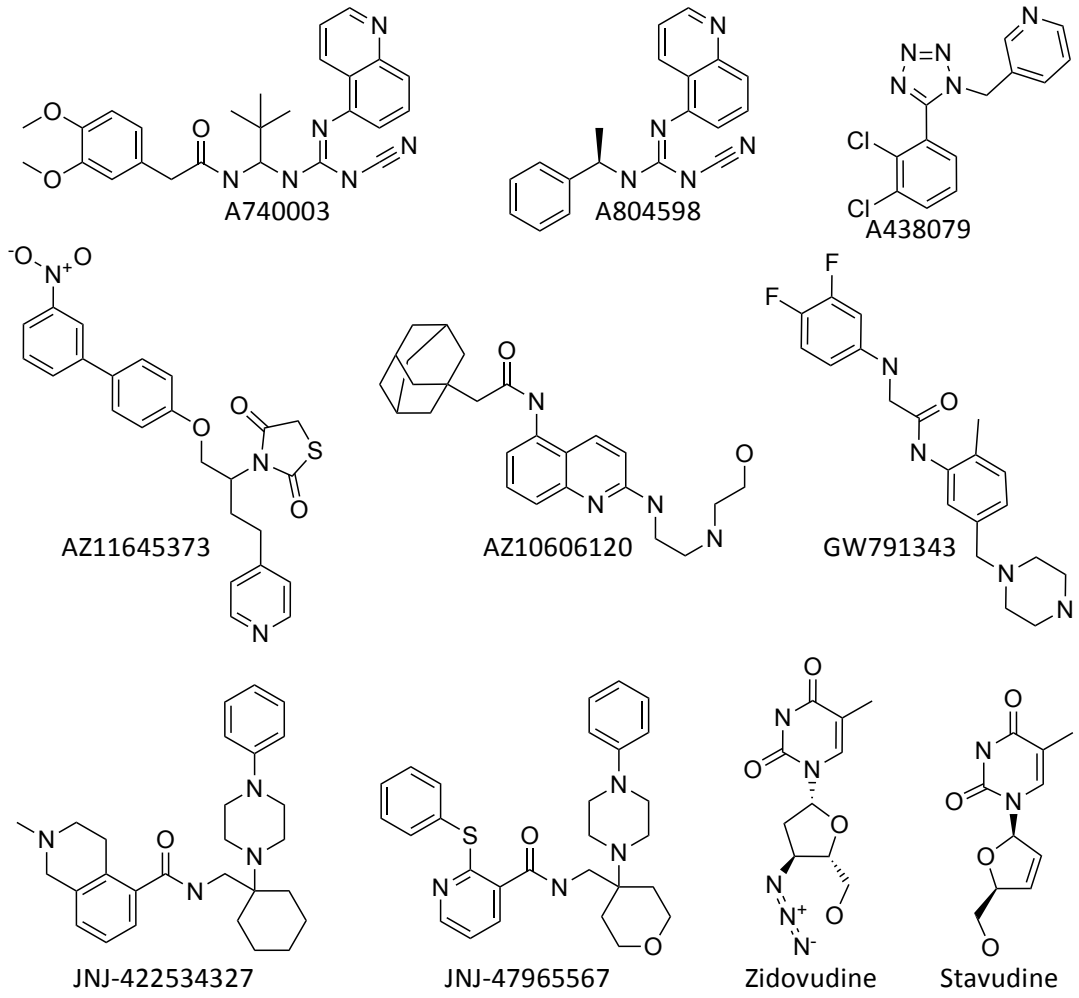

Figure 1-16: Structures of reported selective and potent P2X7 antagonists (selection).

In addition to PET tracers, multiple compounds have entered clinical trials and been demonstrated to be to safe and well tolerated in humans (Bhattacharya 2018). For some of the compounds the published information is minimal. For EVT-401, the structure has very recently been disclosed along with data regarding its instability in alkaline, acidic and oxidative stress conditions (Zhu et al. 2017), but there is still no published information regarding its advancements in clinical trials with the exception of press releases reporting the completion of Phase I trials and the continuation of the EVT-401 programme towards Phase II (Lanthaler 2012) (Evotec-AG 2012).

The safety and pharmacokinetics of CE-224,535 (Pfizer) and AZD-9056 (Astra Zeneca) were investigated in multiple Phase I trials (NCT00838058, NCT00782600,

NCT00446784 and NCT00908934, NCT00700986, NCT00920608, NCT00736606 respectively) before advancing to Phase II trials as treatment for rheumatoid arthritis and Chron's disease (NCT00628095 and NCT00520572) and osteoarthritis (NCT00418782) where, although a significant reduction in swollen joints and pain for patients administered with AZD-9056 versus placebo was observed (Eser et al. 2015; Keystone et al. 2012a), both drugs failed to show a reduction in inflammatory biomarkers and an improvement in patient conditions (Eser et al. 2015; Keystone et al. 2012a) (Stock et al. 2012). A detailed report for the investigation of GSK1482160 in Phase I (NCT00849134) is available at the GSK Clinical Study Register (Study ID: 111383), reporting good tolerability for doses between 0.3 and 1000 mg with a single severe adverse event at the highest concentration that was not considered to be related to the treatment. The drug showed rapid absorption (1-2 hours, slowed down by concomitant food ingestion) and a rapid clearance (half life of 3 hours) and a concentration of GSK1482160 in blood approximately correlated to the administered dose was observed. To date there is no current information regarding Phase II testing of GSK1482160.

Although there are currently no small molecule P2X7 modulators reported in clinical trials with anti-cancer properties, a 10% ointment formulation of antibody targeting non-functional P2X7 (nfP2X7, see **Section 1.4.4.4**) has shown promising results in a Phase I trial for patients with basal cell carcinoma (NCT02587819) where an average reduction of over 12% of cancer lesion was observed after twice daily treatment for 28 days (Gilbert et al. 2017). These results give new hope for the development of P2X7-targeted drugs after the failure of Phase II clinical trials targeting P2X7 as rheumatoid arthritis treatment.

P2X7 antagonists in clinical trials			
CE224535; 2-chloro-N-[(1-hydroxycycloheptyl)methyl]-5-[4-[(2R)-2-hydroxy-3-methoxypropyl]-3,5-dioxo-1,2,4-triazin-2-yl]benzamide	0.0014-0.004	IL-1β release, yo-pro assay	(Duplantier et al. 2011)
AZD-9056; N-(1-adamantylmethyl)-2-chloro-5-[3-(3-hydroxypropylamino) propyl]benzamide	Not reported	Not reported	(Keystone et al. 2012a)
EVT-401; 2-(3-fluoro-4-(trifluoromethyl)phenyl)-N-(2-(1-hydroxypropan-2-yl)-6-methyl-1-oxo-1,2-dihydroisoquinolin-5-yl)acetamide	Not reported	Not reported	(Lanthaler 2012) (Evotec-AG 2012)
GSK1482160; (2S)-N-[[2-chloro-3-(trifluoromethyl)phenyl]methyl]-1-methyl-5-oxopyrrolidine-2-carboxamide	0.002-0.01	Ethidium bromide uptake	(Abdi et al. 2010; Gao et al. 2015; Han et al. 2017; Jin et al. 2018)
JNJ-54175446; (R)-(2-chloro-3-(trifluoromethyl)phenyl)(1-(5-fluoropyrimidin-2-yl)-4-methyl-1,4,6,7-tetrahydro-5H-[1,2,3]triazolo[4,5-c]pyridin-5-yl)methanone	Not reported	Not reported	(Alcazar-Vaca et al. 2013)
JNJ-55308942; (S)-(3-fluoro-2-(trifluoromethyl)pyridin-4-yl)(1-(5-fluoropyrimidin-2-yl)-6-methyl-1,4,6,7-tetrahydro-5H-[1,2,3]triazolo[4,5-c]pyridin-5-yl)methanone	0.010	Ca^{2+} influx assay	(Chrovian et al. 2017)
^{18}F-JNJ-64413739; (S)-(3-fluoro-2-(trifluoromethyl)pyridin-4-yl)(6-methyl-1-(pyrimidin-2-yl)-1,4,6,7-tetrahydro-5H-[1,2,3]triazolo[4,5-c]pyridin-5-yl)methanone	~0.001-0.012	Not reported	(Kolb et al. 2016)

Table 1.9: List of P2X7 antagonists entered in clinical trials.

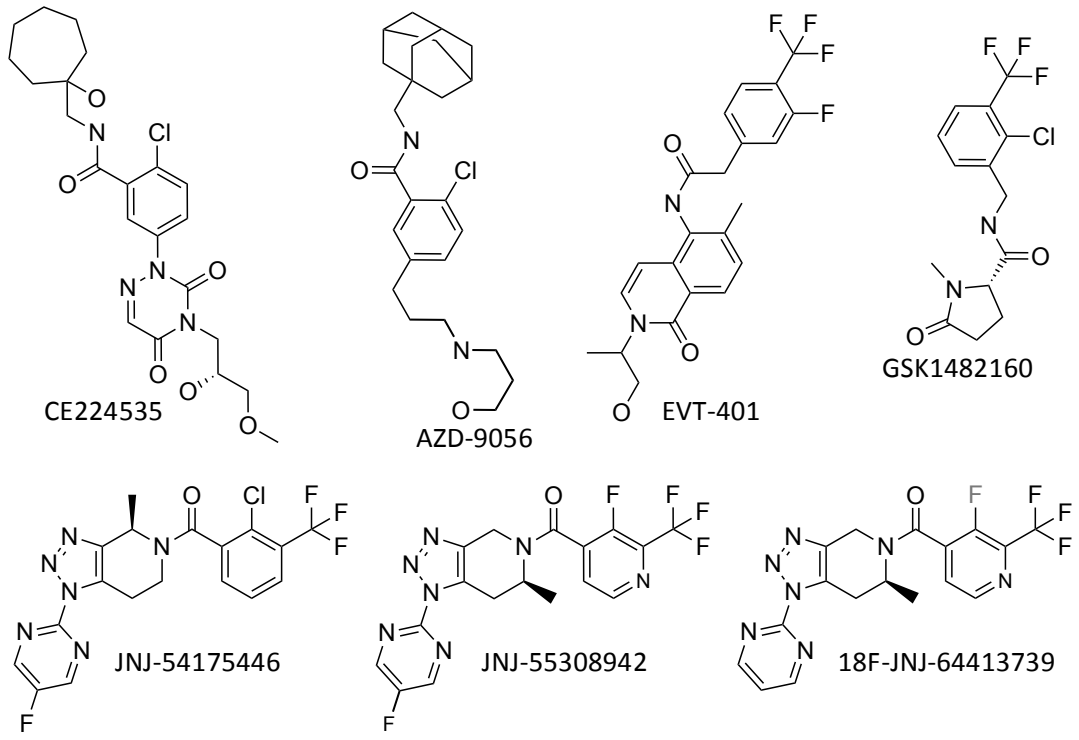

Figure 1-17: Structures P2X7 antagonists entered in clinical trials.

Drug	Clinical trial ID	Phase	Indication	Status
GSK1482160	NCT00849134	Phase I	Pain, Inflammatory	Completed: safe and tolerated in 25 healthy volunteers
CE-224,535	NCT00838058	Phase I	Rheumatoid Arthritis	Completed on 11 healthy volunteers, no results available
CE-224,535	NCT00782600	Phase I	Rheumatoid Arthritis	Completed on 16 healthy volunteers. Oral Suspension Controlled Release Formulation. no results available
CE-224,535 + methotrexate	NCT00446784	Phase I	Rheumatoid Arthritis	Completed on 20 patients receiving methotrexate: no results available
CE-224,535	NCT00628095	Phase IIa	Rheumatoid Arthritis	Completed on 100 patients. (Stock et al. 2012)
CE-224,535 vs. naproxen	NCT00418782	Phase II	Osteoarthritis	Completed on 212 patients: no results available.
JNJ-54175446 + ^{18}F-JNJ-64413739	NCT03088644	Phase I	Healthy	Completed on 16 healthy volunteers: no results available
JNJ-55308942 + ^{18}F-JNJ-64413739	NCT03437590	Phase I	Healthy	Recruiting (estimated 24 healthy participants)
AZD9056	NCT00908934	Phase I	Healthy	Completed on 24 healthy volunteers: no results available
AZD9056	NCT00700986	Phase I	Rheumatoid Arthritis. **Study focused on retinal function**	Completed on 12 healthy volunteers: no results available.
AZD9056 + methotrexate	NCT00920608	Phase I	Rheumatoid Arthritis	Withdrawn (12 patients)
AZD9056 + simvastatin	NCT00736606	Phase I	Healthy	Completed on 12 healthy volunteers: no results available.
AZD9056 vs. Etanercept	NCT00520572	Phase II	Rheumatoid Arthritis	Completed on 385 patients: etanercept demonstrated approximately double

				efficacy compared to AZD9056.
anti-nf-P2X7 (antibody)	NCT02587819	Phase I	Carcinoma, Basal Cell	Completed on 21 patients: well tolerated with one severe adverse effect unrelated to the drug. Reduction of cancer lesion of 12.86% in 20 patients.

Table 1.10: Clinical trials for small molecules and antibodies targeting P2X7 receptor.

1.5 The P2X crystal structures: a substantial help in homology modelling

1.5.1 Crystal structures of P2X receptors: state-of-art

In 2009 the apo-form of zebrafish P2X4a receptor was the first published high-resolution crystal structure of a member of the P2X receptor family (Kawate et al. 2009a). Kawate et al. introduced the concept of visualizing each P2X receptor subunit as shaped like a dolphin in order to simplify the description of the subdomains (see **Figure 1-18**). The first structure was followed by those of zebrafish P2X4 in the apo- and ATP-bound states in 2012 (PDB ID: 4DW0 at 2.8Å and 4DW1 and 2.9Å resolution respectively) (Hattori and Gouaux 2012), shedding light on the mechanism of gating, the detailed 3-dimensional structure of the ATP binding site, and confirming the previous experimental data aimed at the identification of the residues lining in the ATP-binding site (Jiang et al. 2000b; Marquez-Klaka et al. 2007; Roberts and Evans 2004, 2006; Young 2010). The description of the gating and conformational changes induced by ATP-binding is described in more detail in **Section 1.5.2** while the ATP-binding site is treated in **Section 1.5.3.1**. Although showing impaired receptor function, the crystal structure of a Gulf Coast tick (*Ambylomma maculatum*) P2X receptor solved in the presence of zinc and ATP, published in 2016 (PDB ID: 5F1C) permitted the first comparative studies among P2X receptor homologues (Kasuya, et al., 2016). Another important milestone was reached in the same year with the report of a series of human P2X3 crystal structures in the apo-, ATP-bound and antagonist-bound forms; these structures were the first to describe the intracellular cytosolic cap architecture (see **Section 1.5.2** for more information of the involvement of the cap in the receptor desensitization mechanism), and the first human P2X receptor structures to be solved (Mansoor et al. 2016). Most recently, further advancements have been achieved in our understanding of partial agonist, competitive antagonist and allosteric antagonist binding modes thanks to the publication of crystal structures of the CTP-bound form of zebrafish P2X4 (Kasuya et al. 2017a), giant panda P2X7 bound to a series of allosteric modulators (extremely important for the design of allosteric modulators using a structure-based approach) (Karasawa and Kawate 2016), chicken P2X7 bound to the

competitive antagonist TNP-ATP (Kasuya et al. 2017b) and human P2X3 bound to the allosteric antagonist AF-219 (Wang et al. 2018). **Table 1.11** lists all the P2X receptor structures (crystal data and NMR) published to date.

It is important to note that the majority of the constructs used in crystal trials bears at least one point mutation, and that none of the crystal structures represents the full-length wild-type protein, all bearing some degree of truncation that in some cases drastically impairs receptor function (e.g. the first zebrafish P2X4, the Gulf Coast tick and the chicken P2X7 constructs (Kasuya et al. 2016; Kasuya et al. 2017b; Kawate et al. 2009b)). Notably, in other cases, including the zebrafish P2X4 constructs published in 2012 (used extensively for the homology modelling present in this work) and human P2X3, the 'crystal constructs' showed a functional profile comparable to the wild type receptor (Hattori and Gouaux 2012; Mansoor et al. 2016).

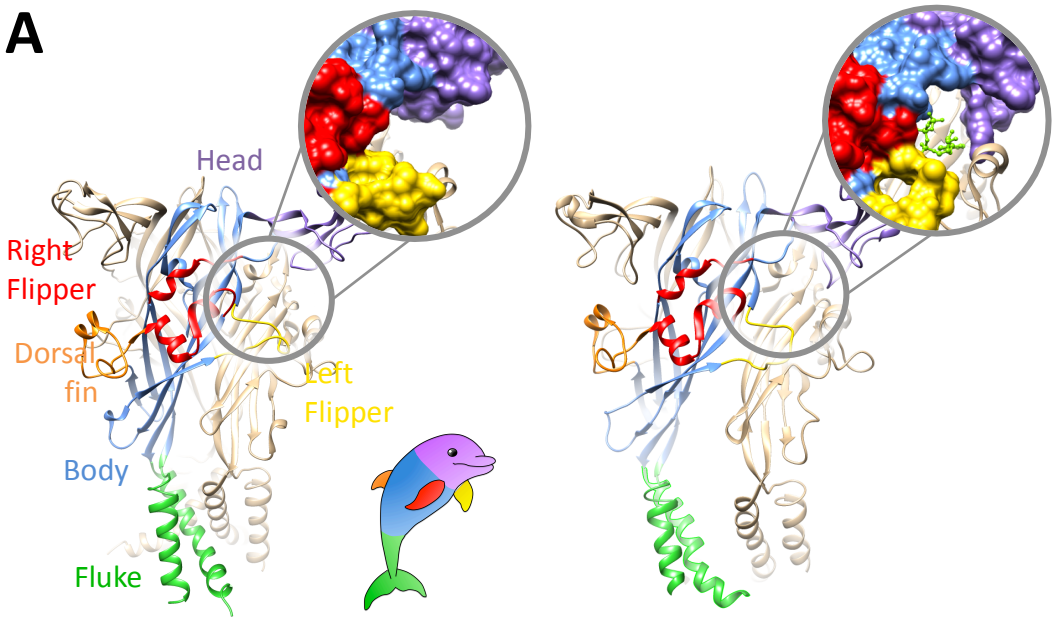

B

```
4DW1   36 RFTQALVIAY VIGYVCVYNK GYQDTDTVLS SVTTKVKGIA LTKTSELGER  85
hP2X4  33 RAVQLLILAY VIGWVFVWEK GYQETDSVVS SVTTKVKGVA VTNTSKLGFR  82

4DW1   86 IWDVADYIIP PQEDGSFFVL TNMIITTNQT QSKCAENPTP ASTCTSHRDC 135
hP2X4  83 IWDVADYVIP AQEENSLFVM TNVILTMNQT QGLCPEIPDA TTVCKSDASC 132

4DW1  136 KRGFNDARGD GVRTGRCVSY SASVKTCEVL SWCPLEKIVD PPNPPLLADA 185
hP2X4 153 TAGSAGTHSN GVSTGRCVAF NGSVKTCEVA AWCPVEDDTH VPQPAFLKAA 182

4DW1  186 ERFTVLIKNN IRYPKFNFNK RNILPNINSS YLTHCVFSRK TDPDCPIFRL 235
hP2X4 183 ENFTLLVKNN IWYPKFNFSK RNILPNITTT YLKSCIYDAK TDPFCPIFRL 232

4DW1  236 GDIVGEAEED FQIMAVRGGV MGVQIRWDCD LDMPQSWCVP RYTFRRLDNK 285
hP2X4 233 GKIVENAGHS FQDMAVEGGI MGIQVNWDCN LDRAASLCLP RYSFRRLDTR 282

4DW1  286 DPDNNVAPGY NFRFAKYYKN SDGTETRTLI KGYGIRFDVM VFGQAGKFNI 335
hP2X4 333 DVEHNVSPGY NFRFAKYYRD LAGNEQRTLI KAYGIRFDII VFGKAGKFDI 332

4DW1  336 IPTLLNIGAG LALLGLVNVI CDWI 359
hP2X4 333 IPTMINIGSG LALLGMATVL CDII 356
```

Figure 1-18: Cartoon of zebrafish P2X4 highlighting the canonical dolphin shape features (**A**) and their correspondence to the protein sequence (**B**). Each receptor subunit is formed by the subdomains such as the head, the flippers, the body the fluke and the dorsal fin. The ATP binding site (**A**, right) is enclosed between the left (in yellow) and the right (in red) flippers, the right the body (in blue) and the head (in purple) and the dorsal fin of the adjacent subunit (tan ribbon).

PDB ID	Resolution (A)	P2X subtype (Specie)	State (ligand)
2BP5	2.8	P2X4 (rat)	n/a
2RUP	*	P2X4 (rat)	n/a
4DW0	3.1	P2X4 (zebrafish)	apo
4DW1	3.46	P2X4 (zebrafish)	bound (ATP)
5F1C	2.9	P2X (Gulf Coast tick)	bound (ATP)
5SVJ	2.98	P2X3 (human)	apo
5SVK	2.77	P2X3 (human)	bound (ATP); open
5SVL	2.9	P2X3 (human)	bound (ATP); desensitised
5SVM	3.09	P2X3 (human)	bound (2-methylthio-ATP); desensitised
5SVP	3.3	P2X3 (human)	bound (2-methylthio-ATP); desensitised
5SVQ	3.25	P2X3 (human)	bound (TNP-ATP)
5SVR	3.13	P2X3 (human)	bound (A-317491)
5SVS	4.03	P2X3 (human)	apo
5SVT	3.79	P2X3 (human)	apo
5U1L	3.4	P2X7 (giant panda)	apo
5U1U	3.6	P2X7 (giant panda)	bound (A740003)
5U1V	3.4	P2X7 (giant panda)	bound (A804598)
5U1W	3.5	P2X7 (giant panda)	AZ10606120
5U1X	3.2	P2X7 (giant panda)	JNJ47965567
5U1Y	3.3	P2X7 (giant panda)	GW791343
5U2H	3.9	P2X7 (giant panda)	bound (ATP, A804598)
5WZY	2.8	P2X4 (zebrafish)	bound (CTP)
5XW6	3.1	P2X7 (chicken)	bound (TNP-ATP)
5YVE	3.4	P2X3 (human)	bound (AF-219)
* NMR structure			

Table 1.11: List of P2X receptor structures published to date (September 2018). Structures were obtained through X-ray diffraction pattern if not otherwise specified. * refers to structures obtained through NMR. n/a refers to short fragment sequences (less than 60 residues) where the canonical ligand binding pocket is not present.

1.5.2 Insight in the molecular mechanism of the receptor activation based on crystal structure data

Among the available structures, the zebrafish P2X4 and human P2X3 structures are valuable candidates for the analysis of the conformational changes upon agonist and antagonist binding. By comparing the ATP-bound structure to the *apo*- form of zebrafish P2X4 it was possible to observe the tightening of the head around the ATP, the downward motion of the left flipper domain, the upward movement of the dorsal fin domain and the subsequent arching of the body domain induced by ATP binding (Hattori and Gouaux 2012). These movements create a conformational strain which is transmitted through the entire subunit, leading to the movement of the second transmembrane domain (TM2) relative to TM1, which opens the channel in a way similar to that of the iris of a camera, allowing cations to exchange from the extracellular lateral fenestration through the central pore and *vice versa* (Hattori and Gouaux 2012). A remarkable new advance was made with the solution of human P2X3 crystal structures in the open, closed and desensitized state (Mansoor et al. 2016). These structures give an insight into the presence and function of the cytoplasmic cap not captured in previous structures (**Figure 1-19**). In the crystal, both N- and C-terminus amino acids are part of the cytoplasmic cap with each N-terminal contributing with two consequent beta-strands to one beta-strand of each of the C-terminal (Mansoor et al. 2016). The cap sits beneath the transmembrane domains and stabilizes the pore. Since it is only seen in the open ATP-bound structure, the hypothesis is that the cap forms a disordered domain in the closed state. As previously seen in zebrafish P2X4 (Hattori and Gouaux 2012), the binding of ATP leads to closure of the head on the binding site and the upright movement of the dorsal fin, which transduces the movement to the TMs and ultimately leads to the opening of the pore. In human P2X3 TM2 rotates relative to TM1 and the α-helix gets stretched to a 3_{10} helix. In the rotation, amino-acid residue I323 (that in the *apo*- state defines the inner pore on the extracellular side) moves outward, and a similar movement is mimicked by the residue defining the pore in the *apo*- state from the cytoplasmic space (T330) (Mansoor et al. 2016) (see **Figure 1-19**).

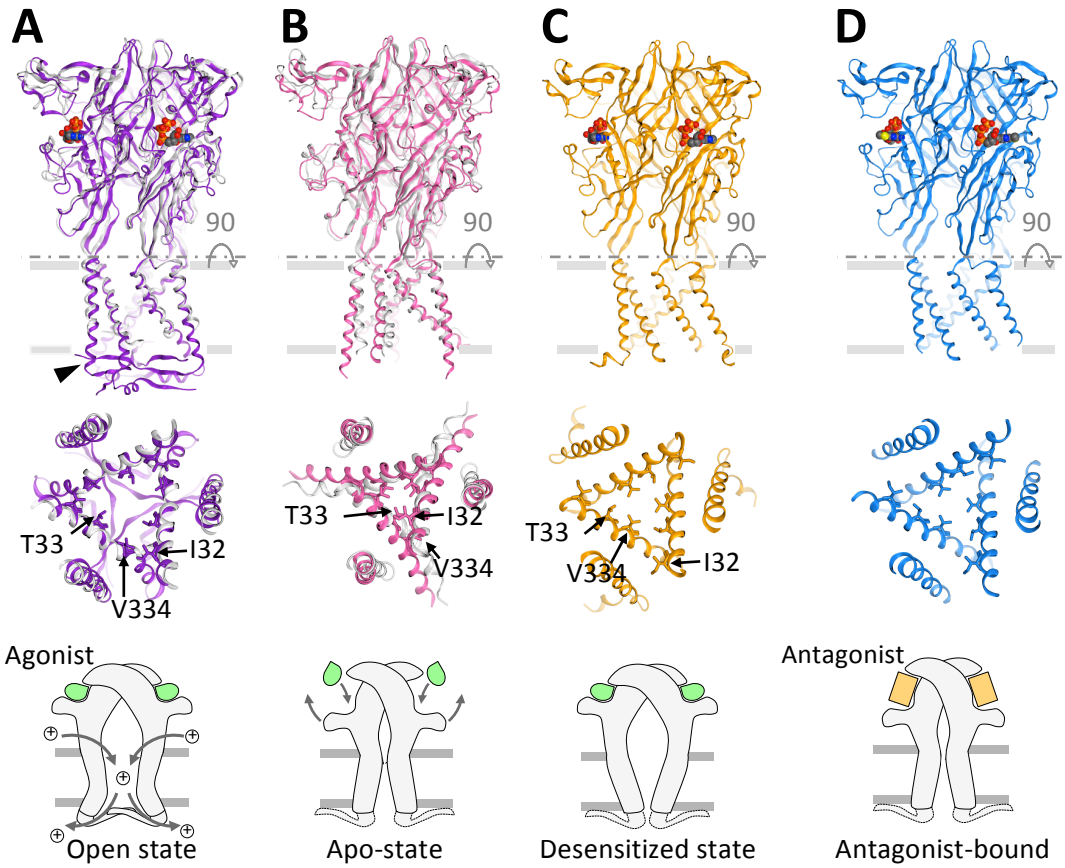

Figure 1-19: Receptor gating mechanism. Crystal structures of P2X3 in the ATP-bound open state (**A**), unbound state (**B**), ATP-bound desensitized state (**C**) and antagonist-bound state (**D**) highlighting the conformation of the trasmembrane helixes and the position of the residues lining the channel pore. A simplified cartoon represents the overall changes in receptor conformation. The cytoplasmic cap stabilizes the open state of the receptor (**A**). To date, the cytoplasmic cap has not been crystalized in other receptor conformations (dot lines).

1.5.3 Ligand binding pockets

1.5.3.1 Orthosteric binding site

The structural data of the ATP-bound zebrafish P2X4 obtained by *Hattori et al.* enabled the research group to identify 8 amino acids located between two subunits that directly interact with the physiological agonist ATP mainly through hydrogen bond (H-bond) interactions (Lys-70, Lys-72, Thr-189, Leu-191, Lys-193, Ile-232, Asn-296, Arg-298, Lys-316, see **Figure 1-20A**) (Hattori and Gouaux 2012). A sequence comparison between zfP2X4 and different receptor subtypes showed that the 8 aforesaid amino acids are not subtype-specific and are conserved across many species including rodent and human (Xu et al. 2014). ATP adopts a particular U-shaped conformation with the adenine moiety inserting in a narrow pocket within the lower body while the phosphates make contacts with a polar region in the upper body of the adjacent subunit. It is possible that the U-shape is favoured by a polar interaction between the 2' hydroxyl of the ribose and the gamma-phosphate. The hypothesis is supported by activity and docking studies on the 2'deoxy ATP and 3'deoxy ATP where there is a further reduction of agonist activity when the hydroxyl responsible for the intra-molecular H-bond is removed (Fryatt et al. 2016). The adenine and the gamma phosphate are crucial for agonist potency and efficacy and this is supported by the observation that ADP and CTP are extremely weak or only partial agonists (Bowler et al. 2003; Soto et al. 1996), although covalent tethering of ADP to Arg-125 in P2X7 is capable of rendering ADP an agonist (Adriouch et al. 2008; Browne and North 2013). The partial agonist CTP displays a similar conformation of the 3 phosphate groups with the gamma phosphate interacting with the same polar residues and in close proximity to the 2'-OH of the ribose (maybe forming a H-bond in a similar fashion to that hypothesized in ATP, see **Figure 1-20B**). As seen in **Figure 1-20B**, the cytosine moiety sits in a similar position to the adenine (although smaller) forming two H-bonds between the N4 of the cytosine and the main chain of the Thr-189 and N4 and Lys-70 backbone respectively. A further H-bond is formed between O2 and Arg-143 and the longer H-bond length might be the reason for CTP only being a partial agonist (Kasuya et al. 2016).

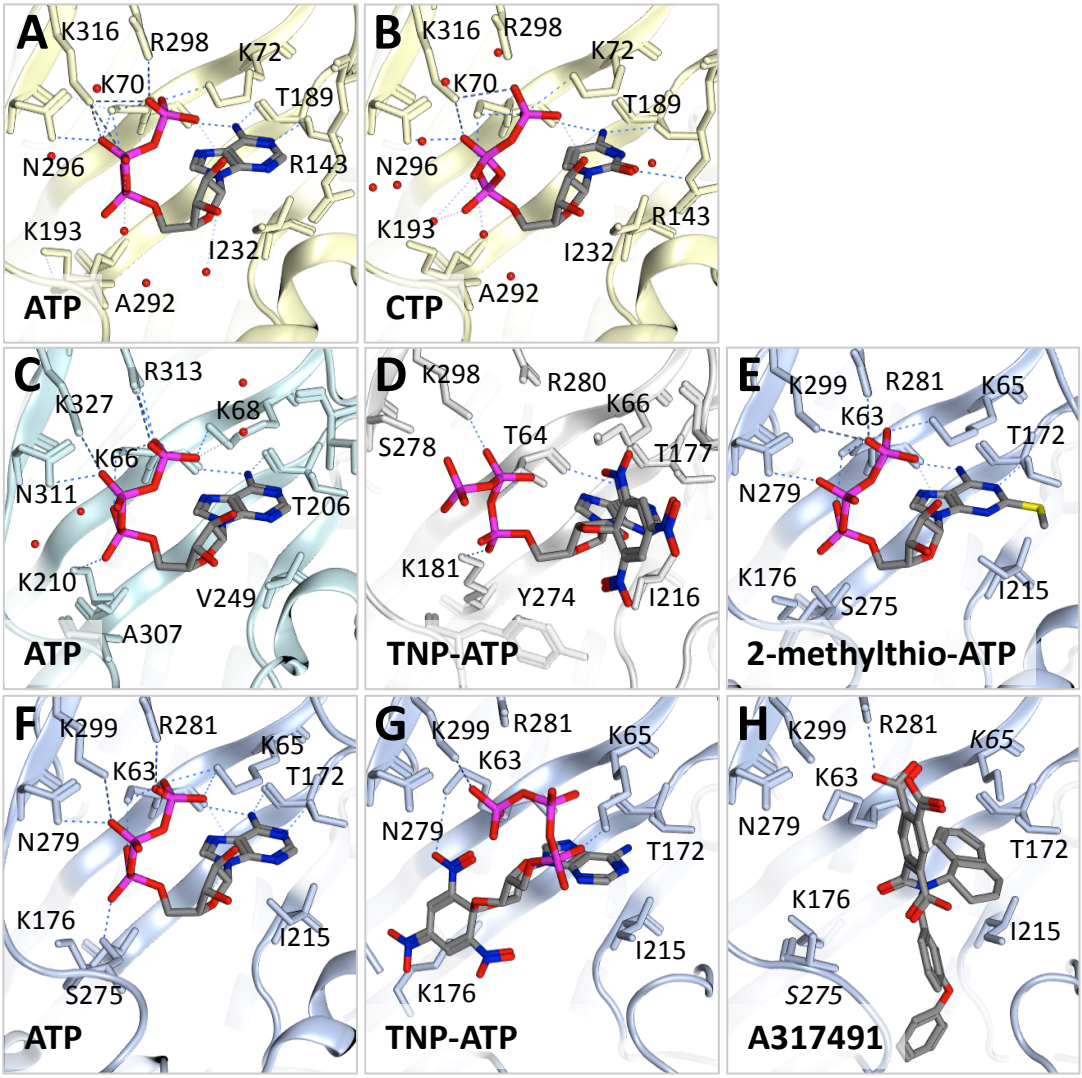

Figure 1-20: Binding of competitive ligands. ATP (4DW1, (**A**)) and CTP (5WZY, (**B**)) bound to crystal structures of zebrafish P2X4 respectively (water molecules shown in red). ATP (5F1C, (**C**)) bound to Gulf coast tick crystal structure. ATP (5SVK, (**F**)), 2-methylthio-ATP (5SVP, (**E**)), TNP-ATP (5SVQ, (**G**)) and A317491 (5SVR, (**H**)) bound to human P2X3 crystal structures. TNP-ATP (5XW6, (**D**)) bound to the crystal structure of Chicken P2X7. H-bond interactions between ligand and receptor are displayed with blue dot lines. Crystal data is incomplete in the PDB file 5SVQ, (**G**) where the loop containing S275 is missing and in 5SVR (**H**) where K65 and S275 (labeled in italic) have missing atoms. Figure made with MOE2014.09 and modified from (Pasqualetto et al. 2018).

The structures of competitive antagonists have also been reported including A-317491 and the non-selective TNP-ATP, co-crystallized in human P2X3 (**Figure 1-20H**) and in both human P2X3 (hP2X3) (**Figure 1-20G**) and chicken P2X7 (chP2X7) (**Figure 1-20D**) respectively. In both crystals the adenine moiety of the TNP-ATP sits in a similar conformation to the ATP while the gamma phosphate does not adopt the classical U-shape observed in the available ATP-bound P2X structures (Hattori and Gouaux 2012; Mansoor et al. 2016) (**Figure 1-20D,G**). When comparing the conformation of the tri-nitro phenyl group in hP2X3 and in chP2X7, their position is strikingly different with the tri-nitro phenyl pointing inward the pocket in the first and outward in the latter. Interestingly in the case of A-317491, the antagonist protrudes downwards into a hydrophobic pocket that is not being explored by agonists in the known structures.

1.5.3.2 Allosteric sites

Two different research groups demonstrated the presence of a binding site for multiple antagonists at P2X7 (Allsopp et al. 2017; Karasawa and Kawate 2016), some of which were previously considered competitive (Bhattacharya et al. 2013; Donnelly-Roberts et al. 2009; Honore et al. 2006). An extensive mutagenesis and *in silico* analysis enabled the prediction of the allosteric binding site for AZ10606120 (Allsopp et al. 2017), later confirmed by structural and functional data of the co-crystallized ligand in the giant panda P2X7 receptor homologue (Karasawa and Kawate 2016) (ligands co-crystallised in the allosteric pocket are represented in **Figure 1-21**). The binding site is situated in the ectodomain between the head and the upper body domains of adjacent subunits and is mainly delimited by hydrophobic residues (Phe-95, Phe-103, Met-105, Phe-293, Tyr-295; panda P2X7 numbering). A charged residue (Lys-110) near the pocket entrance makes polar interactions with the quinolone group of A740003 and A804598 or the pyridine group of JNJ47965567 (**Figure 1-21E,F,G**). The sidechain of another lysine (Lys-297) further inside the pocket - fully resolved only in the structure bound to JNJ47965567 (shown in **Figure 1-21E**, residue label in bold; PDB ID: 5U1X) - forms an H-bond with the aromatic amide of JNJ47965567. In all the other structures the missing atoms of Lys-297 (presents as solely backbone) do not allow the identification of possible H-bonds but may suggest a high degree of conformational flexibility for this residue side-chain. In comparison to the

orthosteric binding pocket, the entrance to the allosteric pocket is much narrower and deeper. Interestingly, the allosteric binding site extends towards and is in direct communication with the upper vestibule of the channel pore. Among the co-crystalized antagonists, JNJ47965567 is the molecule that extends the deepest with the phenyl-piperazinyl moiety lying almost completely in the upper vestibule (**Figure 1-21B**).

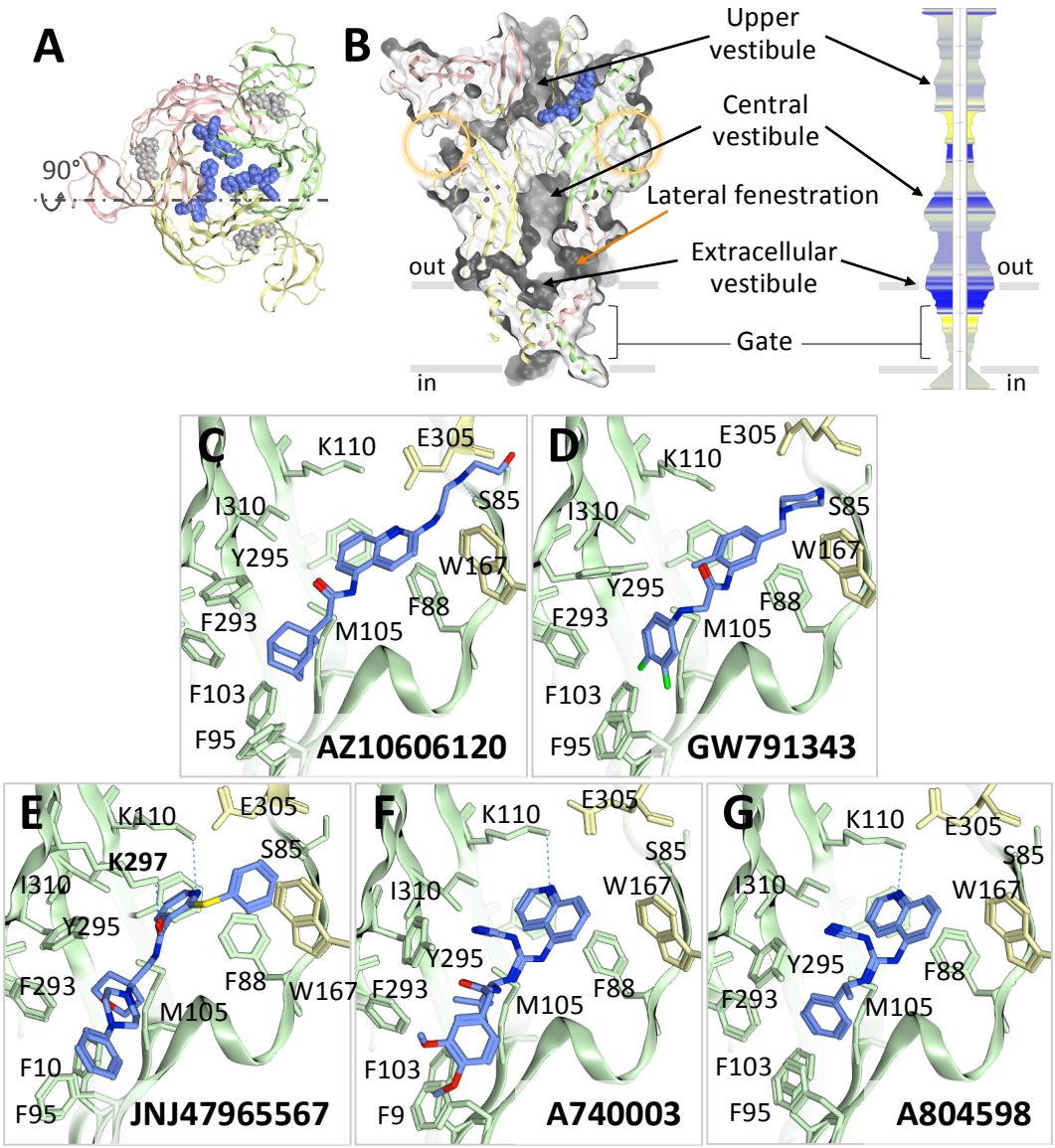

Figure 1-21: Allosteric antagonists bound to giant panda P2X7. (**A**) Top view of crystal structure (PDB ID: 5U1X) bound to JNJ47965567 antagonist (blue), ATP (in grey) was superposed as reference for comparison with the location of the orthosteric binding site. (**B**, Left) JNJ47965567 molecule protruding from the allosteric pocket to the upper vestibule of the channel pore as seen from a mid-section of 5U1X. Only one molecule of antagonist is shown for clarity. Approximate location of residues of the orthosteric pocket is circled in orange. (**B**, right) Schematic representation of the channel pore width computed and generate with MOLE*online* *(https://mole.upol.cz)*. Approximately 5.25 Å on the widest section of the cavity and 139.8 Å of cavity path-length. Colors represent increasing hydropathy of the residues facing the pore (from low, in yellow, to high, in blue) Crystal structure of panda P2X7 bound to AZ10606120 (5U1W, (**C**)), GW791343 (5U1Y, (**D**)), JNJ47965567 (5U1X, (**E**)), A740003 (5U1U, (**F**)) and A804598 (5U1V, (**G**)) and residues lining the allosteric pocket. Residues and ribbons colored according the color subunit in (**A**). F108 is not labelled for clarity. Figure C to G modified from (Pasqualetto et al. 2018).

Very recently, the crystal structure of human P2X3 bound to AF-219 has unveiled the presence of an allosteric pocket with a different location compared to the binding site identified by Karasawa and Kawate in the P2X7 receptor subtype (Wang et al. 2018). AF-219 binds in a pocket located between two adjacent subunits and formed by the left flipper and lower body of one subunit (light aqua in **Figure 1-22**) and the head, dorsal fin and lower body of the adjacent subunit (light slate, **Figure 1-22**). The 4-isopropyl-2-methoxybenzenesulfonamide moiety of AF-219 is buried deep in the site with the isopropyl group pointing inward where prevalently hydrophobic amino acids (Val-61, Leu-191, Val-238) are present while the sulphonamide group is establishing an H-bond with the sidechain of Lys-176 (following a brief molecular dynamics simulation *Wang et al*. noted that the H-bond could be formed between Lys-176 and either of the O of the sulphonamide). The 2,4-diaminopiyrimidine occupies the solvent exposed portion of the pocket and establishes a H-bond with Asn-190. Multiple additional H-bonds formed between the backbone of Leu-191 were not observed in the crystal structure but were seen by *Wang et al*. after a brief (10-20 ps) molecular dynamics simulation (Wang et al. 2018).

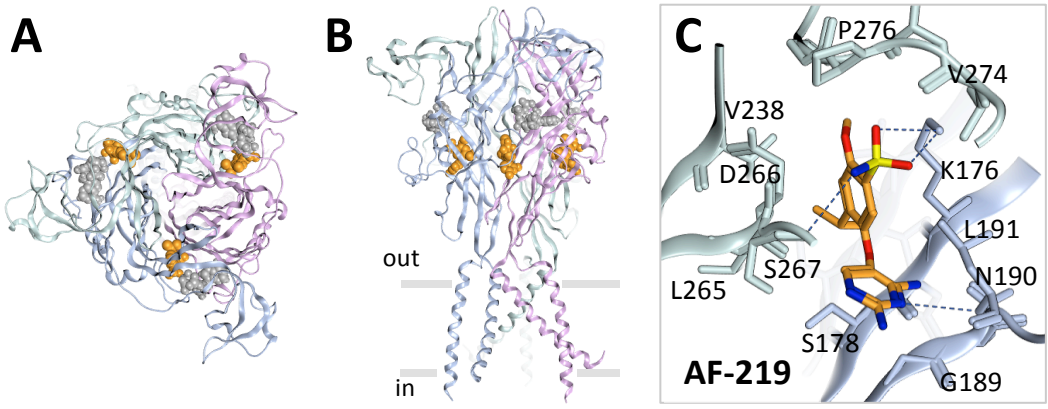

Figure 1-22: AF-219 allosteric antagonist bound to human P2X3. Top (**A**) and side (**B**) view of human P2X3 highlighting the location of the AF-219 binding site (AF-219 in orange). ATP (in grey) was superposed as orthosteric pocket reference. (**C**) Site view of AF-219 and nearby residues. Val-61 is not shown in (**C**). Note that an H-bond between Ser-267 backbone and N of the sulfonamide was recognized as interaction in MOE2014.09 during the making of this figure but has not been reported by *Wang et al*. (Wang et al. 2018).

Hypotheses have been advanced concerning the presence in other receptor subtypes of allosteric pockets corresponding to the ones identified to date (Karasawa and Kawate 2016), although no data is currently available to support this hypothesis. The confirmation of these hypotheses would be of great significance for the rational design of novel P2X allosteric modulators.

1.5.4 P2X receptor structures as homology model template

The recent publications of multiple crystal structures of P2X receptors has contributed a deep understanding of the receptor at a molecular level, although the human P2X3 structure is the sole human structure published to date. Therefore structural studies still rely heavily on homology models based on templates (NMR and crystal structures) available (further details regarding molecular modelling and homology modelling tools will be discussed in **Section 1.6** and **Section 3.1**). Fortunately, the sequence identity between of the human P2X subtypes and the crystal structures currently available is sufficient (sequence identity approximately 50% across subtypes and reaching even higher level of identity zebrafish P2X4 vs. hP2X4 and panda P2X7 and human P2X7) to allow their use as templates for human model generation (see **Figure 1-23**). It is important to note that none of the solved structures represents the full-length receptors and most of the truncations removed portions of the cytoplasmic domain, for which the structural data is still extremely limited, impacting unfavourably on any attempt at C-terminus structure prediction and validation (especially for P2X7). The modelling of human P2X receptor structures has been used successfully in previous studies to interpret functional and pharmacological data (Allsopp et al. 2017; Evans 2010) and has also been extensively used in this work.

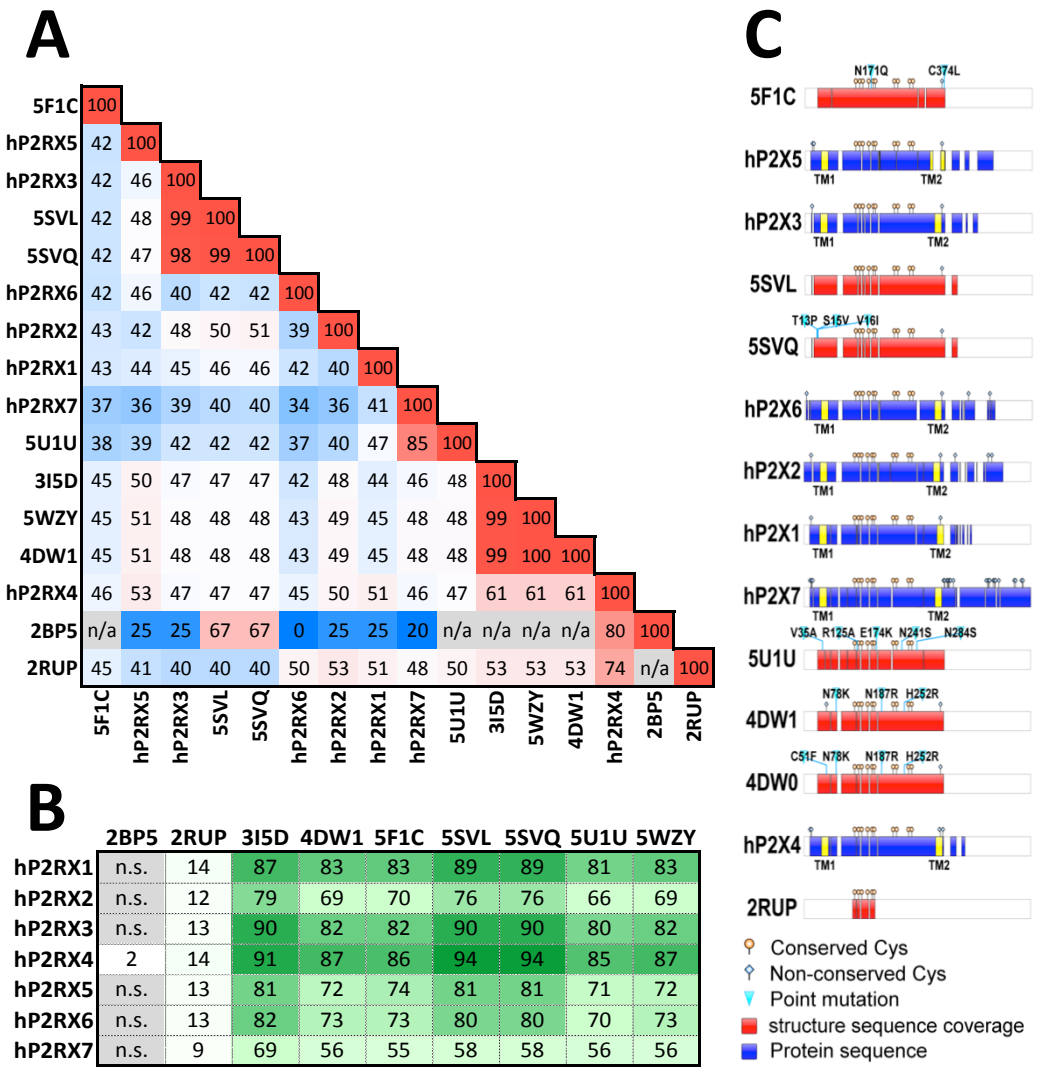

Figure 1-23: Comparison of structural data available to date in relationship to human P2X receptor sequences. 5XW6 and 5YVE are not included. For clarity purpose, sequences with over 99.5% identity were grouped together under a single PDB ID (e.g. 5SVL with 5SVM and 5SVP; 5SVQ with 5SVJ, 5SVK, 5SVR, 5SVT and 5SVS; 4DW1 with 4DW0 and 3H9V; 5U1U with 5U1L, 5U1V, 5U1W, 5U1X, 5U1Y and 5U2H). (**A**) Sequence identity among solved structures and human P2X sequences (Uniprot IDs: P51575, hP2RX1; Q9UBL9, hP2RX2; P56373, hP2RX3; Q99571, hP2RX4; Q93086, hP2RX5; O15547, hP2RX6; Q99572, hP2RX7). Sequence alignment and percentage identity obtained with ClustalW (values in percentage; from blue, low identity, to red for high identity; n/a, non-aligned). (**B**) Percentage coverage of human P2Xs sequence by crystal structures (calculated using Blastp). (**C**) Graphical representation of coverage of human P2Xs sequence by crystal structures showing aligned domains. Gaps are represented with white sections. 3ID5 and 3H9V not included. 2BP5, which consists in a 10 amino acids long cytosolic C-terminal peptide was also not represented. Image made using Illustrator for Biological Sequences (IBS, http://ibs.biocuckoo.org). Image modified from (Pasqualetto et al. 2018).

1.6 Structure-based drug design using P2X receptor homology models

1.6.1 Drug discovery

For most of the commercialized drugs, their initial discovery dates back to several years before their first entry on the market with an estimated average of 14 years time-lapse between their identification as candidate and their official approval by the Food and Drug Administration (FDA) (Myers and Baker 2001). Any discovery has unique features but the overall process can be generalized in two main stages (**Figure 1-24**): (i) drug discovery – leading to the identification of suitable drug candidates – and (ii) drug development, which involves *in vivo* characterization in terms of pharmacokinetics, toxicology and activity. The deep understanding of the role of the target in pathological conditions, biological pathways and the surrounding network of interactors is the first fundamental step to avoid drug development fails or market withdrawals (Wang et al. 2013). Once the target has been identified and validated, High Throughput Screening (HTS) biological assays on large compound libraries or *in silico* technique combined to biological evaluation of small-scale libraries are deployed to identify active compounds ('hits'), whose activity and chemical profiles are further characterized and improved for the proof-of-concept and cytotoxicity evaluation. Optimized compounds ('leads') proceed to *in vivo* tests using animal models of disease for the evaluation of activity and the ADMET (Absorption, Distribution, Metabolism, Excretion and Toxicity) profile (Williams and Lemke 2002). Pre-clinical data must show a positive safety profile for the drug candidates to proceed to the clinical trials where the drug is initially tested in a small group of healthy volunteers to assess tolerability and dosage (Phase I, 'first-in-human'). Subsequently, the efficacy of the drug is evaluated in patients (Phase II) further comparing the new drug to the others commercially available treatments focusing on patient outcome, compliance and severity and recurrence of adverse and side effects (Phase III) (Williams and Lemke 2002). The drugs that successfully pass the clinical trials are subjected to review and approval from the Food and Drug Administration (FDA) and can be commercialized. Their long-term effects on a worldwide scale are monitored post-approval through pharmaco-surveillance (Williams and Lemke 2002).

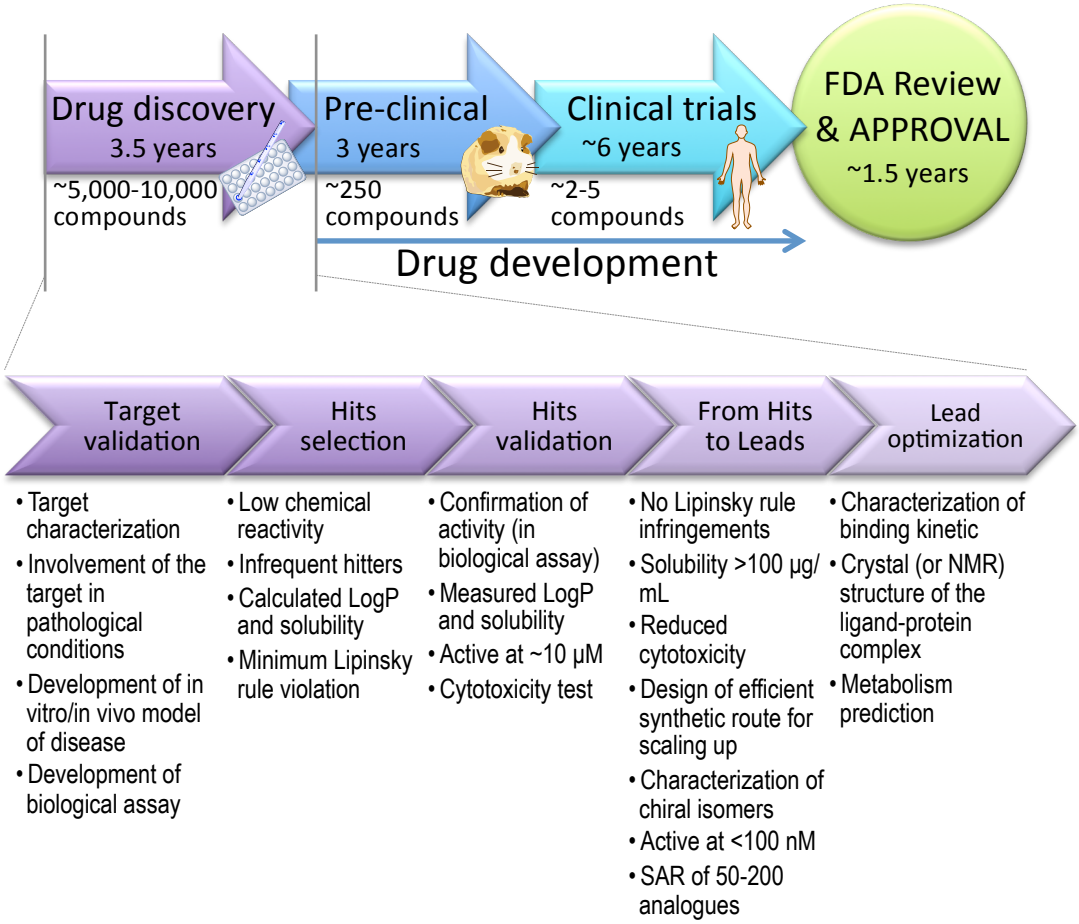

Figure 1-24: The drug discovery and development process and stage requirements within the drug discovery phase (Bottom). During these stages compounds initially found active are regarded as 'hits' while compounds that presents improved physical- pharmacological- and chemical- properties are defined as 'leads'.

Each stage of the drug discovery and development process bears exponentially increasing costs that are highly aggravated by the elevated percentage of fails leading, in recent years, to an average of $2.5 billion in development costs per drug entered in the market (Plenge 2016). This, combined to a stalling trend in the number of approved drug per year, has urged pharmaceutical companies to approach the drug discovery and development process from different angles in order to reduce costs and increase success-rate by introducing strategies such as drug repositioning, phenotypic screening and computer-aided drug design (Ashburn and Thor 2004; Zheng et al. 2013) (Ooms 2000).

1.6.2 Computer-aided drug design: introducing molecular mechanics and quantum mechanics

The introduction of computers as drug design tools backtracks to 1980s with the first attempts to relate compound structures to their activity and rationally predict the properties of molecules with similar 3-Dimensional features (Gund 1977; Kaul 1998). Since then, computer-aided drug design has extensively risen in its application thanks to the exponential increase in computing power, which allows the handling of far more difficult tasks (Hassan Baig et al. 2016; Macalino et al. 2015; Song et al. 2009). While this work does not aim at describing the physics theories, mathematics and computer science principles on which computational chemistry and molecular modelling are based, a brief acknowledgement of some fundamentals is required. In computational chemistry, the description of a molecular or macromolecular system is indeed complex and can be studied at two different levels *via* Quantum Mechanics (QM) and Molecular Mechanics (MM) (Leach 2001; Williams and Lemke 2002). Although QM applies the Schrödinger's equation and the molecular orbital theory to the modelling of the system being the most accurate approach available, it is extremely computationally demanding and therefore its use is often limited to the description of electron density studies or in simulations where studying chemical bond formation is the main goal (Leach 2001; Williams and Lemke 2002). In MM the molecules are seen as ball-and-spring models where atoms are usually treated as solid spheres and bonds are unbreakable; thus MM describes a system through classical mechanics *via* a potential energy function (namely 'force field'), which represents the sum of bonded atoms interactions (e.g. bond stretching, angle bending and torsion rotation) and non-bonded atoms interactions (e.g. van der Waals and electrostatic interactions). Calculations through this potential energy function are less complex than Schrödinger's equation allowing significantly lower computational costs – still largely the limiting factor in molecular modelling - and thus MM is the approach of choice in many of the techniques employed in computer-aided drug discovery (Leach 2001; Williams and Lemke 2002).

1.6.3 Virtual Screening and Structure based-drug design

Nowadays, computer-aided techniques are established tools implemented in the drug discovery workflow - sometimes alongside or replacing the high throughput biological screening of large libraries. Aiming at time- and cost-effective identification of active compounds, virtual screenings are often performed on large virtual compound libraries in order to identify just a relatively small subset of compounds to be synthetized and biologically evaluated. This is usually attained by filtering a virtual library of compounds on the basis of the essential features that an 'ideal compound' specific for the target of choice should present (Bissantz et al. 2010). These features may be identified through a (i) ligand-based or (ii) structure-based approach depending on the availability of activity data of multiple ligands for the specific biological target to optimise ligand properties or on the availability of 3D structure of the target in order to enhance drug-target interactions, respectively (Leach 2001). Structure-based drug design relies on the availability of an X-ray crystal, NMR or cryo-EM structure of the biological target or the ligand-target complex (Leach 2001) and online databases such as the Protein Data Bank (PDB) give the opportunity to any researcher to access all the published structures (www.rcsb.org). Ideally, founding the design of active compounds on the study on multiple structures of the biological target in complex with diverse ligands gives the best chances of success but this is a rather rare situation. In most cases - where available - the structure is truncated, missing an important portion of the target, in the *apo*- state or is a homologue from a phylogenetically distant species, thus homology-modelling techniques are widely used (França 2015) for further applications such as docking simulations, molecular dynamics and target-based pharmacophore searches. A brief description of the homology modelling process is described in **Section 3.1**.

1.6.4 Docking

Docking simulations are one of the most widely used computational tools in structure-based modelling, aiming to evaluate the 'fit' of a set of molecular conformations (derived from a compound library or a single molecule) in a protein cavity by estimating favourable protein-ligand interactions and steric hindrance. The method relies entirely on the availability of structural data of the target,

whether a crystal or NMR structure is available or a reliable homology model could be obtained from a closely related protein structure. The less complex docking scenario accounts only for the flexibility of the ligand - interacting with non-covalent bonds - while the protein is treated as a rigid body, which is an approximation that needs to be carefully evaluated case by case (more complex scenarios that calculate protein flexibility are possible but not herein described). In general, every docking simulation is the result of the symbiotic combination of a (i) 'searching algorithm' and a (ii) 'scoring function'. While the first is responsible for generating multiple ligand poses within the pocket (sampling) accounting for molecule rotations, translations, angle bending and torsions, the latter evaluates plausible poses and ranks them according to a non-exhaustive estimation of binding free energy value (therefore designated as 'score' instead) – an approximation that is due to the otherwise non-feasible and computationally demanding calculations (Trist et al. 2018). The searching algorithms are based on either stochastic (randomised) or systematic methods for the pose sampling whilst scoring functions can approximate binding energies through interaction predictions based on molecular mechanics, estimates based on experimental measurements of binding phenomena or from calculations derived from crystallographic data (Ferreira et al. 2015; Kitchen et al. 2004). To keep in mind as take-away message, the number of parameters considered within the 'score' calculations is directly correlated to the ameliorated accuracy but also to the time required to assign the 'score' to each sampled pose. This concept is particularly important when performing docking of large libraries of compounds – for instance as part of structure-based virtual screenings - where accuracy and speed needs to be finely balanced (Lyne 2002). One approach to speed up the process whilst maintaining good accuracy in final pose selection and ranking is based on multiple rounds of docking – each with increasing accuracy in the scoring function - where poorly scored poses are filtered out at the end of each round, effectively and drastically reducing the number of poses carried onward to the next round. This is, for instance, the method used by the automated Maestro Virtual screening workflow (Small-Molecule Drug Discovery Suite, Schrödinger, LLC, New York, NY) in combination with physico-chemical drug-likeness filters (i.e. predicted octanol/water repartition, reactivity, etc.). Another approach is the *consensus score* where the top-ranked poses obtained through a docking scoring function are rescored through diverse scoring functions and the final

selection falls on the poses that top-scored with each of the scoring functions (Charifson et al. 1999). Although scoring functions and in general all the computer-aided techniques are extremely helpful tools in the identification of drug candidates, researcher intervention and judgement still has a pivotal role in each step of the drug discovery process.

1.6.5 Examples of drugs designed using in silico techniques

Ultimately, the effectiveness of a methodology needs to be supported by experimental data. There are numerous recent examples of successful identification of drug candidates through computer-aided drug design, among whose the discovery of potent carbonic anhydrase II inhibitors (using FlexX) (Grüneberg et al. 2001), the discovery and ligands targeting Factor Xa, Thrombin and Estrogen receptor (Baxter et al. 2000) and the development of farnesyltransferase inhibitors into 'lead' compounds (Perola et al. 2000). Most importantly, drugs already successfully approved by FDA such as Imatinib - initially known as CGP 57148 and STI571 - (now Glivec®, by Novartis) and indicated for chronic myeloid leukemia and Gefitinib (Iressa®, by AstraZeneca) for non-small cell lung cancer therapy have been some of the first to be developed through a rational and computational approach (Hickey et al. 1994; Traxler and Furet 1999; Ward et al. 1994). These examples indicate that using a rational design approach and computer-aided techniques can notably help in the discovery of active candidates and could improve the success rate while reducing time and costs related to the high throughput biological screening methods. Computer-aided drug design is a particularly relevant strategy in an academic setting where funds, time and 'workforce' involved in a project may be substantially reduced compared to industry.

1.7 Aims and objectives of the project

The importance of developing novel compounds active at P2X4 and P2X7 receptors is underlined by their roles in control of vascular tone, neurotransmission, neuropathic pain, cancer, immunity and inflammation.

Furthermore, the recently published structural data has given a very valuable opportunity for the use of structure-based drug design in an attempt to find hit compounds. This project aims:

(i) to identify and develop novel P2X4 and P2X7 receptors small-molecule modulators with the assistance of structure-aided drug design;

(ii) to understand the molecular basis for modulator selectivity at P2X4 and P2X7, using a combination of molecular docking and analysis of inter-species and -subtype differences in pharmacology and selectivity.

Chapter 2:

Materials and Methods

2 MATERIALS AND METHODS

2.1 Materials

All chemicals and reagents were obtained from Sigma-Aldrich (Sigma-Aldrich Corporation, Dorset, UK), unless otherwise specified. Phosphate Saline Buffer (PBS, #10010023), Foetal bovine serum (FBS; #10270106), penicillin-streptomycin (10,000 U/mL; #15140122), trypsin-EDTA (0.05%) with phenol red (#2500062), Dulbecco's modified Eagle's medium (DMEM/F-12) with Glutamax (cat. No. #31331093), G-418 (Geneticin®; #10131027) and DMSO (#BP231-100) were purchased from Fisher Scientific (Fisher Scientific UK, Loughborough, UK). Cell culture flasks, 6-wells plates and 96-wells plates were obtained from Sarstedt (Sarstedt AG & Co. KG, Germany).

2.2 Cell culture and protein expression

2.2.1 Cell culture and preparation of frozen stocks

HEK293 and 1321N1 astrocytoma cells were pre-owned by Dr Mark Young's lab and originally purchased from the European Collection of Authenticated Cell Cultures (ECACC, Salisbury, UK; catalogue no. #85120602 and #86030402, respectively). All cell lines were cultured (at 37°C, 5% CO_2) in DMEM/F-12 with Glutamax supplemented with 10% FBS and 200 unit/mL of penicillin-streptomycin antibiotics. Stably transfected clones were grown in DMEM/F-12 with Glutamax medium supplemented with G-418, 600 µg/ml and 150 µg/ml during selection and maintenance respectively. Stable cells line expressing N-terminally Halo-tagged mouse P2X7 (Met-283 variant) receptor (HNFL2 cell line; see **Appendix 3**) were kindly provided by Dr Marta Radwan. Frozen stocks for each stable cell line were prepared by gently resuspending (pelleted at 1200 rpm, 4 min, room temperature) with ice cold 10% DMSO in FBS and quickly transferring 1mL of the suspension in cryo-vials to be stored long-term in liquid nitrogen (3x and 5x 1mL aliquots were prepared from a confluent 75 cm^2 and 175 cm^2 flask respectively).

2.2.2 Transient transfection and stable cell line generation

Cells were seeded in 6-well plates (at $5x10^5$-$1x10^6$ cells/well) and transfected the following day with 1 µg plasmid DNA (see **Table 2.1**) and FuGene HD Transfection Reagent (Promega, Southampton, UK; #E2311) using a 1:3 (µg:µl) DNA:Fugene HD ratio, according to the manufacturer's protocol (https://www.promega.co.uk). For transient transfection, subsequent analysis was performed on cells 24-72 hours post-transfection, as indicated. For stable cell line generation, sufficient time (30-48h) was given to permit the development of antibiotic resistance before starting single colony selection, by plating transfected cells into 96-wells plates (10-100 cells/well) with culture medium containing 600 µg/mL G418. Colony growth was monitored for 4-6 weeks and resistant single colonies were grown up via 24-well plates to confluent 25 cm^2 flasks (or 2x9 cm^2 wells). Each clone was tested for P2X4 receptor expression by Western blot and clones, which displayed receptor expression, were assessed for functionality using the Ca^{2+} influx assay (**Section 2.3.1 and Appendix 1**). P2X7 stable cell line generation followed the same procedure but functionality was tested using the YO-PRO dye uptake assay (**Section 2.3.2 and Appendix 3**).

Species	Receptor	Plasmid name
rat	P2X4	RML2 (a kind gift from Prof Murrell-Legnado) (Royle et al. 2005)
rat	P2X4	RML2 T312I (MTY)
human	P2X4	pL118, I312T (MTY)
human	P2X4	pL118, (MTY)
human	P2X7	hP2X7 (EE-tagged); (MTY) midi prep; 28/11/13

Table 2.1: List of constructs used in the transfection protocol. All the constructs were prepared with Qiagen mini- or midi-prep. The concentration was measured with a Nanodrop spectrophotometer (Thermo Scientific) at 260 nm. Constructs were provided by Dr Mark Young (MTY) unless otherwise specified.

2.2.3 Bradford protein assay

A series of BSA (Fraction V; Fisher Scientific; #BP1600-100) standards and each protein lysate sample were prepared in half-micro cuvettes (Fisher Scientific) (as reported in **Table 2.2**) and their absorbance (595 nm, n=2-3) was measured with a Biorad SmartSpec Plus spectrophotometer. The standard curve built with the known concentrations of the BSA (ranging between 0.5 µg/mL and 6 µg/mL) was used to approximate the overall protein concentration of each sample.

Component	Blank	0.5 µg/mL standard	1 µg/mL standard	2 µg/mL standard	4 µg/mL standard	6 µg/mL standard	Sample
1x Protein Assay Reagent	980 µL	980 µL	980 µL	980 µL	980 µL	980 µL	980 µL
PBS	20 µL	19 µL	18 µL	16 µL	12 µL	8 µL	18 µL
BSA (1 mg/mL)	-	1 µL	2 µL	4 µL	8 µL	12 µL	-
Protein lysate	-	-	-	-	-	-	2 µL

Table 2.2: Details of sample and standards preparation for Bradford assay. 1x Protein Assay reagent was prepared by diluting Bio-Rad concentrated Protein Assay reagent (1:5 in distilled water).

2.2.4 Cell lysis, SDS-PAGE and Western blotting

2.2.4.1 Cell lysis and loading sample preparation

Cells in individual wells from a 6-well plate were washed with 1 mL ice-cold PBS buffer then transferred to a 1.5 mL tube, either by pipetting up and down or using a cell scraper, and centrifuged at 4000x *g* for 3 minutes at room temperature. Cell pellets were resuspended in 100 µL of lysis buffer (see **Table 2.3**) and incubated on ice for 20 min with occasional gentle mixing. The supernatant containing solubilized protein was separated from cell debris by centrifugation (5 min at 4°C, 16000*x g*) and the overall protein concentration of the supernatant was assessed by Bradford assay (**Section 2.2.3**). 80µL of protein lysate was mixed with 20 µL SDS-PAGE sample buffer (see **Table 2.3**) and denatured at 95°C for 5 min.

Buffer	Components and final concentration
Lysis buffer (modified Schindler buffer)	150 mM NaCl
	50 mM HEPES pH 7.5
	10% glycerol
	1 mM EDTA
	1 mM DTT*
	1% DDM*
	1x Protease inhibitors* (Complete –EDTA, Roche)
SDS-PAGE sample buffer (5x)	12% (w/v) SDS
	10mM EDTA
	10% (v/v) Glycerol
	100 mM Tris-HCl, ph 6.8
	0.05% (w/v) Bromophenol Blue
	50 mM TCEP
	NaOH to pH 6.8

Table 2.3: Buffers and gel compositions for the cell lysis and the sample preparation. *added fresh every time.

2.2.4.2 Gel electrophoresis

Either 10% or 12% polyacrylamide gels were prepared according to **Table 2.4**, allowing time for polymerisation of the separating gel before pouring the stacking gel (4.5% polyacrylamide). An equal quantity of each protein sample (3.5-10 μg) prepared as described above was loaded (alongside 4-5 μL of Precision Plus Protein Standard marker, BioJRad®, Hemel Hemstead) and gels were run in 1x TGS running buffer (**Table 2.4**) for 10min at 100 V (to allow the proteins to align at the bottom of the stacking gel) followed by 1 hour at 120 V.

SDS-Page electrophoresis		
Polyacrylamide gel	Component	Volume to add (mL)
Stacking gel (5 mL)	H_20	3.5
	1 M Tris-HCl pH 6.8	0.625
	30%/0.8% Acrylamide/Bis-acrylamide (w/v)	0.75
	20% SDS (w/v)	0.025
	30% APS ammonium persulfate (w/v)	0.015
	TEMED	0.0040
10% polyacrylamide Separating gel (10 mL)	H_20	4.1
	1.5 M Tris-HCl pH 8.8	2.5
	30%/0.8% Acrylamide/Bis-acrylamide (w/v)	3.4
	20% SDS (w/v)	0.050
	30% APS ammonium persulfate (w/v)	0.035
	TEMED	0.010
12% polyacrylamide Separating gel (10 mL)	H_20	3.5
	1.5 M Tris-HCl pH 8.8	2.5
	30%/0.8% Acrylamide/Bis-acrylamide (w/v)	4.0
	20% SDS (w/v)	0.050
	30% APS ammonium persulfate (w/v)	0.035
	TEMED	0.010
Buffer	Component and final concentration	Quantity to add (g)
1x Running buffer (1 L)	25 mM Tris-HCl	3.0
	192 mM Glycine	14.4
	0.1% SDS (w/v)	1.0

Table 2.4: SDS-Page buffers and gel composition.

2.2.4.3 Blotting and protein detection

A Trans-blot Turbo Transfer system (Biorad Laboratories, Hercules, CA, USA) was used to transfer (7 min) the size-separated proteins from the polyacrylamide gel to PVDF membrane (Biorad), according to manufacturer's instructions. The membrane was briefly rinsed in TBS-T buffer (**Table 2.5**), blocked on a rocking platform with 5% skimmed milk powder (in 20 mL TBS-T, at room temperature, 1 hour) and then washed in TBS-T (3x5 min, room temperature) before overnight incubation (4°C) with the specific primary antibody solution on a rocking platform (see **Table 2.5**). Excess primary antibody was removed by repeated washing (TBS-

T, 3x15 min, room temperature) before application of the secondary antibody solution under gentle shaking (in 20 mL TBS-T, at room temperature, 1 hour). The membrane was sequentially washed (TBS-T, 3x20 min, room temperature) and finally developed with 1.5 mL of ECL solution (Biorad; or LI-COR, Cambridge) using a Biorad ChemiDoc XRS chemiluminescence detector.

Blotting, membrane blocking and incubation					
Buffer	Component				
1x TBS-T buffer	25 mM Tris/HCl pH 7.4				
	150 mM NaCl				
	0.02 % Tween 20				
Antibody	Concentration	Host	Specificity	Supplier	Cat. No.
Anti-P2X4	1:2000 in 5% milk, TBS-T (from 0.8 mg/ml stock, after reconstitution)	Rb	H, M, R	Alomone (Jerusalem, Israel)	#APR-002
Anti-P2X7	1:2000 in 5% milk, TBS-T (from 0.6 mg/ml stock, after reconstitution)	Rb	H, M, R	Alomone	#APR-004
Anti-rabbit HRP[b]	1:2000 in 5% milk, TBS-T (from 0.25g/L stock)	G	Rb	Dako (Glostrup, Denmark)	#P0448
Anti-mouse HRP[b]	1:5000 in 5% BSA, TBS-T (from 0.25g/L stock)	Rb	M	Dako	#P0260

[a] H: human (*Homo sapiens*); M: mouse (*Mus musculus*); R: rat (*Rattus norvegicus*); G: goat (*Capra aegagrus hircus*); Rb: rabbit.

[b] HRP: Horseradish Peroxidase

Table 2.5: Buffer composition used for washing, blocking and incubation and list of antibodies and their optimum concentration.

2.3 FUNCTIONAL ASSAYS

2.3.1 FLUO-4 fluorescent Ca^{2+} influx assay

Cells were plated the day before assay into poly-Lysine (35 µL poly-Lysine incubation for 20 min followed by PBS wash) pre-treated 96-well plate at 40-65,000 cells/ml concentration. Culture medium was replaced with modified Ringer's buffer (140 mM NaCl, 10 mM HEPES, 10 mM Glucose, 1 mM $MgCl_2$, 1 mM $CaCl_2$, 2.5 mM KCl, 0.5% BSA, pH=7.4) containing 2.6 µM FLUO4-AM (Fisher Scientific, UK; #F14201) and 250 µM Probenecid (#P8761), cells were incubated for 20-30 min and buffer was replaced with fresh Ringer's buffer (containing 500 µM Probenecid). For compound testing, 1 µL of compound dissolved in a compatible vehicle was diluted 1:100 in modified Ringer's buffer prior to addition of 1:10 volume of the total well buffer volume (1% or 0.1% final concentration of ethanol or DMSO respectively). Appropriate vehicle controls were used in each experiment accordingly. Before the assay optimization, experiments to identify functional clones were conducted using extracellular solution (ECS; 147 mM NaCl, 10 mM HEPES, 13 mM Glucose, 1 mM $MgCl_2$, 2 mM $CaCl_2$, 2 mM KCl. pH=7.3 in MilliQ water) containing 2.6 µM FLUO4-AM. A Fluoroskan Ascent FL plate reader (Fisher Scientific) equipped with a solution dispenser and an appropriate filter pair (excitation: 485 nm, emission: 538 nm) was used to record 5 sec baseline followed by P2X4-mediated Ca^{2+} influx measurements for 20-25 sec after ATP (Sigma, #A26209) stimulation (20 µL injection). The collected responses were normalized to the first data-point recorded after ATP injection. The amplitude of ATP responses was calculated as $\Delta F/F_0$, where $\Delta F = F_1 - F_0$, subtracting the fluorescent background as suggested by Bootman *et al.* (Bootman et al. 2013).

2.3.2 YO-PRO fluorescent dye uptake assay

Cells were plated the day before assay in a 96-well plate at 35-45,000 cells/mL concentration (n=3-6). Culture medium was replaced with low divalent cation-containing extracellular solution (ECS-LD; 147 mM NaCl, 10 mM HEPES, 13 mM Glucose, 0.2 mM $CaCl_2$, 2 mM KCl. pH=7.4 in MilliQ water) - to reduce the inhibition caused by divalent cations at P2X7 (Young et al. 2007) – and containing

5 μM YO-PRO1 (Fisher Scientific, UK; #Y3603) . A Fluostar Optima plate reader (BMG Labtech, Ortenberg, Germany) was used for the fluorescence recording (filter pair: excitation 485 nm, emission 538 nM). The baseline was measured for 10-12 cycles, followed by manual addition of ATP (1 μL) and a further 120 cycles recording. For recording and data analysis, only wells with cells that were initially impermeable to YO-PRO1 or did not present a de-touched layer of cells were selected. The initial gradient of the dye uptake curve was used to calculate the response to ATP.

2.3.3 Electrophysiology

Dr Mark Young conducted part of the electrophysiology experiments. Briefly, whole-cell patch-clamp traces were recorded at room temperature using patch pipettes pulled from borosilicate glass (World Precision Instruments, Sarasota, FL, USA). Pipettes were filled with internal solution (IS) containing (in mM): 145 NaCl, 10 EGTA and 10 HEPES, with the pH adjusted to 7.3 with NaOH and had resistances of 3–5 MΩ. Cells were constantly perfused in a bath with extracellular solution contained low concentration of divalent cations (ECS-LD, see **Section 2.3.2** for composition). Currents were recorded at a holding membrane potential of −60 mV using an Axon Instruments Axopatch Multiclamp 700A amplifier and Digidata 1322A A/D interface (Molecular Devices, Sunnyvale, CA, USA). ATP working solutions were prepared fresh and solutions with compounds had a final concentration of DMSO equal or lower than 0.1% (0.1% DMSO was included as vehicle control). ATP applications were made at 90-s intervals. Solutions were applied to patch-clamped cells with the help of a rapid perfusion system (RSC-160, Biologic, Claix, France), allowing solution exchange times in the range 20–100 ms.

2.3.4 Data processing and statistical analysis

2.3.4.1 General expression in the figures (mean +/- SEM), ANOVA and other tests used

Data processing and data analysis were carried out with Microsoft Excel (2011) and Graphpad Prism version 6 for Mac (GraphPad Software, La Jolla California USA, www.graphpad.com), employing the latter for any bioassay data plotting. Figures are presented as Mean ± SEM (unless otherwise specified). In figures plotting data obtained through Ca^{2+} influx assay 'Responses' are expressed as (**Formula 1**):

Formula 1:

$\Delta F/F_0$

Where:
$\Delta F = F_1 - F_0$
F_0= Fluorescence intensity measured ~1 s after addition of ATP (or vehicle)
F_1= Maximal fluorescence intensity measured withing a 20 s time-window after addition of ATP (or vehicle)

While responses obtained from YO-PRO assay represent the rate of fluorescence intensity increase and calculated as gradient (**Formula 2**):

Formula 2:

$\Delta F/\Delta t$

Where:
$\Delta F = F_1 - F_0$
F_0= Fluorescence intensity measured at time 0 after addition of agonist (or vehicle)
F_1= Maximal fluorescence intensity measured after 10 cycles of recordings from when the addition of agonist (or vehicle) was made
$\Delta t = t_1 - t_0$
t_0= time of the first fluorescence recording after addition of agonist (or vehicle)
t_1= time after 10 cycles of recordings

Statistical significance of any difference observed between samples was calculated through one-way ANOVA followed by Dunnett's multiple comparisons test with a single pooled variance (control, unless otherwise specified) or, when

comparing only two sets of data, using an unpaired t test with Welch's correction. When comparing data obtained from multiple independent experiments (N), each dataset was normalised to the mean value obtained for the vehicle control. The mean value was calculated also each sample (average of technical repeats, n) and then merged. Statistical analysis was conducted on the merged data constituted by N mean values. This applied also to the calculation of the EC_{50} and IC_{50} values and the following statistical analysis.

2.3.4.2 Calculation of the standard curve (Bradford assay) and concentration of samples

A standard curve was calculated using known concentrations of BSA standards plotting Concentration (mg/mL) vs. Absorbance at 595 nm and fitting the date using a linear regression plot (Y = mX + q; where 'Y' is the absorbance measured for the standard, 'X' is the known concentration of the standard, 'm' is the slope and 'q' the intercept on Y axis). Concentration of unknown samples was estimated applying the following equation (**Formula 3**):

Formula 3:

$$X = (Y - q)/m$$

Where:
X = unknown concentration of the sample
Y = absorbance measured for the sample
m = slope
q = intercept on Y axis

2.3.4.3 Calculation of curve-fit (EC_{50}, IC_{50}, etc.)

A non linear regression (curve fit) with four parameters (constraints to Bottom=0 and Top=100 where applied when considering ATP concentration-response curves) was applied to determine any dose-response correlation and the presence of any inhibition trend during the compound testing (**Formula 4**) (curve-fit constraints were applied to normalized data). The ATP EC_{20} and EC_{80} were calculated applying **Formula 5.**

Formula 4:

$Y = Bottom + (Top-Bottom)/(1+10^{((LogEC_{50}-X)*HillSlope)})$

Where:
X: agonist (or antagonist) concentrations expressed as logarithmic scale.
Y: response measurements (raw or normalized value)

This formula was also used for inhibition curve fitting by substituting the value of EC_{50} with IC_{50}.

Formula 5:

$LogEC_{50} = logEC_F - (1/HillSlope)*log(F/(100-F))$

Where:
X: agonist (or antagonist) concentrations expressed as logarithmic scale.
Y: response measurements (raw or normalized value)
EC_{50}: agonist concentration corresponding to the 50% of the total response.
IC_{50}: antagonist concentration corresponding to the 50% of inhibition of the total response
Top and Bottom are defined as plateau values (in Y axis units).
HillSlope: steepness of the curve.
F: fraction of EC_{50} value to be calculated (to give EC_{20} or EC_{80})

2.4 MUTAGENESIS

2.4.1 Site-directed mutagenesis

2.4.1.1 Mutagenesis and transformation of DH5a Mix&Go competent cells

Dr Mark Young generated the mutated plasmids containing rat P2X4 T312I and human P2X4 I312I. Briefly, after primer design (QuikChange Primer Design tool, http://www.genomics. agilent.com/primerDesignProgram.jsp) the two-step QuikChange site-directed mutagenesis method was applied by amplifying the desired templates with QuikChange Lightning Kit DNA polymerase (Agilent Technologies, Santa Clara, CA; #210518 or #210519) in 50 µL reactions (**Table 2.6** and **Table 2.7** report details of the PCR reactions and the designed primers respectively). The thermal cycler was programmed as follows: initial denaturation at 95°C for 2 min; 18 cycles at 95°C for 20 s, 60°C for 10 s and 68°C for 3 min 30 s; final extension at 68°C for 5 min. The unmutated (methylated) original templates were digested with 2 µL DpnI (5 min at 37°C, enzyme from QuikChange Lightning Kit; or 1 hour at 37°C, enzyme from NEB) and 2-3 µL of the PCR products were transformed into 50 µL aliquots of XL10 Gold ultracompetent cells according to the manufacturer's protocol (Agilent Technologies, Santa Clara, CA; cells provided as part of the QuikChange Kit). Briefly; competent cells were thawed on ice, DNA was added and mixed gently, followed by heat shock for 30 seconds at 42°C, the addition of 250 µL SOC medium (NEB; #B9020S) and outgrowth for 1h at 37°C with shaking at 250 rpm to permit development of antibiotic resistance (required for kanamycin). 200 µl of cell suspension was plated onto sterile Lysogeny Broth (LB) Agar plates (Formedium, UK; #LMM0202) containing 50 µg/mL kanamycin (Formedium, UK) (or 100 µg/mL ampicillin in the case of pL118) and incubated overnight, 37°C to permit growth of colonies.

Step 1: Point mutation			
Reaction Component	Qty for 50 µL reaction	Final Concentration	
10X QuikChange Reaction Buffer	5 µL	1X	
10 mM dNTPs	1 µL	200 µM	
10 µM forward primer	2.5 µL	0.5 µM	
10 µM reverse primer	2.5 µL	0.5 µM	
50 ng/µL DNA template	1 µL	1 ng/µL	
QuikSolution Reagent	1.5 µL	1X	
Nuclease-free water	to 50 µL	-	
QuikChange Lighting Enzyme OR Phusion High-Fidelity DNA Polymerase	1 µL	1.0 unit/reaction (OR 2.0 unit/reaction)	
Polymerase used	Thermal cycler program		DNA Template
QuikChange Lighting Enzyme	95°C for 2 min; 95°C for 20 s, 60°C for 10 s and 68°C for 3 min 30 s (18 cycles); final extension at 68°C, 5 min		RML2, pL118
Step 2: *DpnI* digestion			
Enzyme used	Incubation	Qty in 50 µL	Supplier
DpnI QuikChange Lighting Enzyme	5 min at 37°C	2 µL	Agilent Technologies, Santa Clara, CA

Table 2.6: QuikChange Lightning Site-directed mutagenesis reaction conditions.

Template	Desired Mutation	Primer sequence	Supplier
RML2	T312I	5'-cagcgcacactcatcaaggcgtacggc -3'	IDT (Integrated DNA Technologies, Inc., Coralville, Iowa)
RML2	T312I	5'-gccgtacgccttgatgagtgtgcgctg -3'	IDT (Integrated DNA Technologies, Inc., Coralville, Iowa)
pL118	I312T	5'-cagcgcacgctcaccaaggcctatggc -3'	IDT (Integrated DNA Technologies, Inc., Coralville, Iowa)
pL118	I312T	5'-gccataggccttggtgagcgtgcgctg -3'	IDT (Integrated DNA Technologies, Inc., Coralville, Iowa)

Table 2.7: Specifications of primers used for site-directed mutagenesis reactions

2.4.1.2 Isolation and verification of mutant DNA constructs

From each transformation, 2-3 single colonies of *E. coli* were grown overnight (37°C) in 5 mL LB medium (Formedium; #LMM0102) with 50 µg/mL kanamycin (for RLM2-derived plasmids, or 100 µg/mL ampicillin in the case of the pL118), and DNA was purified using the QIAprep® Spin Miniprep Kit (Qiagen, Duesseldorf, Germany) according to manufacturer's instructions, and quantified using a Nanodrop spectrophotometer, 260 nm (Thermo Scientific TM, Life Technologies). A diagnostic enzymatic double-digestion was used to identify constructs corresponding to the correct band sizes (vector backbone and insert) by incubating (1h at 37°C) 1 µL of each enzyme (NEB, see Table 2.6), 6 µL H20, 1 µL DNA and 1 µL enzyme compatible buffer. After mixing the restriction digest with 2 µl 6x Purple Gel Loading Dye (NEB), each sample was loaded in a 1% agarose gel along with 5 µL of 1 kb DNA ladder (New England Biolabs, Ipswich, MA), and run for 1hr in 1x TAE (40 mM Tris, pH 7.6, 20 mM acetic acid, 1 mM EDTA). Gel images were recorded using GelDocJItTM Imaging System (UVP, CA) and the selected mutants were DNA sequenced to confirm the presence of the desired mutation (MWG Eurofins).

2.4.2 Genomic DNA Purification

Approx. 6-7 x 10^6 of mammalian cells, washed and pelleted in a 1.5 mL tube, were re-suspended in 120 µL ice-cold PBS, 3 parts (v/v) of deionized water and 1 part (v/v) ice-cold sucrose buffer (1.28 M Sucrose, 40 mM Tris-HCl, pH 7.5, 20 mM $MgCl_2$, 4% Triton X-100). After 10 min incubation on ice, the suspension was centrifuged (1300 x *g*, 15-20 min at 4°C) and pellets (cell nuclei) were washed in sucrose buffer diluted 1:4 in deionized water to remove any remaining cell debris. Nuclei were thoroughly resuspended in 450µL of H-bond disrupting buffer (800 mM guanidine HCl, 30 mM Tris-HCl, 30 mM EDTA, pH 8.0, 5% Tween-20, 5% Triton-100, 100 µg/ml RNAse) and 5 µL of Proteinase K (20mg/mL); this solution was then neutralized with 0.1 volumes (v/v) of 3M sodium Acetate (pH 5.2). To precipitate DNA, 0.7 volumes (v/v) of ≥98% isopropanol was added, the solution was centrifuged (13300 rpm for 15 min at 4°C), the precipitate washed (1-1.5 mL ≥98% ethanol, 13300 rpm for 15 min at 4°C), air-dried for 2-3 min and, finally, the purified DNA was solubilized in 30-50 µL TE buffer (10 mM Tris-HCl, pH 8.0, 1 mM EDTA).

2.5 MOLECULAR MODELLING AND COMPUTER-AIDED DRUG DESIGN

In silico simulations were performed on a MAC pro 2.80 GHz Quad-core Intel Xeon running Ubuntu 12.04 LTS. Graphical representations of molecular structures were generated using UCSF Chimera package (http://www.rbvi.ucsf.edu/chimera) (Pettersen et al. 2004) on a MacBook Pro (Retina, Mid-2014) 2.6 GHz Intel Core i5 processor running OS X Yosemite (v 10.10.2) or with MOE (Molecular Operating Environment (MOE), 2014.09; Chemical Computing Group ULC, 1010 Sherbooke St. West, Suite #910, Montreal, QC, Canada, H3A 2R7, 2018.), if not otherwise specified. Within Chimera molecular environment, the molecular surfaces were created with the help of MSMS package (Sanner et al. 1996). All crystal structure files used were retrieved from RCSB Protein Data Bank (http://www.rcsb.org) as PDB file format. All the compound structures considered in this work were sourced either from the specs.net database (a commercially available drug-like compound library) or PDB database, or were built using MOE Builder tool, protonated and energy minimised using MMFF94x forcefield.

2.5.1 Preliminary model and initial virtual screening

The hP2X4 homology model was built by Dr Mark T. Young with MODELLER software (Šali and Blundell 1993) adopting the zfP2X4 ATP-bound crystal structure (PDB ID: 4DW1) as template. A conformational library based on specs.net database was generated with LigPrep module (LigPrep, Schrödinger, LLC, New York, NY, 2018) and subsequently screened through docking with the PLANTS (Korb et al. 2006) in the competitive site. 16 of the compounds that displayed the best-fitting profile were selected, purchased and subsequently biologically evaluated. All the above *in silico* simulations were performed by Dr Marcella Bassetto.

2.5.2 Homology models

All the subsequent homology models were generated with MOE 2014.09 (or more recent version), Chemical Computing Group ULC) using the single template mode (unless otherwise stated. See **Table 2.8** for further details and the list of templates used). Briefly, the protein sequence of interest (in FASTA file format,

containing three consecutive whole-sequence repeats) and the sequence of the crystal structure (as PDB file format) to be used as template were aligned and checked manually by constraining the alignment of conserved cysteines. Further preparation implied the deletion of water molecules, cations and ligands (such as sugar or solvent molecules), joining the chains, the automatic calculation of hydrogens and partial charges according to AMBER99 force field or AMBER10:EHT force field when the induced-fit option was selected and a small molecule was included in the environment (**Table 2.8**). MOE homology model tool was then employed with default settings and the final model was refined from the best-scored among 10 intermediate models. Each model was checked visually and *via* Rampage Server, Molprobity (Lovell Simon et al. 2003) and PROCHECK (Laskowski et al. 1993) to exclude gross errors in protein geometry.

Model	Sequence (Uniprot ID)	Template(s) PDB ID	Force field
hP2X4 ATP-bound	Q99571	4DW1	AMBER10:EHT
hP2X4 APO form	Q99571	4DW0	AMBER99
rP2X4 ATP-bound	P51577	4DW1	AMBER10:EHT
rP2X4 APO form	P51577	4DW0	AMBER99
hP2X4 I312IT APO form	Q99571 (manually mutated)	4DW0	AMBER99
rP2X4 APO form	P51577 (manually mutated)	4DW0	AMBER99
hP2X7 ATP-bound	Q99572	5U2H.B	AMBER10:EHT
hP2X7 APO form	Q99572	5U1L	AMBER99
mP2X7 A127K ATP-bound	Q9Z1M0 (manually mutated)	5U2H.B	AMBER10:EHT

Table 2.8: list of homology models, force fields, templates and sequences used.

2.5.3 Docking with LeadIT FlexX and PLANTS

Molecules prepared with MOE2014.09 were exported in PLANTS-compatible or FlexX-compatible format before use. The structure of ATP from the crystal was superposed to binding site of the homology model prior docking, thus serving as mere reference for the centroid coordinates of the grid. A box of 10Å^3 served as grid for the docking for both LeadIT FlexX 2.1.3 (Rarey et al. 1996) and PLANTS (Korb et al. 2006) simulations (same used for Glide, validation of the model). 20 aco ants were set as parameter for simulations with PLANTS and 25 poses were generated per simulation and subsequently visually inspected.

2.5.4 Maestro LigPrep ligand preparation

Molecules and databases generated with MOE2014.09 or imported as 2-Dimensional structures from Specs.net, were prepared using LigPrep with standard settings: all ionization state between pH:7.0 ± 2.0 using Epik (Epik, Schrödinger, LLC, New York, NY, 2018) (Greenwood et al. 2010; Shelley et al. 2007) and OPLS_2005 forcefield. For the virtual screenings performed in the ATP-binding site and in the allosteric binding pocket, the downloaded library of SPECS commercially available compounds (~300,000 entries) was exploited.

2.5.5 Glide docking

When appropriate, the homology model file was pre-processed with MOE2014.09 by superposition of the ATP structure in the binding pocket with the sole intent of simplifying the identification of the ATP-binding site by Glide. In all cases, the protein structure was prepared with Maestro Protein Preparation Wizard (Schrödinger Suite, Protein Preparation Wizard; Epik, Schrödinger, LLC, New York, NY, 2016; Impact, Schrödinger, LLC, New York, NY, 2016; Prime, Schrödinger, LLC, New York, NY, 2018) − correcting any bond order wrongly assigned − before grid generation. The centre of the binding region was defined by either manual selection of the pocket residues or by selecting the superposed ligand. The area for the docking was confined within a box set to be similar in size to the length of the superposed ligand (if present) or appropriate to the dimensions of the ligands to be docked during the simulation. Usually the box size was <20 Å^3 (unless

otherwise stated); grids used in blind docking were 32 $Å^3$ and had centroids set manually in order to have a consistent overlap of >10 Å per side. Glide Standard Precision (SP) protocol was used in all simulations (unless otherwise specified) while the number of generated poses per ligand and retained after the post-docking minimization stage was chosen accordingly to the dimension of the database of ligands, generally 3 poses per ligand when the database contained >20 distinct molecules. **Table 2.9** lists Schrodinger packages directly used in this work or as crucial components of it.

Application	Main use
Canvas	Analysis of 2-Dimensional fingerprints for improved virtual screening
Epik	Prediction of ionization states and favoured tautomers
Glide	Docking and scoring.
LigPrep	Preparation of the small-molecule ligands by generating a database, which includes possible tautomers, enumeration of enantiomers, ionization stages.
Maestro	Graphical interface
OPLS3, OPLS_2005	Force fields used to define the molecular environment and as part of ligand preparation
Prime	Protein structure preparation (employed by Protein Preparation Wizard)
Protein Preparation Wizard	Protein structure prepossessing; correction of common structure mistakes.
QikProp	Calculation of ligand-based Absorption, Distribution, Metabolism, Excretion (ADME) prediction

Table 2.9: Schrodinger packages. Schrodinger suite offers a wide range of applications to manage modelling and drug design tasks; each of these packages can be accessed and managed by the same graphical interface, Maestro.

2.5.6 Virtual screening workflow *via* combined scoring functions

This method uses a combination of consecutive Glide docking simulations followed by the rescoring of the generated poses with three different docking algorithms (Glide, FlexX LeadIT and PLANTs) and filtered according a consensus score.

2.5.6.1 Serial Glide docking simulations

For the virtual screenings, the library of prepared ligands was initially docked using Glide High throughput Screening (HTVS) protocol allowing flexibility to the ligand but penalizing non-planar conformations of amides. No additional constraints were applied while the number of docked conformations (poses) were limited to 2 per ligand after post-docking minimization (3 poses were retained in the virtual screening of the allosteric pockets). The top 15% best scored poses were re-docked with Glide Standard Precision protocol maintaining the same protein grids and settings. Poses were then rescored (without performing ulterior docking) through Glide Extra Precision (XP) protocol. The top 15% poses were rescored through additional scoring functions as lower number of final selected molecules was desired.

2.5.6.2 LeadIT FlexX and PLANTs rescoring, Consensus *score*

Both LeadIT FlexX and PLANTS were employed in parallel at this stage. Each scored docked conformation of the output library - obtained from the Glide XP step – was re-scored in place (receptor grid of 16 Å radius) applying both scoring functions and therefore obtaining 3 docking scores values for each pose, which served for the calculation of the consensus score developed in Prof Andrea Brancale's research group (Bassetto et al. 2013). In brief, this consisted in assigning a positive value (+1) to the top scored quartile conformations according to each function. Poses that obtained a total value equal to 3 – meaning that ranked among the best scored quartile according to Glide XP, FlexX and PLANTS – were selected for visual inspection.

2.5.7 Maestro virtual screening workflow (vsw)

For the screening in the allosteric binding site (and the blind docking), the Virtual screening workflow was employed in order to automate the consecutive Glide docking (HTVS, SP then XP) on multiple receptor grids. For the allosteric pocket, 3 conformations for each compound were generated for each grid in during the HTVS stage, 10% of those were retained for the re-dock with Glide SP and the subsequent Glide XP stage. A total of 5,000 best scored poses obtained for each receptor grid input were merged, clustered according to molecular descriptors and visually inspected. A pre-dock filter, which included Lipinski's rule of 5 (molecular weight <500 g/mol,LogP <5, number of H-bond acceptor <10, number of H-bond donor <5) and the removal of molecules with reactive groups was included to skim the initial compound library. For the blind dock simulations, the virtual screening workflow was employed merely for the possibility to handle a large number of receptor grids through a semi-automated process thus no pre-dock filter was applied, 3 poses were generated in the HTVS stage retaining 34% of them after docking, while the later re-dock stages maintained 100% of poses with good score. Poses generated from each grid were subsequently merged in one database and visually inspected.

2.5.8 Pharmacophore

All pharmacophores were built employing MOE2014.09 Pharmacophore Query Editor after superposition of ligands. The Unified scheme was selected and features in common to ≥2/5 were considered essential. The radius of the spheres assigned to each feature was visually inspected to determine if a manual adjustment was needed.

Chapter 3:

P2X4 modulators, competitive binding site

3 P2X4 MODULATORS, COMPETITIVE BINDING SITE

3.1 Chapter introduction

As previously discussed (**Section 1.2**), P2X4 plays an important role in neurotransmission and pathological conditions, particularly in rodent models of neuropathic pain where P2X4 expression is up-regulated in microglial cells (in the spinal cord) after nerve injury, leading to pain-hypersensitivity (Tsuda et al. 2003; Ulmann et al. 2008). The activation of P2X4 in microglia causes the release of brain-derived neurotrophic factor (BDNF), which in turn affects intracellular Cl^- levels, changing GABAergic signalling from inhibitory to excitatory (Coull et al. 2005; Hildebrand et al. 2016). Also, in rodent models of neuropathic pain, P2X4 pharmacological blockage or silencing (*via* siRNA) results in a decrease of pain hypersensitivity (Matsumura et al. 2016; Nagata et al. 2009; Yamashita et al. 2016). Despite rising interest and effort in the development of novel P2X4 antagonists, only relatively few selective modulators – including 5-BDBD (Fischer et al. 2004), PSB-12054 and PSB-12062 (Hernandez-Olmos et al. 2012) and carbamazepine derivatives (Tian et al. 2014) - had been described before the beginning of this work. Most of them display an insufficient drug-likeness profile and none of them progressed to clinical trials. During the course of this study, more novel P2X4 antagonists structures were reported – namely BX430 (Ase et al. 2015) and NP-1815-PX (Matsumura et al. 2016). The latter compound showed an anti-allodynic effect in pre-clinical trials (Matsumura et al. 2016) and a blood brain barrier (BBB)-permeable analogue (undisclosed structure) has very recently progressed to Phase I clinical trials (Inoue and Tsuda 2018).

3.1.1 Ca^{2+} influx assay

Measuring ATP-induced responses in P2X-expressing cells - in order to test the activity of small molecules at P2X4 – can be achieved through different established methods such as Ca^{2+} imaging, electrophysiology recording and Ca^{2+} influx assay with fluorescent reporter. The latter was elected as the method of choice for this project. Briefly, the assay involves the pre-incubation on P2X-

expressing cells with FLUO-4AM, a membrane permeant dye that is retained in the cell upon hydrolysis (non-permeant), forming complexes with Ca^{2+}, which emit fluorescence (**Figure 3-1**). Essentially, the assay measures the ATP-induced increase of fluorescence caused by activation of P2X receptors and consequence influx of Ca^{2+} in the cytoplasm. In presence of a P2X antagonist, the increased of fluorescence would look reduced or abolished. This is an indirect measure of the receptor functionality that measure the total changes of Ca^{2+} concentration in the cytoplasm and for this reason the presence of other purinoceptors in the cells used in the assay is quite important.

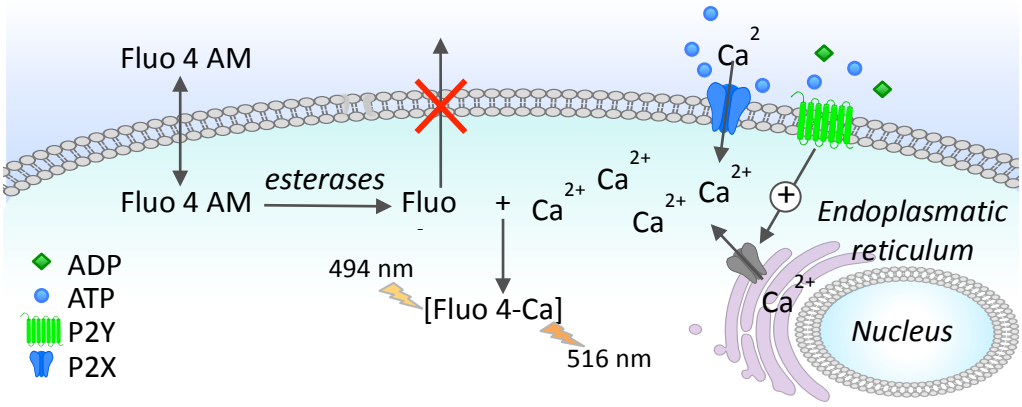

Figure 3-1: Schematic of the Ca2+ influx assay principle.

3.1.2 HEK293 and 1321N1 cell lines

Preliminary Ca^{2+} assay experiments performed by Dr Leanne Grimes conducted on HEK293 stably expressing human P2X4 indicated low cell responses to ATP and significant limitations in assay reproducibility (data not shown). The initial hypothesis attributed the poor quality of signal and variability to (i) the low solubility of 5-BDBD and PSB-12054 (used as controls) and (ii) the activation of P2Y receptors (endogenously present in HEK293 by ATP (Schachter et al. 1997). The pre-incubation with 2-Aminoethoxydiphenyl borate (2-APB; a blocker of intracellular Ca^{2+}-release) (Bootman et al. 2002) did not improve the data quality (Dr Leanne Grimes, unpublished) prompting the need of a more appropriate cell model. Therefore, the 1321N1 astrocytoma cell line (reported not to express any endogenous P2X or P2Y receptors) (Ullmann et al. 2005) was used in this work to

generate a cell model stably expressing human P2X4 subsequently employed in testing anti-P2X4 activity of compound candidates selected through an *in silico* approach.

3.1.3 Homology modelling

Back at the start of the project, the low number of reported ligand structures limited their use to design novel antagonists through a ligand-based approach. Conversely, the publication of zebrafish P2X4 structure in the apo- and ATP-bound state – the only structures available at the start of my research – strongly impacted on the direction of this study towards a structure-based approach.

Often, species-specific structural information is not available for the target protein and this was indeed the case for human receptors at the start of this project, and is still the case for human P2X4. *In silico* tools offer the opportunity to build a model of the desired biological target starting from an empirically determined structure of a homologue protein that shares enough similarity. This is based on the observation that the 3-dimensional structure of evolutionary related proteins is more conserved than their amino acid sequences (Kaczanowski and Zielenkiewicz 2010); therefore using as template a structure with over 50% sequence identity with the target usually results in model suitable for drug design applications (Baker and Sali 2001). The sequence identity observed between human P2X receptors and the available templates (reported in **Figure 1-23**) is generally approximately 50-60%, which combined with the conservation of important structural features (i.e. disulfide bonds, residues interacting with the ATP as identified by Hattori *et al.* (Hattori and Gouaux 2012)) allow the creation of an adequate model. Once the appropriate template has been identified and aligned with the target sequence the model is built starting from the core structure with sequence identity. Loops and non-conserved regions are usually modelled with lower reliability (Baker and Sali 2001). Importantly, many of the factors influencing the model quality are strongly related to the quality of the template used such as resolution (if X-ray crystal structure), percentage of residues with favourable geometry, flexibility of sidechains and loops. The model quality can be assessed to exclude substantial errors through visual inspection, computing the RMSD between the template and the model backbone, using online

servers (e.g PROCHECK (Laskowski et al. 1993), Rampage Server and MolProbity (Lovell Simon et al. 2003)) – usually assessing the model geometry through the Ramachandran plot – and docking known ligands in the binding site.

3.1.4 Docking simulations: Glide, FlexX and PLANTs

Docking is a widely used structure-based method estimating the fit of a molecule within a target cavity. Each simulation is formed by a first phase where ligand poses are generated through a searching algorithm and a second phase consisting in selecting and ranking the poses according to a scoring function. In this work the simulations were conducted using Glide (HTVS, SP and XP), PLANTS (Korb et al. 2009) and FlexX (LeadIT). The 3 tools employ different searching algorithms for the generation of the pool of ligand conformations. Glide, for instance, uses a complete systematic approach where the space is thoroughly explored in a positional, conformational and orientational manner (Friesner et al. 2004). Both FlexX and PLANTS instead adopt stochastic methods. The first uses and incremental construction approach by placing a first ligand fragment within the pocket and rebuilding the complete molecule using a greedy strategy to drive the process (Rarey et al. 1996). A greedy algorithm is a problem solving strategy that aims at finding the local optimal solution for each step of the process, usually not producing 'the' optimal global solution but identifying a relative optimal solution that approximate to the global solution within an acceptable number of steps. PLANTS uses the nature-inspired artificial ant colony optimization (ACO) algorithm, which drives the conformational space exploration toward the best solutions on the basis of 'rewards' given to acceptable conformations generated in previous algorithm iterations similarly to ants laying down and following pheromone trails (left by other ants of the swarm) in the search for food (Korb et al. 2006). The scoring functions used to rank the best fit conformation can also be very diverse depending on the number of parameters considered in order to assign the score, which also impacts on the computation speed. Glide offers 3 different scoring functions from less accurate but less computationally demanding (HTVS, approximately 2 seconds/compound), to increasingly accurate but more time-consuming SP (10 seconds/compound) and XP (2 minutes/compound) (Friesner et al. 2006; Schrödinger 2018). Such flexibility is easily applicable to virtual screening workflows where Glide HTVS is used to quickly exclude non-fitting

compounds from >100,000 compound libraries before iterating the docking with more accurate scoring functions. Finally, the combination of multiple docking tools through applying a post-docking *consensus score* has resulted in the discovery of potent hits (Bissantz et al. 2000; Wang et al. 2018).

3.2 Generation of human P2X4 1321N1 stable cell line

1321N1 cells were transfected with 1 µg DNA and antibiotic-resistant single-cell foci were selected with 600 µg/mL G418. 22 colonies were assessed through western blotting for protein expression and positive clones were tested for function through Ca^{2+} assay with a single dose of 100 µM ATP (**Appendix 1**). Clone WB34 (later named G34) showed high expression levels of human P2X4 receptor and the highest functionality and therefore it was chosen for all the subsequent experiments involving human P2X4.

3.3 Development and optimization of the Ca^{2+} influx assay

Initial experiments on 1321N1 P2X4-expressing cells revealed very high sample-to-sample variability and although the maximal response to ATP (100 µM) exhibited by the clone G34 was significant, the responses to lower concentrations of ATP were unacceptably inconsistent. This indicated that the background noise caused by P2Y activation in HEK cells was not the only aspect affecting the consistency of the results. For this reason, a number of factors, which could affect the consistency of results were considered (**Table 3.1**) and certain were optimised, including buffer and seeding conditions, dye loading and ATP preparation and storage.

Factor	Variables
ATP	Degradation rate, pH and concentration of stock solution Storage temperature Supplier Water purity (used to make the stock solution)
Cell preparation	Seeding concentration Time before measurement
Cell health	Passage number Growing medium
Extracellular Solution	Components concentrations
Equipment	Top/bottom reading Settings
Fluo-4 Dye	Solubilisation Loading time Stability

Table 3.1: List of factors influencing the measurements outcome in the Ca^{2+} influx assay including some considered during assay optimization.

The use of a more complex buffer (**Figure 3-2A**), in line with similar studies by Ase *et al*. (Ase et al. 2015) but different from Hernandez-Olmos *et al*. (Hernandez-Olmos et al. 2012)), considerably increased the cellular response (buffer composition and calculated osmolarity is listed in **Table 3.2**). Responses registered using modified Ringer's buffer were remarkably improved by the introduction of Pluronic-127 and Probenecid, which might acted as dye loading enhancers (**Figure 3-2B,C**).

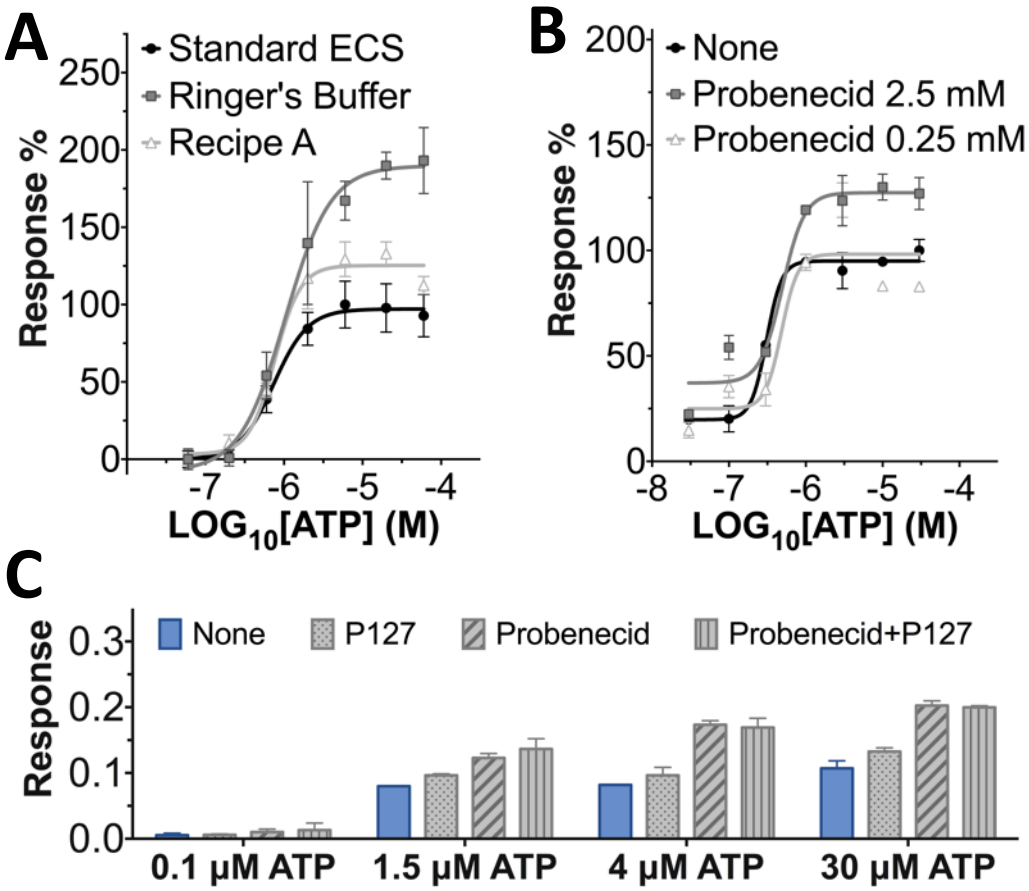

Figure 3-2: Impact of buffer composition and FLUO4-AM loading enhancers on ATP responses. Response is expressed as Relative Fluorescence Unit (RFU). ΔRFU = (max-min)/min and calculated from 1 or 2 independent experiments (n=3-4)**. A.** Influence of the different types of extracellular buffers during incubation and measurements (n=3). Buffers were prepared according to the recipe reported in **Table 3.2**. Data were recorded using a Fluoroskan Ascend and normalized to the maximal response recorded with Standard ECS solution, which was the buffer used in the preliminary work conducted before optimization. **B.** Influence of Probenecid at 0.25mM and 2.5mM concentrations on ATP dose-responses. Data were measured with a Fluorostar Optima. **C.** influence of absence/presence of Probenecid (2.5 mM) and/or Pluronics-P127 (P-127, at final concentration of 0.02%) on responses elicited by 0.1 µM, 1.5 µM, 4 µM and 30 µM.

Buffer	Components	Osmolarity (mOsm)
ECS	147 mM NaCl, 10 mM HEPES, 13 mM Glucose, 1 mM $MgCl_2$, 2 mM $CaCl_2$, 2 mM KCl, pH=7.3 in MilliQ water.	330
Recipe A	140 mM NaCl, 10 mM HEPES, 10 mM Glucose, 1 mM $MgCl_2$, 5mM $CaCl_2$, 2 mM KCl, pH=7.35 in MilliQ water.	322
Modified Ringer's	140 mM NaCl, 10 mM HEPES, 10 mM Glucose, 1 mM $MgCl_2$, 1 mM $CaCl_2$, 2.5 mM KCl, 0.5% BSA, pH=7.4.	311

Table 3.2: Composition of the buffers used in the optimization trials. Osmolarity was calculated considering the contribution of each ionic species. All calculated buffer osmolarities resulted within the range of osmolarity values guaranteed by the supplier for the culture medium (290-330 mOsm/kg). The general addition of NaOH to adjust the pH did not change the osmolarity considerably as calculated for the modified Ringer buffer for which approx. 2 mM was used.

The optimization included also the test of the optimal number of cells seeded, the ideal time window between seeding and the assay and the preparation and storage of ATP stock solutions (data not shown). Overall the assay conditions found optimal included the following and were used in subsequent experiments:

- Cells seeded between 35'000 and 45'000 cells/mL
- Measurements taken approx. 14-20 hours after seeding (depending on seeding cell concentration of 35'000 cells/mL or 45'000 cells/mL)
- Modified Ringer's buffer added with 500 µM Probenecid as extracellular solution
- 100 mM ATP (pH = 7.5 - 8) stock at -80°C prepared in ultra-pure water. Working concentration diluted just before the injection.

3.4 Concentration-response curve and EC_{50} of ATP at human P2X4

Once the optimization was completed, the ATP dose-response was calculated using ATP concentrations ranging from 100 to 0.003 μM obtaining an ATP EC_{50} of 1.3 μM (**Figure 3-3** and **Table 3.3**), which was in good agreement with previously published data (Jones et al. 2000; Soto et al. 1996; Stokes et al. 2011) and has been used as reference for all the further experiments.

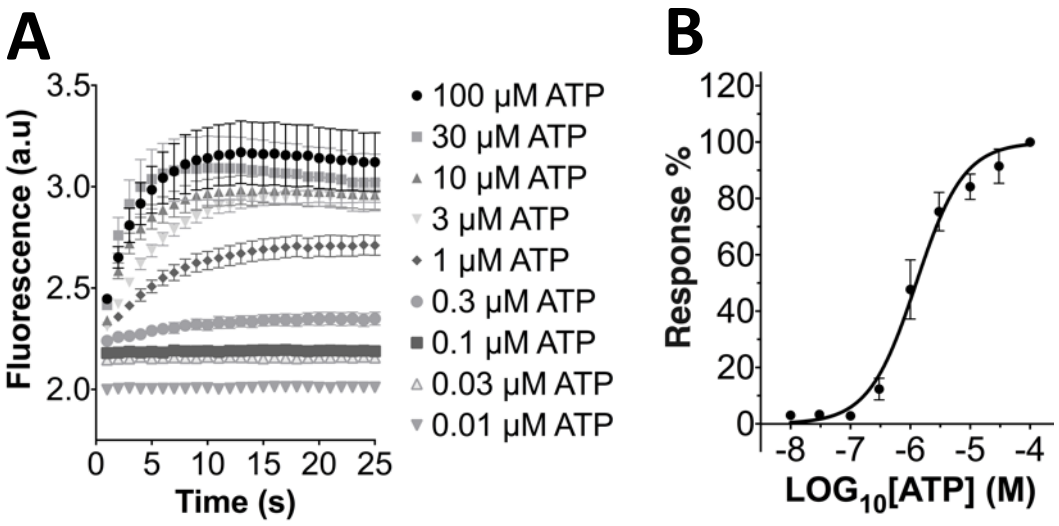

Figure 3-3: ATP-induced response in human P2X4-expressing cells. **A.** Cell Ca2+ influx upon addition of increasing concentrations of ATP (at time = 0 s). Data represents fluorescence intensity increase (Raw data, representative traces) and is expressed in arbitrary units. B. ATP dose-response curve. Response is calculated as ΔRFU = (max-min)/min from 3 independent experiments (n=5-6) and was normalized to the mean of the maximal response obtained for each independent experiment. GraphPad Prism 6 was used to compute a nonlinear regression (curve fit) with variable slope and the values of EC_{20}, EC_{50} and EC_{80} reported in **Table 3.3**.

ATP at human P2X4 WT	
Hill Slope:	1.094 (±0.1359)
LogEC_{50}	-5.901 (±0.05549)
EC_{20}	0.35 μM
EC_{50}	1.3 μM
EC_{80}	4.4 μM

Table 3.3: ATP EC50 and Hill Coefficient calculated for human P2X4-experessing cells.

3.5 Assay validation with a known human P2X4 antagonist

To validate our antagonist screening assay with an appropriate positive control, we measured the concentration-inhibition curve of BX-430, a reported antagonist of human P2X4 (Ase et al. 2015) demonstrating that it was capable of antagonizing ATP responses with a calculated IC_{50} of 2.02 μM (**Figure 3-4**), compared to reported IC_{50} of 0.54 μM (Ase et al. 2015).

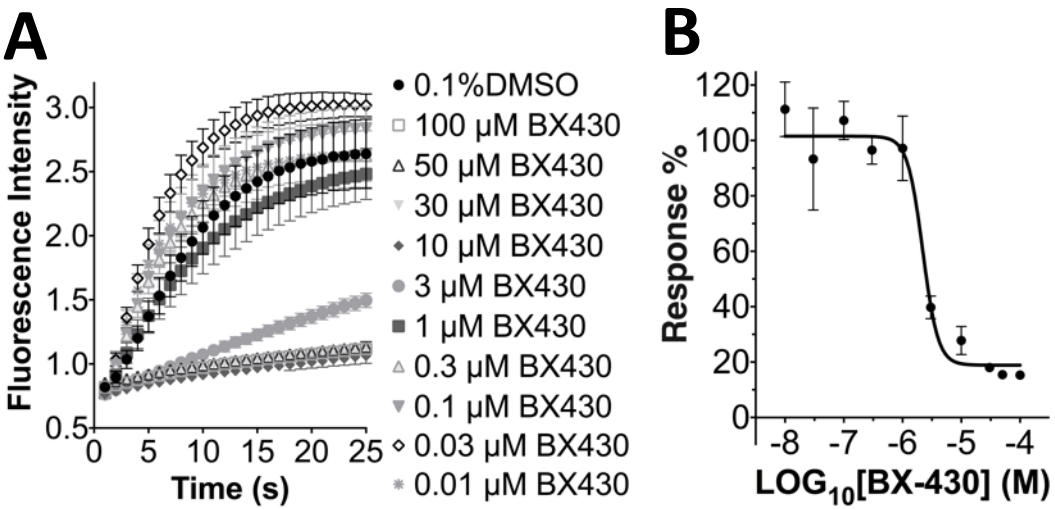

Figure 3-4: Block of ATP-induced response by BX-430 in human P2X4-expressing cells. Final concentration of DMSO (vehicle) did not exceeded 0.1%. **A.** Reduction in fluorescence Intensity increase (Raw data, representative traces from a single experiment) caused by incubation with increasing concentration of antagonist. Fluorescence intensity increase expressed in arbitrary units. **B.** BX-430 dose-inhibition curve. Response is calculated as ΔRFU = (max-min)/min from 3 independent experiments (n=4-5) and was normalized to the mean of the maximal response obtained from the vehicle control of each independent experiment. GraphPad Prism 6 was used to compute a nonlinear regression (curve fit) with variable slope.

3.6 Preliminary model and initial virtual screening on human P2X4

3.6.1 Previous virtual screening

In previous work, Dr Mark Young built the hP2X4 homology model with MODELLER software (Šali and Blundell 1993) employing the zfP2X4 ATP-bound crystal structure (PDB ID: 4DW1). *In silico* tools were also employed to (i) generate a conformational database of small-molecules from a commercially available drug-like compound library (www.specs.net) using LigPrep (Schrödinger) and to (ii) identify drug candidates through a structure-based drug design approach. A virtual screening was performed - by Dr Marcella Bassetto - by docking the molecule conformations into the ATP-binding site using the PLANTS algorithm (Korb et al. 2006). The 16 compounds that displayed the best-fitting profile were selected and purchased from Specs (www.specs.net). The list of compounds (in this work referred as compounds from 1 to 16) and their corresponding molecular structures are reported in **Table 3.4** while an example of selected compounds docked in the ATP-binding site is displayed in **Figure 3-5**.

ID	Structure	Specs ID	MW	Chemical Name
1	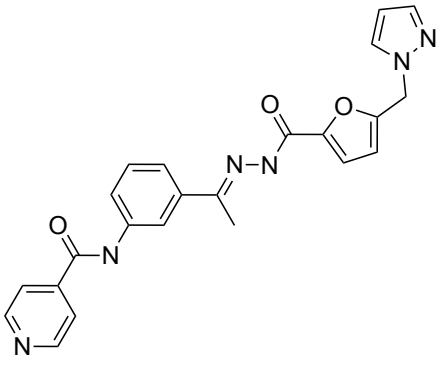	AK-968/ 15604856	428.45	N-(3-(N-(5-(1H-pyrazol-1-ylmethyl)-2-furoyl) ethanehydrazonoyl)phenyl)isonicotinamide
2	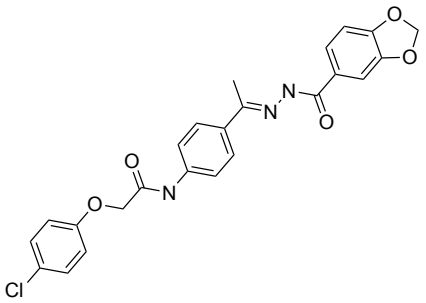	AK-968/ 15603434	465.89	N-(4-(N-(1,3-benzodioxol-5-ylcarbonyl) ethanehydrazonoyl) phenyl) -2-(4-chlorophenoxy) acetamide
3	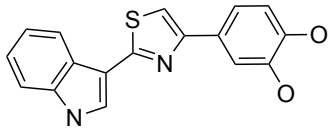	AP-048/ 15614119	308.36	4-(2-(1H-indol-3-yl)-1,3-thiazol-4-yl)-1,2-benzenediol
4	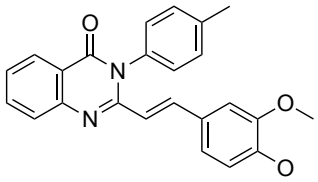	AJ-292/ 11658708	384.43	2-(2-(4-hydroxy-3-methoxyphenyl) vinyl)-3-(4-methylphenyl)-4(3H)-quinazolinone
5	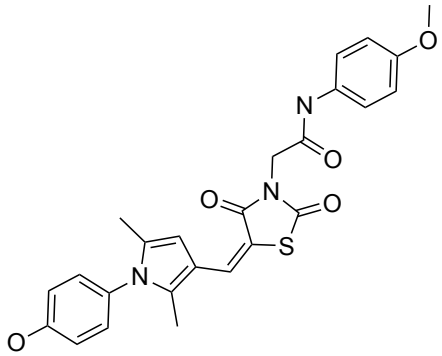	AO-081/ 42039434	477.54	2-(5-((1-(4-hydroxyphenyl)-2,5-dimethyl-1H-pyrrol-3-yl) methylene)-2,4-dioxo-1,3-thiazolidin-3-yl)-N-(4-methoxyphenyl)acetamide
6	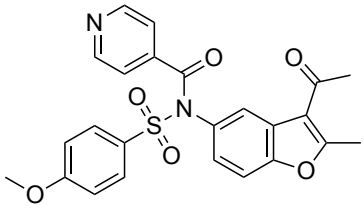	AQ-390/ 41639213	464.49	N-(3-acetyl-2-methyl-1-benzofuran-5-yl)-N-isonicotinoyl-4-methoxybenzenesulfonamide

7	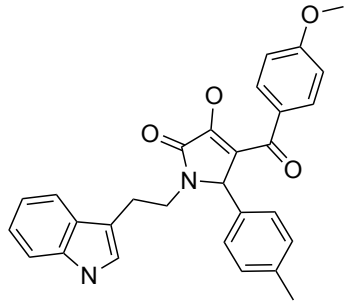	AQ-149/ 43243677	466.53	3-hydroxy-1-(2-(1H-indol-3-yl)ethyl)-4-(4-methoxybenzoyl)-5-(4-methylphenyl)-1,5-dihydro-2H-pyrrol-2-one
8	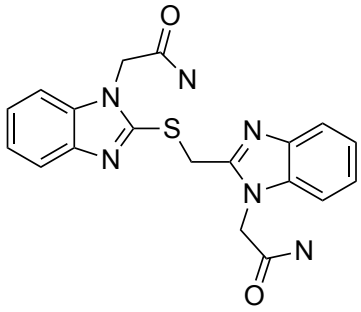	AN-465/ 12944090	394.46	2-(2-(((1-(2-amino-2-oxoethyl)-1H-benzimidazol-2-yl)methyl) sulfanyl)-1H-benzimidazol-1-yl) acetamide
9	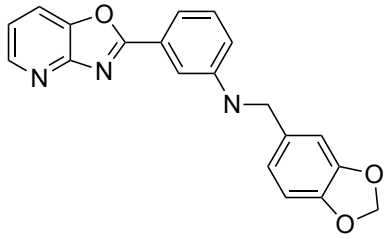	AN-465/ 43369673	345.36	N-(1,3-benzodioxol-5-ylmethyl)-N-(3-(1,3)oxazolo(4,5-b)pyridin-2-ylphenyl)amine
10	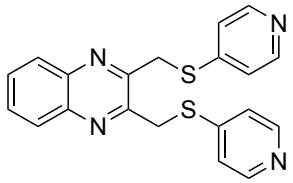	AI-204/ 31689056	376.51	2,3-bis((4-pyridinylsulfanyl) methyl)quinoxaline
11	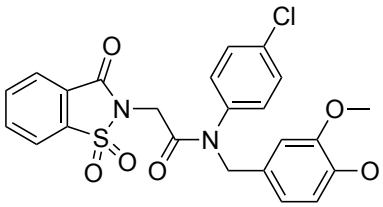	AP-853/ 42476447	486.93	N-(4-chlorophenyl)-2-(1,1-dioxido-3-oxo-1,2-benzisothiazol-2(3H)-yl)-N-(4-hydroxy-3-methoxybenzyl) acetamide
12	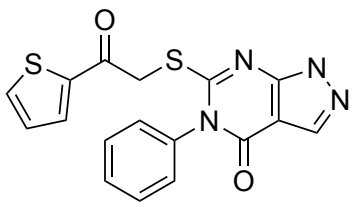	AO-476/ 43417572	368.44	6-((2-oxo-2-(2-thienyl)ethyl)thio)-5-phenyl-1,5-dihydro-4H-pyrazolo(3,4-d) pyrimidin-4-one

13	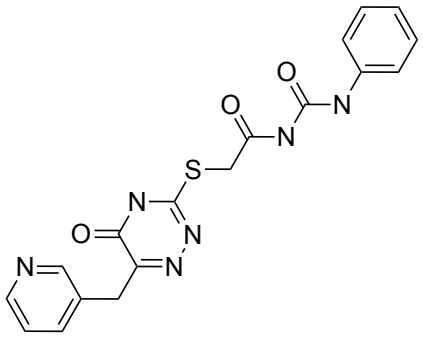	AO-476/ 43421005	396.43	N-(((5-oxo-6-(3-pyridinylmethyl)-4,5-dihydro-1,2,4-triazin-3-yl)thio)acetyl)-N'-phenylurea
14	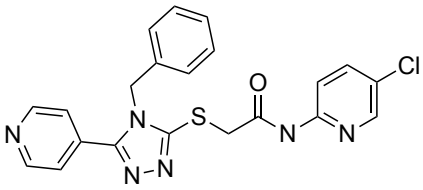	AP-853/ 43445408	436.95	2-((4-benzyl-5-(4-pyridinyl)-4H-1,2,4-triazol-3-yl)sulfanyl)-N-(5-chloro-2-pyridinyl)acetamide
15	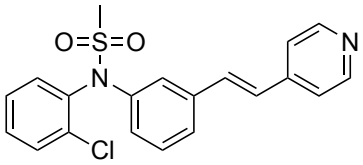	AO-080/ 43441481	384.89	(2-chlorophenyl)-N-(3-(2-(4-pyridinyl)vinyl)phenyl) methanesulfonamide
16	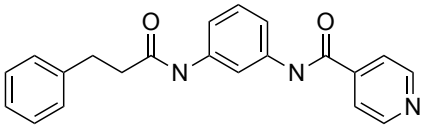	AN-329/ 43449168	345.40	N-(3-((3-phenylpropanoyl) amino)phenyl)isonicotinamide

Table 3.4: List of compounds (1-16) resulted from the preliminary screening and purchased from Specs.net. Specs ID, Compound Identifier as in Specs.net commercially available library; MW, molecular weight (g/mol).

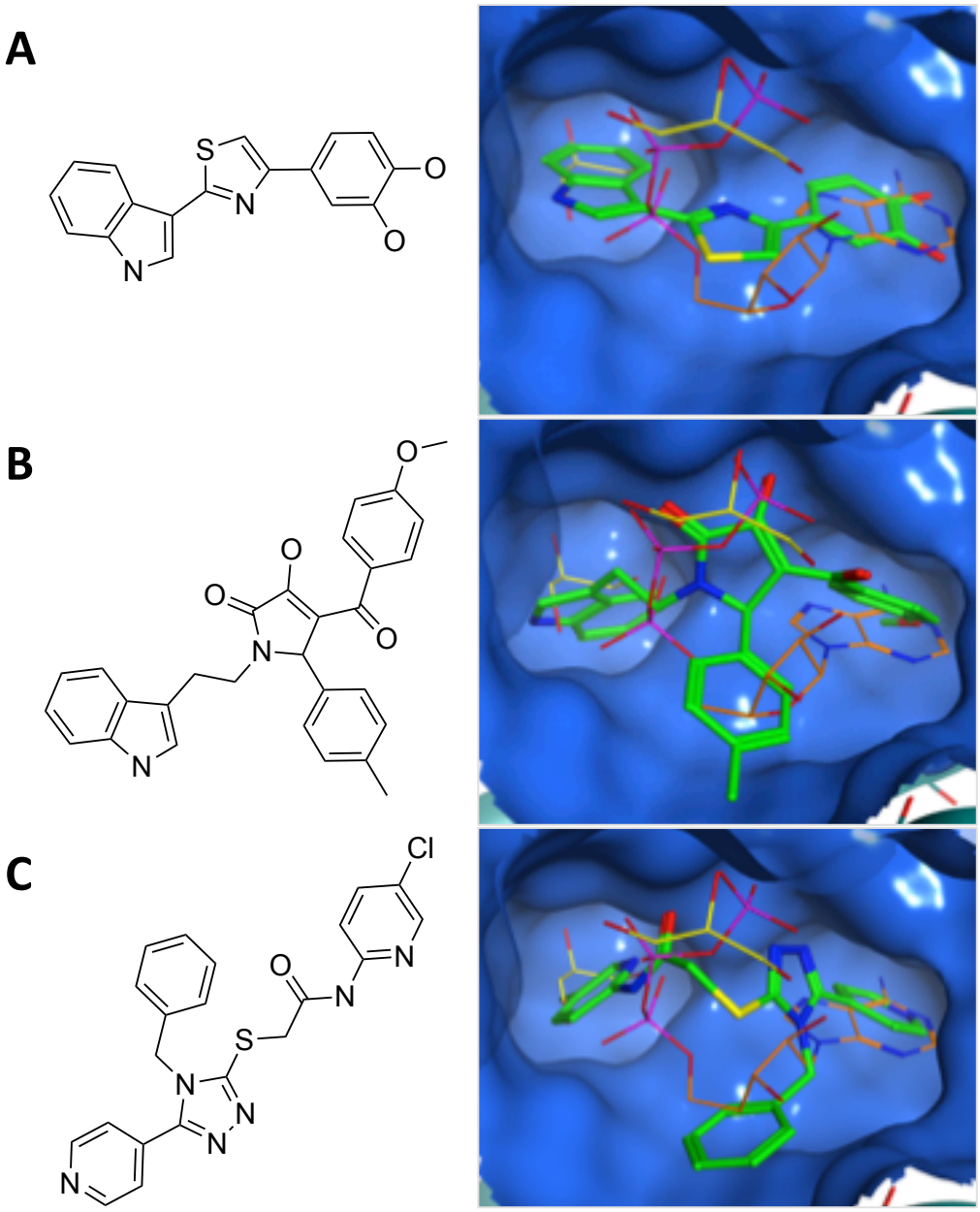

Figure 3-5: Compound 3 (**A**), Compound 7 (**B**) and Compound 14 (**C**) (in green) docked inside the human P2X4 model compared to the conformation of the ATP (orange) solved in the zebrafish P2X4 crystal (PDB ID: 4DW1). In yellow, the two molecules of glycerol present in the crystal. (Left) 2D structures of Compound 3, Compound 7 and Compound 14.

3.7 Biological evaluation of compounds 1-16 from the preliminary virtual screening

The activity of the 16 compounds purchased from SPECS was assessed at 10 μM concentration (20 minutes pre-incubation) using a Ca^{2+} influx assay on stably hP2X4-expressing cell line (G34 cell line, described and characterised in **Section 3.2 - 3.5**). **Figure 3-6** summarises the effect of the compounds on the cell response elicited by ATP at a concentration corresponding to EC_{20}, EC_{50} or EC_{80} (values calculated from the ATP concentration-response curve presented in **Section 3.4** and corresponding to ~0.4 μM, ~1.2 μM and ~4 μM, respectively). The experimental data showed that none of the compounds displayed a statistically significant reduction in the response compared to the 0.1% DMSO control (P value = 0.8719, Ordinary One-way ANOVA and Dunnett's multiple comparison test). The negative outcome of the first compound screening led me to perform a second virtual screening within the ATP-binding site, and new human P2X4 molecular models were also generated for this task.

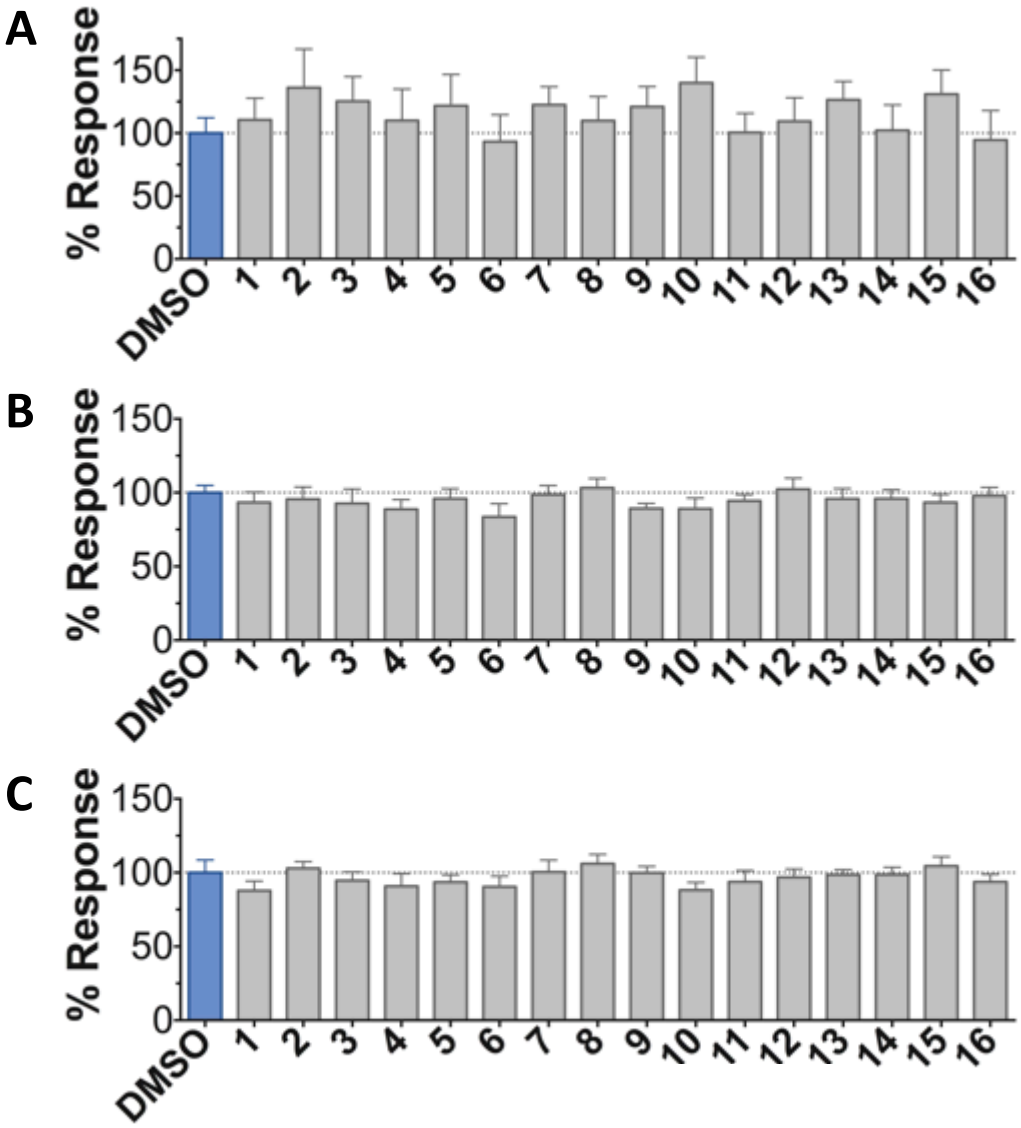

Figure 3-6: Reduction of ATP responses caused by incubation with 10 μM SPECS compounds (1 to 16) when receptor activation was induced by concentration of ATP corresponding to EC_{20} (**A**), EC_{50} (**B**) and EC_{80} (**C**). DMSO final concentration was not higher than 0.1% One-way ANOVA and Dunnet's test performed on the set highlighted not significance differences between the compounds and ctrl in all the different experiments ($P>0.05$). Data represents 2 or more independent experiments (n=3-4 each).

3.8 Homology models

The human P2X4 model in the closed state and in the ATP-bound state were modelled from 4DW0 and 4DW1 employing MOE software (according to the procedure described in the **Section 2.4.2**). For the ATP-bound model, the induced fit option was chosen and the 3 ATP molecules present in 4DW1 were selected for this purpose. The models were then minimized and checked using PROCHECK (Laskowski et al. 1993), Rampage Server and Molprobity (Lovell Simon et al. 2003) to exclude gross errors due to bad geometry or implausible angles of the backbone. Finally, the ATP-bound model was visually inspected and a computed RMSD of 0.541 Å over 22 residues defining the binding pocket was obtained between the model and the crystal structure (PDB ID: 4DW1). The RMSD for the superposed model-crystal whole structures was 0.642 Å and 0.714 Å for the backbone and for all atoms respectively. A further check of the model used for the virtual screening was carried out with docking simulations to ensure the ATP could be harboured in the binding site retaining the expected interactions.

3.9 Docking of ATP in human P2X4 homology model

As seen in **Figure 3-7A-C**, the docking simulations performed on the open-state human P2X4 model using Glide SP, FlexX and PLANTS algorithms shown that ATP poses had a good overlapping with the conformation of the ATP co-crystalized in 4DW1 (in dark gray, superposed to the docked pose for clarity). Indeed the particular U-shaped ATP conformation observed in the ATP-bound crystals of both P2X4 and P2X3 was retained in the docked poses obtained from all three docking algorithms with a calculated RMSD of 1.2496 Å, 1.5754 Å and 2.5540 Å for Glide SP, PLANTS and FleXX respectively (*via* Schrodinger atom-pairing ligand superposition tool). A visual inspection revealed that the ATP triphosphate group of all the docked conformations entertains multiple H-bonds interactions with Lys-67, Lys-69, Arg-295 and Lys-313 of the human P2X4 model (corresponding to the Lys-70, Lys-72, Arg-298, Lys-316 zfP2X4 numbering). The H-bond with Thr-186 and Asn-293 (Thr-189 and Asn-296 in the crystal) was retained in most of the poses. Interestingly, two additional interactions were observed between both Lys-190

and the sidechain of Ser-289 (non-conserved in the crystal and corresponding to Ala-292) and the alpha phosphate of the poses obtained with Glide SP and PLANTS. In the crystal structure the OH group of the ribose (in 3' position) interacts with nearby residues *via* a molecule of water. As the model and the docking simulation did not include any water molecules, this interaction is not present, although the same group is stabilized by an H-bond with the nearby Leu-214 backbone (Leu-217 in the zfP2X4) in both Glide SP and PLANTS conformations. A Protein-Ligand Interaction Fingerprint (PLIF), generated using MOE tool and reported in **Figure 3-7D,** summarizes and compares the interactions detected in the crystal versus the docked poses. With the assumption that ATP would make similar contacts with interacting residues conserved in the human receptor, the docking simulations showed (i) a satisfactory ability of all the three docking algorithms in predicting plausible conformations and ligand-protein interactions − also re-confirmed by docking of ATP in the zfP2X4 structure (data not shown) − and (ii) a reasonable pocket residue sidechain conformation.

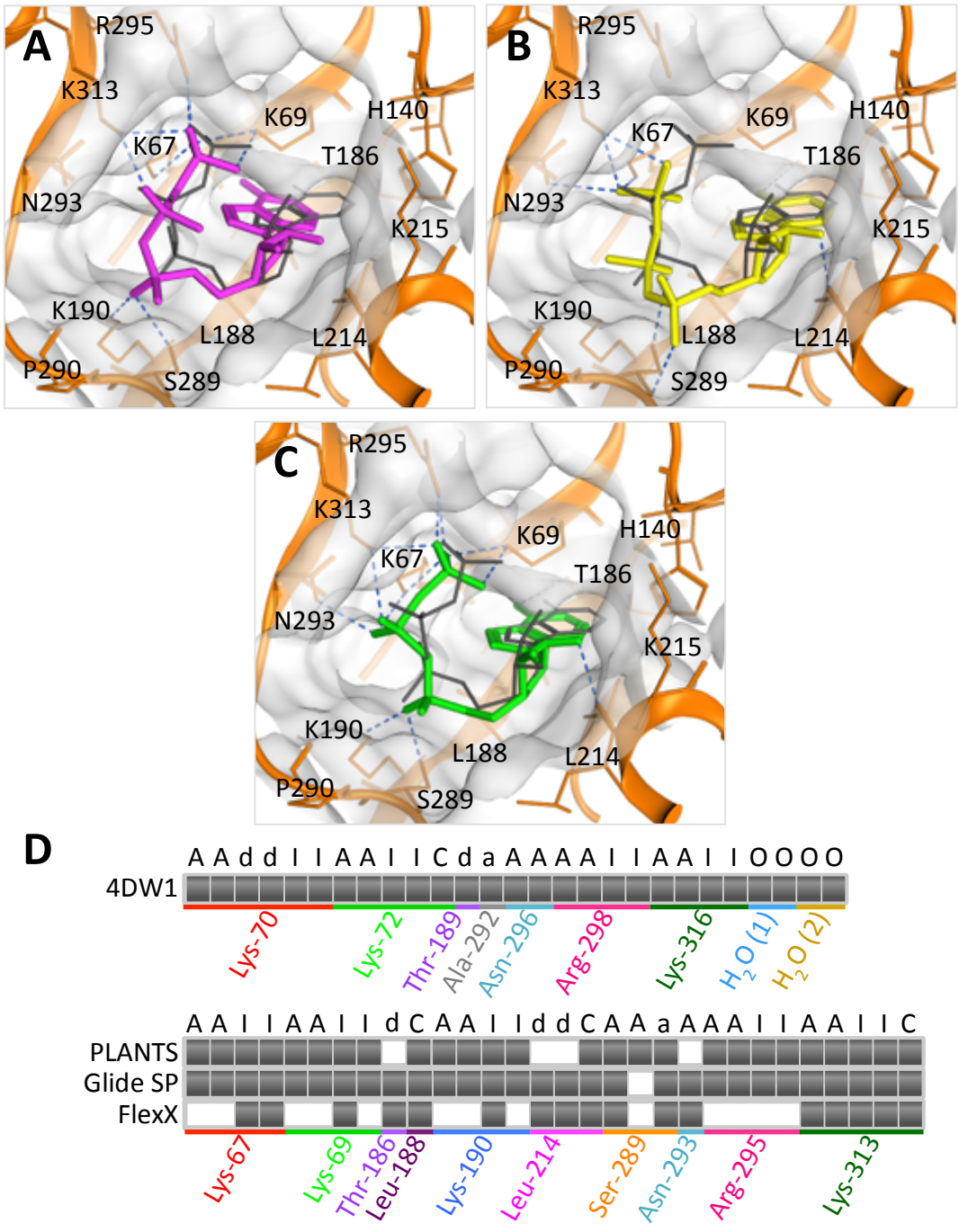

Figure 3-7: Dock of ATP in human P2X4 model (generated from 4DW1) using PLANTS (**A**, magenta) FlexX (**B**, yellow) and Glide SP (**C**, green) docking algorithm. Residues lining the pocket have been labelled according to human P2X4 numbering. H-bond interactions are shown in blue dot lines and the ATP crystal conformation (dark grey) has been superposed for ready comparison. (**D**) Barcode plot representing Protein-ligand Interaction Fingerprint (PLIF) of the interactions formed between each docked pose (PLANTS, Glide SP, FlexX) and the human model compared to the ones detected in the crystal (4DW1), where grey-filled boxes indicate presence of the interaction type specified by single-letter (at the top) for the indicated residue (at the bottom). White boxes

indicate no such interactions. Interaction types obey the following single-letter coding: ‘A’, sidechain hydrogen bond acceptor; ‘a’, backbone hydrogen bond acceptor, ‘C’, surface contact, ‘d’, sidechain hydrogen bond donor; ‘I’, ionic attraction; ‘O’, solvent hydrogen bond.

3.10 Virtual screening and selection of compounds (compound 17-42)

A database of ~300,000 commercially available compounds (from SPECS) was screened through docking in the ATP-binding site of human P2X4 homology model using Glide for their ability to fit the pocket. The number of docking poses was repeatedly filtered through docking iterations with increasing precision (Glide HTVS, SP and XP) obtaining 138,840 docking poses, which were re-scored using PLANTS and LeadIT-FlexX docking programs. An internal *consensus* score – a method routinely applied in Prof Andrea Brancale's research group (Bassetto et al. 2013) - was applied to the values obtained from each scoring functions and only the 25% best ranked poses in all the three scoring functions were retained for further analysis. These 5561 compound conformations were subsequently clustered according to their similarity in functional groups, in 3-dimensional occupancy and in interactions with residues within the pocket. After visual inspection, 26 compounds were selected - favouring a choice of molecules with diverse chemical scaffolds - and finally purchased from SPECS (see **Figure 3-8** for example of docked ligands). **Table 3.5** lists the selected compounds that were biologically evaluated in human P2X4-expressing cells through Ca^{2+} influx assay as illustrated in the following section.

ID	Structure	Specs ID	MW	Chemical Name
17	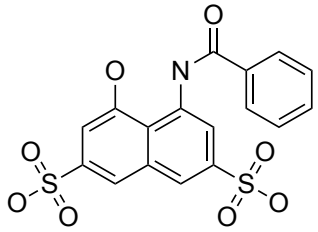	AE-641/ 00786016	423.42	4-(benzoylamino)-5-hydroxy-2,7-naphthalenedisulfonic acid
18	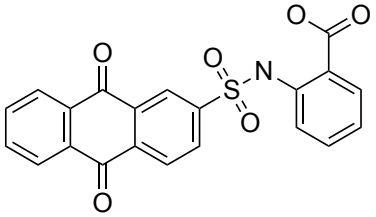	AE-641/ 42133418	407.40	2- ((9,10-dioxo-9,10-dihydro-2-anthracenyl)sulfonyl) amino)benzoic acid
19	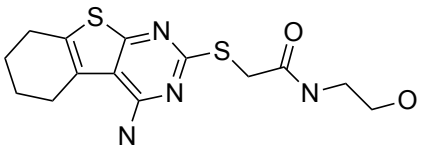	AF-399/ 40634562	338.45	2-((4-amino-5,6,7,8-tetrahydro(1)benzothieno(2,3-d)pyrimidin-2-yl)sulfanyl)-N-(2-hydroxyethyl)acetamide
20	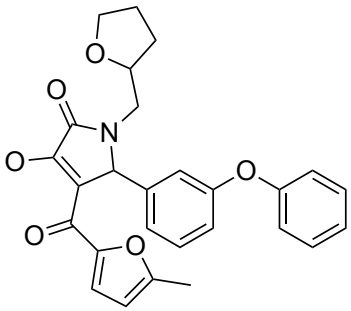	AF-399/ 41900709	459.50	3-hydroxy-4-(5-methyl-2-furoyl)-5-(3-phenoxyphenyl) -1-(tetrahydro-2-furanylmethyl)-1,5-dihydro-2H-pyrrol-2-one
21	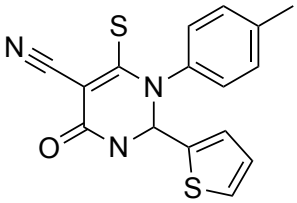	AF-399/ 42810490	327.43	1-(4-methylphenyl)-4-oxo-6-sulfanyl-2-(2-thienyl)-1,2,3,4-tetrahydro-5-pyrimidinecarbonitrile
22	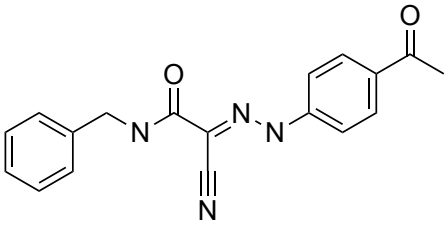	AF-407/ 33312043	320.35	2-((4-acetylphenyl)hydrazono)-N-benzyl-2-cyanoacetamide

23	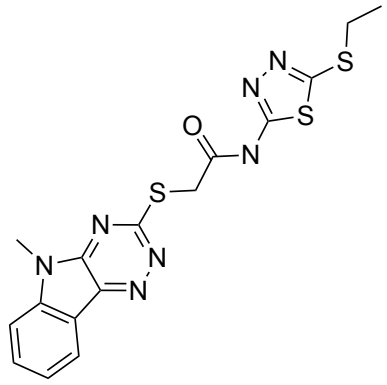	AG-205/ 36698032	417.54	N-(5-(ethylsulfanyl)-1,3,4-thiadiazol-2-yl)-2-((5-methyl-5H-(1,2,4)triazino(5,6-b)indol-3-yl)sulfanyl)acetamide
24	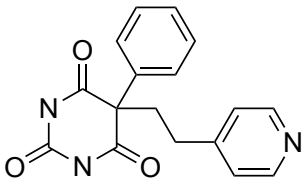	AG-670/ 36765017	309.32	5-phenyl-5-(2-(4-pyridinyl) ethyl)-2,4,6(1H,3H,5H)-pyrimidinetrione
25	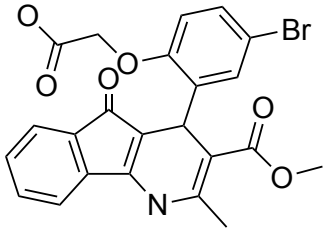	AH-487/ 14758206	484.30	(4-bromo-2-(3-(methoxycarbonyl)-2-methyl-5-oxo-4,5-dihydro-1H-indeno(1,2-b)pyridin-4-yl)phenoxy)acetic acid
26	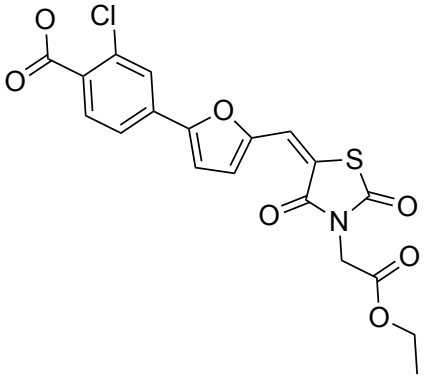	AH-487/ 40935627	435.84	2-chloro-4-(5-((3-(2-ethoxy-2-oxoethyl)-2,4-dioxo-1,3-thiazolidin-5-ylidene)methyl)-2-furyl)benzoic acid
27	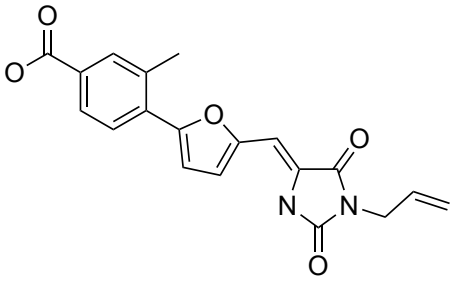	AH-487/ 41955121	352.34	4-(5-((1-allyl-2,5-dioxo-4-imidazolidinylidene) methyl)-2-furyl)-3-methylbenzoic acid

28	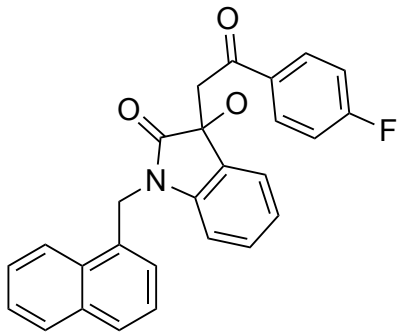	AK-778/ 40984985	425.46	3-(2-(4-fluorophenyl)-2-oxoethyl)-3-hydroxy-1-(1-naphthylmethyl)-1,3-dihydro-2H-indol-2-one
29	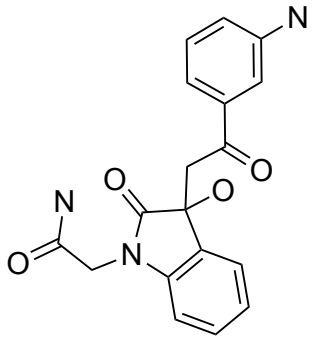	AK-778/ 41182449	339.35	2-(3-(2-(3-aminophenyl)-2-oxoethyl)-3-hydroxy-2-oxo-2,3-dihydro-1H-indol-1-yl)acetamide
30	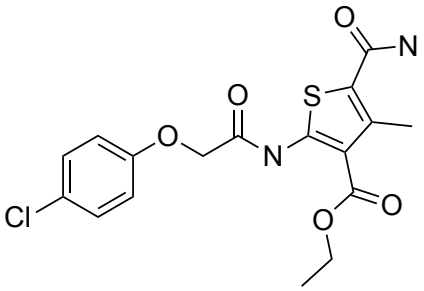	AK-968/ 41925442	396.85	ethyl 5-(aminocarbonyl)-2-(((4-chlorophenoxy)acetyl)amino)-4-methyl-3-thiophenecarboxylate
31	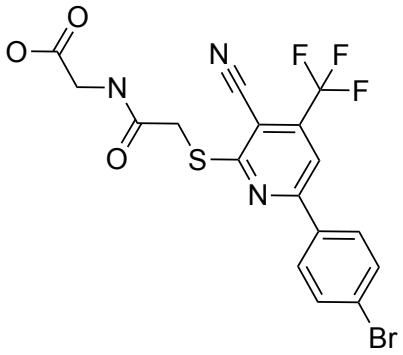	AM-807/ 41462255	474.26	((((6-(4-bromophenyl)-3-cyano-4-(trifluoromethyl)-2-pyridinyl)sulfanyl)acetyl)amino)acetic acid

32	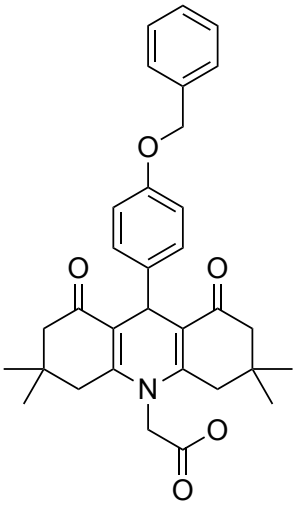	AN-988/ 40787450	513.63	(9-(4-(benzyloxy)phenyl)-3,3,6,6-tetramethyl-1,8-dioxo-2,3,4,5,6,7,8,9-octahydro-10(1H)-acridinyl)acetic acid
33	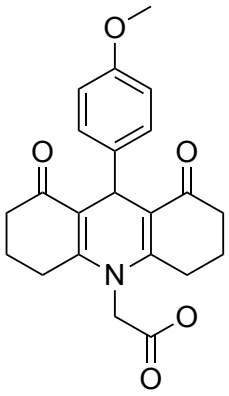	AN-988/ 40787687	381.43	(9-(4-methoxyphenyl)-1,8-dioxo-2,3,4,5,6,7,8,9-octahydro-10(1H)-acridinyl)acetic acid
34	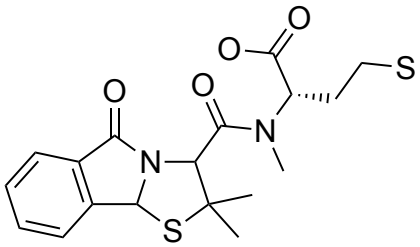	AO-022/ 43453859	394.51	N-((2,2-dimethyl-5-oxo-2,3,5,9b-tetrahydro(1,3)thiazolo(2,3-a)isoindol-3-yl)carbonyl)(methyl) homocysteine
35	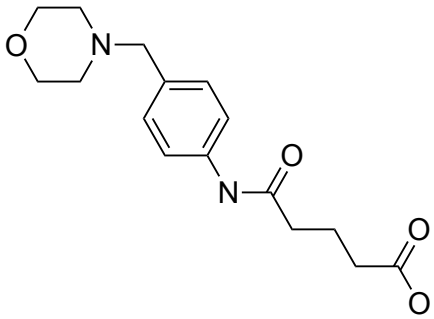	AO-080/ 43441580	306.36	5-(4-(4-morpholinylmethyl)anilino)-5-oxopentanoic acid

36	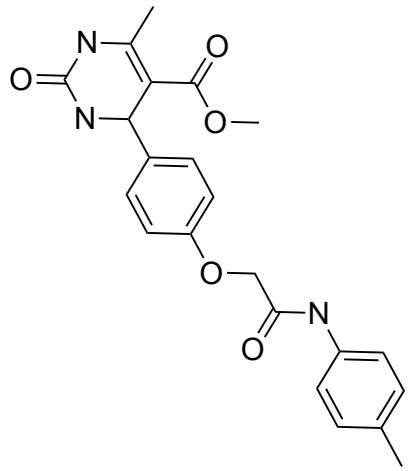	AO-081/ 42096259	409.44	methyl 6-methyl-2-oxo-4-(4-(2-oxo-2-(4-toluidino) ethoxy)phenyl)-1,2,3,4-tetrahydro-5-pyrimidinecarboxylate
37	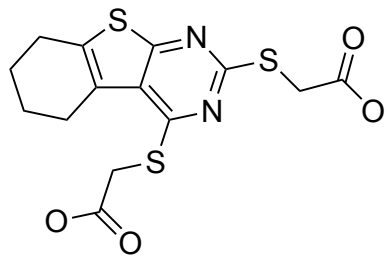	AO-476/ 41610193	370.47	((2-((carboxymethyl)sulfanyl)-5,6,7,8-tetrahydro(1)benzothieno(2,3-d)pyrimidin-4-yl)sulfanyl)acetic acid
38	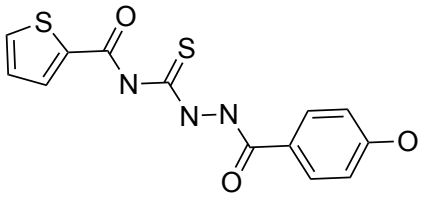	AO-990/ 15068055	321.38	N-((2-(4-hydroxybenzoyl)hydrazino)carbothioyl)-2-thiophenecarboxamide
39	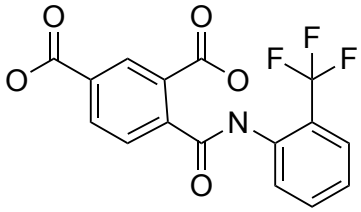	AP-263/ 43370864	353.25	4-((2-(trifluoromethyl)anilino)carbonyl)isophthalic acid
40	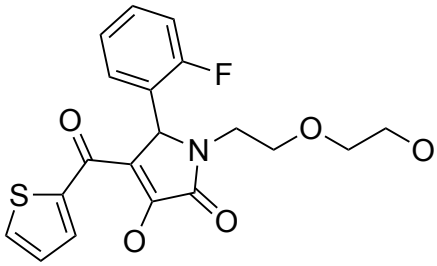	AQ-149/ 43372338	391.42	5-(2-fluorophenyl)-3-hydroxy-1-(2-(2-hydroxyethoxy)ethyl)-4-(2-thienylcarbonyl)-1,5-dihydro-2H-pyrrol-2-one

41	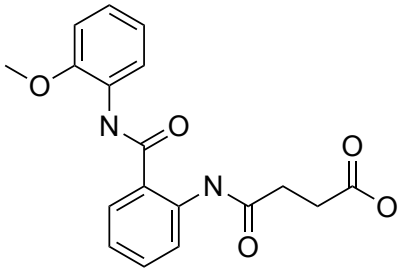	AQ-360/ 42595959	342.35	4-(2-((2-methoxyanilino)carbonyl)anilino)-4-oxobutanoic acid
42	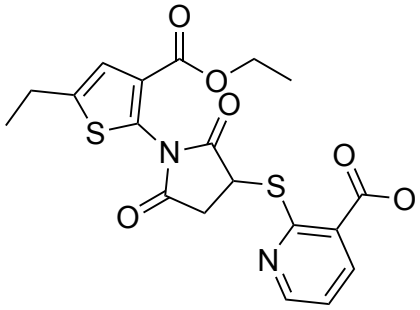	AS-871/ 41438012	434.49	2-((1-(3-(ethoxycarbonyl)-5-ethyl-2-thienyl)-2,5-dioxo-3-pyrrolidinyl)sulfanyl) nicotinic acid

Table 3.5: List of compounds (17-42) identified in the virtual screening performed in the ATP-binding site described in **Section 3.10**. Specs IDs, identification number according to the supplier (specs.net). MW, molecular weight (g/mol).

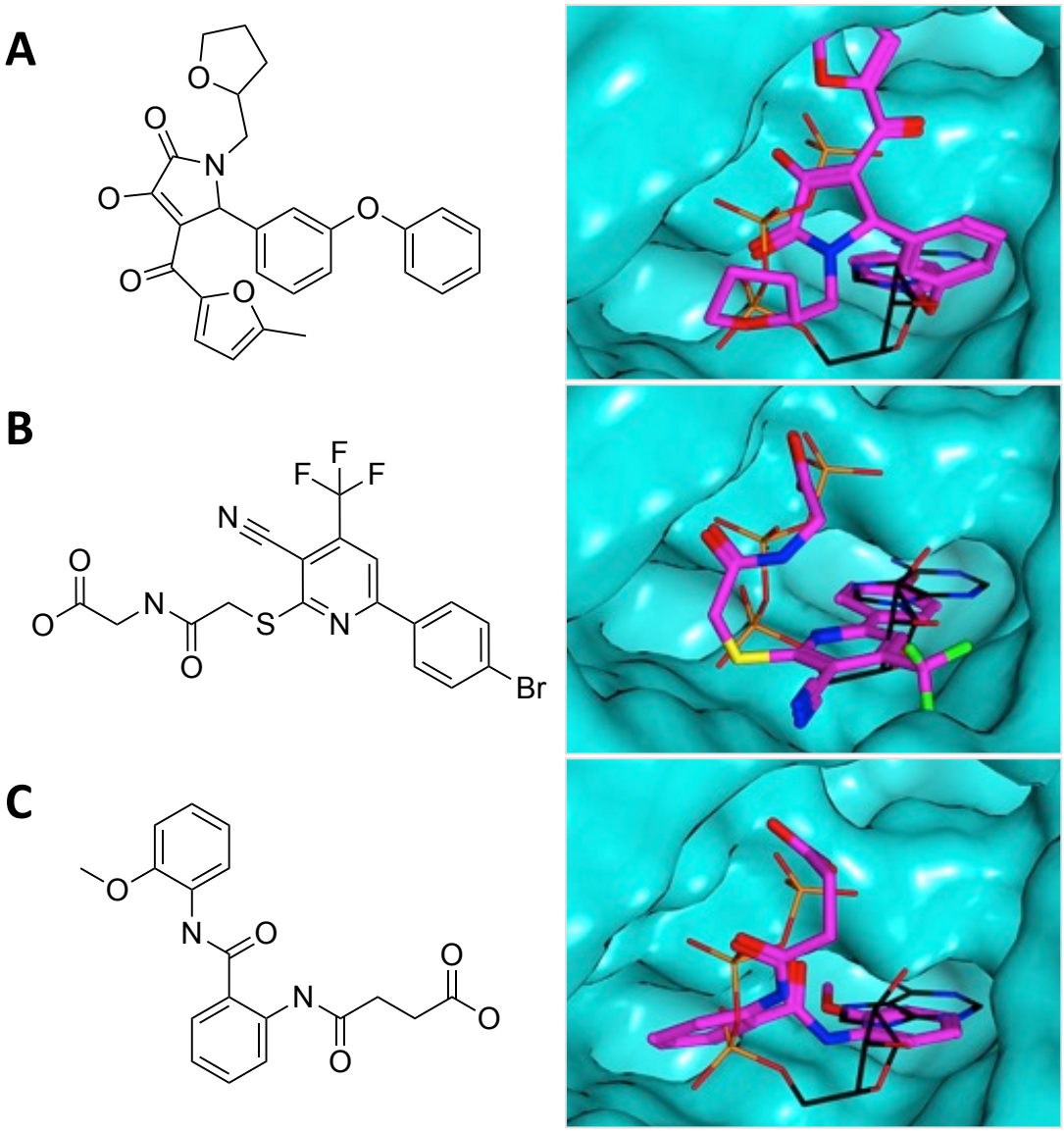

Figure 3-8: Dock of compound 20 (**A**), compound 31 (**B**) and compound 41 (**C**) and their molecular structures (on the left handside).

3.11 Biological evaluation of compounds 17-42

SPECS compounds identified through the virtual screening where purchased and tested on hP2X4-expressing cells through Ca^{2+} influx assay similarly to that described in **Section 2.2.1**. **Figure 3-9A** reports ATP responses elicited by 1.2 μM ATP after cells were pre-incubated with 10 μM compounds, vehicle only or 2 μM BX430 – a concentration corresponding to the approximated IC_{50} value (as calculated in **Section 3.5**). Compound 23 was not included in the test at 10 μM due to its extremely poor solubility in DMSO. Normalised data from 3 independent experiments were combined and analysed through One-way ANOVA followed by Dunnet's multiple comparison test (P=0.0102). None of the compound tested showed a statistically significant reduction in receptor activation at 10 μM, besides 2 μM BX430 (used as positive control). Additionally, for each compound, a single experiment with increasing concentration (ranging from 0.003 μM to 100 μM) was performed to measure any inhibitory effects at higher concentrations. Such an experiment performed using Compound 25 (#25) is shown in **Figure 3-9B-C** as an example. No compounds showed an inhibition-curve trend within the range of tested concentrations and no further compound characterisation was carried out. These negative results led to the development of an alternative strategy to identify potential hit compounds.

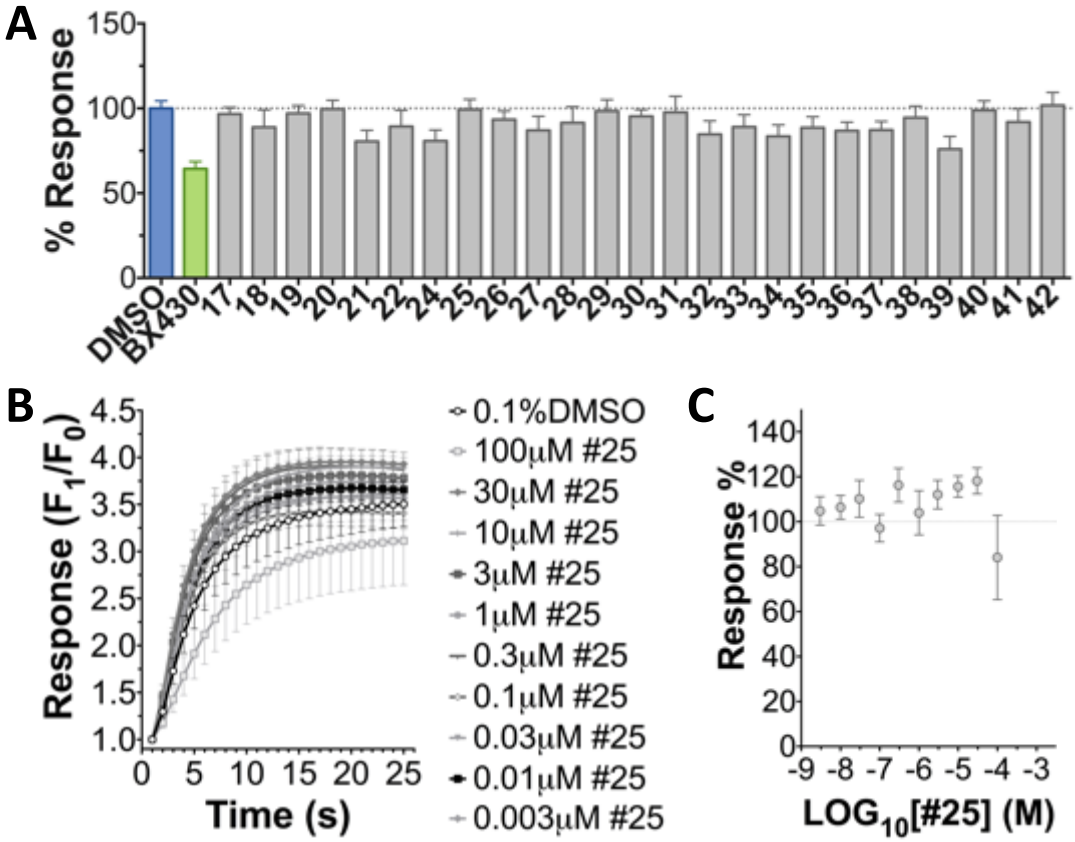

Figure 3-9: Biological evaluation of Compound 17-42 through Ca^{2+} influx assay. (**A**) ATP responses (at 1.2 μM ATP) when cells were pre-incubated (20 min) with 10 μM compounds (labeled 17-42) compared to the vehicle (0.1% DMSO, blue) or 2 μM BX-430 (green). Final concentration of DMSO did not exceed 0.1%. Normalized data (to the vehicle) combined from 3 independent experiments (n=2-4/each). (**B**) and (**C**) Lack of inhibitory effects at increasing concentrations of Compound 25 on ATP responses (elicited by 1.2 μM ATP). Data from single experiment (n=5) was normalized to the 0.1% DMSO (100% response).

3.12 Discussion

The initial low reproducibility of the Ca^{2+} influx assay improved mainly by the use of Probenecid - an inhibitor of various drug transporters - that reduced the dye leakage during the incubation potentially caused by the expression of multi-drug resistant proteins (BCRP and PgP) in 1321N1 (Bhatia et al. 2012).

Following two rounds of virtual screening and manual inspection of binding poses a total of 42 compounds were selected and 41 were tested at 10 μM (Compound 23 was tested at 2 μM, data not shown), yet none displayed a statistically significant antagonist activity at human P2X4. There could be several potential explanations for this disappointing outcome ranging from inaccuracies in the initial starting human P2X4 models to straightforward 'bad luck' (i.e. not enough compounds were tested). The models used in the two different rounds of screening were created independently with two different modelling software (MODELLER and MOE) but using the zebrafish P2X4 ATP-bound crystal as template, which bears 61% sequence identity to human P2X4 and multiple conserved features (i.e. disulphide bonds, numerous conserved residues within the ATP-binding site). Though the percentage identity is suitable to build a reliable model for drug discovery applications (Baker and Sali 2001) and indicates quite reliably a conserved 3-dimensional structure similarity, it also bears some limitations derived from the nature itself of a computational prediction. However, a similar recent structure-based approach successfully identified hit compounds active against human P2X7 creating a valid precursor for the application of structure-based drug design for the receptor family (Caseley et al. 2016), perhaps suggesting that it is not our molecular modelling or virtual screening approach that is responsible for the negative result.

Interestingly, no potent orthosteric P2X4 antagonists have been reported to date, in contrast to the situation for other P2X receptor subtypes, such as TNP-ATP and A-317491 co-crystallised in the ATP-binding site of P2X3 (Mansoor et al. 2016). The lack of reported orthosteric antagonists binding P2X4 raises the intriguing possibility that, for some reason, it is harder to 'fit' the ATP-binding site of P2X4 with a ligand than for other subtypes.

Notably, while the selected compounds lacked activity at human P2X4, more than one compound displayed antagonist activity at P2X7 (this will be the focus of **Chapter 5**).

The negative results obtained from virtual screenings performed on the ATP-binding site has led to a different approach in identifying potential P2X modulators by considering allosteric binding sites and modulators and will be described in **Chapter 4.**

Chapter 4:

P2X4 modulators, allosteric binding sites

4 P2X4 MODULATORS, ALLOSTERIC BINDING SITES

4.1 Chapter introduction

4.1.1 Defining allosteric binding sites of human P2X4

To date, most of the available modulators of P2X4 are reported to be allosteric (Ase et al. 2015; Hernandez-Olmos et al. 2012) (Matsumura et al. 2016; Wang et al. 2017), although their binding locations remain unknown. The following sections (i) attempt to give an *in silico* interpretation of ivermectin (IVM) positive allosteric modulator dual effect contextualizing available pharmacological and mutagenesis data within the human P2X4 homology model (**Section 4.2**), (ii) explore the hypothesis of further allosteric binding sites in the P2X4 receptor subtype corresponding to the pocket recently identified in giant panda P2X7 (**Section 4.3** to **Section 4.6**) and (iii) employ this hypothesis to conduct a virtual screening for negative allosteric modulators (**Section 4.7**).

4.1.2 Ivermectin – a positive allosteric binding site in the transmembrane domain

Ivermectin (IVM) is an FDA-approved anti-helminthic drug acting on glutamate-gated chloride channels of nematodes and is indicated in the treatment of onchocerciasis (human river blindness) and lice in humans and for parasitosis in veterinary medicine (Zemkova et al. 2014). IVM also modulates the activity of numerous other receptors (Chen and Kubo 2018) including GABA receptors, nicotinic acetylcholine receptors, glycine receptors (Du et al. 2015; Huang et al. 2017), Farnesoid X receptors (Jin et al. 2013) and P2X4 (Zemkova et al. 2014). The potential toxicity of IVM is due to its non-selectivity, although risks of CNS effects are observed only in animals that bear mutations in P-glycoprotein, as IVM does not readily cross the blood brain barrier (Menez et al. 2012).

Structural data from glycine receptors and glutamate-gated chloride receptors reveals that IVM exerts its positive allosteric modulation by binding between the

helices of the transmembrane domain and favouring the channel open state (Du et al. 2015; Hibbs and Gouaux 2011; Huang et al. 2017). When bound to P2X4, IVM has two effects: it decreases the deactivation rate (with a EC_{50} of 2 μM) and increases the maximum current amplitude (with an EC_{50} of 0.25 μM) in electrophysiology experiments (Priel and Silberberg 2004). However both effects might be due to two (or more) binding modes in the same receptor domain – potentially between transmembrane domains (TMs) as observed in cys-loop ligand gated ion channels (Du et al. 2015; Huang et al. 2017). Extensive mutagenesis and structure-function studies (mainly on rat P2X4) strongly corroborate this hypothesis by identifying residues important for IVM activity to be located in the lower portion of the TM2 and the upper portion of the TM1 (Samways et al. 2012; Silberberg et al. 2007; Tvrdonova et al. 2014). In this chapter, we suggest a possible binding mode for IVM using the rat P2X4 homology model.

4.1.3 BX430 – hypothesising a negative allosteric binding site in the extracellular domain

The rationale behind the hypothesis of the allosteric pocket location herein described is based upon (i) the recently published P2X7 crystallographic data combined with (ii) species-specific pharmacology data available for the human P2X4 allosteric antagonist, BX430.

The giant panda P2X7 crystal structures in complex with A740003, A804598, AZ10606120, GW791343 and JNJ47965567 were the first to report the location of an allosteric pocket (Karasawa and Kawate 2016). Prof. Kawate's research group compared the newly solved crystal structures of P2X7 with those of zebrafish P2X4 (Hattori and Gouaux 2012) and human P2X3 (Mansoor et al. 2016) observing that in P2X3 and P2X4 the pocket is narrower (Karasawa and Kawate 2016). With this observation in mind the question that followed next was: Is it possible that any of the known P2X4 allosteric antagonists binds to the same binding site? Our interest was directed towards BX430 – among other compounds initially considered such as 5-BDBD, PSB-12054, PSB-12062 – due to its extremely interesting pharmacology data. According to Ase *et al.*, BX430 displays different pharmacological profiles among human, zebrafish, mouse and rat P2X4 receptor (Ase et al. 2015). Indeed, BX430 displayed similar potency at human and zebrafish P2X4 subtypes (reported

IC_{50} values of 0.54 μM and 1.89 μM, respectively), whereas it was ineffective at 10 μM on rat and mouse P2X4 despite their higher sequence identity to human P2X4 (Ase et al. 2015). Considering the high level of sequence identity among rat, mouse and human P2X4, such a difference in potency could likely be affected by a difference in a small number of amino acids or even a single point mutation in the binding pocket. In order to identify any residue potentially affecting BX430 specie-selectivity and to reduce the risk of biased development and testing of the hypothesis, the whole aligned sequences of the extracellular domain were searched for residues that shared (i) identity ('restrictive criteria') or (ii) similarity (similar residue properties or retention of the ability to form H-bond, 'less-restrictive criteria') within the zebrafish/human subgroups and the mouse/rat subgroups but differing between the two subgroups. Ile-312 (human P2X4 numbering) is the only residue that obeys to the 'restrictive criteria' (above mentioned) by sharing identity in zebrafish but being a threonine at the corresponding position in mouse and rat sequence (Thr-312) therefore having a polar amino acid sidechain (instead of hydrophobic) (**Figure 4-1A**, highlighted in green). Three residues (Val-68, Val-101, Lys-222) obey to the 'less-restrictive' criteria maintaining either hydrophobicity or the ability to act as H-bond donor (**Figure 4-1A**, highlighted in yellow). **Figure 4-1B** shows the location of the 4 residues in the human P2X4 homology model.

A

```
hP2X4  ---MAGCCAALAAFLFEYDTPRIVLIRSRKVGLMNRAVQLLILAYVIGWVFVWEKGYQET  57
zfP2X4 MSESVGCCDSVSQCFFDYYTSKILIIRSKKVGTLNRFTQALVIAYVIGYVCVYNKGYQDT  60
mP2X4  ---MAGCCSVLGSFLFEYDTPRIVLIRSRKVGLMNRVVQLLILAYVIGWVFVWEKGYQET  57
rP2X4  ---MAGCCSVLGSFLFEYDTPRIVLIRSRKVGLMNRAVQLLILAYVIGWVFVWEKGYQET  57

hP2X4  DSVVSSVTTKVKGVAVTNTSKLGFRIWDVADYVIPAQEENSLFVMTNVILTMNQTQGLCP  117
zfP2X4 DTVLSSVTTKVKGIALTNTSELGERIWDVADYIIPPQEDGSFFVLTNMIITTNQTQSKCA  120
mP2X4  DSVVSSVTTKAKGVAVTNTSQLGFRIWDVADYVVPAQEENSLFIMTNMIVTVNQTQGTCP  117
rP2X4  DSVVSSVTTKAKGVAVTNTSQLGFRIWDVADYVIPAQEENSLFIMTNMIVTVNQTQSTCP  117

hP2X4  EIPDATTVCKSDASCTAGSAGTHSNGVSTGRCVAFNGSVKTCEVAAWCPVEDDTHVPQPA  177
zfP2X4 ENPTPASTCTSHRDCKRGFNDARGDGVRTGRCVSYSASVKTCEVLSWCPLEKIVDPPNPP  180
mP2X4  EIPDKTSICDSDANCTLGSSDTHSSGIGTGRCVPFNASVKTCEVAAWCPVENDAGVPTPA  177
rP2X4  EIPDKTSICNSDADCTPGSVDTHSSGVATGRCVPFNESVKTCEVAAWCPVENDVGVPTPA  177

hP2X4  FLKAAENFTLLVKNNIWYPKFNFSKRNILPNITTTYLKSCIYDAKTDPFCPIFRLGKIVE  237
zfP2X4 LLADAENFTVLIKNNIRYPKFNFNKRNILPNINSSYLTHCVFSRKTDPDCPIFRLGDIVG  240
mP2X4  FLKAAENFTLLVKNNIWYPKFNFSKRNILPNITTSYLKSCIYNARTDPFCPIFRLGQIVA  237
rP2X4  FLKAAENFTLLVKNNIWYPKFNFSKRNILPNITTSYLKSCIYNAQTDPFCPIFRLGTIVE  237

hP2X4  NAGHSFQDMAVEGGIMGIQVNWDCNLDRAASLCLPRYSFRRLDTRDVEHNVSPGYNFRFA  297
zfP2X4 EAEEDFQIMAVHGGVMGVQIRWDCDLDMPQSWCVPRYTFRRLDNKDPDNNVAPGYNFRFA  300
mP2X4  DAGHSFQEMAVEGGIMGIQIKWDCNLDRAASHCLPRYSFRRLDTRDLEHNVSPGYNFRFA  297
rP2X4  DAGHSFQEMAVEGGIMGIQIKWDCNLDRAASLCLPRYSFRRLDTRDLEHNVSPGYNFRFA  297

hP2X4  KYYRDLAGNEQRTLIKAYGIRFDIIVFGKAGKFDIIPTMINIGSGLALLGMATVLCDIIV  357
zfP2X4 KYYKNSDGTETRTLIKGYGIRFDVMVFGQAGKFNIIPTLLNMGAGLALLGLVNVICDWIV  360
mP2X4  KYYRDLAGNEQRTLTKAYGIRFDIIVFGKAGKFDIIPTMINVGSGLALLGVATVLCDVIV  357
rP2X4  KYYRDLAGKEQRTLTKAYGIRFDIIVFGKAGKFDIIPTMINVGSGLALLGVATVLCDVIV  357

hP2X4  LYCMKKRLYYREKKYKYVEDYEQGLASELDQ  388
zfP2X4 LTFMKRKQHYKEQKYTYVDDFGLLHNEDK--  389
mP2X4  LYCMKKRYYYRDKKYKYVEDYEQGLSGEMNQ  388
rP2X4  LYCMKKKYYYRDKKYKYVEDYEQGLSGEMNQ  388
```

B

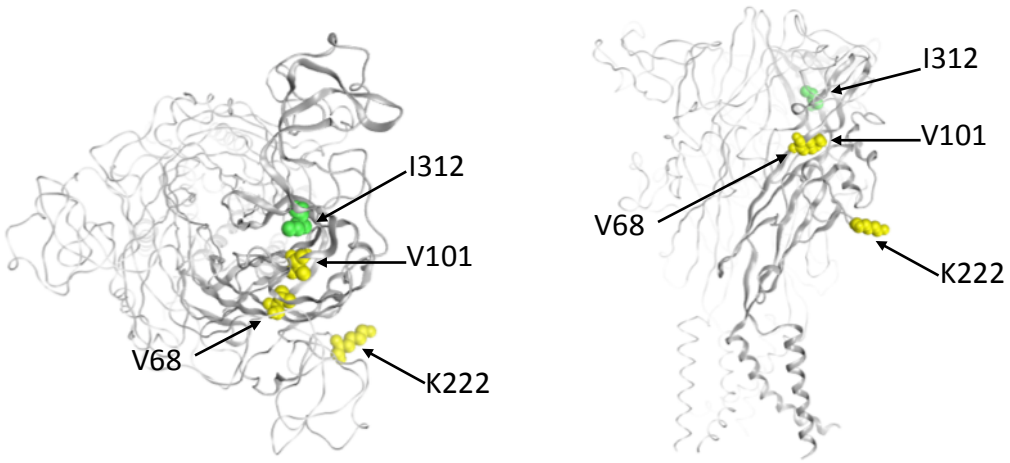

Figure 4-1: Identification of the residues potentially responsible for BX430 specie-selectivity. (**A**) Sequence alignment of zebrafish (zf), human (h), rat (r) and mouse (m) P2X4. Residues that share identity with human P2X4 sequence are highlighted in gray, residues obeying to the 'restrictive

criteria' in green, residues obeying to the 'less-restrictive criteria' in yellow. Leu-107 corresponding to valine in rodents and describe in **Section 4.6** is highlighted in cyan. Residues of human P2X4 corresponding to the transmembrane domains are underlined. (**B**) Location of the residues obeying to the selection criteria in the human P2X4 homology model, top view (Left) and side view (Right).

Val-68 is located in the ATP-binding pocket, Lys-222 appears to be in a loop almost completely exposed to solvent while Val-101 and Ile-312 are buried in the receptor within the same site and Ile-312 corresponds to one of the residues of the allosteric pocket identified by Karasawa *et al.* in giant panda P2X7 crystal structure (see **Figure 4-2** and **Section 1.5.3.2**). For these reasons our interest has been focused on Ile-312 (described in **Section 4.3** and following).

```
5U1X   KAEILENGMKKMVSGVFDTADYTFPLQ-GNSFFVMTNFIKTEG 93
hP2X7  KEEIVENGVKKLVHSVFDTADYTFPLQ-GNSFFVMTNFLKTEG 113
4DW0   KTS-------ELGERIWDVADYIIPPQEDGSFFVLTNMIITTN 88
zfP2X4 NTS-------ELGERIWDVADYIIPPQEDGSFFVLTNMIITTN 113
hP2X4  NTS-------KLGFRIWDVADYVIPAQEENSLFVMTNVILTMN 110
rP2X4  NTS-------QLGFRIWDVADYVVPAQEENSLFIMTNMIVTVN 110
mP2X4  NTS-------QLGFRIWDVADYVIPAQEENSLFIMTNMIVTVN 110

5U1X   GYNFRYAKYYKEN-NVEKRTLIKVFGIRFDILVFGTGGKFNVI 311
hP2X7  GYNFRYAKYYKEN-NVEKRTLIKVFGIRFDILVFGTGGKFDII 331
4DW0   GYNFRFAKYYKNSDGTETRTLIKGYGIRFDVMVFGQAGKFNII 311
zfP2X4 GYNFRFAKYYKNSDGTETRTLIKGYGIRFDVMVFGQAGKFNII 336
hP2X4  GYNFRFAKYYRDLAGNEQRTLIKAYGIRFDIIVFGKAGKFDII 333
rP2X4  GYNFRFAKYYRDLAGNEQRTLTKAYGIRFDIIVFGKAGKFDII 333
mP2X4  GYNFRFAKYYRDLAGKEQRTLTKAYGIRFDIIVFGKAGKFDII 333
```

Figure 4-2: Sequence alignment of giant panda P2X7 residues in the allosteric pocket with P2X4 sequences. Zebrafish (zf), human (h), rat (r) and mouse (m) residues that share identity with PDB 5U1X sequence are in dark aqua, residues facing the allosteric pocket identified by *Karasawa et al.* highlighted in cyan, residues corresponding to Ile-312 across P2X4 subtype highlighted in green, residues corresponding to Val-101 across P2X4 subtype highlighted in yellow.

4.2 Docking of ivermectin (IVM)

An homology model of rat P2X4 (Uniprot sequence: P51577) was built using the ATP-bound zebrafish P2X4 crystal (PDB ID: 4DW1), assessed with PROCHECK (Laskowski et al., 1993) and Rampage Server (Lovell Simon et al. 2003) and prepared with Protein Preparation Wizard (Schrödinger Suite 2015-1 Protein Preparation Wizard; Epik, Schrödinger, LLC, New York, NY, 2018; Impact, Schrödinger, LLC, New York, NY, 2018; Prime, Schrödinger, LLC, New York, NY, 2018) prior to performing the docking simulation. Site Finder (Molecular Operating Environment (MOE), 2014.0901; Chemical Computing Group ULC, 1010 Sherbooke St. West, Suite #910, Montreal, QC, Canada, H3A 2R7, 2018) was used to identify a potential binding site at the level of the trasmembrane domains that was taken as reference to position the receptor grid (box) while LigPrep (LigPrep, Schrödinger, LLC, New York, NY, 2018) served to prepare IVM. **Figure 4-3A** highlights the dioleandrose disaccharide (boxed in salmon), the hydrogenated benzofuran (in liliac) and the spiroketal (yellow) moieties – same color-coding is maintained in **Figure 4-3B-D** for clarity. The docking simulation was performed within a 35$Å^3$ box using Glide XP - whose scoring function also accounts for hydrophobic interactions. The docked IVM inserts between subunits like a 'wedge' with the disaccharide moiety (dioleandrose, salmon) located near the extracellular face of the membrane entertaining hydrophobic interactions with Tyr-42, Trp-46, and Val-47 at the TM1 of one subunit (light blue, **Figure 4-3C,D**) while forming a H-bond between the hydroxyl of the disaccharide and the side-chain of Asn-338 in the TM2 of the adjacent subunit (light green, **Figure 4-3C,D**). The hydrogenated benzofuran moiety (liliac) instead points toward the intracellular face of the lipid bilayer (**Figure 4-3B**) establishing hydrophobic interactions with Leu-345 and Val-348 near the bottom of the TM2 of one subunit (light blue, **Figure 4-3C,D**). According to our docking IVM is therefore stabilizing the open state of the channel by entertaining interactions with the top of TM1 and TM2 of one subunit and the bottom of TM2 of the adjacent subunits. The conformation obtained from the docking simulation does not prevent IVM from binding to more than one equivalent sites between the subunits of the trimer. Residues of rat P2X4 sequence (in bold) nearby IVM are indicated in **Figure 4-3E** by arrows (light blue or green according to subunit colour scheme) while the arrowhead indicates Asn-338, which entertains a H-bond interaction with the disaccharide moiety of IVM. Sequences of

IVM-sensitive P2X receptors along with non-sensitive subtypes were compared aiming at the identification of key amino acids determining IVM selectivity. **Figure 4-3E** reports aligned sequences of transmembrane domains of rat, mouse and human P2X1, P2X1, P2X3, P2X4, and P2X7, together with those of *Schistosoma mansoni* (sm)P2X (Agboh et al. 2004) and *Hypsibius dujardini* (Hd)P2X (Bavan et al. 2009) – both also found sensitive to IVM (IVM-sensitive receptors are encapsulated in a yellow box). Human P2X7 has not been included in the yellow box as it had been initially reported as positively modulated by IVM in whole-cell patch clamp experiments (Nörenberg et al. 2012), however a later study investigating IVM activity in human P2X7 expressed in *Xenopus* oocytes detected no potentiation (Schneider et al. 2017).

Silberberg et al. identified 9 rat P2X4 residues (highlighted in red boxes in **Figure 4-3E**) that significantly reduced IVM activity when mutated to tryptophan (Silberberg et al. 2007). In our docking, IVM is located within 4.5 Å distance from 7 out of 9 residues – indicated by arrows and arrowheads in **Figure 4-3E** (the colour of the arrows match the colour of the receptor subunit) showing an interesting parallel between the docking simulation and the experimental data.

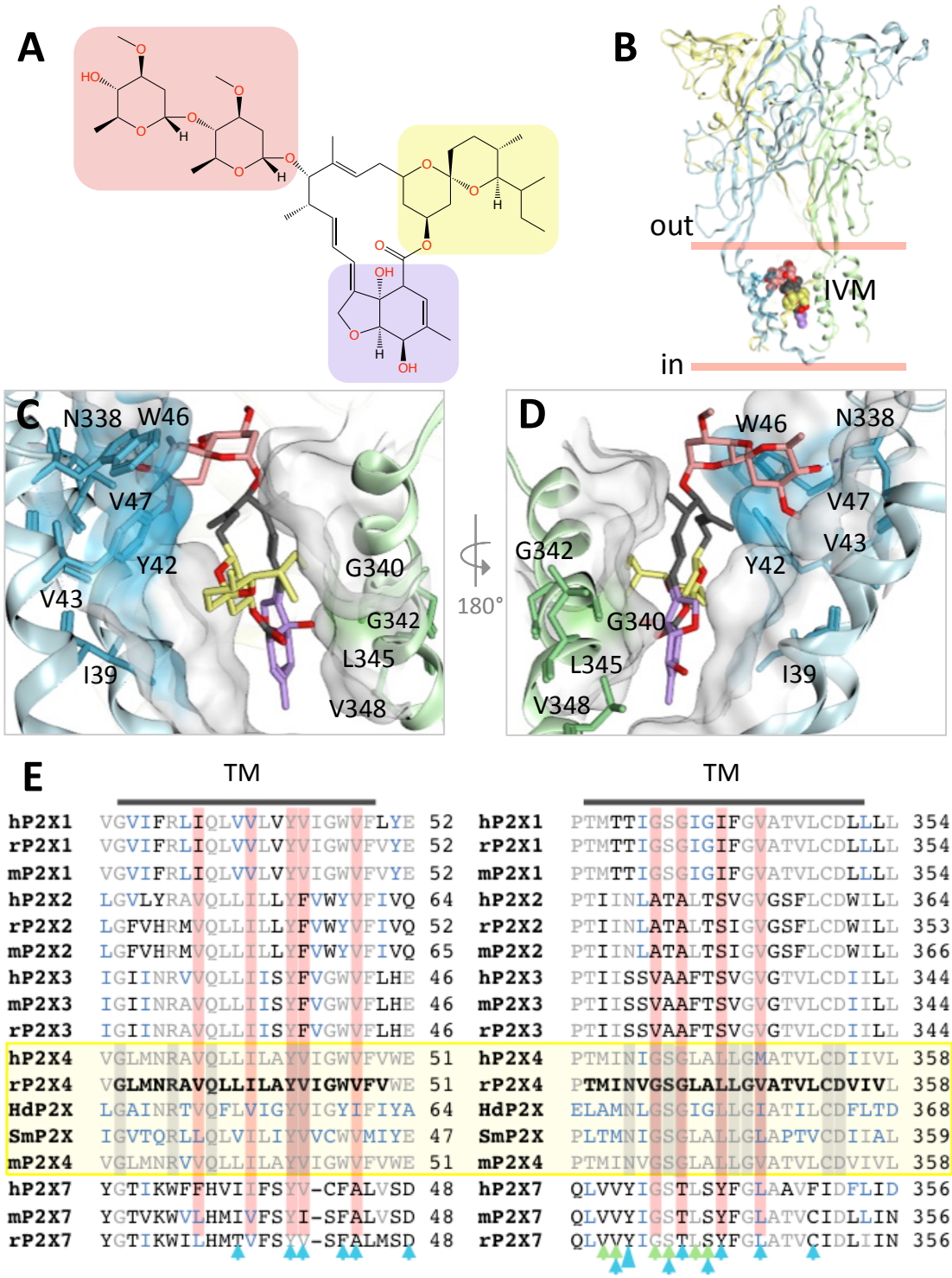

Figure 4-3: Docking of ivermectin (IVM) in the rat P2X4 homology model. Figure reproduced from (Pasqualetto et al. 2018). **(A)** Important chemical groups of IVM B1a including the dioleandrose (disaccharide) (salmon), spiroketal (yellow), and hydrogenated benzofuran (liliac) moieties. The color scheme is maintained throughout the **Figure 4-3** for clarity. **(B)** Predicted IVM binding site in rat P2X4. Receptor structure represented in ribbons and colored according to different subunits while red lines delimit the membrane bilayer for reference. **(C)** Dock of IVM between two subunits and nearby residues are displayed (same color coding as in **(A)**). Receptor

surface nearby the ligand is shown in white; colored areas correspond to the highlighted residues. **(D)** 180◦ rotation of the IVM pose displayed in **(C)**. The transmembrane (TM) domains of the third subunit (yellow in **B**) are omitted for clarity. **(E)** Sequence alignment of the transmembrane domains of rat (r), human (h), mouse (m) P2X1, P2X2, P2X3, P2X4 and together with *Schistosoma mansoni* (Sm) and *Hypsibius dujardini* (Hd) P2X receptor sequences; rP2X4 TMs in bold. Receptors sensitive to IVM are enclosed in a yellow box while conserved residues across all IVM-sensitive receptors are boxed in gray. Conserved residues are represented in grey fonts while blue fonts are used for conserved residues in IVM-sensitive receptors. Red boxes indicate residues that reduce IVM activity when mutated to tryptophan as identified by Silberberg *et al*. (Silberberg et al. 2007). Arrows highlight the amino acid within a distance of 4.5Å of IVM in our docking simulation (arrow color according to the subunits, as in **B-D**); while the arrow head indicates Asn-338 that interacts through an H-bond with the disaccharide moiety of IVM.

According to the conformation obtained in our docking simulation, the dioleandrose moiety of IVM entertains a hydrogen bond with the sidechain of Asn-338. In their tryptophan mutagenesis study, *Silberberg et al*. observed that the rat P2X4 N338W retained IVM sensitivity with a fold effect of IVM on current amplitudes comparable to rat P2X4 wild-type (Silberberg et al. 2007). Interestingly their reported traces suggest that the N338W mutant decreases the IVM effect on receptor desensitization (faster rate of desensitization compared to wild-type treated with IVM), however this effect has not been investigated further in the study (Silberberg et al. 2007). By mutating the rat P2X4 model at Asn-338 to an energetically favorable Trp rotamer (using the Protein Builder tool, MOE), we briefly explored whether the hindrance of Trp was impeding the IVM fit. Interestingly, IVM was still able to make an H-arene interaction with the tryptophan (**Figure 4-4**) - however this type of interaction is usually weaker than a hydrogen bond, which may give a potential explanation to the lower ability of IVM in slowing down the deactivation in rat P2X4 N338W mutant (Silberberg et al. 2007).

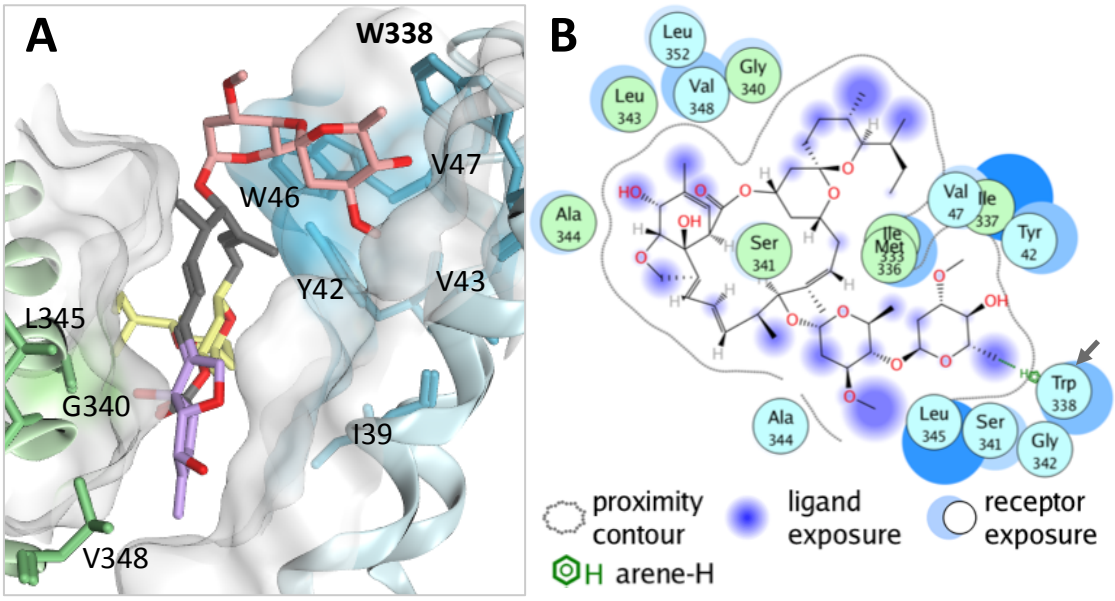

Figure 4-4: IVM superposed to rat P2X4 mutant N338W (labeled in bold in (**A**)). (**A**) Predicted Trp-338 rotamer position relative to IVM. Color scheme as in **Figure 4-3**. (**B**) Ligand-protein interaction diagram highlighting residues located near IVM (residues color-coded according to the corresponding receptor subunit). A grey arrow indicates the mutated residue forming a H-arene interaction with IVM.

The binding site of IVM has several limitations to be used for drug discovery (see also **Section 4.8** - chapter discussion) ranging from higher inaccuracy of the model to the actual volume of the site. Therefore this binding pocket has not been used for a structure-based drug design approach. Instead, following the hypothesis described in the introduction of this chapter an alternative allosteric pocket has been identified (see following sections).

4.3 BX430 binding site discovery - generation, selection and validation of RML2, RTI-13 and HIT-08 cell lines

To test our hypothesis that BX430 occupies the corresponding binding pocket to that of the allosteric P2X7 modulators (**Section 4.1.2**), cell lines expressing rat P2X4 wild type, rat P2X4 Thr-312 to Ile mutant (RTI in this work) and human P2X4 Ile-312 to Thr mutant (HIT) were generated according to the procedure described in **Section 2.2.1**. Refer to **Appendix 1** for protein expression levels and functionality of single-cell clones. RML2 13, HIT 08 (name standing for 'Human, Ile to Thr', clone 8) and RTI 13 (standing for 'Rat, Thr to Ile', clone 13) clones showed high level of protein expression and receptor functionality in Ca^{2+} influx assay and were therefore selected and expanded for the experiments described in the following sections.

4.4 ATP concentration-response curves for wild-type and mutant rat and human P2X4

ATP concentration-responses were measured through Ca^{2+} influx assay for cell lines stably expressing rat P2X4 wild-type (RML2 13), human P2X4 bearing the I312T mutation (HIT 08) and rat P2X4 T312I 'mirror' mutant (RTI 13). Applied concentrations of ATP ranged from 0.03 μM to 100 μM. Data for human P2X4 wild type ATP is repurposed here from **Section 3.4** for easier comparison and clarity (dotted line in **Figure 4-5** and **Table 4.1)**. ATP EC_{50} values for human and rat mutated P2X4 were 0.77 μM and 0.73 μM respectively, compared to 1.26 μM and 1.70 μM, for human and rat P2X4 wild type. Hill slopes values for human I312T and rat T312I were 2.057 and 2.475, while rat wild type and human wild type had a lower values. (1.441 and 1.098, respectively) Notably, a reduction in ATP responses was observed for both mutants when high ATP doses were applied (especially at 30 μM and 100 μM) with a decrease in the response up to approximately 25% (see **Figure 4-5:** Mean ATP concentration-response curves of rat P2X4 wild type (rP2X4 WT, grey full squares), rat P2X4 T312I mutant (rP2X4 T312I, gray empty squares), human P2X4 wild type (hP2X4 WT, black full circles), human P2X4 I312T (hP2X4 WT, black empty circles). Human P2X4 wild type data

repurposed from **Section 3.4** (black dotted line). Responses represent fluorescent increase following ATP addition (see **Section 2.2**) and were normalized to the maximum response mean value recorded among the concentration tested. Data merged from 3 or more independent experiments (n=4-6/each) representing data as mean ± SEM. EC_{50} and Hill coefficient values reported in **Table 4.1** were calculated with GraphPad through curve fit (using log(agonist) vs. normalized response with variable slope equation). Statistical analysis showed no significant difference (ns) when comparing ATP $LogEC_{50}$ values from the 4 different cell lines, exception made for rat P2X4 WT vs. human P2X4 I312T (One-way ANOVA, Tukey's multiple comparison test, p=0.0321, *).

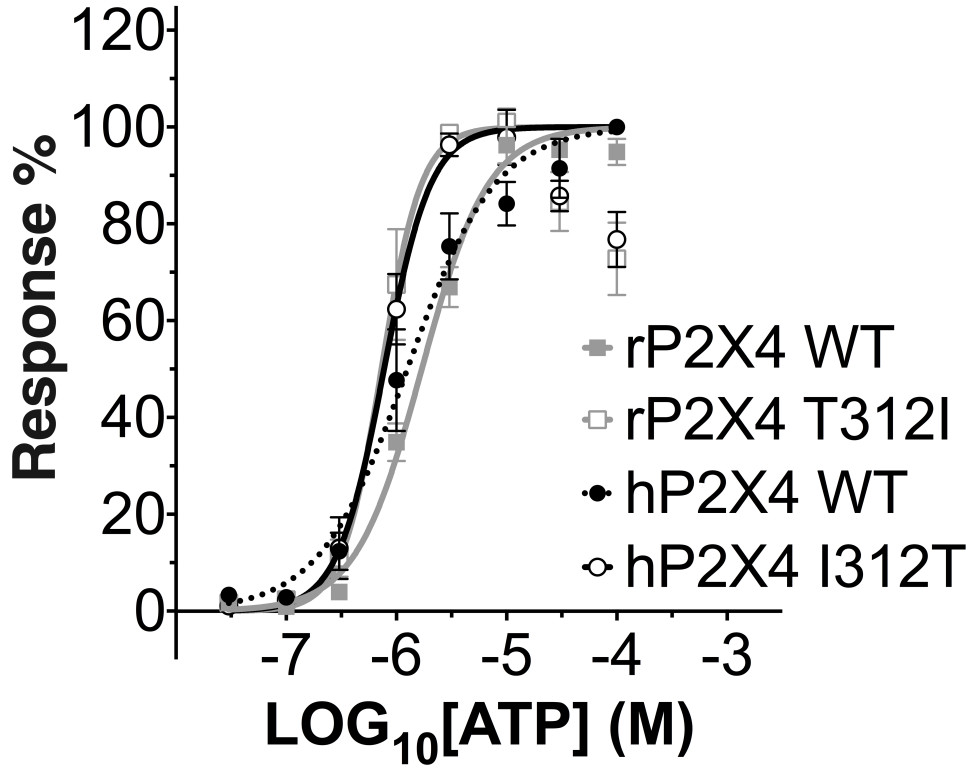

Figure 4-5: Mean ATP concentration-response curves of rat P2X4 wild type (rP2X4 WT, grey full squares), rat P2X4 T312I mutant (rP2X4 T312I, gray empty squares), human P2X4 wild type (hP2X4 WT, black full circles), human P2X4 I312T (hP2X4 WT, black empty circles). Human P2X4 wild type data repurposed from **Section 3.4** (black dotted line). Responses represent fluorescent increase following ATP addition (see **Section 2.2**) and were normalized to the maximum response mean value recorded among the concentration tested. Data merged from 3 or more independent experiments (n=4-6/each) representing data as mean ± SEM. EC_{50} and Hill coefficient values reported in **Table 4.1** were calculated with GraphPad through curve fit (using log(agonist) vs. normalized response with variable slope equation).

Cell line	ATP EC_{50}	ATP $LogEC_{50}$ (±SEM)	Hill Coefficient
Human P2X4 WT	1.26 μM	-5.901 (± 0.0577)	1.098
Rat P2X4 WT	1.70 μM	-5.770 (*) (± 0.0507)	1.441
Human P2X4 I312T	0.77 μM	-6.112 (*) (± 0.0.028)	2.057
Rat P2X4 T312I	0.73 μM	-6.136 (± 0.0645)	2.475

Table 4.1: ATP EC_{50}, pEC_{50} and Hill Coefficient values for wild type and mutated rat and human P2X4 cell lines. *statistical significance between rat P2X4 WT and human P2X4 I312T $LogEC_{50}$ values ($P \leq 0.05$; One-way ANOVA, Tukey's multiple comparison test)

4.5 BX430 inhibition curves for wild type and mutant receptors

BX430 potency was determined through Ca^{2+} influx assay using 1 μM ATP concentration for both mutants and wild types. As reported in **Section 3.5** and repurposed here for comparison (**Figure 4-6**, dotted line), BX430 inhibited ATP responses at human P2X4 wild type with an IC_{50} of 2.12 μM (see **Table 4.2**). In accordance with what previously reported (Ase et al. 2015), BX430 was only a weak antagonist at rat P2X4 homologues displaying approximately 30-fold decrease in potency when rat P2X4 receptor was activated with 1 μM ATP (computed IC_{50} of 66.1 μM). Remarkably, BX430 potency was reduced by approximately 46-fold in cells expressing human P2X4 bearing the I312T mutation (calculated IC_{50} of 102.4 μM over 2 independent experiments). Conversely, the rat P2X4 T312I point-mutation alone accounted for a far higher susceptibility to BX430 inhibition compared to rat P2X4 wild type (48-fold) with a calculated IC_{50} of 1.4 μM, restoring BX430 potency to a IC_{50} value comparable to the one calculated for human P2X4 wild type (IC_{50} of 2.12 μM). Inhibition curve-fits for each independent experiment are reported in **Appendix 2**. Note that IC_{50} values for human P2X4 I312T and rat P2X4 WT are largely approximated due to a poor fit (no inhibition) or interrupted curve fit (see **Appendix 2**), therefore $LogIC_{50}$ values for human P2X4 cell lines were not included in the statistical analysis (only the values calculated with no ambiguity in the fit were considered for rat). An ordinary One-way ANOVA followed by Dunnett's multiple comparison test, with a single pooled variance revealed a statistically significant difference in $LogIC_{50}$ mean values (P=0.0006, ***) between human P2X4 WT and rat P2X4 WT (***) but no statistical

significance (ns) when comparing human P2X4 WT and rat P2X4 T312I. This results reveals that the single point mutation alone is capable of rescuing BX-430 potency at rat P2X4.

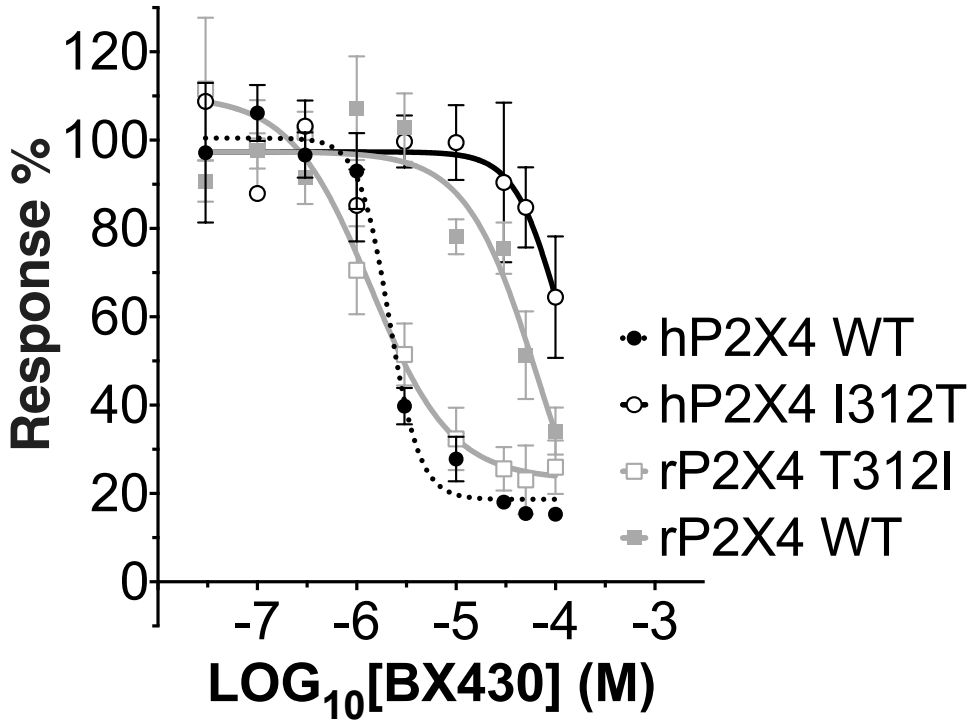

Figure 4-6: Mean BX430 inhibition curves of rat P2X4 wild type (rP2X4 WT, grey full squares), rat P2X4 T312I mutant (rP2X4 T312I, gray empty squares), human P2X4 wild type (hP2X4 WT, black full circles), human P2X4 I312T (hP2X4 WT, black empty circles). Human P2X4 wild type data repurposed from **Section 3.5** (black dot line). Responses represent fluorescent increase elicited by 1 uM ATP addition after incubation with increasing concentrations of BX430. Data points were normalized to the response obtained with vehicle-only (0.1% DMSO) and are presented as mean ± SEM. IC_{50} and Hill coefficient values reported in **Table 4.2** calculated with GraphPad through curve fit (using log(antagonist) vs. response, parameters equation). Data merged from 2 (for hP2X4 WT) or more independent experiments (n=3-5/technical repeats each).

Cell line	BX-430 IC_{50}	BX-430 $LogEC_{50}$ (±SEM)	Hill Coefficient
Human P2X4 WT	2.12 µM	-5.673 (± 0.06963)	-2.793
Rat P2X4 WT	66.1 µM	-4.180 $^{(\star)}$ (± 0.6884)	-1.213
Human P2X4 I312T	>100 µM	-3.990 $^{(\star)}$ (± 2.641)	-1.977
Rat P2X4 T312I	1.4 µM	-5.858 (± 0.1575)	-1.072

* **n.c.:** non congruent when calculated from each independent experiment.

Table 4.2: BX430 IC_{50} values for wild type and mutated rat and human P2X4 cell lines.

4.6 Docking of BX430 in human P2X4 and rat P2X4 models

A docking simulation of BX430 in the pocket of the human P2X4 homology model where Ile-312 is located was performed to assess from an *in silico* molecular modelling perspective whether BX430 is able to sterically fit the allosteric site and form interactions with residues nearby. Additionally to the homology model of human P2X4 in the closed state (described in **Section 3.1.3**), a rat P2X4 model in the closed state was also generated using zebrafish P2X4 crystal structure (PDB ID: 4DW0) as template and subsequently validated with Rampage Server (Lovell Simon et al. 2003) and PROCHECK (Laskowski et al. 1993) obtaining a model with satisfactory geometry (84.2% residues found in the most favourable region and 0.0% residues in the disallowed regions of the computed Ramachandran Plot) given the sequence identity between rat and the template (62.4% respectively) and its resolution (2.9 Å). To a visual inspection, the region of the human P2X4 model corresponding to the pocket identified in panda P2X7 presents a cavity with narrower entrance at the top of the trimer that connects it - similarly to a tunnel – to the vestibule at the receptor core. The presence of such a cavity in the model allowed its exploration through performing docking. The Glide Standard Precision (SP) protocol was employed for the docking simulation considering only the ligand as flexible entity and taking the location of the co-crystallised P2X7 allosteric antagonist GW791343 (PDB ID: 5U1Y) as a reference (after superposition) for the centroid of a 30Å cubical docking grid (**Figure 4-7A** depicts the location set for the docking grid). As seen in **Figure 4-7B**, all BX430 output conformations adopt a similar orientation with the pyridine portion close to the solvent-exposed cavity entrance whilst the di-bromo-isopropyl-phenyl moiety occupies a deeper and more hydrophobic portion of the pocket at close proximity to Ile-312, Tyr-299 and Leu-107, which may establish hydrophobic interactions with BX430. The carbamide group of BX430 potentially stabilizes the conformation by forming two H-bond interactions with the Glu-307 sidechain (**Figure 4-7B**). In addition, a docking simulation was run maintaining the same settings and utilizing rat P2X4 homology model and aiming at the identification of any remarkable difference in the ligand binding conformation. In this case the output conformations could be clustered according to the two opposite ligand orientations as shown in **Figure 4-7D** and **Figure 4-7E**. No conformation was able to emulate the double H-bond observed in

the docking of BX430 in the human model homologue, instead a single H-bond interaction was observed between the carbamide and the Arg-301 sidechain when the pyridine moiety was oriented towards the pocket entrance.

As described in the **Section 1.5.3.2** for panda P2X7 crystal structures, Lys-297 (panda P2X7 numbering) – corresponding to Lys-298 in the human P2X4 model – has missing atoms, which suggests a high degree of flexibility (not surprising for a lysine residue). From a visual inspection of the human P2X4 model, Lys-298 appears to be capable of assuming multiple conformations within the nearby space and might therefore operate as 'gateway' controlling the access to the upper vestibule of the channel pore – as seen partially occupied by allosteric antagonists (such as JNJ47965567) in panda P2X7. For this reason a docking simulation of BX430 was performed also in the human P2X4 model with the Lys-298 assuming a different energetically-allowed rotamer. In this case, the isopropyl moiety lies near Ile-312 and Leu-107 – both residues not conserved in rat and mouse (corresponding to threonine and valine in rodents). Together with Ile-312, the close proximity of Leu-107 may increase the contribution of hydrophobic interactions due to its longer aliphatic chain compared to Val (**Figure 4-7C**). While the dibromo-4-(isopropyl)phenyl moiety occupies a similar location to that observed with the non-rotated Lys-298 (although an opposite orientation, **Figure 4-7B**), the pyridinyl-urea moiety inserts deeper in the cavity with the pyridine accessing the upper vestibule and the urea entertaining a double hydrogen bond interaction with the backbone of Asp-88 (**Figure 4-7C**). In the following sections the cavity explored through docking simulations and virtual screening will be referred to as the 'BX-430 pocket'.

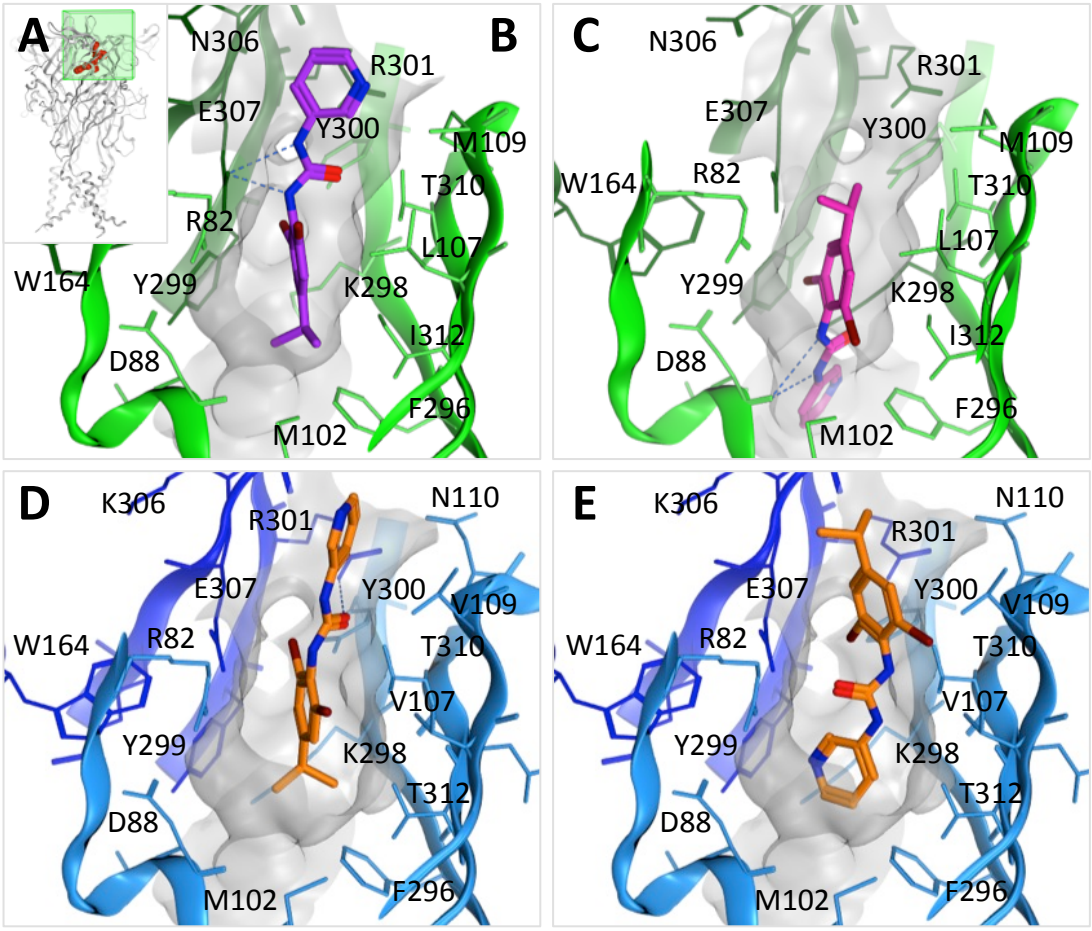

Figure 4-7: Docking of BX430 in P2X4 homology models (green ribbons for human P2X4 model, blue ribbons for rat). (**A**) Location and box dimensions (in green, 30Å x 30Å x 30Å) used as grid for the docking of BX430. As reference for the location of the allosteric pocket identified in panda P2X7, one molecule of GW791343 (in red spheres) present in the crystal (PDB ID: 5U1Y) was superposed to the human P2X4 model (closed state). (B) docking of BX430 in human P2X4 model. All poses obtained showed similar orientation with the di-bromo-isopropyl-phenyl moiety pointing inward the pocket. (C) docking of BX-430 in human P2X4 when an alternative conformation of Lys-298 was considered. (D), (E) Docking of BX430 in rat P2X4 gave poses showing two opposite ligand orientations.

4.7 Virtual screening in the 'BX430 pocket'

According to visual inspection, the flexibility of Lys-298 influences the volume and the conformation of the 'BX-430 pocket' and therefore both models described in **Section 4.6** (bearing 2 different Lys-298 residues conformations) were used to perform a virtual screening. This was achieved with the use of the Virtual Screening Workflow tool (Schrödinger), which allows the use of multiple receptor grids as ensemble and automatizes the docking iterations (Glide HTVS followed by Glide SP and finally Glide XP) after applying drug-likeness filters to the SPECS library (used as source of ligand conformations). The resulting dataset of docked ligands (10,000 poses) included the 5,000 top-scored structures from each receptor grid used, which were filtered, clustered and visually inspected selecting 20 hits. **Table 4.3** lists the structures of compounds that are proposed for purchase and biological assay while **Figure 4-8** displays selected examples of hit compounds docked in the binding site.

ID	Structure	Specs ID	MW	Chemical Name
70	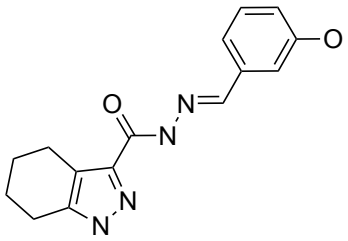	AG-690/ 09390064	284.32	N'-(3-hydroxybenzylidene)-4,5,6,7-tetrahydro-1H-indazole-3-carbohydrazide
71	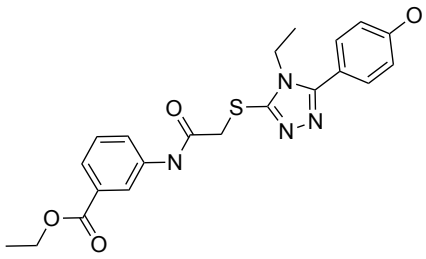	AG-690/ 40751404	426.5	ethyl 3-((((4-ethyl-5-(4-hydroxyphenyl)-4H-1,2,4-triazol-3-yl)sulfanyl)acetyl)amino)benzoate

72	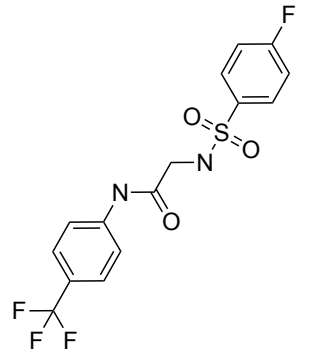	AH-487/ 41938124	376.33	2-(((4-fluorophenyl)sulfonyl) amino)-N-(4-(trifluoromethyl) phenyl)acetamide
73	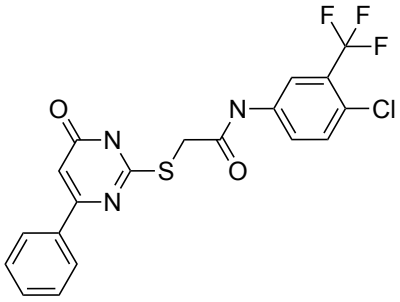	AJ-292/ 14921026	439.84	N-(4-chloro-3-(trifluoromethyl)phenyl)-2-((6-oxo-4-phenyl-1,6-dihydro-2-pyrimidinyl)sulfanyl) acetamide
74	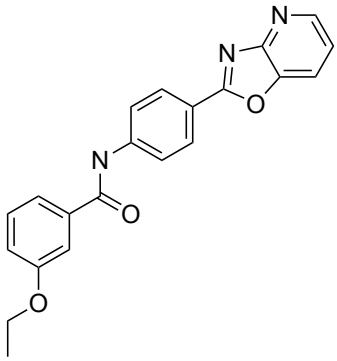	AK-778/ 11467118	359.38	3-ethoxy-N-(4-(1,3)oxazolo(4,5-b)pyridin-2-ylphenyl)benzamide
75	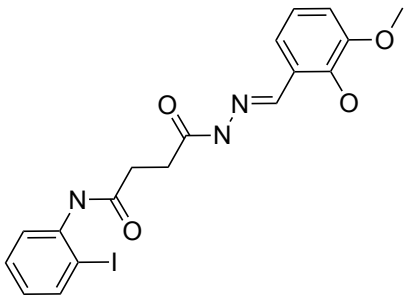	AK-968/ 40605344	467.26	4-(2-(2-hydroxy-3-methoxybenzylidene)hydrazino)-N-(2-iodophenyl)-4-oxobutanamide
76	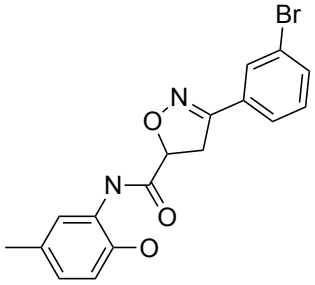	AN-329/ 43211370	375.22	3-(3-bromophenyl)-N-(2-hydroxy-5-methylphenyl)-4,5-dihydro-5-isoxazolecarboxamide

77	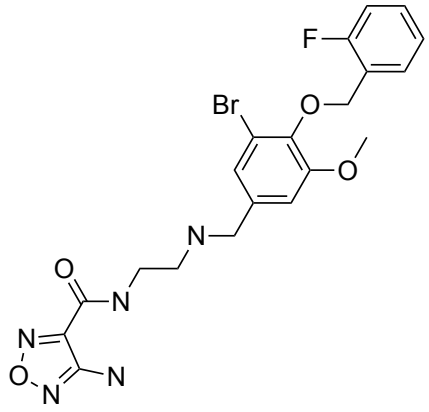	AN-465/ 42784360	494.32	4-amino-N-(2-((3-bromo-4-((2-fluorobenzyl)oxy)-5-methoxybenzyl)amino)ethyl)-1,2,5-oxadiazole-3-carboxamide
78	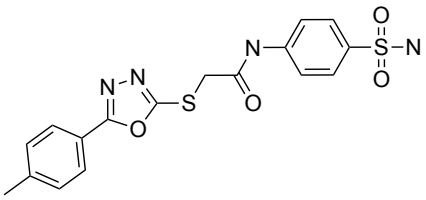	AO-476/ 43071656	404.47	N-(4-(aminosulfonyl)phenyl)-2-((5-(4-methylphenyl)-1,3,4-oxadiazol-2-yl)sulfanyl)acetamide
79	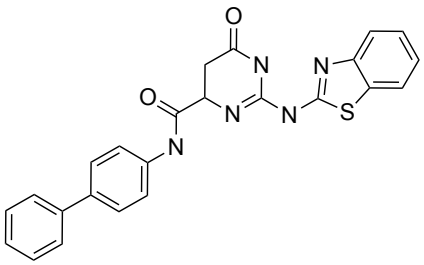	AO-567/ 40646811	441.51	2-(1,3-benzothiazol-2-ylamino)-N-(1,1'-biphenyl)-4-yl-6-oxo-1,4,5,6-tetrahydro-4-pyrimidinecarboxamide
80	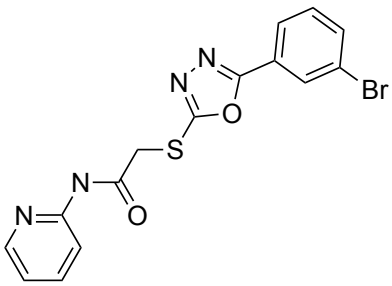	AP-853/ 42877593	391.25	2-((5-(3-bromophenyl)-1,3,4-oxadiazol-2-yl)sulfanyl)-N-(2-pyridinyl)acetamide
81	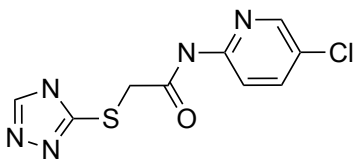	AP-853/ 43387162	269.72	N-(5-chloro-2-pyridinyl)-2-(4H-1,2,4-triazol-3-ylsulfanyl) acetamide
82	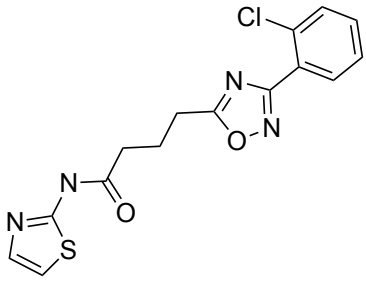	AP-853/ 43405648	348.81	4-(3-(2-chlorophenyl)-1,2,4-oxadiazol-5-yl)-N-(1,3-thiazol-2-yl) butanamide

83	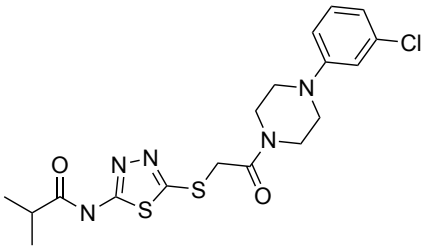	AQ-088/ 42471813	439.99	N-(5-((2-(4-(3-chlorophenyl)-1-piperazinyl)-2-oxoethyl)sulfanyl)-1,3,4-thiadiazol-2-yl)-2-methylpropanamide
84	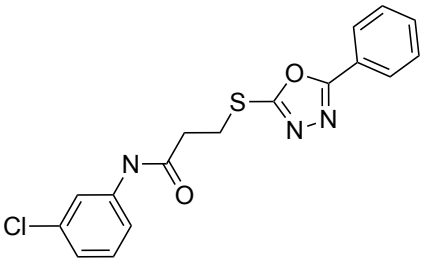	AP-853/ 42160294	359.84	N-(3-chlorophenyl)-3-((5-phenyl-1,3,4-oxadiazol-2-yl) thio)propanamide
85	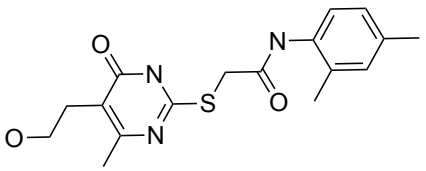	AS-871/ 43478038	347.44	N-(2,4-dimethylphenyl)-2-((5-(2-hydroxyethyl)-4-methyl-6-oxo-1,6-dihydro-2-pyrimidinyl)sulfanyl) acetamide
86	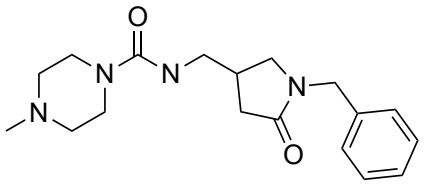	AE-641/ 40262184	330.43	N-((1-benzyl-5-oxo-3-pyrrolidinyl)methyl)-4-methyl-1-piperazine carboxamide
87	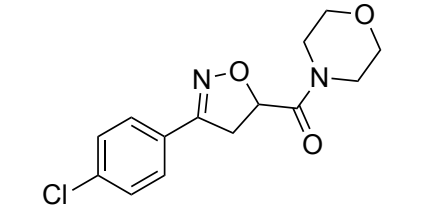	AN-329/ 43211272	294.74	4-((3-(4-chlorophenyl)-4,5-dihydro-5-isoxazolyl)carbonyl) morpholine
88	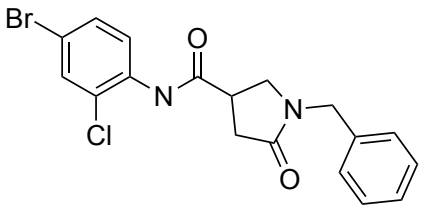	AK-918/ 42814019	407.69	1-benzyl-*N*-(4-bromo-2-chlorophenyl)-5-oxopyrrolidine-3-carboxamide
89	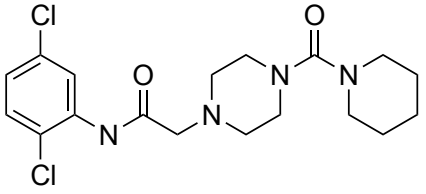	AP-124/ 42855935	399.32	*N*-(2,5-dichlorophenyl)-2-(4-(piperidine-1-carbonyl)piperazin-1-yl)acetamide

Table 4.3: List of compounds (70-89) obtained from the virtual screening performed in the BX430 bindig site.

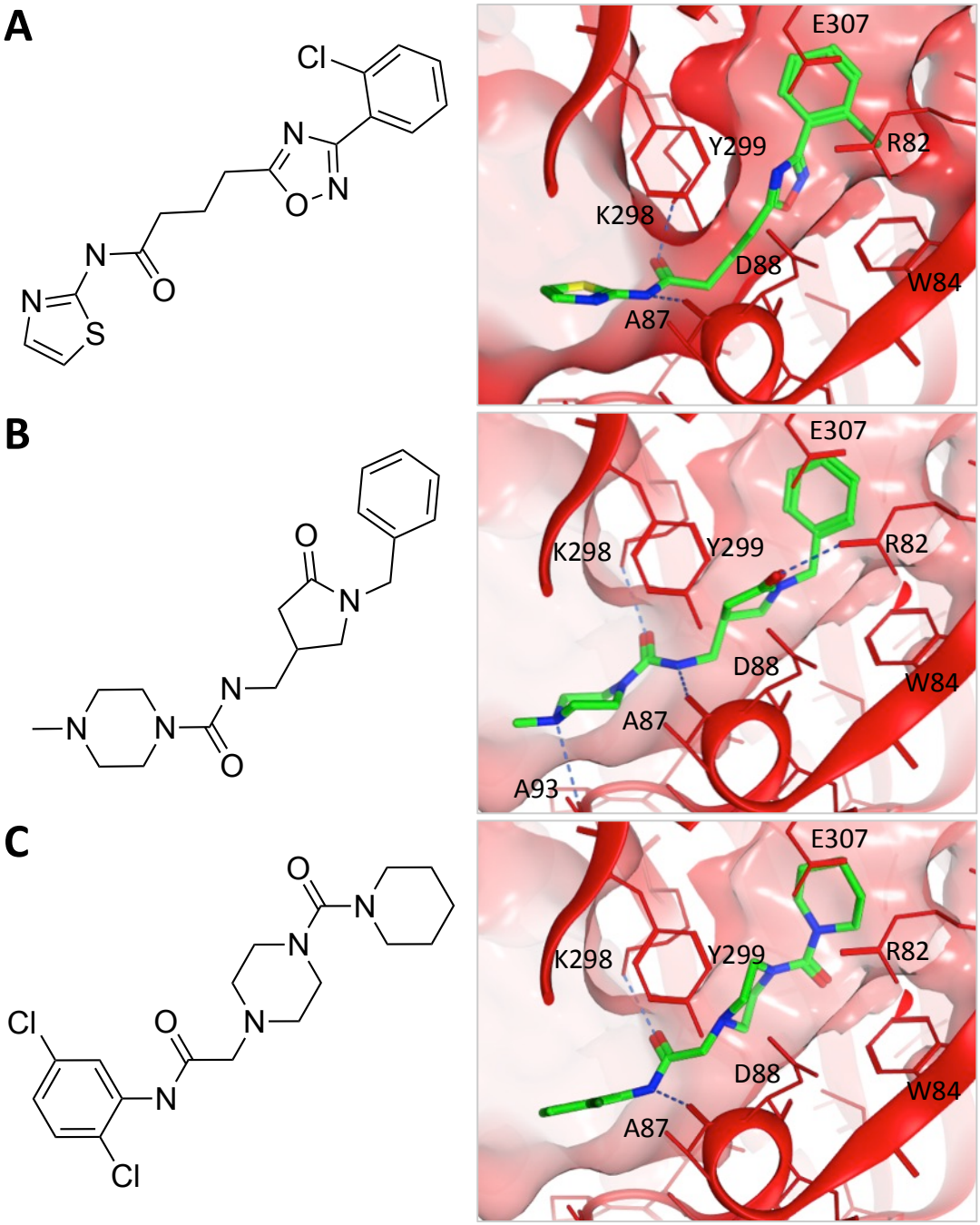

Figure 4-8: Dock of Compound 82 (AP-853/43405648, **A**), Compound 86 (AE-641/40262184, **B**) and Compound 89 (AP-124/42855935, **C**) obtained from the virtual screening and comprising examples comparing ligands binding either of the two different Lys-298 conformations (**A** versus **B, C**) used for the generation of the docking grid.

A retrospective check found that - although the structure of BX430 does not appear in the compound library sourced from SPECS (~300,000 compounds) and used in the virtual screening - a small proportion of structures belonged to the same class of compounds as BX430 (containing a carbamate moiety bound to a pyridine and/or a phenyl). Notably, among the 5% top-scored conformations (500 poses) obtained from the screening in the BX430 pocket, numerous compounds showed remarkable similarity to BX430 (selected example of such compounds are reported in **Table 4.4**). All these compounds docked in the deeper site of the cavity of the receptor bearing the Lys-298 as shown in **Figure 4-9** with a similar binding mode to that observed in the corresponding BX430 docked pose (dark grey for reference), which suggests that the BX430 pose situated deeper in the cavity might be more favoured.

ID	Structure	Specs ID	MW	Chemical Name
B01	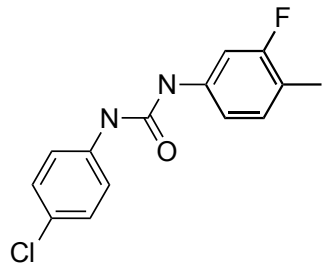	AN-329/ 40200574	278.71	N-(4-chlorophenyl)-N'-(3-fluoro-4-methylphenyl)urea
B02	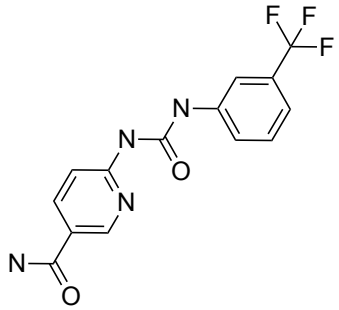	AI-204/ 31695001	324.26	6-(((3-(trifluoromethyl)anilino)carbonyl)amino) nicotinamide
B03	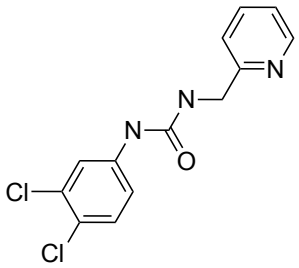	AI-204/ 31695053	296.16	N-(3,4-dichlorophenyl)-N'-(2-pyridinylmethyl)urea
B04	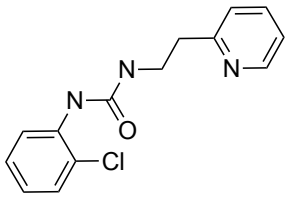	AI-204/ 31696018	275.74	N-(2-chlorophenyl)-N'-(2-(2-pyridinyl)ethyl)urea
B05	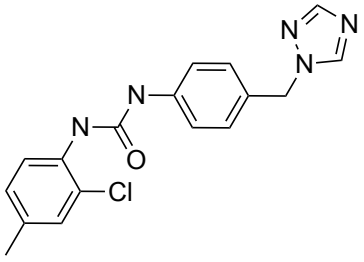	AT-057/ 43469652	341.8	N-(2-chloro-4-methylphenyl)-N'-(4-(1H-1,2,4-triazol-1-ylmethyl)phenyl)urea

Table 4.4: list of selected compounds that present similar structural features to BX430 and were among the 5% top-scored 10,000 poses obtained from the virtual screening.

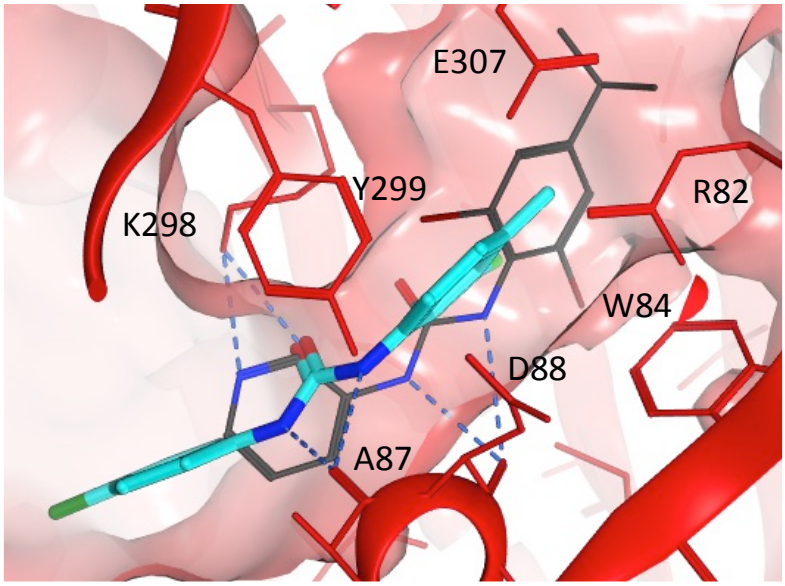

Figure 4-9: Dock of compound B01 (AN-329/40200574) in human P2X4 model. BX430 pose described in **Section 4.6** was superposed as reference (dark grey wires). H-bonds are depicted in blue dotted lines.

4.8 Chapter discussion

IVM has been proposed by *Davies et al.* as a potential treatment for alcohol dependence disorder acting at the CNS level (Franklin et al. 2015) (Roche et al. 2016). However there are multiple challenges and drawbacks for this therapeutic indication, for example IVM's low permeability through the blood brain barrier (Schinkel et al. 1997) (Turner et al. 2005), which is responsible for its good safety profile (otherwise worsened by IVM interaction at the GABAergic system in the CNS) (Menez et al. 2012). Nevertheless, IVM has been a pivotal pharmacological tool in the study of P2X receptors and its binding site has been extensively explored through mutagenesis studies. This work applied *in silico* tools (namely homology modelling and docking) to combine structural and mutagenesis data in order to describe the IVM binding mode in 3-dimensional molecular space. Our docked ligand agrees with the experimental data by fitting IVM in close proximity to 7 out of 9 amino-acids identified by *Silberberg et al.* (Silberberg et al. 2007) in a tryptophan mutagenesis study to be important for IVM activity. Futhermore, the docking simulation shows a potential interaction between the Asn-388 sidechain and the disaccharide moiety of the ligand. As reported in **Section 4.2**, we explored potential interactions when mutated to tryptophan – as the rat P2X4 N338W mutant investigated by *Silberberg et al.* maintained an IVM effect on current amplitudes similar to that observed forrat P2X4 wild-type (Silberberg et al. 2007). We found that IVM can entertain a potential H-arene interaction with the tryptophan, which is generally weaker than a hydrogen bond and may explain why IVM potentiation was comparable to that observed at rat P2X4 wild-type, while showing a lower ability to decrease receptor deactivation (Silberberg et al. 2007). Unfortunately the study conducted by *Silberberg et al.* did not further focus on the IVM effect on receptor deactivation. In order to test our hypothesis, we suggest the mutation of Asn-338 to a residue incapable of forming H-bonds or H-arene interactions (such as Ala, Val, Ile or Leu). This should significantly weaken IVM binding and therefore impact on IVM's ability to potentiate current responses at rat P2X4. We also propose that a combination of F33N, T333I, T334N, I341L, and F342L mutations at human P2X1 may confer IVM sensitivity to this subtype since a sequence alignment of the transmembrane domains revealed that human P2X1 has the highest sequence similarity to the IVM-sensitive subtypes.

The IVM binding site presents an atypical cavity – non-enclosed and of large volume – in a challenging location where lipids are closely interacting with the transmembrane domains and therefore potentially playing a crucial role in the ligand binding mode. A further limitation in simulating ligand binding between transmembrane domains is the lower structural resolution of the transmembrane region in the crystal, which may negatively impact on the accuracy of the model. These represent highly challenging pitfalls in the use of the IVM binding site for structure-based drug design and therefore, in this work, the focus has been directed to other potential allosteric sites.

The search for allosteric pockets in P2X4 receptor took full advantage of the recently published structures of giant panda P2X7 co-crystallised with 5 different allosteric antagonists (Karasawa and Kawate 2016). *Karasawa et al*. spotted that a corresponding pocket to the one discovered is detectable in the crystal structures of P2X3 and P2X4 although smaller (Karasawa and Kawate 2016). The hypothesis that BX430 binds to P2X4 in that pocket was tested through mutagenesis studies based on the different pharmacology that BX430 displays at human and rodents P2X4 (Ase et al. 2015). The observed difference in BX430 potency between the generated stable cell lines expressing rat P2X4 and human P2X4 wild-types is in line with the BX430 species-selectivity reported by *Ase et al*. (Ase et al. 2015). A single point mutation (I312T) at human P2X4 revealed to be responsible for a 49-fold reduction in BX430 activity according to the calculated IC_{50} measured by Ca^{2+} influx assay. Conversely, the corresponding point mutation (T312I) in rat P2X4 increased the potency of BX430 by 48-fold (compared to rat P2X4 wild-type), effectively making BX430 as potent as in human P2X4 wild-type. These results strongly support the hypothesis that BX430 binds in close proximity to Ile-312.

A docking simulation was employed in the attempt to explain the potential reasons for such an effect caused by a single point mutation. Two simulations were generated – one taking into account the flexibility of Lys-298, which may play a crucial role in determining the volume of the narrow tunnel-like cavity and the access to the upper vestibule of the channel. Both BX430 poses suggest that Ile-312 may directly stabilize the ligand through hydrophobic interactions with the hydrophobic and aromatic portion of BX430. The cavity is solvent-accessible and water molecules might be less favourably displaced in the presence of a polar residue (Thr-312 in rat P2X4) – providing an alternative explanation to BX430

species-selectivity. According to the docking, the major interactions between P2X4 and BX430 major interactions are 2 or 3 hydrogen bonds entertained between the carbamate and residue backbones and with Lys-298. The design of potential mutations that abolish BX430 activity is therefore challenging and might be accomplished by focusing on Lys-298, which appears to be spatially distant from the orthosteric binding site (according to both ATP-bound and apo-state models) and has not been reported as a residue interacting with ATP by *Hattori et al.* (Hattori and Gouaux 2012).

The positive outcome of the mutagenesis study that led to the identification of the BX430 binding site has enabled us to perform a virtual screening in the pocket and select 20 hit candidates for biological assay, which unfortunately could not be performed due to time constraints of this project. Interestingly, among the top scored structures obtained through the structure-based simulations, many show structural similarity to BX430. This further suggests, together with the mutagenesis study and the docking of BX430, that BX430 might bind to the identified pocket and that BX430 more favourably binds deeper in the tunnel-like pocket with the Lys-298 controlling the access to the upper vestibule of the channel.

Taken together the results strongly supports (i) the identification of an allosteric binding site in P2X4 not previously discovered and (ii) the discovery and validation of the binding site for one of the most potent P2X4 allosteric antagonists reported to date.

Unfortunately, due to limited time, this work only focuses on the identification and experimental validation of only one allosteric binding site, however the recent publication of the human P2X3 bound to AF-219 raises the question of whether a corresponding allosteric pocket might be found in P2X4 (Wang et al. 2018).

Chapter 5:

Identification of a novel P2X7 antagonist

5 IDENTIFICATION OF A NOVEL P2X7 ANTAGONIST

5.1 Chapter introduction

In evolutionary terms, P2X7 is closely related to P2X4 bearing ~48% amino acid sequence identity in human and the two genes are located only ~26 kBp apart in the same chromosome, thus *P2rx7* gene is likely to have originated by gene duplication (Buell et al. 1998; Dubyak 2007). Compared to the other receptor subtypes, P2X7 possesses an additional ~240 amino acids at the C-terminal, which may have resulted from a transposon insertion event involving a family member of the Kolobok transposons in a common vertebrate ancestor, leading to the fusion protein that is now termed P2X7 (Kapitonov and Jurka 2007). The much longer C-terminal domain – unique to the subtype 7 – is responsible for interacting with multiple proteins and strongly involved in trafficking and subtype-specific signalling pathways, mainly pro-apoptotic (http://www.p2x7.co.uk) (see **Section 1.4**). P2X7 activation in M1 macrophages leads to the activation of NLRP3 inflammasome, the rapid release of pro-inflammatory cytokines via microvescicle shedding and the activation of the immune response (Dubyak 2012; Kanneganti et al. 2007; MacKenzie et al. 2001). In pathophysiology, P2X7 plays a significant yet dualistic role in the destiny of the cell as seen in cancer cells and mouse embryonic stem cells (Thompson et al. 2012) where its activation has been linked both to increased proliferation – potentially when the ATP stimulation is at a basal level (Ferrari et al. 2017; Thompson et al. 2012) – and – when over-stimulated – to apoptosis with further activation of the immune system response (Garg et al. 2017; Savio et al. 2018; Thompson et al. 2012). Due to its complex involvement in cell signalling, P2X7 has been identified as potential target for multiple conditions including cancer (Gilbert et al. 2017), inflammatory and neuropathic pain (Honore et al. 2006), diseases and disorders of the central nervous system (Basso et al. 2009; Carmo et al. 2014; Csölle et al. 2013; Gubert et al. 2016; Jorg et al. 2014; Wang et al. 2017) and age-related macular degeneration (Fowler et al. 2014) (further details of the role played by P2X7 in pathophysiology can be found in **Section 1.4**). P2X7 pharmacology has been extensively explored and numerous classes of antagonists have been developed over the recent years (Gunosewoyo and Kassiou 2010) (see **Section 1.4**), including A804598, AZ10606120, GW791343, JNJ47965567 and A740003 - of interest for this work primarily because co-

crystallised with panda P2X7 receptor, shedding new light on allosteric modulation at P2X7 (Karasawa and Kawate 2016) and because A740004 has been employed as control in the course of this work. Bearing in mind that P2X7 is an attractive target and that the receptor share substantial structural similarities with P2X4, the original compounds obtained from the virtual screening conducted on P2X4 were tested also on P2X7 receptor.

5.5.1 BzATP

P2X7 subtype requires very high concentration of ATP for its activation, although a significant variability is observed in EC_{50} across subtypes, ranging from ~120 μM at rat to ~900 μM at mouse (Young et al. 2007). P2X7 is also strongly activated by 2′-(3′)-O-(4-benzoyl)benzoyl ATP (BzATP), a structural analogue of ATP with the addition of a di-benzoyl moiety substituting the –OH of the ribose either in position 2' or 3'. It was initially synthetized by Williams *et al.* and reported as single isomer (with substitution in 3') (Williams and Coleman 1982), however later characterization of the synthetic product reported a mixture of 2' and 3' in a 60:40 ratio (Mahmood et al. 1987) and it is commercially available as isomeric mixture. BzATP is only partially selective towards P2X7 as it has also been reported to be the full agonist at P2Y (Boyer and Harden 1989), P2X1, P2X2 and P2X5 (Bo et al. 2003; Evans et al. 1995) and a partial agonist at P2X4 (Bowler et al. 2003). Yet, at P2X7, BzATP causes larger responses - as observed by *Suprenant et al.* through whole-cell patch clamp experiments (Surprenant et al. 1996) - and is more potent than ATP (~3-fold more potent at mouse and 34-fold at rat). A surprisingly difference in pharmacology - though a very high amino acid sequence identity - was explored through the generation of chimeras and mutagenesis finally identifying Lys-127 as responsible for a much higher potency at rat P2X7, which may stabilise the distal benzoyl moiety through a π-cation interaction (Young et al. 2007). In **Section 5.9** we report the use of *in silico* tools (docking) to suggest BzATP binding mode and an interpretation and contextualization of experimental data.

5.5.2 YO-PRO uptake assay

As well as peculiar pharmacology, P2X7 presents also the distinctive characteristic of forming a large-conductance pore (also known as 'macropore') upon prolonged activation allowing the influx in the cytosol of large charged molecules (Di Virgilio et al. 2018). In normal conditions, living cells are non-permeable to YO-PRO – a fluorescent dye upon binding to DNA – therefore YO-PRO is commonly used to identify dead cells (Idziorek et al. 1995). The activation of P2X7 allows YO-PRO to enter directly through the large-conductance pore – as recently demonstrated by Karasawa *et al*. (Di Virgilio et al. 2018; Karasawa et al. 2017) - and thus the YO-PRO assay relies on the measurement of the rate in fluorescence intensity increase as indirect measure of the channel activation (Virginio et al. 1999).

5.2 Generation of human and rat P2X7-expressing cell lines

1321N1 cells expressing human P2X7 (EE-tagged) and HEK293 cells rat P2X7-GFP were generated by transfection and selection of single foci as previously described (see **Section 4.2** and **Section 2.1.2**). Single-cell clone WB50 (human P2X7) and A3E10 (rat P2X7) showed high protein expression and strong ATP responses as measured by YO-PRO assay and were therefore used in the experiments described in the following sections. **Appendix 3** contains more detailed information regarding selection of P2X7-expressing clones including protein expression level and ATP responses.

5.3 Agonist EC_{50} at human and rat P2X7

As observed by Surprenant *et al*. and Rassendren *et al*. (Surprenant et al. 1996) (Rassendren et al. 1997), P2X7 receptor is inhibited by concentration of divalent cations, however magnesium and calcium display species-dependent potency being 10-fold more potent at human P2X7 compared to rat. For this reason all experiments were conducted in low-divalent extracellular solution (ECS-LD). **Figure 5-1A** presents ATP dose response curves for stable cell lines expressing human and rat P2X7 subtypes as calculated *via* YO-PRO assay. ATP concentration applied ranged from 1 μM to 3mM for human subtype (from 1 μM to 1 mM ATP for rat). Calculated EC_{50} values (reported in Table 5.1) for both rat P2X7 and human P2X7 were consistent with those previously reported when buffer with low-divalent cation was used in the experiments (Young et al. 2007) (Stokes et al. 2006). To further check the functionality of rat P2X7 stable cell line in preparation for the experiment described in **Section 5.5.2**, a dose-response curve for BzATP was also measured (**Figure 5-1B**). The calculated EC_{50} of 8.1 μM fell within the previously reported range (4-10 μM) (Young et al. 2007) (Donnelly – Roberts et al. 2009).

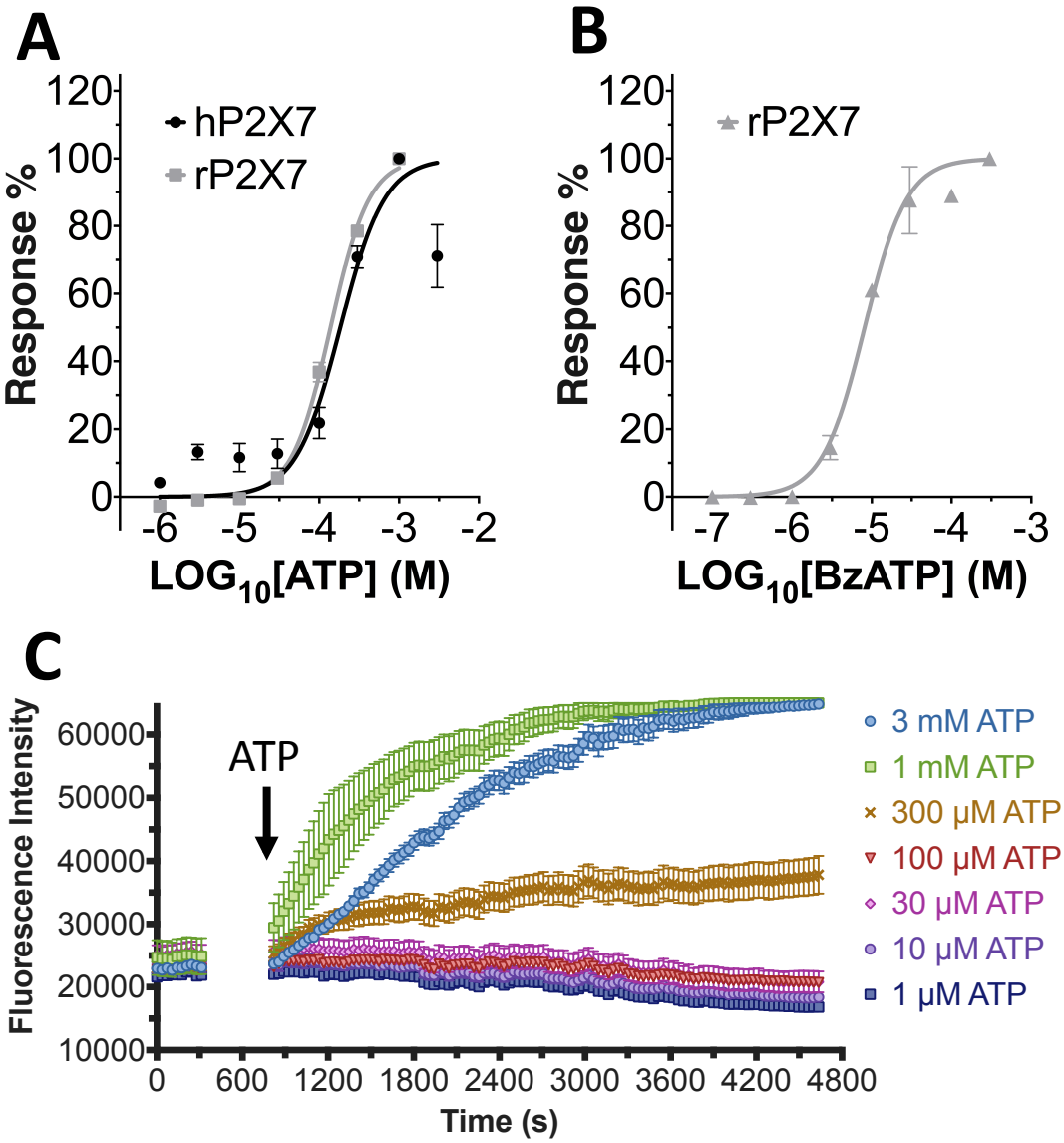

Figure 5-1: Agonist-induced YO-PRO uptake in cells expressing human (hP2X7) and rat P2X7 (rP2X7). **A.** Dose-dependent ATP responses expressed as dye uptake rate (gradient) measured by fluorescence increase and calculated over the first 10 cycles after addition of ATP (55 s/cycle) then normalized to the highest response values. Data merged from 2 or 3 independent experiments for each species tested (3-5 repeats/plate). **B.** BzATP-induced responses in rat P2X7. Data pooled from 2 independent experiments and normalized to the highest response obtained for each. **C.** Representative traces obtained for ATP concentration responses curve measured YO-PRO dye uptake at human P2X7 (raw data). After 10 recording cycles of baseline, the ATP was manually added to the plate (black arrow) and increased in fluorescence intensity was recorded.

ATP	EC_{50} (μM)	$LogEC_{50}$ (± SEM)	Hill slope
Human P2X7	183.5	-3.736 (± 0.07)	1.563
Rat P2X7	138.3	-3.859 (± 0.014)	1.785
BzATP			
Rat P2X7	8.1	-5.089 (± 0.036)	1.633

Table 5.1: ATP and BzATP EC_{50} values at human and rat P2X7. SEM: standard error of the mean.

5.4 Biological screening of compounds 1-42 on human P2X7

Due to the structural similarity and the high sequence identity between P2X4 and P2X7, the compounds from 1 to 42 (originally selected as potential candidate for P2X4) were also screened on human P2X7-expressing cells. **Table 3.5** reports the complete list of molecular structures and Specs IDs. **Figure 5-2** reports a single-experiment screening to determine whether 30 μM of compounds (20 minutes incubation) were able to decrease the cell responses elicited by 300 μM ATP by more than 50%. 0.1 μM A740003 was used as positive control to obtain an almost complete blockage of dye uptake. Surprisingly, multiple compounds reduced responses by more than 25% at 30 μM, while Compound 25 reduced ATP responses by over 60% and therefore was selected for confirmation and further characterization.

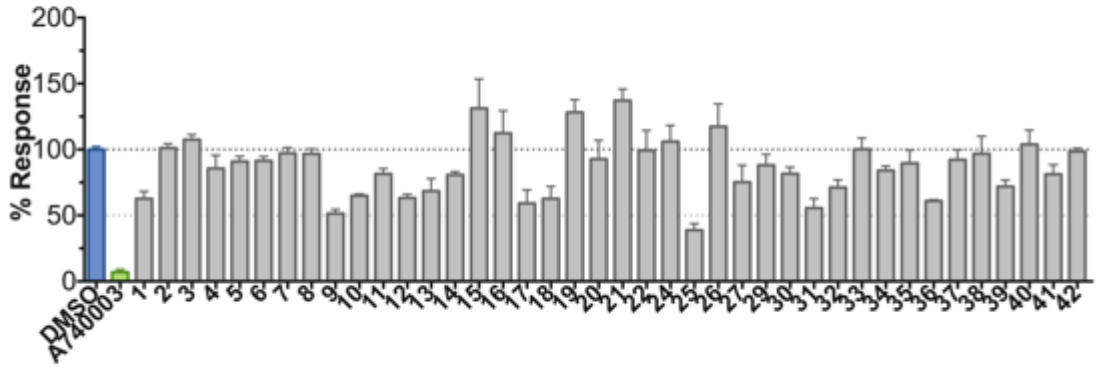

Figure 5-2: Screening of compounds 1 to 42 on human P2X7 through YO-PRO uptake assay. Compounds were incubated 20 minutes before application of 300 μM ATP (corresponding to approximately the concentration needed to elicit ~70% of the ATP maximal response). Responses were calculated as rate of fluorescence increase (gradient) over the first 10 cycles (55 seconds/cycle) and normalized to the vehicle (0.1% DMSO). 0.1 μM A740003 was used as positive control. Data represents a single experiment (n=3-4).

5.5 Compound 25 characterization

5.5.1 Compound 25 blocks YO-PRO uptake in human and rat P2X7-expressing cells

In 1321N1 cells stably expressing the cDNA encoding for human P2X7, Compound 25 exhibited a dose-dependent ability to decrease YO-PRO uptake rate elicited by 300 μM ATP, which approximately corresponded to the ATP EC_{70} value. The calculated IC_{50} value as result of 3 independent experiments was 8.7 μM (**Figure 5-3** and **Table 5.2**). The concentrations of Compound 25 used to determine the IC_{50} value ranged from 0.03 μM to 100 μM and the compound was pre-incubated for at least 20-30 minutes prior to the recording of the baseline. To assess any species-selectivity, Compound 25 was also tested on rat P2X7-expressing HEK-293 cells. Compound 25 blocked ATP responses (300 μM ATP, corresponding to the concentration needed in order to obtain ~80% of the ATP maximal receptor activation) with an IC_{50} value of 24.4 μM (see **Figure 5-3** and **Table 5.2**). The newly discovered antagonist displayed a ~3-fold higher potency at human receptor compared to the rat homologue however this difference in potency was not significant (p value = 0.0692, unpaired t test Welch-corrected for not assuming equal SDs, two-tailed P value).

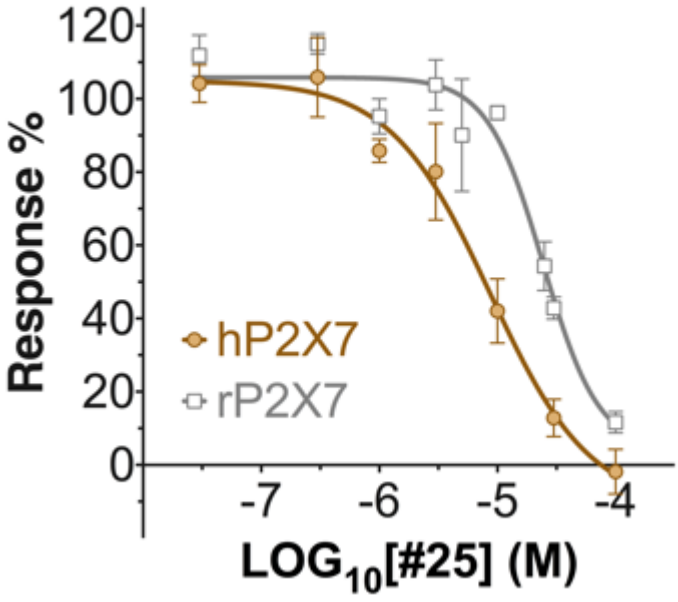

Figure 5-3: Dose-dependent antagonist effect of Compound 25 on dye uptake in human P2X7 and rat P2X7-expressing cells.

	IC_{50} (μM)	$LogIC_{50}$ (± SEM)	Hill slope
Human P2X7	8.7	-5.061 (± 0.167)	-1.026
Rat P2X7	24.4	-4.613 (± 0.082)	-1.847

Table 5.2: Compound 25 IC_{50} values at human and rat P2X7. Values calculated from 3 independent experiments. IC_{50} for human P2X7 was not significantly lower than rat P2X7 (p value = 0.0692, unpaired t test Welch-corrected for not assuming equal SDs, two-tailed P value). SEM: standard error of the mean.

5.5.1 Compound 25 blocks ion currents in rat P2X7-expressing cells

Whole cell patch clamp was employed to confirm the activity of the antagonist with an independent assay. Due to the intrinsic difficulties in patching 1321N1 cell due to their morphology, rat P2X7-GFP HEK-293 cells were used instead. **Figure 5-4A** shows representative traces for responses obtained applying 300 μM ATP with or without co-application of two different concentrations of Compound 25 (5 μM and 25 μM). Applications of 25 μM of Compound 25 - corresponding to ~EC_{50} value calculated through YO-PRO assay - significantly blocked membrane currents in response to ATP (**Figure 5-4B (Right)**, $p<0.05$, One-way ANOVA). These results

strongly confirmed the activity and the potency of Compound 25 as novel P2X7 antagonist.

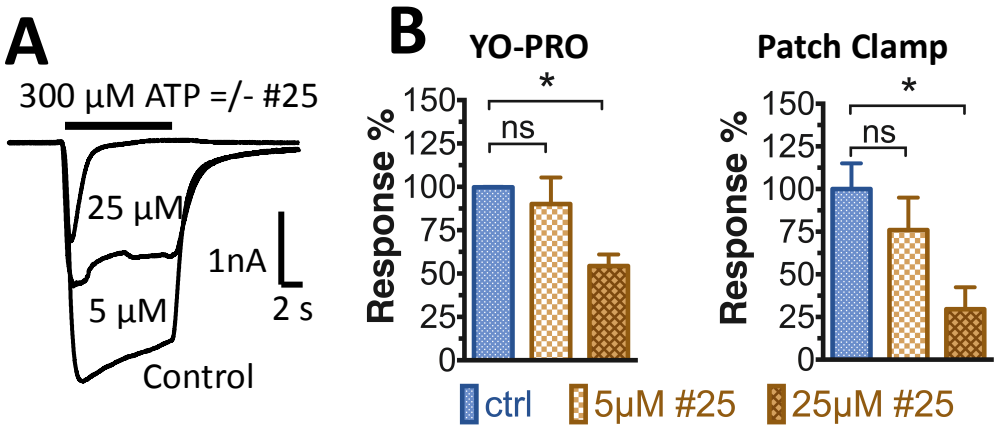

Figure 5-4: Inhibition of ATP response by Compound 25 ('#25' in this figure) in rat P2X7-expressing cells confirmed by two independent assays. **A.** Inhibition of ATP-evoked current by #25 in whole-cell patch clamp experiments (representative traces). **B.** Data summary of the inhibition effect measured through two independent assays (YO-PRO uptake, left; whole-cell patch clamp, right). YO-PRO data reported in **Section 5.5.1** is repurposed here for comparison. Whole-cell patch clamp experiments showed reduced currents with 5 µM #25 (n =7) and significant channel blockage with 25 µM #25 (n =5) compared with vehicle (0.1% DMSO, ctrl) with $p<0.05$ (One-way ANOVA followed by Dunnett's multiple comparison test).

5.5.2 Compound 25: allosteric or competitive?

Initially, Compound 25 was one of the molecules selected as result of a virtual screening in the ATP-binding site of human P2X4 homology model. However, its biological testing on human P2X4-expressing cells did not display any activity up to 100 µM - the highest concentration tested. This combined with the rather surprising antagonist activity of Compound 25 at human and rat P2X7 subtypes raised the question whether the binding site of Compound 25 is orthosteric or we made the serendipitous discovery of an allosteric modulator. To investigate in this direction, multiple concentration-response curves of BzATP for rat P2X7 in absence and in presence of increasing concentrations of compound 25 ranging from 10 µM to 100 µM were constructed, similarly to what has been described by *Karasawa et al.* (Karasawa and Kawate 2016). Each dose-response corresponding to a concentration of compound was measured through a single experiment (n=3).

These preliminary results were fitted with a competitive model as shown in **Figure 5-5A** and subsequently the calculated BzATP EC_{50} were employed to generate a Schild plot (**Figure 5-5B**). Compound 25 appears to show a competitive action, according to the good linear regression fit (R=0.9875). However, on close inspection of **Figure 5-5A** it is possible to notice that when cells were incubated with the highest concentration of Compound 25 the responses tend to be lower than the maximal response obtained in absence of antagonist. Hence suggesting that at very high concentration the non-linear fit using a competitive model is less reliable. More accurate experiments, including the use of human P2X7, are required for a better understanding of the mode of action of the antagonist. Currently, the preliminary data suggests that an allosteric mode cannot be completely excluded due to (i) the micromolar potency – that allows only the test of one-Log range of Compound 25 concentrations - and (ii) the low solubility of Compound 25 at 100 μM, which did not permit the assessment of higher concentrations.

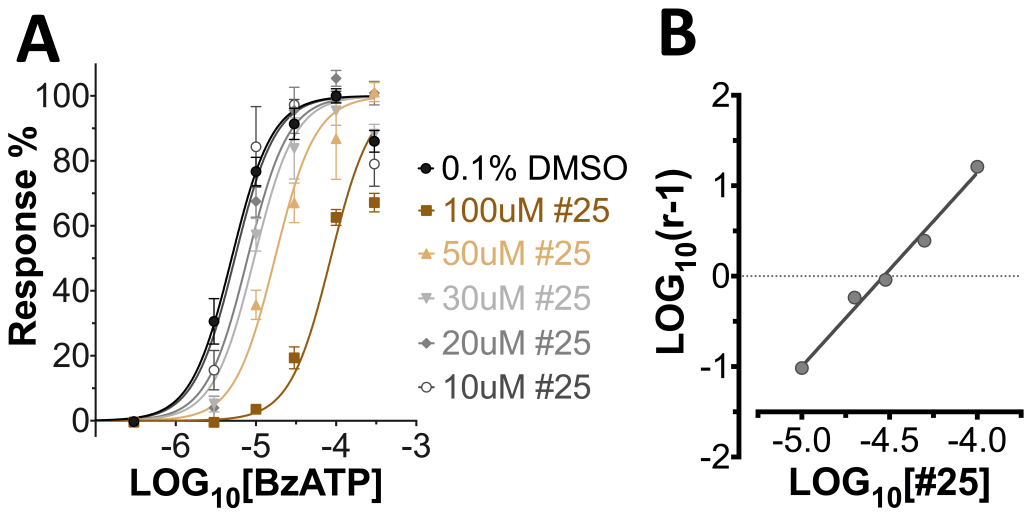

Figure 5-5: BzATP dose-response of rat P2X7-GFP in the presence of increasing concentrations of Compound 25 (#25). **A.** Percentage responses calculated as initial rates of YO-PRO uptake (first 10 cycles after agonist addition) and normalized to the maximal response obtained for the control (0.1% DMSO) were plotted and the dose-response curves were fitted with a competitive inhibition model (constraining top and bottom to 0% and 100% respectively, Hill Slope calculated collectively). Notably BzATP responses for cells incubated with 100 μM are notably lower than the maximal. Data obtained from a single-experiment (n=3). **B.** Schild plot obtained using EC_{50} calculated from the BzATP dose-responses in presence of antagonist (**A**) suggesting a competitive inhibition mode. Y axis represents the logarithm of (r-1), where $r=EC_{50}'/EC_{50}$; EC_{50}' is the BzATP EC_{50} calculated in presence of the antagonist while EC_{50} is the BzATP EC_{50} calculated in absence of the antagonist. A linear regression fit was applied (R=0.9875).

5.6 Activity of analogues at human P2X7 (compound 43-69)

Aiming at the identification of the chemical features necessary for compound activity, the Specs.net library was searched for molecules with a similar structure to Compound 25. The selection criteria included similar or same scaffold and presence of at least a functional group, which hypothetically contributed to Compound 25 activity (e.g. carboxylic acid, halogen substituent to the aromatic ring, ester, etc.). **Table 5.3** lists the 27 compound analogues selected (named herein Compound 43 to Compound 69), purchased and tested. At 30 μM, several analogues were able to substantially decrease the dye uptake induce by application of 300 μM ATP (**Figure 5-6A**, pooled data from 2 or more independent experiments). More than 4 analogues showed a response reduction of 50% or over. Compound 47 and compound 68 were among the molecules with higher potency therefore a single-experiment (n=4) was conducted to determine whether the inhibition was dose-dependent (**Figure 5-6B,C**). This was the case for both compounds, which showed an IC_{50} (preliminary) of approximately 30 μM and 5.2 μM, respectively.

ID	Structure	Specs ID	MW	Chemical Name
25	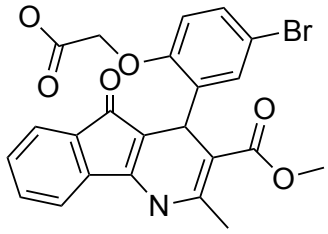	AH-487/ 14758206	484.30	(4-bromo-2-(3-(methoxycarbonyl)-2-methyl-5-oxo-4,5-dihydro-1H-indeno(1,2-b)pyridin-4-yl)phenoxy)acetic acid
43	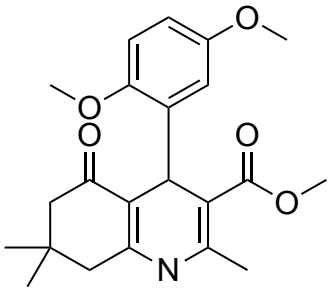	AG-690/ 36535013	385.46	methyl 4-(2,5-dimethoxyphenyl)-2,7,7-trimethyl-5-oxo-1,4,5,6,7,8-hexahydro-3-quinolinecarboxylate

44	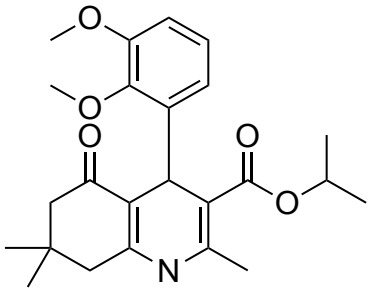	AG-690/ 36718061	413.51	isopropyl 4-(2,3-dimethoxyphenyl)-2,7,7-trimethyl-5-oxo-1,4,5,6,7,8-hexahydro-3-quinolinecarboxylate
45	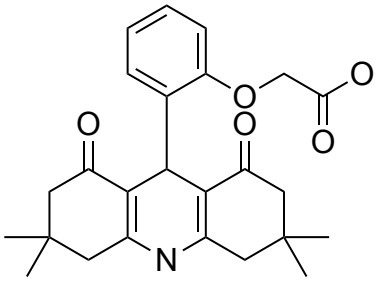	AK-968/ 15604330	423.51	(2-(3,3,6,6-tetramethyl-1,8-dioxo-1,2,3,4,5,6,7,8,9,10-decahydro-9-acridinyl)phenoxy)acetic acid
46	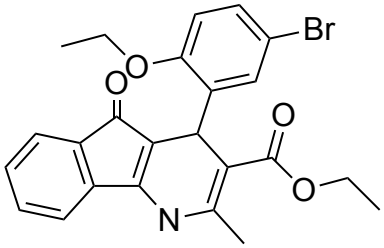	AH-487/ 15150556	468.35	ethyl 4-(5-bromo-2-ethoxyphenyl)-2-methyl-5-oxo-4,5-dihydro-1H-indeno(1,2-b)pyridine-3-carboxylate
47	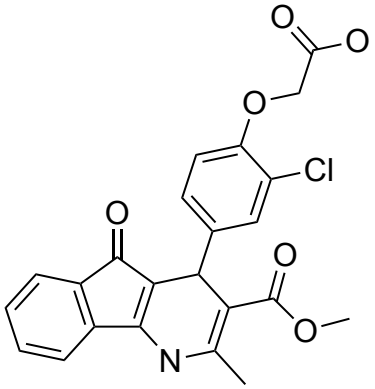	AH-487/ 14757970	439.85	(2-chloro-4-(3-(methoxycarbonyl)-2-methyl-5-oxo-4,5-dihydro-1H-indeno(1,2-b)pyridin-4-yl)phenoxy)acetic acid
48	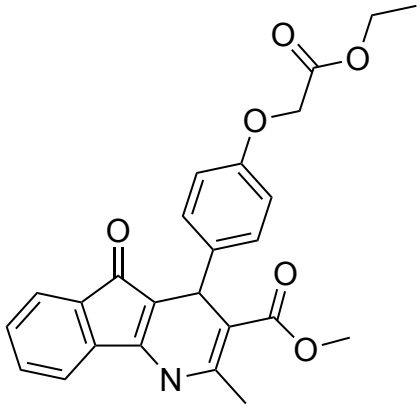	AH-487/ 14758229	433.46	methyl 4-(4-(2-ethoxy-2-oxoethoxy)phenyl)-2-methyl-5-oxo-4,5-dihydro-1H-indeno(1,2-b)pyridine-3-carboxylate

49	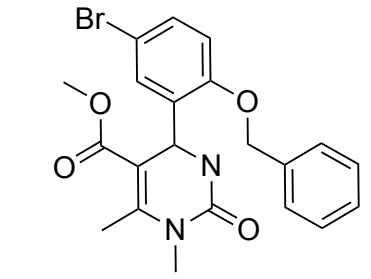	AN-655/ 14768403	445.31	methyl 4-(2-(benzyloxy)-5-bromophenyl)-1,6-dimethyl-2-oxo-1,2,3,4-tetrahydro-5-pyrimidinecarboxylate
50	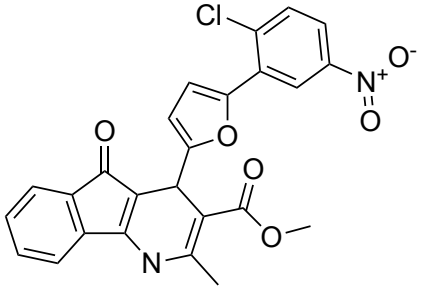	AG-690/ 40638872	476.87	methyl 4-(5-(2-chloro-5-nitrophenyl)-2-furyl)-2-methyl-5-oxo-4,5-dihydro-1H-indeno(1,2-b)pyridine-3-carboxylate
51	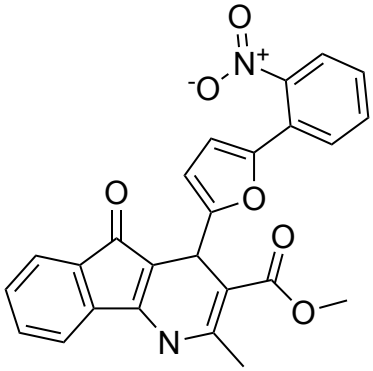	AG-690/ 40638873	442.43	methyl 4-(5-(2-nitrophenyl)-2-furyl)-2-methyl-5-oxo-4,5-dihydro-1H-indeno(1,2-b)pyridine-3-carboxylate
52	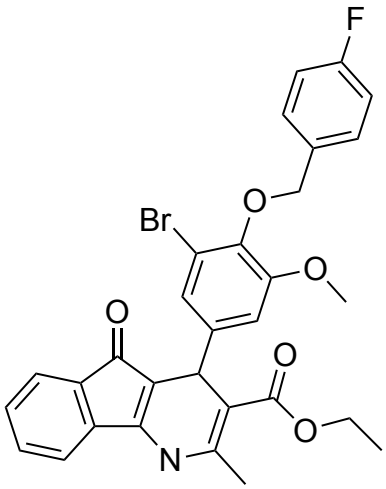	AN-988/ 40667255	578.43	ethyl 4-(3-bromo-4-((4-fluorobenzyl)oxy)-5-methoxyphenyl)-2-methyl-5-oxo-4,5-dihydro-1H-indeno(1,2-b)pyridine-3-carboxylate
53	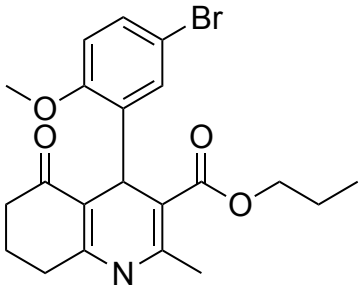	AG-205/ 40649486	434.33	propyl 4-(5-bromo-2-methoxyphenyl)-2-methyl-5-oxo-1,4,5,6,7,8-hexahydroquinoline-3-carboxylate

54	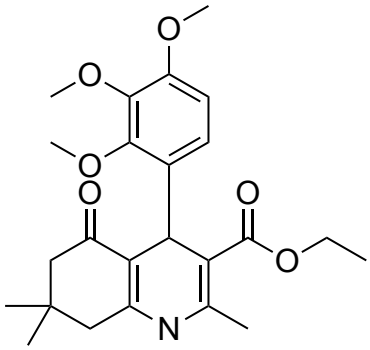	AG-690/ 10380042	429.51	ethyl 2,7,7-trimethyl-5-oxo-4-(2,3,4-tris(methyloxy)phenyl)-1,4,5,6,7,8-hexahydroquinoline-3-carboxylate
55	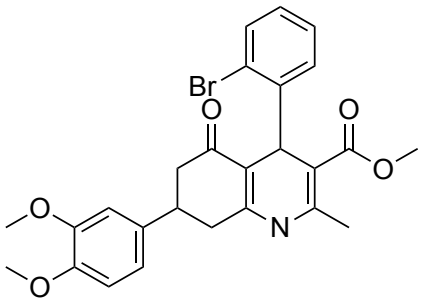	AG-690/ 40749289	512.4	methyl 4-(2-bromophenyl)-7-(3,4-dimethoxyphenyl)-2-methyl-5-oxo-1,4,5,6,7,8-hexahydro-3-quinolinecarboxylate
56	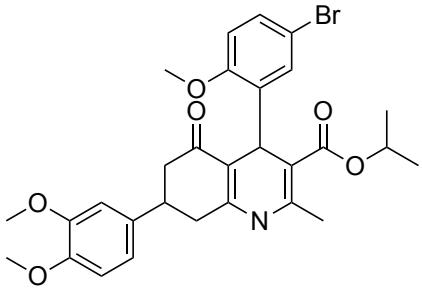	AG-690/ 40751831	570.48	isopropyl 4-(5-bromo-2-methoxyphenyl)-7-(3,4-dimethoxyphenyl)-2-methyl-5-oxo-1,4,5,6,7,8-hexahydro-3-quinolinecarboxylate
57	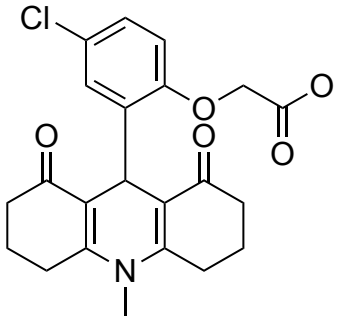	AM-879/ 42012121	415.87	(4-chloro-2-(10-methyl-1,8-dioxo-1,2,3,4,5,6,7,8,9,10-decahydro-9-acridinyl)phenoxy)acetic acid
58	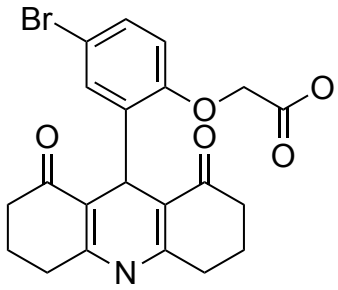	AM-879/ 42012369	446.3	(4-bromo-2-(1,8-dioxo-1,2,3,4,5,6,7,8,9,10-decahydro-9-acridinyl)phenoxy) acetic acid

59	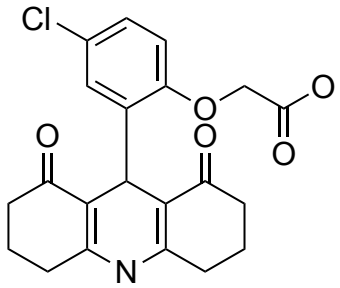	AM-879/ 42012458	401.84	(4-chloro-2-(1,8-dioxo-1,2,3,4,5,6,7,8,9,10-decahydro-9-acridinyl)phenoxy) acetic acid
60	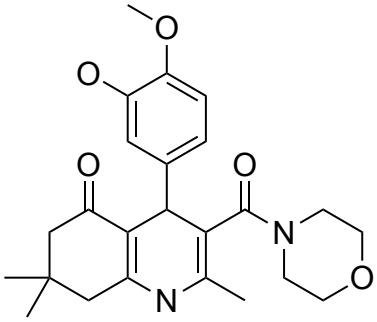	AE-848/ 42025036	426.51	4-(3-hydroxy-4-methoxyphenyl)-2,7,7-trimethyl-3-(4-morpholinylcarbonyl)-4,6,7,8-tetrahydro-5(1H)-quinolinone
61	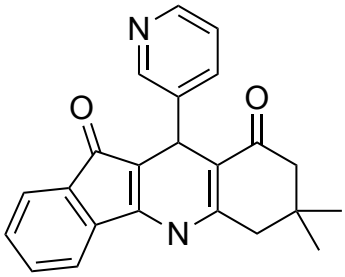	AJ-292/ 42032071	356.42	7,7-dimethyl-10-(3-pyridinyl)-6,7,8,10-tetrahydro-5H-indeno(1,2-b)quinoline-9,11-dione
62	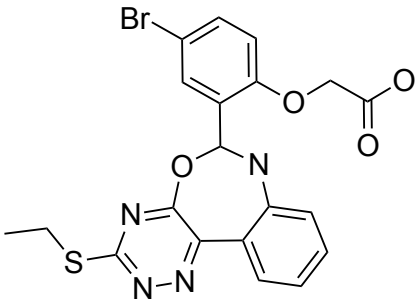	AK-968/ 11109126	489.35	(4-bromo-2-(3-(ethylsulfanyl)-6,7-dihydro(1,2,4)triazino(5,6-d)(3,1)benzoxazepin-6-yl)phenoxy)acetic acid
63	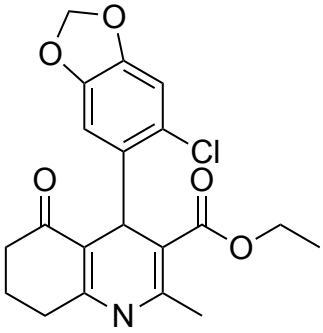	AG-205/ 11447043	389.83	ethyl 4-(6-chloro-1,3-benzodioxol-5-yl)-2-methyl-5-oxo-1,4,5,6,7,8-hexahydro-3-quinolinecarboxylate

64	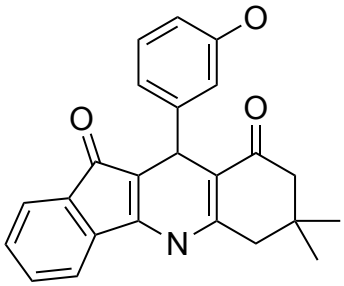	AJ-292/ 14827035	371.43	10-(3-hydroxyphenyl)-7,7-dimethyl-6,7,8,10-tetrahydro-5H-indeno(1,2-b)quinoline-9,11-dione
65	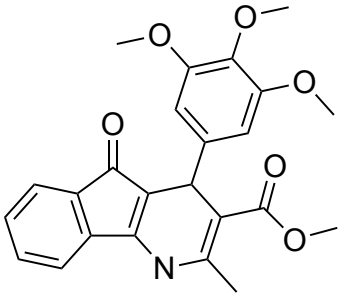	AH-487/ 14758041	421.45	methyl 2-methyl-5-oxo-4-(3,4,5-trimethoxyphenyl)-4,5-dihydro-1H-indeno(1,2-b)pyridine-3-carboxylate
66	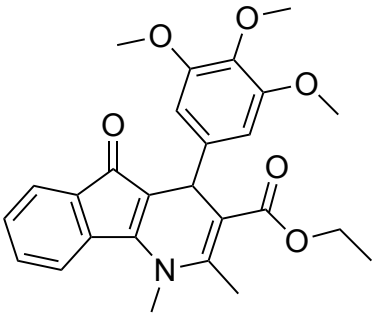	AK-454/ 40961396	449.5	ethyl 1,2-dimethyl-5-oxo-4-(3,4,5-trimethoxyphenyl)-4,5-dihydro-1H-indeno(1,2-b)pyridine-3-carboxylate
67	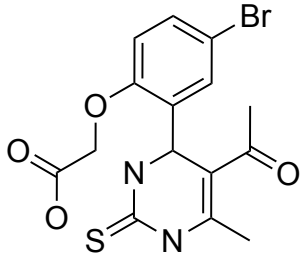	AN-655/ 41064474	399.27	(2-(5-acetyl-6-methyl-2-thioxo-1,2,3,4-tetrahydro-4-pyrimidinyl)-4-bromophenoxy)acetic acid
68	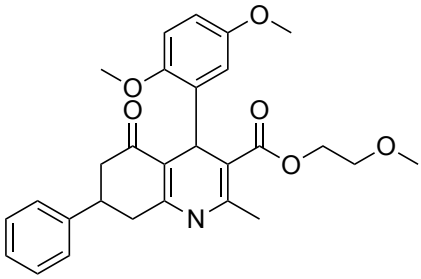	AG-690/ 12892844	477.56	2-methoxyethyl 4-(2,5-dimethoxyphenyl)-2-methyl-5-oxo-7-phenyl-1,4,5,6,7,8-hexahydro-3-quinolinecarboxylate

69	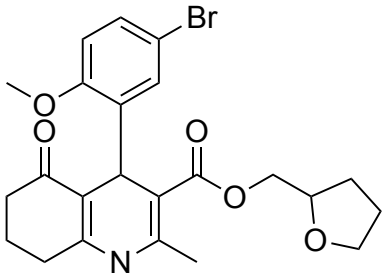	AG-205/ 15156184	476.36	tetrahydro-2-furanylmethyl 4-(5-bromo-2-methoxyphenyl)-2-methyl-5-oxo-1,4,5,6,7,8-hexahydro-3-quinolinecarboxylate

Table 5.3: Compound 25 analogues (Compound 43 to 69). Compound 25 is also included for reference.

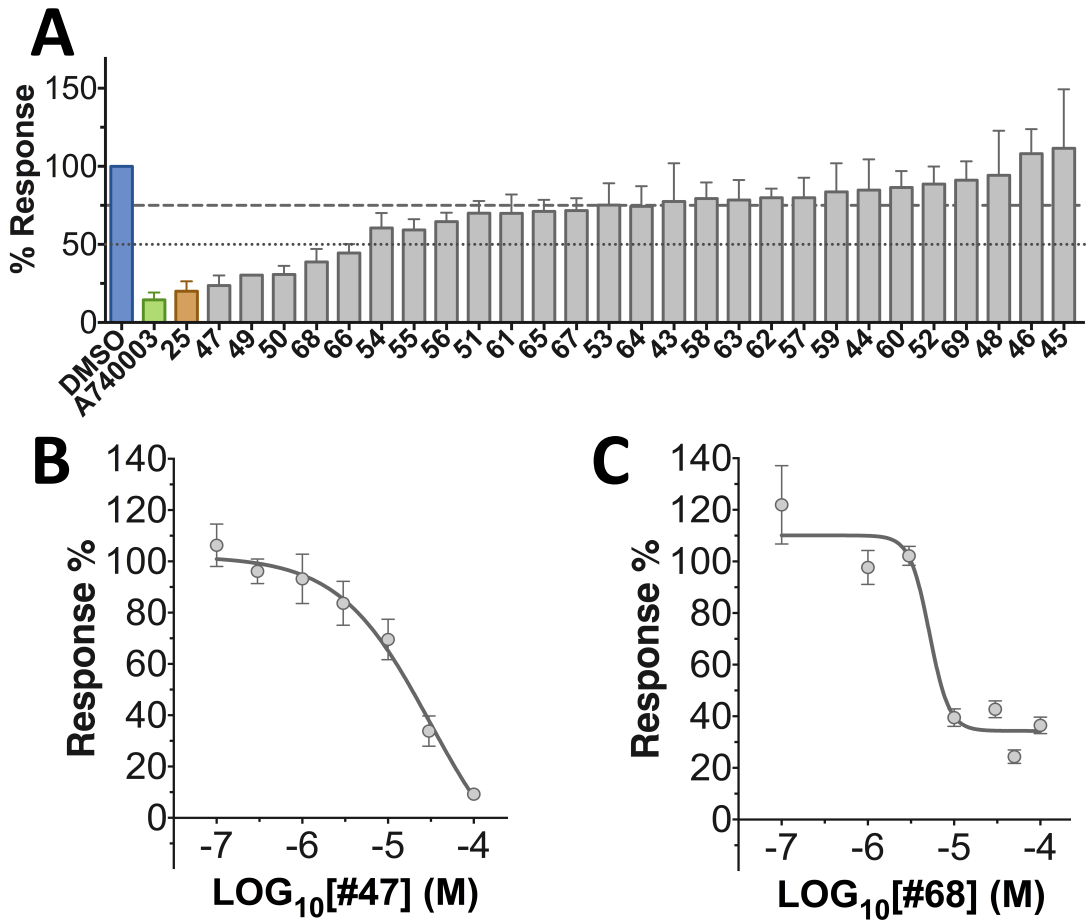

Figure 5-6: Antagonist activity of Compound 43-69 at human P2X7. **A.** Inhibition of ATP-induced (300 μM) cell response by 30 μM compound. 0.1 μM A74000s and 0.1% DMSO functioned as controls. Responses correspond to the gradient over the first 10 cycles after ATP addition (55 s/cycle) and are normalized to the DMSO (100% response). Compounds are in decreasing order (from left to right) according to their potency at 30 μM. and were considered weakly active if able to reduce responses by at least 25% (dashed line) and active if their inhibition was 50% or over (dotted). Data represents 2 or more independent experiments (n=3-4/each). **B, C.** Dose-inhibition curves for Compound 47 (**B**) and Compound 68 (**C**) (single experiment, n=4) with an approximated IC50 of 30 μM and 5.2 μM.

Overall - although the number of analogues tested was relatively low and only few of the desired substituents were available or present in the SPECS library - it was possible to build a basic Structure-Activity relationship (SAR) to identify some of the molecular features important for activity. 24 of the 27 analogues shared similar scaffolds, whose common structures are depicted in **Figure 5-7**. Scaffold IB is substantially similar to Scaffold IA differing only for the presence of a furanyl linker and it is presented separately for clarity purpose of the description. Most of the compounds that showed moderate or good activity shared a common scaffold (**Figure 5-7 IA-B** or **IV**). The presence of the methoxyl acetate as substituent (R_1) on the phenyl ring (Scaffold IA) seems important for compound activity as the substitution with a methoxyl (as for Compound 46, **Table 5.3**) completely abolished the activity. According to the IC_{50} calculated for Compound 25 (8.7 μM) and Compound 47 (~30 μM, single-experiment), the presence of the methoxyl acetate in *para*- was tolerated but the *ortho*-substituent was favoured. Halogen substituents in *meta*- position of the phenyl ring (Scaffold IA and IB) seem to improve activity and their absence (Compound 50 compared to Compound 51) may contribute to a reduced activity although the presence of a Bromine in Compound 46 was not sufficient to obtain an IC_{50} below 30 μM. The introduction of a furan linker between the dihydro-1H-indeno(1,2-b)pyridine-3-carboxylate and the phenyl moiety (Scaffold IB) was quite well tolerated provided the presence of an halogen in *ortho*- and a nitro-group in *para*-position (Compound 50).

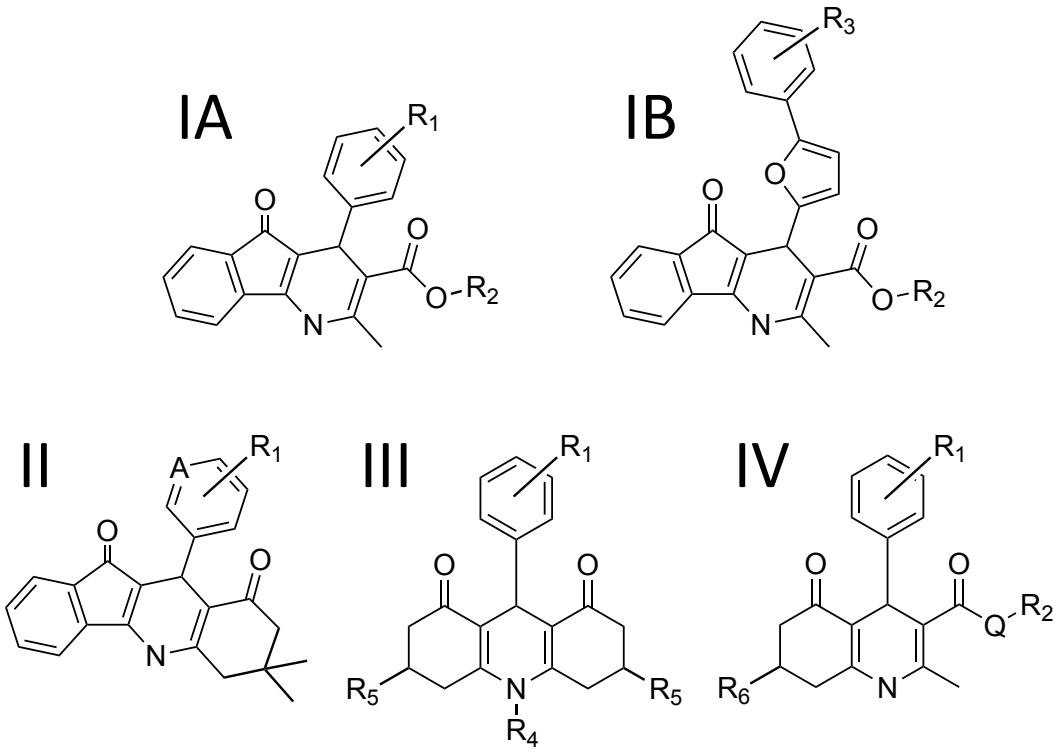

Figure 5-7: Common scaffold shared by 24 of the 27 analogues of Compound 25. Structure **Ia** and **Ib** differs only from the aromatic substituent (phenyl in **Ia**, or furanyl-phenyl in **Ib**) to the dihydro-1H-indeno(1,2-b)pyridine-3-carboxylate. R1: (1 or more) halogen, metoxyl, methoxyl acetate, etc. R2: methyl, ethyl, propyl, iso-propyl, methoxyethyl, tetrahydro-2-furanylmethyl, etc. R3: (1 or more) halogen, nitro. R4: H, methyl. R5: H, (2) methyl. R6: methyl, phenyl, dimethoxy-phenyl. A: C or N. Q: O or N.

No inhibition over ~25% was observed at 30 uM for compounds bearing the Scaffold II or Scaffold III, which may indicate that the substitution of the carboxylate to a cyclic ketone is not favoured. Interestingly, Compound 68 - that presents Scaffold IV – blocked YO-PRO uptake with a measured IC_{50} (preliminary) comparable to Compound 25. According to its structure, a metoxyethyl substituent at R2 is well tolerated and the presence of a phenyl substituent in R6 may be significant to the activity at human P2X7 (in comparison with Compound 43). Compound 68 - presenting 2 chiral centres - was purchased as racemic mixture with no knowledge of the enantiomers ratio and composition. It is possible that not all the enantiomers share the same activity and potentially, the isolation and test of each one of them alone could lead to the observation of a much higher potency.

5.7 Activity of analogues at rat P2X7 (compound 43-69)

In parallel to what described in **Section 5.5.1** for compound 17 to 42, the 27 analogues of compound 25 were also tested on cells expressing rat P2X7-GFP at the same concentration tested against human P2X7 (30 μM). Overall, compounds showed lower potency in reducing cell responses induced by 300 μM ATP, which might be partially attributed to a lower ATP EC_{50} at rat P2X7 receptor, therefore 300 μM approximately corresponded to EC_{80} rather than EC_{70}. However, as presented in **Figure 5-8**, the overall trend in compound activity was remarkably different and most of the compounds found active against human P2X7 showed almost no activity against rat homologue (exception made for Compound 68) whereas molecules such as Compound 69 showed selectivity towards rat over human receptor. Compared to compounds with which it shares the same scaffold (Scaffold IV, **Figure 5-7**. e.g Compound 68), Compound 69 does not bear a phenyl substituent in R6 position and presents at R2 the inclusion of the distal methoxyl group of the methyl-carboxylate in a 5-membered ring constituting a more hindered functional group with an additional chiral centre and a reduction in the number of rotable bonds. According to the biological tests, this is more tolerated by the rat P2X7 pocket. Conversely, the >50% inhibition of Compound 47 and Compound 50 (scaffold IA and IB, respectively) observed in human but not rat suggests that a difference in one or more amino acid residues in the pocket, lining nearby the phenyl (scaffold IA) or the furanyl-phenyl (Scaffold IB) may be responsible for species-selectivity. For the human receptor, large substituents in *para*- position or the furanyl linker are quite well tolerated whereas for rat homologues they are not.

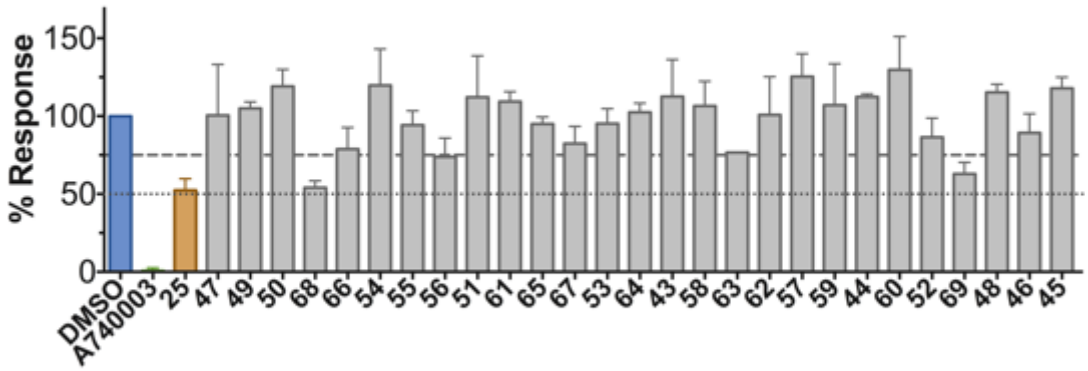

Figure 5-8: Screening of Compound 25 analogue on rat P2X7-GFP expressing cells. Data represents 2 or more independent experiments (n=3-4/each). Cells were pre-incubated 20-30 minutes with 30 μM compound before baseline measurement and following addition of 300 μM ATP. 0.1 μM A740003 and 0.1% DMSO served as controls. Responses were calculated as gradient for the first 10 cycles (55 s/cycle) and are presented as percentage response compared to the vehicle (DMSO). The compound order presented is the same as in **Figure 5-6A** to simplify the comparison of compound activity at human and rat receptor. As in **Figure 5-6A**, thresholds for active compounds (50% inhibition or over) and weakly active compounds (response reduction by 25% or over) are marked by dotted and dashed lines respectively.

Compound 68 was confirmed to be a hit both at human and rat homologues although as previously discussed it was tested as racemic mixture and no knowledge of which enantiomer(s) is responsible for activity and whether different enantioners show different specie-selectivity. In the attempt to suggest which enantiomer may interact more favourably with human P2X7 a number of *in silico* simulations were conducted and described in the following section.

5.8 *In silico* studies of Compound 25 and 68 in human P2X7 models

A 'blind docking' is usually employed to investigate potential binding pockets for a ligand when little or no biological data is known regarding its interaction site with the target. In this work, the blind docking has been employed as a less biased method to investigate potential binding sites for compound 25 and Compound 68, which were found active at human P2X7 however their binding site has not been confirmed by mutagenesis or extensive competitive binding assay (due to time limitations).

Homology models of human P2X7 were built with MOE aligning the amino acid sequence (Uniprot ID: Q99572) to either the panda P2X7 crystal structure in the closed state (PDB ID: 5U1L) or to Chain B of the ATP-bound panda P2X7 structure (PDB ID: 5U2H.B), then checked for gross geometry errors and finally prepared through Protein Preparation Wizard (Schrödinger Suite 2015-1 Protein Preparation Wizard; Epik, Schrödinger, LLC, New York, NY, 2018; Impact, Schrödinger, LLC, New York, NY, 2018; Prime, Schrödinger, LLC, New York, NY, 2018). Prior to protein preparation the two models were superposed in order to have comparable coordinates in the virtual molecular space. The structures of Compound 25 and 68 were prepared using LigPrep (LigPrep, Schrödinger, LLC, New York, NY, 2018) following the general procedure described in **Section 2.4.7**. As Glide does not support a specific and automated workflow for blind docking, a total of 122 receptor grids (32 $Å^3$) were manually created for each ecto-domain of the two models (apo state or ATP-bound) allowing overlapping between adjacent grids and having pair-wise identical centroids coordinates between the 2 models. Instead the Virtual Screening workflow (vsw) was employed as it allows multiple grids as input. As in this case the use of the vsw workflow was not to screen large library of compounds but rather semi-automate the docking on a large number of grids, the docking settings applied were quite conservative. The first HTVS step included the generation of 3 docked poses and retention of best 34% poses for the subsequent step - ideally obtaining the same number of poses as the number of confomers entered (both compounds presenting chiral centres and potential tautomers). The Standard Precision (SP) and the Extra precision (XP) steps aimed at re-docking and rescoring the poses with more accuracy maintaining all the

poses with good scores. 122 docking simulations (using reiteratively increasing precision from HTVS to XP) were conducted for each receptor state and results were merged, ranked according to the docking score and clustered for further comparison. Top ranked poses for Compound 25 could be grouped roughly in 2 sets according to the two most populated regions of binding with top ranked conformations. **Figure 5-9A** depicts the approximate location of these two regions showing Compound 25 in yellow or gold spheres, ATP (in black wires) and JNJ47965567 (in blue wires) were superposed as reference. The two regions correspond to the upper vestibule in direct communication with the pocket corresponding to the allosteric site identified by *Karasawa et al*. (Karasawa and Kawate 2016) and the ATP-binding site. In the first case, the poses – either located entirely within the vestibule or partially in the vestibule and partially protruding in the allosteric site - were mainly obtained by docking in the apo-form of the receptor while in the second instance the poses were obtained from docking simulations in the open state model. Notably, **Figure 5-9C** shows that multiple poses of Compound 25 docked in the ATP-binding pocket occupying the cavity roof defined by the head domain (pose in yellow) rather than the site that interacts with the ribose and the adenine moieties of the ATP (pose in gold, superposed ATP in black for reference).

Interestingly the top-scored poses for Compound 68 were strongly clustered in one single group, which included poses (i) entirely within the upper vestibule of the receptor and (ii) poses located in the allosteric binding site (Karasawa and Kawate 2016) and partially protruding towards the upper vestibule (**Figure 5-9B**). **Figure 5-9D** shows an example of high scored docked pose of Compound 68 fitting the allosteric binding site. Strikingly, no high scored poses - obtained neither from the apo nor from the open state - were found in the ATP-binding site.

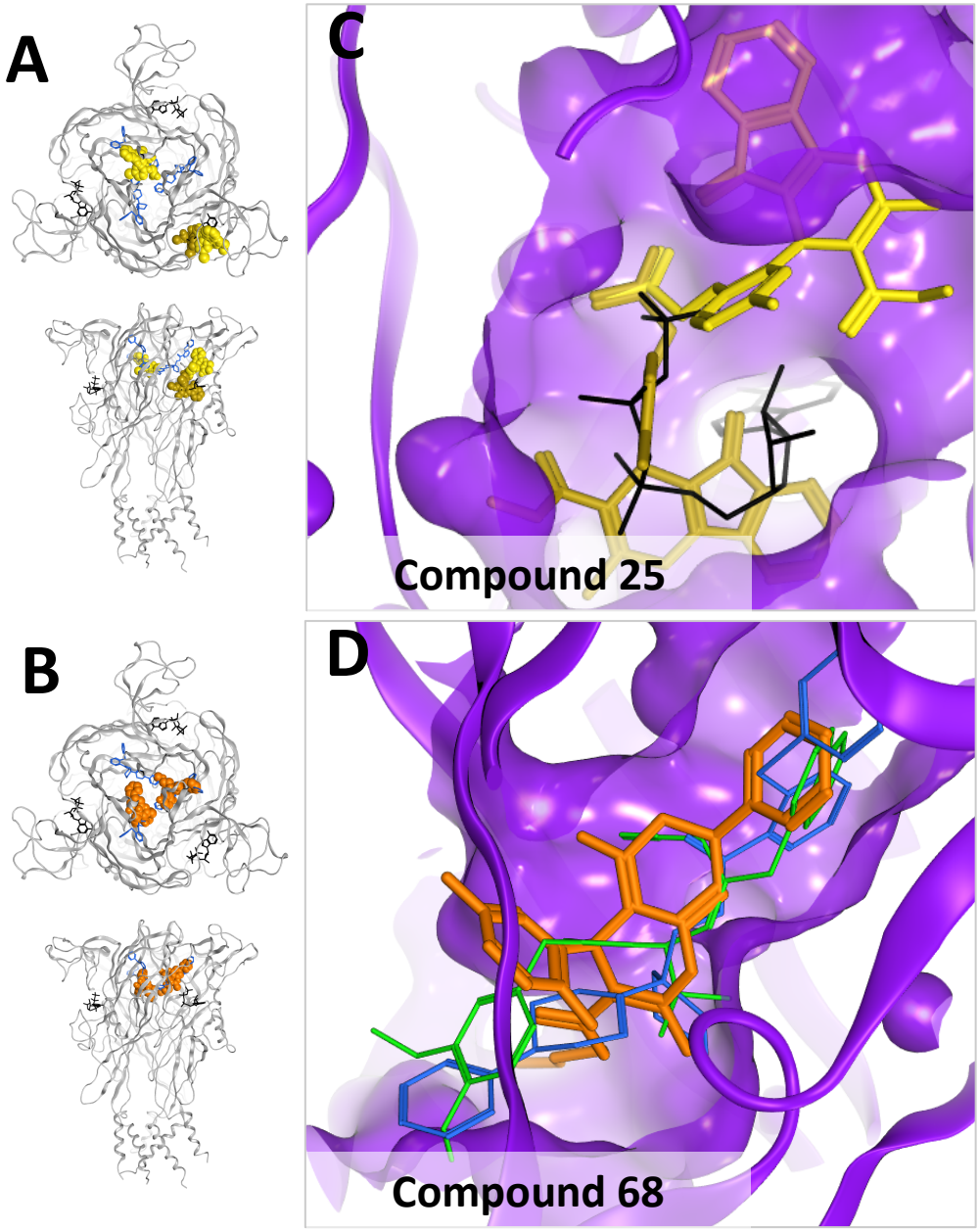

Figure 5-9: Blind docking of Compound 25 and Compound 68 in human P2X7 homology model. Top-ranked poses obtained from docking simulations conducted on 122 receptor grids (generated for the open and closed human P2X7 models) were clustered into different populations according to the region of binding. Representative of these populations are depicted in spheres in yellow and gold (**A** and **C**, Compound 25) and in orange (**B** and **D**, Compound 68). Superposed ATP (in black wires) and JNJ47965567 (in blue wires) in **A-D** are employed as reference for the location of the ATP-binding site and the allosteric binding pocket, respectively. **C.** Pocket view (ATP-binding site) with two docked conformations of Compound 25. **D**. Docked Compound 68 in the allosteric binding site (Karasawa and Kawate 2016) in comparison with superposed JNJ47965567 and A740003 (in blue and green wires, respectively).

As the dock of Compound 68 surprisingly showed strong preference for the allosteric site identified by Karasawa et al. (Karasawa and Kawate 2016) (**Figure 5-9D**), the next hypothesis was that a superposition between the structures of the 5 allosteric antagonists co-crystallised in the panda P2X7 receptor (A740003, A804598, AZ10606120, JNJ47965567 and GW791343) and Compound 68 may reveal important shared features. Structures of panda P2X7 bound to each of the 5 antagonists were superposed, the receptor structures were removed and the 5 superposed antagonist molecules were analysed with the Pharmaphore Consensus tool (MOE) generating pharmacophore descriptors for features present in at least 2 of the 5 structures. **Figure 5-10** presents the pharmacophore features (depicted as green and cyan spheres and labelled F1 to F6) superposed to Compounds 68 structure. Some spheres include functional groups of Compound 68 with the same properties of the corresponding pharmacophore features. For example, F3 and F4 denote areas occupied by hydrophobic groups (Hyd) of at least 3 of the panda P2X7 antagonists and overlap with a phenyl and a methyl group of Compound 68, respectively. F5 and F6 (partially), both indicating an H-bond acceptor group (Acc), is also a common feature shared with Compound 68 (or located within ~2 Å). According to the pharmacophore model reported in **Figure 5-10**, the activity of Compound 68 might be increased by the introduction of a H-bond acceptor substituent to the phenyl group to satisfy Feature F2 (currently not satisfied).

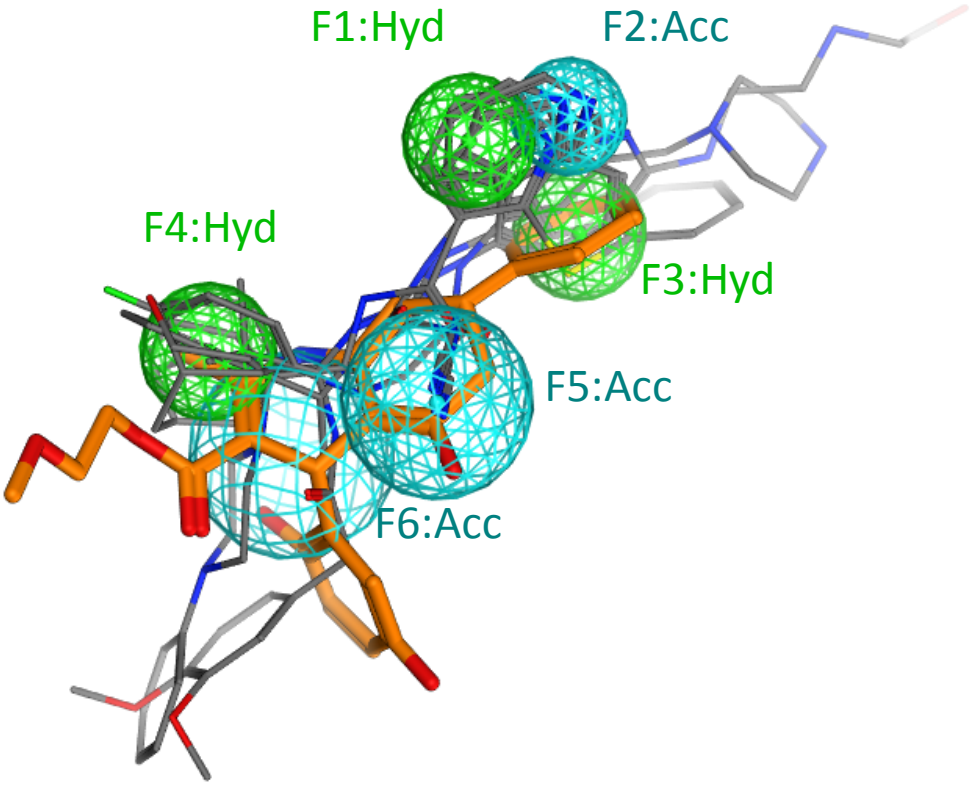

Figure 5-10: Ligand-based pharmacophore highlighting common features among P2X7 antagonists co-crystallised in panda P2X7 and comparison with Compound 68. Pharmacophore features in common among 2 or more structures (named F1 to F6). Acc: H-bond acceptor feature. Hyd: hydrophobic centre.

5.9 Dock of BzATP in mouse P2X7 mutant A127K

Docking was employed to investigate a molecular justification for the large difference in BzATP potency at rat and mouse P2X7 in line with the experimental data and the hypothesis proposed by Young *et al*. (Young et al. 2007). A model of mouse P2X7 (Uniprot sequence: Q9Z1M0, modified) bearing the A127K mutation was built with MOE (MOE 2014.10; Chemical Computing Group ULC, 1010 Sherbooke St. West, Suite #910, Montreal, QC, Canada, H3A 2R7, 2018) employing the panda P2X7 crystal structure bound to ATP as a template (PDB ID: 5U2H, chain B) and following the general procedure described in **Section 2.4.2**. The model was assessed then prepared for docking using protein preparation Wizard (Schrödinger Suite 2015-1, Protein Preparation Wizard; Epik, Schrödinger, LLC, New York, NY; Impact, Schrödinger, LLC, New York, NY; Prime, Schrödinger, LLC, New York, NY), while both isomers where are you using MOE Builder tool and parameterized with LigPrep (Schrödinger, LLC, New York, NY). Ligands were docked with Glide XP in the orthosteric binding site within a receptor grid of 38 $Å^3$ centred on superposed ATP from the crystal (in dark grey wires in **Figure 5-11**). Conformations obtained – for both isomers – showed the distal aromatic ring of the benzoylbenzoyl moiety in proximity of Lys-127 suggesting that a pi-cation interaction is possible (colored in blue in **Figure 5-11**). The dock of isomer 2' resulted in a confirmation extremely similar to ATP including the position of the gamma phosphate and entertaining strikingly similar interaction to ATP (**Figure 5-11A**). In the case of isomer 3' the particular U-shape was not retained (**Figure 5-11B**).

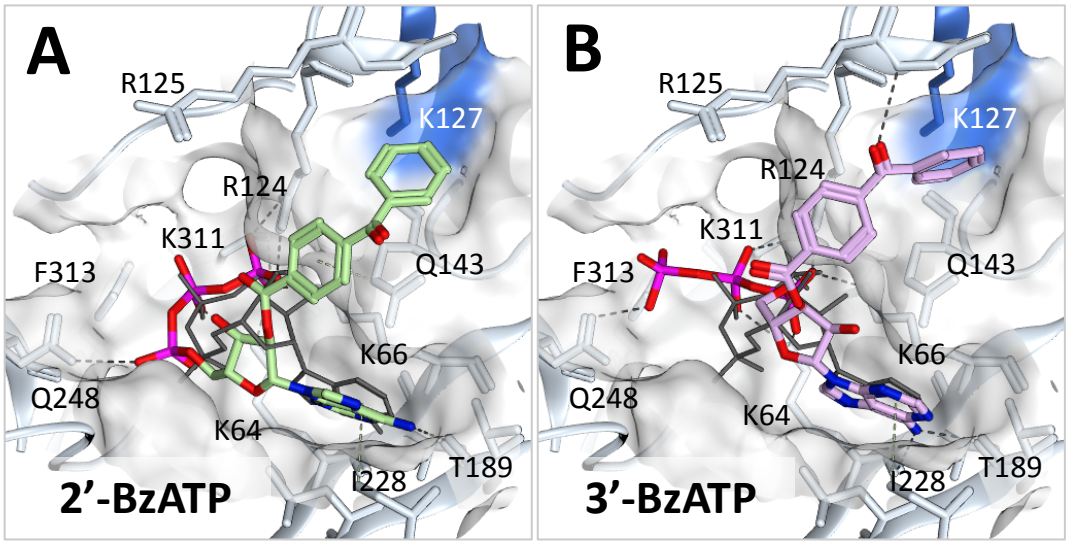

Figure 5-11: dock of BZ ATP into mouse P2X7 A127K mutant model.

5.10 Chapter discussion

Compounds from 1 to 42 were originally discussed in **Chapter 3** as results from two virtual screenings on human P2X4 orthosteric binding pocket, which unfortunately provided no active hits. These same compounds were tested on human P2X7 resulting in the identification of multiple active compounds at 30 μM. Compound 25 was selected for further characterization being the most active with an IC_{50} of 8.7 μM in subsequent experiments. Its activity was also observed at rat P2X7 although the IC_{50} resulted 3-fold higher (24.4 μM). ATP-induced membrane currents were blocked by co-application of 25 uM Compound 25 in rat P2X7-GFP expressing cells strongly confirming the antagonist activity observed in YO-PRO assay. From preliminary investigation, Compound 25 appears to inhibit BzATP responses in a competitive manner although at high concentrations the maximal responses is never reached. More thorough experiments are needed although the solubility of the compound (<100 μM) combined with an IC_{50} in the low micromolar range may limit to test of a wide range of concentrations. 27 analogues were selected based on similarity with Compound 25 structure helping in the study of the structure-activity relationship (SAR). Although relying on the purchase of compounds as source of analogues does limit the number and the choice of structures to be tested, it was possible to determine some of the features that may contribute to the antagonist activity of Compound 25, 47, 50 and 68. Aiming at increasing activity and compound drug-likeness, we also suggest the test of very similar scaffolds (to Scaffold I and IV, **Figure 5-7**) with either completely saturated bonds or entirely heteroaromatic to reduce the potential reactivity ought to the presence of an α,β-unsaturated carbonyl group.

Compound 25 inactivity at human P2X4 (as shown in **Chapter 3**) and conversely the activity at human p2x7 was particularly interesting in terms of structure-activity relationship given the fact that Compound 25 scaffolds shows similarity to a series of compounds patented by Sunovion Pharmaceuticals Inc. and described as P2X4 anatgonist with nanomolar potency (Newcom and Spear 2015). Most structures reported by *Newcom et al*. present substituents at the phenyl in ortho-position and lack of chiral centre (therefore enhanced planarity) due to the hetero-aromatic scaffold. It may be interesting to test Compound 25 analogues on human P2X4 to investigate the presence of features that may confer subtype-

selectivity. To our knowledge the compounds presented by Newcom *et al*. have never been reported in any scientific journal and their binding site is currently unknown although the patent briefly alludes to an allosteric mechanism of inhibition (Newcom and Spear 2015).

A preliminary assessment of mechanism of action conducted on Compound 25 has not resolutely ruled out an allosteric mode of action. A thorough mutagenesis study would be needed for this purpose, although due to time limitations a blind docking has been used as initial tool to probe potential binding sites. An example of blind docking use in the purinergic field was presented by *Allsopp et al*. as preliminary and less biased tool to probe where the antagonist was more likely to interact (Allsopp et al. 2017). In this work, a blind docking was conducted for Compound 25 and Compound 68 on both the apo and the ATP-bound state of the human P2X7 model and the top-ranked poses were analysed. Intriguingly, while multiple potential binding sites were found for Compound 25, Compound 68 preference for the allosteric binding site corresponding to the site identified by Karasawa *et al*. in panda P2X7 (Karasawa and Kawate 2016) was striking. A ligand-based pharmacophore based on the superposition of the 5 antagonists co-crystalised with panda P2X7 (Karasawa and Kawate 2016) was then superposed to the docked pose of Compound 68. This highlighted the presence of common features between the published antagonists and Compound 68 and could be a useful tool to further suggest scaffold modifications and or functional groups substitutions/additions to Compound 68 structure aiming at potency increase.

Contrary to the compounds tested in this Chapter – where still little is clear regarding their binding site, plenty of experiments have been conducted with BzATP to determine the binding site. Here we presented the dock of BzATP for both isomers observing conformation that supports the hypothesis of the formation of a π-cation interaction with Lys-127 (Young et al. 2007). Lys-127 was previously found by *Young et al*. to be responsible for the increased potency of BzATP at rat P2X7 (Young et al. 2007). To our knowledge it is not known which isomer is more potent. According to our docking, isomer 2' seems the one capable of better retaining ATP conformation and interaction seen in the crystal (Hattori and Gouaux 2012) and therefore we suggest it might be the most potent between the two isomers. Testing each of the purified isomer is needed to validate this hypothesis. In 2015, an *in silico* study of BzATP binding mode was presented by

Dal Ben et al. (Dal Ben et al. 2015). In comparison, our BzATP poses show similar location of the adenine and of the triphosphate (in the case of the 2' isomer) but substantial differences in the conformation of the benzoyl-benzoyl moiety. According to *Dal Ben et al*. (Dal Ben et al. 2015), the benzoyl-benzoyl moiety is plausibly stabilized by aromatic and hydrophobic residues including Phe-288 (Tyr-288 in human), Phe-218 and Ile-214. However their dock does not show any involvement of Lys-127, which has instead been strongly and elegantly supported by experimental data (Young et al. 2007).

Chapter 6:

Conclusions and future directions

6 CONCLUSIONS AND FUTURE DIRECTIONS

During the course of this work, the activity of potential P2X4 and P2X7 antagonist candidates has been evaluated and the pharmacological properties of a known P2X4 antagonist and a novel P2X7 antagonist were investigated. The most important findings and achievements of this work are summarized below:

- The differential potency of BX-430 at rat and human P2X4 was confirmed and provided the basis for the discovery of the BX-430 allosteric binding pocket *via* mutagenesis and functional assay.
- A virtual screening was conducted in the identified BX-430 pocket and a list of hit candidates has been selected for future biological evaluation.
- Multiple compounds, initially selected as 'hits' from virtual screening in human P2X4, were found to be active at human P2X7 with micromolar potency, leading to the characterisation of Compound 25, a novel P2X7 antagonist.
- *in silico* docking simulations were used to (i) provide a molecular basis for differential BzATP potency at rat and mouse P2X7 from a structural analysis of the mouse P2X7 A127K mutant and (ii) provide a plausible binding mode for ivermectin at rat P2X4 which was in good agreement with published pharmacological data.

This chapter gives a synopsis of the work conducted and − at the end of each of the following sections – proposes directions for future experiments and outlines hypotheses that have arisen during the course of this work.

6.1 Attempts to identify a novel competitive P2X4 antagonist

Efforts to identify a novel P2X4 competitive antagonist were unsuccessful. Indeed, none of the 42 compounds identified through two rounds of virtual screening were significantly active at 10 μM (Compound 23 was tested at 2 μM, due to low solubility). The negative results could be explained by a number of factors varying from inaccuracies in the homology model or hit selection, to not having tested a sufficient number of compounds. However the 'hit' candidates were selected independently in two rounds of screening (carried out by Dr Marcella Bassetto and the author of this thesis) and two different homology modelling softwares were employed to generate the models, reducing the margin for human error. Additionally, the group of LinHua Jiang demonstrated the effectiveness of a structure-based approach by identifying hit compounds active against human P2X7 (Caseley, Muench, Fishwick, & Jiang, 2016) and highlighted the direct application of *in silico* tools to the drug discovery of P2X antagonists. The absence of reported P2X4 competitive antagonists (compared to antagonists selective for other subtypes (Mansoor et al., 2016)) may suggest a structural reason peculiar to this subtype for the increased difficulty in finding ligands that 'fit' the ATP-binding site.

However, while initially discouraging, this result sparked a series of new experiments which led to: (i) the exploration of alternative (allosteric) binding sites and (ii) the assay of the same 42 compounds (and more) at human P2X7, which led to the identification of a novel P2X7 antagonist with micromolar potency.

6.2 Exploring allosteric binding sites in human P2X4

The design of novel human P2X4 antagonists was approached from a different angle. Rather than searching for a competitive ligand, the focus moved to P2X4 allosteric pockets, which led to a complication: although most P2X4 antagonists show an allosteric mechanism of action (Ase, Honson, Zaghdane, Pfeifer, &

Séguéla, 2015; Hernandez-Olmos et al., 2012; Matsumura et al., 2016; M. Wang et al., 2017), no allosteric pocket had been reported before besides the ivermectin binding site. The ivermectin binding site has been identified through mutagenesis to lie between transmembrane domains, which (due to the large size of the pocket, the lack of resolution in the crystal structures, and the lack of information about the lipid conformation in this region of the protein) precludes its use in structure-based drug design. Therefore the identification of a second allosteric binding site at human P2X4 had become pivotal to the project. The recent report of the allosteric pocket in panda P2X7 using direct structural data (Karasawa & Kawate, 2016), combined with the pharmacological data for the commercially available allosteric P2X4 antagonist BX430 (Ase et al., 2015), suggested the potential presence in human P2X4 of a binding pocket corresponding to the one identified by Karasawa *et al*. This hypothesis was confirmed by analyzing the difference in pharmacology of the single point mutant I312T at human P2X4, which revealed to be responsible for a greater than 40-fold reduction in BX430 activity with a calculated IC_{50} >100 μM compared to an IC_{50} of 2.2 μM measured for human P2X4 wild-type. The 'mirror' point mutation (T312I) in rat P2X4 decreased the IC_{50} to 1.4 μM, a value comparable to human P2X4 (over 40-fold more potent than at rat P2X4 wild-type), further supporting the hypothesis that BX430 binds in proximity of Ile-312. This important discovery led to a new virtual screen and a selection of 20 potential 'hits', whose biological activity can be assayed in future work.

The latest solved crystal structures reporting the allosteric binding site at P2X3 raised a similar hypothesis of a third potential pocket present in human P2X4 and corresponding to the AF-219 binding site (J. Wang et al., 2018). This was briefly explored but has not been included in this thesis and may constitute the basis for further future work. More modulator-binding pockets may be potentially present (i) at the interface of 2 different subunits or (ii) in a very flexible domain whose conformational changes are crucial for channel activation (e.g. head domain). An intriguing hypothesis is that NP-1815-XP and molecules with similar scaffolds may bind to the apo-state in the head domain near the residues involved in the ATP-binding site. Circumstantial evidence arises from the publication of the NMR structure of rat P2X4 head domain with direct reference to a potential use in structure-based drug design (Igawa, Abe, Tsuda, Inoue, & Ueda, 2015) and

authored by the same research group that – years later - has developed NP-1815-XP and numerous analogues mentioned in multiple patents (Inoue, Tsuda, Koizumi, & Kohsaka, 2005; Matsumura et al., 2016; Sakuma, Takahashi, Ushioda, Imai, & Inoue, 2013). A binding site in a similar location in human P2X1 has been very recently reported by Huo *et al.* (Huo, Fryatt, Farmer, Schmid, & Evans, 2018), which confirmed the involvement of Lys-249 and identified 3 further residues important in PPADS binding through an exhaustive cysteine mutagenesis study.

6.3 Compounds with antagonist activity at human P2X7

Novel P2X7 antagonists were discovered among the molecules selected after two rounds of virtual screening as human P2X4 'hit' candidates, which were yet inactive at human P2X4 in calcium influx assay. In particular, Compound 25 blocked YO-PRO uptake (induced by 300 μM ATP) in human P2X7 and rat P2X7 cell lines with an IC_{50} value of 8.7 μM and 24.4 μM, respectively. The antagonist effect was confirmed through whole-cell patch clamp on rat P2X7 cells, however, more experiments are needed for a correct determination of the mechanism of inhibition, which from initial data appears to be competitive at concentrations lower than the maximal concentration tested (100 μM). 27 analogues were then purchased and tested on human P2X7. Compounds 47, 50 and 68 showed activity at <30 μM, helping in the identification of important moieties, which may be exploited in future to synthesise analogues with improved drug-likeness and activity profile.

According to the sequence alignment, human P2X4 and human P2X7 share 46% identity at the amino acid level. The reason underlining the unexpected finding of multiple active compounds with selectivity towards P2X7 – while originally selected after screen in the orthosteric site of a different receptor subtype – still needs further investigation although one could be the difficulty in modelling intrinsically similar – yet sufficiently different – pockets for the two distinctive receptor subtypes. A comparison between Compound 25 and a series of potent anti-P2X4 patented compounds sharing a similar scaffold reported by Newcom *et*

al. (Newcom & Spear, 2015) may shed more insight regarding the features that confer subtype selectivity between P2X4 and P2X7.

6.4 *In silico* studies of well-known P2X4 and P2X7 ligands

This work also applied *in silico* simulations in order to correlate structural and mutagenesis data regarding two P2X ligands – BzATP and ivermectin – that have been intensively studied as important pharmacological tools to investigate the properties of P2X subtypes (North, 2002). Although no crystal structure of any P2X receptor has been solved in presence of BzATP or IVM, substantial mutagenesis analysis has identified the binding site for each of the ligands (Silberberg, Li, & Swartz, 2007; Young, Pelegrin, & Surprenant, 2007), the first corresponding to the ATP-binding site while the second was identified in transmembrane domain.

Docking simulations of BzATP (both 2' and 3'-isomer) sustains the hypothesis of the formation of a π-cation interaction between the benzoyl-benzoyl moiety and Lys-127 (in mouse P2X7) – a pivotal residue responsible for the increased BzATP potency at rat P2X7 (Young et al., 2007). Furthermore, our dock indicates that isomer 2' may retain a conformation and interactions that are more similar to those observed for ATP observed in the crystal structure of zfP2X4 (Hattori & Gouaux, 2012).

Docking simulations of ivermectin showed a good correlation with experimental data fitting the ligand in close proximity to 7 of the 9 rat P2X4 residues that are important in ivermectin response potentiation action (Silberberg et al., 2007). Based on our docking, we hypothesize that the mutation of Asn-338 – forming a H-bonds with the disaccharide moiety of ivermectin – to a residue unable to form H-bonds or H-arene bond would significantly affect the ivermectin ability to potentiate ATP –induced responses at rat P2X4.

Both *in silico* studies conducted on BzATP and ivermectin were the focus of recently published work (Pasqualetto, Brancale, & Young, 2018).

REFERENCES

Abberley, L. et al. 2010. Identification of 2-oxo-N-(phenylmethyl)-4-imidazolidinecarboxamide antagonists of the P2X 7 receptor. *Bioorganic & medicinal chemistry letters* 20(22), pp. 6370-6374.

Abbracchio, M. P. et al. 2009. Purinergic signalling in the nervous system: an overview. *Trends in Neurosciences* 32(1), pp. 19-29.

Abdi, M. H. et al. 2010. Discovery and structure–activity relationships of a series of pyroglutamic acid amide antagonists of the P2X 7 receptor. *Bioorganic & medicinal chemistry letters* 20(17), pp. 5080-5084.

Abdulqawi, R. et al. 2015. P2X3 receptor antagonist (AF-219) in refractory chronic cough: a randomised, double-blind, placebo-controlled phase 2 study. *The Lancet* 385(9974), pp. 1198-1205.

Acuña – Castillo, C. et al. 2007. Differential role of extracellular histidines in copper, zinc, magnesium and proton modulation of the P2X7 purinergic receptor. *Journal of neurochemistry* 101(1), pp. 17-26.

Adinolfi, E. et al. 2010. Trophic activity of a naturally occurring truncated isoform of the P2X7 receptor. *The FASEB Journal* 24(9), pp. 3393-3404.

Adriouch, S. et al. 2008. ADP-ribosylation at R125 gates the P2X7 ion channel by presenting a covalent ligand to its nucleotide binding site. *The FASEB Journal* 22(3), pp. 861-869.

Agboh, K. C. et al. 2004. Functional characterization of a P2X receptor from Schistosoma mansoni. *Journal of Biological Chemistry* 279(40), pp. 41650-41657.

Albulescu, I. C. et al. 2015. Suramin inhibits chikungunya virus replication through multiple mechanisms. *Antiviral research* 121, pp. 39-46.

Alcazar-Vaca, M. J. et al. 2013. P2X7 modulators.United States: Janssen Pharmaceutica NV.

Alcocer-Gómez, E. et al. 2014. NLRP3 inflammasome is activated in mononuclear blood cells from patients with major depressive disorder. *Brain, behavior, and immunity* 36, pp. 111-117.

Allsopp, R. C. et al. 2017. Unique residues in the ATP gated human P2X7 receptor define a novel allosteric binding pocket for the selective antagonist AZ10606120. *Scientific Reports* 7: 725.

Alves, L. A. et al. 2013. Physiological roles and potential therapeutic applications of the P2X7 receptor in inflammation and pain. *Molecules* 18(9), pp. 10953-10972.

Anderson, O. A. et al. 2013. A2E induces IL-1ss production in retinal pigment epithelial cells via the NLRP3 inflammasome. *PloS one* 8(6), p. e67263.

Ando, J. et al. 1993. Wall shear stress rather than shear rate regulates cytoplasmic Ca++ responses to flow in vascular endothelial cells. *Biochemical and biophysical research communications* 190(3), pp. 716-723.

Antonio, L. S. et al. 2009. Mouse Leydig cells express multiple P2X receptor subunits. *Purinergic signalling* 5(3), pp. 277-287.

Antonio, L. S. et al. 2014. Identification of P2X2/P2X4/P2X6 heterotrimeric receptors using atomic force microscopy (AFM) imaging. *FEBS Letters* 588(12), pp. 2125-2128.

Aprile-Garcia, F. et al. 2016. Co-expression of wild-type P2X7R with Gln460Arg variant alters receptor function. *PloS one* 11(3), p. e0151862.

Asatryan, L. et al. 2010. Ivermectin antagonizes ethanol inhibition in purinergic P2X4 receptors. *Journal of Pharmacology and Experimental Therapeutics* 334(3), pp. 720-728.

Aschrafi, A. et al. 2004. Trimeric Architecture of Homomeric P2X2 and Heteromeric P2X1+2 Receptor Subtypes. *Journal of Molecular Biology* 342(1), pp. 333-343.

Ase, A. R. et al. 2015. Identification and Characterization of a Selective Allosteric Antagonist of Human P2X4 Receptor Channels. *Molecular Pharmacology* 87(4), pp. 606-616.

Ashburn, T. T. and Thor, K. B. 2004. Drug repositioning: identifying and developing new uses for existing drugs. *Nature reviews Drug discovery* 3(8), p. 673.

Baker, D. and Sali, A. 2001. Protein structure prediction and structural genomics. *Science* 294(5540), pp. 93-96.

Balázs, B. et al. 2013. Investigation of the Inhibitory Effects of the Benzodiazepine Derivative, 5-BDBD on P2X4 Purinergic Receptors by two Complementary Methods. *Cellular Physiology and Biochemistry* 32(1), pp. 11-24.

Barden, N. et al. 2006. Analysis of single nucleotide polymorphisms in genes in the chromosome 12Q24. 31 region points to P2RX7 as a susceptibility gene to bipolar affective disorder. *American Journal of Medical Genetics Part B: Neuropsychiatric Genetics* 141(4), pp. 374-382.

Bartlett, R. et al. 2013. P2X7 receptor activation induces reactive oxygen species formation and cell death in murine EOC13 microglia. *Mediators of inflammation* 2013: 271813, pp. 1-18.

Bassetto, M. et al. 2013. Computer-aided identification, design and synthesis of a novel series of compounds with selective antiviral activity against chikungunya virus. *Antiviral research* 98(1), pp. 12-18.

Basso, A. M. et al. 2009. Behavioral profile of P2X 7 receptor knockout mice in animal models of depression and anxiety: relevance for neuropsychiatric disorders. *Behavioural brain research* 198(1), pp. 83-90.

Bavan, S. et al. 2011. The penultimate arginine of the carboxyl terminus determines slow desensitization in a P2X receptor from the cattle tick Boophilus microplus. *Molecular pharmacology* 79(4), pp. 776-785.

Bavan, S. et al. 2009. A P2X receptor from the tardigrade species Hypsibius dujardini with fast kinetics and sensitivity to zinc and copper. *BMC evolutionary biology* 9: 17.

Bavan, S. et al. 2012. Cloning and characterization of a P2X receptor expressed in the central nervous system of Lymnaea stagnalis. *PloS one* 7(11), p. e50487.

Baxter, C. A. et al. 2000. New approach to molecular docking and its application to virtual screening of chemical databases. *Journal of chemical information and computer sciences* 40(2), pp. 254-262.

Berg, A. and Berg, T. 2017. A small-molecule screen identifies the antitrypanosomal agent suramin and analogues NF023 and NF449 as inhibitors of STAT5a/b. *Bioorganic & medicinal chemistry letters* 27(15), pp. 3349-3352.

Beswick, P. J. et al. 2010. Structure–activity relationships and in vivo activity of (1H-pyrazol-4-yl) acetamide antagonists of the P2X7 receptor. *Bioorganic & medicinal chemistry letters* 20(15), pp. 4653-4656.

Bhaskaracharya, A. et al. 2014. Probenecid blocks human P2X7 receptor-induced dye uptake via a pannexin-1 independent mechanism. *PLoS ONE* 9(3), p. e93058.

Bhatia, P. et al. 2012. Breast cancer resistance protein (BCRP/ABCG2) localises to the nucleus in glioblastoma multiforme cells. *Xenobiotica* 42(8), pp. 748-755.

Bhattacharya, A. 2018. Recent Advances in CNS P2X7 Physiology and Pharmacology: Focus on Neuropsychiatric Disorders. *Frontiers in pharmacology* 9: 30.

Bhattacharya, A. et al. 2013. Pharmacological characterization of a novel centrally permeable P2X7 receptor antagonist: JNJ – 47965567. *British journal of pharmacology* 170(3), pp. 624-640.

Bissantz, C. et al. 2000. Protein-based virtual screening of chemical databases. 1. Evaluation of different docking/scoring combinations. *Journal of medicinal chemistry* 43(25), pp. 4759-4767.

Bissantz, C. et al. 2010. A medicinal chemist's guide to molecular interactions. *Journal of medicinal chemistry* 53(14), pp. 5061-5084.

Bo, X. et al. 1999. Localization of ATP – gated P2X2 and P2X3 receptor immunoreactive nerves in rat taste buds. *Neuroreport* 10(5), pp. 1107-1111.

Bo, X. et al. 2003. Pharmacological and biophysical properties of the human P2X5 receptor. *Molecular pharmacology* 63(6), pp. 1407-1416.

Bo, X. et al. 1995. A P2X purinoceptor cDNA conferring a novel pharmacological profile. *FEBS letters* 375(1-2), pp. 129-133.

Bobanovic, L. K. et al. 2002. P2X receptor trafficking in neurons is subunit specific. *Journal of Neuroscience* 22(12), pp. 4814-4824.

Bootman, M. D. et al. 2002. 2-aminoethoxydiphenyl borate (2-APB) is a reliable blocker of store-operated Ca2+ entry but an inconsistent inhibitor of InsP3-induced Ca2+ release. *The FASEB Journal* 16(10), pp. 1145-1150.

Bootman, M. D. et al. 2013. Ca2+-sensitive fluorescent dyes and intracellular Ca2+ imaging. *Cold Spring Harbor Protocols* 2013(2), pp. 83-99.

Bouhassira, D. et al. 2008. Prevalence of chronic pain with neuropathic characteristics in the general population. *Pain* 136(3), pp. 380-387.

Bowler, J. W. et al. 2003. P2X4, P2Y1 and P2Y2 receptors on rat alveolar macrophages. *British journal of pharmacology* 140(3), pp. 567-575.

Boyer, J. L. and Harden, T. K. 1989. Irreversible activation of phospholipase C-coupled P2Y-purinergic receptors by 3'-O-(4-benzoyl) benzoyl adenosine 5'-triphosphate. *Molecular pharmacology* 36(6), pp. 831-835.

Bradford, M. D. and Soltoff, S. P. 2002. P2X7 receptors activate protein kinase D and p42/p44 mitogen-activated protein kinase (MAPK) downstream of protein kinase C. *Biochemical Journal* 366(3), pp. 745-755.

Bradley, H. J. et al. 2011. Residues 155 and 348 contribute to the determination of P2X7 receptor function via distinct mechanisms revealed by single-nucleotide polymorphisms. *Journal of Biological Chemistry* 286(10), pp. 8176-8187.

Bredt, D. S. et al. 1992. Nitric oxide synthase regulatory sites. Phosphorylation by cyclic AMP-dependent protein kinase, protein kinase C, and calcium/calmodulin protein kinase; identification of flavin and calmodulin binding sites. *Journal of Biological Chemistry* 267(16), pp. 10976-10981.

Browne, L. E. and North, R. A. 2013. P2X receptor intermediate activation states have altered nucleotide selectivity. *Journal of Neuroscience* 33(37), pp. 14801-14808.

Buell, G. et al. 1996. An antagonist – insensitive P2X receptor expressed in epithelia and brain. *The EMBO Journal* 15(1), pp. 55-62.

Buell, G. et al. 1998. Gene structure and chromosomal localization of the human P2X7 receptor. *Receptors & channels* 5(6), pp. 347-354.

Burnstock, G. 2014. Purinergic signalling in endocrine organs. *Purinergic signalling* 10(1), pp. 189-231.

Burnstock, G. 2017. Purinergic signalling and neurological diseases: an update. *CNS & Neurological Disorders-Drug Targets (Formerly Current Drug Targets-CNS & Neurological Disorders)* 16(3), pp. 257-265.

Burnstock, G. and Knight, G. E. 2004. Cellular distribution and functions of P2 receptor subtypes in different systems. *International Review of Cytology* 240(1), pp. 31-304.

Cai, X. 2006. Unicellular Ca2+ signaling 'toolkit'at the origin of metazoa. *Molecular biology and evolution* 25(7), pp. 1357-1361.

Cai, X. 2012. P2X receptor homologs in basal fungi. *Purinergic signalling* 8(1), pp. 11-13.

Cao, Y. et al. 2014. Extracellular ATP is a central signaling molecule in plant stress responses. *Current opinion in plant biology* 20, pp. 82-87.

Carmo, M. R. et al. 2014. The P2X7 receptor antagonist Brilliant Blue G attenuates contralateral rotations in a rat model of Parkinsonism through a combined control of synaptotoxicity, neurotoxicity and gliosis. *Neuropharmacology* 81, pp. 142-152.

Carpenter, D. et al. 1999. Site-specific splice variation of the human P2X4 receptor. *Neuroscience Letters* 273(3), pp. 183-186.

Carroll, W. A. et al. 2009. Selective P2X 7 receptor antagonists for chronic inflammation and pain. *Purinergic signalling* 5, pp. 63-73.

Caseley, E. A. et al. 2016. Structure-based identification and characterisation of structurally novel human P2X7 receptor antagonists. *Biochemical pharmacology* 116, pp. 130-139.

Caseley, E. A. et al. 2014. Non-synonymous single nucleotide polymorphisms in the P2X receptor genes: association with diseases, impact on receptor functions and potential use as diagnosis biomarkers. *International journal of molecular sciences* 15(8), pp. 13344-13371.

Charifson, P. S. et al. 1999. Consensus scoring: A method for obtaining improved hit rates from docking databases of three-dimensional structures into proteins. *Journal of medicinal chemistry* 42(25), pp. 5100-5109.

Cheewatrakoolpong, B. et al. 2005. Identification and characterization of splice variants of the human P2X7 ATP channel. *Biochemical and biophysical research communications* 332(1), pp. 17-27.

Chen, I. S. and Kubo, Y. 2018. Ivermectin and its target molecules: shared and unique modulation mechanisms of ion channels and receptors by ivermectin. *The Journal of physiology* 596(10), pp. 1833-1845.

Chen, X. et al. 2014. Brilliant Blue G improves cognition in an animal model of Alzheimer's disease and inhibits amyloid-β-induced loss of filopodia and dendrite spines in hippocampal neurons. *Neuroscience* 279, pp. 94-101.

Chen, X. et al. 2010. Discovery of 2-chloro-N-((4, 4-difluoro-1-hydroxycyclohexyl) methyl)-5-(5-fluoropyrimidin-2-yl) benzamide as a potent and CNS penetrable P2X7 receptor antagonist. *Bioorganic & medicinal chemistry letters* 20(10), pp. 3107-3111.

Chessell, I. P. et al. 2005. Disruption of the P2X7 purinoceptor gene abolishes chronic inflammatory and neuropathic pain. *Pain* 114(3), pp. 386-396.

Cho, S.-H. et al. 2017. Molecular Mechanism of Plant Recognition of Extracellular ATP. In: Atassi, M.Z. ed. *Protein Reviews. Advances in Experimental Medicine and Biology*. Vol. 1051. Singapore: Springer.

Chrovian, C. C. et al. 2017. A Dipolar Cycloaddition Reaction To Access 6-Methyl-4, 5, 6, 7-tetrahydro-1 H-[1, 2, 3] triazolo [4, 5-c] pyridines Enables the Discovery Synthesis and Preclinical Profiling of a P2X7 Antagonist Clinical Candidate. *Journal of medicinal chemistry* 61(1), pp. 207-223.

Clarke, C. et al. 2000. Mutation of histidine 286 of the human P2X4 purinoceptor removes extracellular pH sensitivity. *The Journal of physiology* 523(3), pp. 697-703.

Clyne, J. D. et al. 2002. Mutational analysis of the conserved cysteines of the rat P2X2 purinoceptor. *Journal of Neuroscience* 22(10), pp. 3873-3880.

Cockayne, D. A. et al. 2005. P2X2 knockout mice and P2X2/P2X3 double knockout mice reveal a role for the P2X2 receptor subunit in mediating multiple sensory effects of ATP. *The Journal of physiology* 567(2), pp. 621-639.

Coddou, C. et al. 2007. Dissecting the Facilitator and Inhibitor Allosteric Metal Sites of the P2X4 Receptor Channel: Critical Roles of Cys132 for Zinc potentiation and Asp138 for Copper Inhibition. *Journal of Biological Chemistry* 282(51), pp. 36879-36886.

Coddou, C. et al. 2005. Heavy metals modulate the activity of the purinergic P2X4 receptor. *Toxicology and Applied Pharmacology* 202(2), pp. 121-131.

Codocedo, J. F. et al. 2009. Neurosteroids differentially modulate P2X4 ATP-gated channels through non-genomic interactions. *Journal of Neurochemistry* 110(2), pp. 734-744.

Corrêa, G. et al. 2016. The purinergic receptor P2X7 role in control of Dengue virus-2 infection and cytokine/chemokine production in infected human monocytes. *Immunobiology* 221(7), pp. 794-802.

Coull, J. A. M. et al. 2005. BDNF from microglia causes the shift in neuronal anion gradient underlying neuropathic pain. *Nature* 438(7070), pp. 1017-1021.

Coutinho-Silva, R. et al. 2001. Changes in expression of P2 receptors in rat and mouse pancreas during development and ageing. *Cell and tissue research* 306(3), pp. 373-383.

Csölle, C. et al. 2013. The absence of P2X7 receptors (P2rx7) on non-haematopoietic cells leads to selective alteration in mood-related behaviour with dysregulated gene expression and stress reactivity in mice. *International Journal of Neuropsychopharmacology* 16(1), pp. 213-233.

Dal Ben, D. et al. 2015. Purinergic P2X receptors: structural models and analysis of ligand-target interaction. *European journal of medicinal chemistry* 89, pp. 561-580.

Dao-Ung, P. et al. 2015. Paroxetine suppresses recombinant human P2X7 responses. *Purinergic signalling* 11(4), pp. 481-490.

Datta, S. et al. 2017. The impact of oxidative stress and inflammation on RPE degeneration in non-neovascular AMD. *Progress in retinal and eye research* 60, pp. 201-218.

Davies, D. L. et al. 2002a. Ethanol Sensitivity in ATP-Gated P2X Receptors Is Subunit Dependent. *Alcoholism: Clinical and Experimental Research* 26(6), pp. 773-778.

Davies, D. L. et al. 2002b. Ethanol Sensitivity in ATP – Gated P2X Receptors Is Subunit Dependent. *Alcoholism: Clinical and Experimental Research* 26(6), pp. 773-778.

Denlinger, L. C. et al. 2001. Cutting edge: the nucleotide receptor P2X7 contains multiple protein-and lipid-interaction motifs including a potential binding site for bacterial lipopolysaccharide. *The Journal of Immunology* 167(4), pp. 1871-1876.

Dhulipala, P. D. et al. 1998. The human P2X4 receptor gene is alternatively spliced. *Gene* 207(2), pp. 259-266.

Di Virgilio, F. 2012. Purines, purinergic receptors, and cancer. *Cancer research* 72(21), pp. 5441-5447.

Di Virgilio, F. et al. 2018. The elusive P2X7 macropore. *Trends in cell biology* 28(5), pp. 392-404.

Donnelly-Roberts, D. L. et al. 2009. [3H] A-804598 ([3H] 2-cyano-1-[(1S)-1-phenylethyl]-3-quinolin-5-ylguanidine) is a novel, potent, and selective antagonist radioligand for P2X7 receptors. *Neuropharmacology* 56(1), pp. 223-229.

Donnelly – Roberts, D. L. et al. 2009. Mammalian P2X7 receptor pharmacology: comparison of recombinant mouse, rat and human P2X7 receptors. *British journal of pharmacology* 157(7), pp. 1203-1214.

Du, J. et al. 2012. Gating mechanism of a P2X4 receptor developed from normal mode analysis and molecular dynamics simulations. *Proceedings of the National Academy of Sciences* 109(11), pp. 4140-4145.

Du, J. et al. 2015. Glycine receptor mechanism elucidated by electron cryo-microscopy. *Nature* 526(7572), p. 224.

Dubyak, G. R. 2007. Go It Alone No More-P2X7 Joins the Society of Heteromeric ATP-Gated Ion Channel Receptors. *Molecular pharmacology* 72(6), pp. 1402-1405.

Dubyak, G. R. 2012. P2X7 receptor regulation of non – classical secretion from immune effector cells. *Cellular microbiology* 14(11), pp. 1697-1706.

Duncan, J. S. 2005. Brain imaging in idiopathic generalized epilepsies. *Epilepsia* 46(s9), pp. 108-111.

Duplantier, A. J. et al. 2011. Optimization of the physicochemical and pharmacokinetic attributes in a 6-azauracil series of P2X 7 receptor antagonists leading to the discovery of the clinical candidate CE-224,535. *Bioorganic & medicinal chemistry letters* 21(12), pp. 3708-3711.

Eddy, M. C. et al. 2009. Double P2X2/P2X3 purinergic receptor knockout mice do not taste NaCl or the artificial sweetener SC45647. *Chemical senses* 34(9), pp. 789-797.

Ennion, S. J. and Evans, R. J. 2002. Conserved Cysteine Residues in the Extracellular Loop of the Human P2X1 Receptor Form Disulfide Bonds and Are Involved in Receptor Trafficking to the Cell Surface. *Molecular Pharmacology* 61(2), pp. 303-311.

Erhardt, A. et al. 2007. Association of polymorphisms in P2RX7 and CaMKKb with anxiety disorders. *Journal of affective disorders* 101(1), pp. 159-168.

Eser, A. et al. 2015. Safety and efficacy of an oral inhibitor of the purinergic receptor P2X7 in adult patients with moderately to severely active Crohn's disease: a randomized placebo-controlled, double-blind, phase IIa study. *Inflammatory bowel diseases* 21(10), pp. 2247-2253.

Evans, R. et al. 1995. Pharmacological characterization of heterologously expressed ATP-gated cation channels (P2x purinoceptors). *Molecular pharmacology* 48(2), pp. 178-183.

Evans, R. J. 2010. Structural interpretation of P2X receptor mutagenesis studies on drug action. *British journal of pharmacology* 161(5), pp. 961-971.

Evotec-AG. 2012. *Pharma partnerships - Evotec* [Online]. Available at: https://http://www.evotec.com/en/innovate/pharma-partnerships [Accessed: 2018].

Faletra, F. et al. 2014. A novel P2RX2 mutation in an Italian family affected by autosomal dominant nonsyndromic hearing loss. *Gene* 534(2), pp. 236-239.

Ferla, S. et al. 2018. In silico screening for human norovirus antivirals reveals a novel non-nucleoside inhibitor of the viral polymerase. *Scientific reports* 8: 4129.

Fernando, S. L. et al. 2007. A polymorphism in the P2X7 gene increases susceptibility to extrapulmonary tuberculosis. *American journal of respiratory and critical care medicine* 175(4), pp. 360-366.

Ferrari, D. et al. 1997. Extracellular ATP triggers IL-1 beta release by activating the purinergic P2Z receptor of human macrophages. *The Journal of Immunology* 159(3), pp. 1451-1458.

Ferrari, D. et al. 2017. A purinergic trail for metastases. *Trends in pharmacological sciences* 38(3), pp. 277-290.

Ferreira, L. G. et al. 2015. Molecular docking and structure-based drug design strategies. *Molecules* 20(7), pp. 13384-13421.

Ferreira, M. A. et al. 2008. Collaborative genome-wide association analysis supports a role for ANK3 and CACNA1C in bipolar disorder. *Nature genetics* 40(9), p. 1056.

Finger, T. E. and Kinnamon, S. C. 2013. A taste for ATP: neurotransmission in taste buds. *Frontiers in cellular neuroscience* 7: 264.

Fischer, R. et al. 2004. Benzofuro-1,4-diazepin-2-one derivatives.Canada: Bayer HealthCare AG.

Fois, G. et al. 2017. ATP is stored in lamellar bodies to activate vesicular P2X4 in an autocrine fashion upon exocytosis. *The Journal of General Physiology* 150(2), pp. 277-291.

Fountain, S. J. et al. 2008. Permeation properties of a P2X receptor in the green algae Ostreococcus tauri. *Journal of Biological Chemistry* 283(22), pp. 15122-15126.

Fountain, S. J. et al. 2007. An intracellular P2X receptor required for osmoregulation in Dictyostelium discoideum. *Nature* 448(7150), pp. 200-203.

Fowler, B. J. et al. 2014. Nucleoside reverse transcriptase inhibitors possess intrinsic anti-inflammatory activity. *Science* 346(6212), pp. 1000-1003.

França, T. C. C. 2015. Homology modeling: an important tool for the drug discovery. *Journal of Biomolecular Structure and Dynamics* 33(8), pp. 1780-1793.

Franklin, K. M. et al. 2014. P2X4 receptors (P2X4Rs) represent a novel target for the development of drugs to prevent and/or treat alcohol use disorders. *Frontiers in neuroscience* 8.

Franklin, K. M. et al. 2015. Involvement of purinergic P2X4 receptors in alcohol intake of high – alcohol – drinking (HAD) rats. *Alcoholism: Clinical and Experimental Research* 39(10), pp. 2022-2031.

Frerking, I. et al. 2001. Pulmonary surfactant: functions, abnormalities and therapeutic options. *Intensive care medicine* 27(11), pp. 1699-1717.

Friesner, R. A. et al. 2004. Glide: a new approach for rapid, accurate docking and scoring. 1. Method and assessment of docking accuracy. *Journal of medicinal chemistry* 47(7), pp. 1739-1749.

Friesner, R. A. et al. 2006. Extra precision glide: Docking and scoring incorporating a model of hydrophobic enclosure for protein− ligand complexes. *Journal of medicinal chemistry* 49(21), pp. 6177-6196.

Fryatt, A. G. et al. 2016. Mechanistic insights from resolving ligand-dependent kinetics of conformational changes at ATP-gated P2X1R ion channels. *Scientific reports* 6: 32918.

Gao, M. et al. 2015. Synthesis of [11 C] GSK1482160 as a new PET agent for targeting P2X7 receptor. *Bioorganic & medicinal chemistry letters* 25(9), pp. 1965-1970.

Garg, A. D. et al. 2017. Extracellular ATP and P 2 X 7 receptor exert context-specific immunogenic effects after immunogenic cancer cell death. *Cell death & disease* 7, p. e2097.

Gargett, C. E. and Wiley, J. S. 1997. The isoquinoline derivative KN – 62 a potent antagonist of the P2Z – receptor of human lymphocytes. *British journal of pharmacology* 120(8), pp. 1483-1490.

Gartland, A. et al. 2012. Polymorphisms in the P2X7 receptor gene are associated with low lumbar spine bone mineral density and accelerated bone loss in post-menopausal women. *European Journal of Human Genetics* 20(5), p. 559.

Geistlinger, J. et al. 2012. P2RX7 genotype association in severe sepsis identified by a novel Multi-Individual Array for rapid screening and replication of risk SNPs. *Clinica Chimica Acta* (1-2), pp. 39-47.

Geraghty, N. et al. 2016. P2X7 receptor in skin biology and diseases. *World Journal of Dermatology* 5(2), pp. 72-83.

Ghiringhelli, F. et al. 2009. Activation of the NLRP3 inflammasome in dendritic cells induces IL-1β–dependent adaptive immunity against tumors. *Nature medicine* 15(10), p. 1170.

Gilbert, S. et al. 2017. A phase I clinical trial demonstrates that nfP2X7 – targeted antibodies provide a novel, safe and tolerable topical therapy for basal cell carcinoma. *British Journal of Dermatology* 177(1), pp. 117-124.

Gilbert, S. et al. 2018. ATP in the tumour microenvironment drives expression of nfP2X7, a key mediator of cancer cell survival. *Oncogene* 38, pp. 194-208.

Gilmore, S. A. and Skinner, R. D. 1979. Intraspinal non – neuronal cellular responses to peripheral nerve injury. *The Anatomical Record* 194(3), pp. 369-387.

Giuliani, A. L. et al. 2017. The P2X7 receptor-interleukin-1 liaison. *Frontiers in pharmacology* 8: 123.

Glass, R. et al. 2000. P2 receptors in the thymus: expression of P2X and P2Y receptors in adult rats, an immunohistochemical and in situ hybridisation study. *Cell and tissue research* 300(2), pp. 295-306.

Gnanaguru, G. et al. 2016. Oxidized lipoprotein uptake through the CD36 receptor activates the NLRP3 inflammasome in human retinal pigment epithelial cells. *Investigative ophthalmology & visual science* 57(11), pp. 4704-4712.

Gonnord, P. et al. 2009. Palmitoylation of the P2X7 receptor, an ATP-gated channel, controls its expression and association with lipid rafts. *The FASEB Journal* 23(3), pp. 795-805.

Gorodeski, G. I. 2012. P2X7 receptors and epithelial cancers. *Wiley Interdisciplinary Reviews: Membrane Transport and Signaling* 1(3), pp. 349-371.

Graziano, F. et al. 2015. Extracellular ATP induces the rapid release of HIV-1 from virus containing compartments of human macrophages. *Proceedings of the National Academy of Sciences* 112(25), pp. E3265-E3273.

Green, E. K. et al. 2009. P2RX7: a bipolar and unipolar disorder candidate susceptibility gene? *American Journal of Medical Genetics Part B: Neuropsychiatric Genetics* 150(8), pp. 1063-1069.

Greenwood, J. R. et al. 2010. Towards the comprehensive, rapid, and accurate prediction of the favorable tautomeric states of drug-like molecules in aqueous solution. *Journal of computer-aided molecular design* 24(6-7), pp. 591-604.

Grigoroiu – Serbanescu, M. et al. 2009. Variation in P2RX7 candidate gene (rs2230912) is not associated with bipolar I disorder and unipolar major depression in four European samples. *American Journal of Medical Genetics Part B: Neuropsychiatric Genetics* 150(7), pp. 1017-1021.

Grüneberg, S. et al. 2001. Subnanomolar inhibitors from computer screening: a model study using human carbonic anhydrase II. *Angewandte Chemie International Edition* 40(2), pp. 389-393.

Gu, B. et al. 2000. Expression of P2X7 purinoceptors on human lymphocytes and monocytes: evidence for nonfunctional P2X7 receptors. *American Journal of Physiology-Cell Physiology* 279(4), pp. C1189-C1197.

Gu, B. J. et al. 2013. A rare functional haplotype of the P2RX4 and P2RX7 genes leads to loss of innate phagocytosis and confers increased risk of age-related macular degeneration. *The FASEB Journal* 27(4), pp. 1479-1487.

Gu, B. J. et al. 2015. A rare P2X7 variant Arg307Gln with absent pore formation function protects against neuroinflammation in multiple sclerosis. *Human molecular genetics* 24(19), pp. 5644-5654.

Gu, N. et al. 2016. Spinal microgliosis due to resident microglial proliferation is required for pain hypersensitivity after peripheral nerve injury. *Cell reports* 16(3), pp. 605-614.

Gubert, C. et al. 2016. Role of P2X7 receptor in an animal model of mania induced by D-amphetamine. *Molecular neurobiology* 53, pp. 611-620.

Guha, S. et al. 2013. Lysosomal alkalinization, lipid oxidation, and reduced phagosome clearance triggered by activation of the P2X7 receptor. *The FASEB Journal* 27(11), pp. 4500-4509.

Guile, S. D. et al. 2009. Antagonists of the P2X7 receptor. From lead identification to drug development. *Journal of medicinal chemistry* 52(10), pp. 3123-3141.

Gund, P. 1977. Three-dimensional pharmacophoric pattern searching. In: Hahn, F.E. et al. eds. *Progress in molecular and subcellular biology*. Vol. 5. Berlin Heidelberg: Springer, pp. 117-143.

Gunosewoyo, H. and Kassiou, M. 2010. P2X purinergic receptor ligands: recently patented compounds. *Expert Opinion on Therapeutic Patents* 20(5), pp. 625-646.

Guo, C. et al. 2007. Evidence for Functional P2X4/P2X7 Heteromeric Receptors. *Molecular Pharmacology* 72(6), pp. 1447-1456.

Han, J. et al. 2017. Pharmacologic characterizations of a P2X7 receptor-specific radioligand,[11C] GSK1482160 for neuroinflammatory response. *Nuclear medicine communications* 38(5), pp. 372-382.

Hassan Baig, M. et al. 2016. Computer aided drug design: success and limitations. *Current pharmaceutical design* 22(5), pp. 572-581.

Hattori, M. and Gouaux, E. 2012. Molecular mechanism of ATP binding and ion channel activation in P2X receptors. *Nature* 485(7397), pp. 207-212.

Hausmann, R. et al. 2012. ATP binding site mutagenesis reveals different subunit stoichiometry of functional P2X2/3 and P2X2/6 receptors. *Journal of Biological Chemistry* 287(17), pp. 13930-13943.

He, Y. et al. 2016. Mechanism and regulation of NLRP3 inflammasome activation. *Trends in biochemical sciences* 41(12), pp. 1012-1021.

Hechler, B. et al. 2003. A role of the fast ATP-gated P2X1 cation channel in thrombosis of small arteries in vivo. *Journal of Experimental Medicine* 198(4), pp. 661-667.

Hejjas, K. et al. 2009. Association between depression and the Gln460Arg polymorphism of P2RX7 gene: a dimensional approach. *American Journal of Medical Genetics Part B: Neuropsychiatric Genetics* 150(2), pp. 295-299.

Helliwell, R. et al. 2015. Selected ginsenosides of the protopanaxdiol series are novel positive allosteric modulators of P2X7 receptors. *British journal of pharmacology* 172(13), pp. 3326-3340.

Hempel, C. et al. 2013. The phenothiazine-class antipsychotic drugs prochlorperazine and trifluoperazine are potent allosteric modulators of the human P2X7 receptor. *Neuropharmacology* 75, pp. 365-379.

Hernandez-Olmos, V. et al. 2012. N-Substituted Phenoxazine and Acridone Derivatives: Structure–Activity Relationships of Potent P2X4 Receptor Antagonists. *Journal of Medicinal Chemistry* 55(22), pp. 9576-9588.

Hibbs, R. E. and Gouaux, E. 2011. Principles of activation and permeation in an anion-selective Cys-loop receptor. *Nature* 474(7349), pp. 54-60.

Hickey, K. et al. 1994. Expression of epidermal growth factor receptor and proliferating cell nuclear antigen predicts response of esophageal squamous cell carcinoma to chemoradiotherapy. *Cancer* 74(6), pp. 1693-1698.

Hildebrand, M. E. et al. 2016. Potentiation of synaptic GluN2B NMDAR currents by Fyn kinase is gated through BDNF-mediated disinhibition in spinal pain processing. *Cell reports* 17(10), pp. 2753-2765.

Hodges, R. R. et al. 2009. Characterization of P2X7 purinergic receptors and their function in rat lacrimal gland. *Investigative ophthalmology & visual science* 50(12), pp. 5681-5689.

Honore, P. et al. 2006. A-740003 [N-(1-{[(cyanoimino)(5-quinolinylamino) methyl] amino}-2, 2-dimethylpropyl)-2-(3, 4-dimethoxyphenyl) acetamide], a novel and selective P2X7 receptor antagonist, dose-dependently reduces neuropathic pain in the rat. *Journal of Pharmacology and Experimental Therapeutics* 319(3), pp. 1376-1385.

Hu, B. et al. 2002. P2X4 receptor is a glycosylated cardiac receptor mediating a positive inotropic response to ATP. *Journal of Biological Chemistry* 277(18), pp. 15752-15757.

Hu, H. et al. 2010. Stimulation of the P2X7 receptor kills rat retinal ganglion cells in vivo. *Experimental eye research* 91(3), pp. 425-432.

Huang, P. et al. 2014. P2X4 forms functional ATP-activated cation channels on lysosomal membranes regulated by luminal pH. *Journal of Biological Chemistry* 289(25), pp. 17658-17667.

Huang, X. et al. 2017. Crystal structures of human GlyRα3 bound to ivermectin. *Structure* 25(6), pp. 945-950.

Huo, H. et al. 2018. Mapping the binding site of the P2X receptor antagonist PPADS reveals the importance of orthosteric site charge and the cysteine-rich head region. *Journal of Biological Chemistry* 293, pp. 12820-12831.

Husted, L. et al. 2013. Functional polymorphisms in the P2X7 receptor gene are associated with osteoporosis. *Osteoporosis International* 24(3), pp. 949-959.

Idziorek, T. et al. 1995. YOPRO-1 permits cytofluorometric analysis of programmed cell death (apoptosis) without interfering with cell viability. *Journal of immunological methods* 185(2), pp. 249-258.

Igawa, T. et al. 2015. Solution structure of the rat P2X4 receptor head domain involved in inhibitory metal binding. *FEBS letters* 589(6), pp. 680-686.

Inoue, K. and Tsuda, M. 2018. Microglia in neuropathic pain: cellular and molecular mechanisms and therapeutic potential. *Nature Reviews Neuroscience* 19, pp. 138-152.

Inoue, K. et al. 2005. Drug screening of P2X4 receptor antagonists for treatment of neuropathic pain. Japan Health Sciences Foundation, Japan . p. 27 pp.

Inscho, E. et al. 2004. Renal autoregulation in P2X1 knockout mice. *Acta Physiologica* 181(4), pp. 445-453.

Iwata, M. et al. 2016. Psychological stress activates the inflammasome via release of adenosine triphosphate and stimulation of the purinergic type 2X7 receptor. *Biological psychiatry* 80(1), pp. 12-22.

Jamieson, S. E. et al. 2010. Evidence for associations between the purinergic receptor P2X 7 (P2RX7) and toxoplasmosis. *Genes and immunity* 11(5), p. 374.

Jelínkova, I. et al. 2008. Identification of P2X4 receptor transmembrane residues contributing to channel gating and interaction with ivermectin. *Pflügers Archiv-European Journal of Physiology* 456(5), pp. 939-950.

Jelínková, I. et al. 2006. Identification of P2X4 receptor-specific residues contributing to the ivermectin effects on channel deactivation. *Biochemical and biophysical research communications* 349(2), pp. 619-625.

Jiang, L.-H. et al. 2003. Subunit arrangement in P2X receptors. *Journal of Neuroscience* 23(26), pp. 8903-8910.

Jiang, L.-H. et al. 2000a. Brilliant Blue G Selectively Blocks ATP-Gated Rat P2X7 Receptors. *Molecular Pharmacology* 58(1), pp. 82-88.

Jiang, L.-H. et al. 2000b. Identification of amino acid residues contributing to the ATP-binding site of a purinergic P2X receptor. *Journal of Biological Chemistry* 275(44), pp. 34190-34196.

Jin, H. et al. 2018. Synthesis and in vitro characterization of a P2X7 radioligand [123I]TZ6019 and its response to neuroinflammation in a mouse model of Alzheimer disease. *European Journal of Pharmacology* 820, pp. 8-17.

Jin, L. et al. 2013. The antiparasitic drug ivermectin is a novel FXR ligand that regulates metabolism. *Nature communications* 4: 1937.

Jones, C. et al. 2000. Functional characterization of the P2X4 receptor orthologues. *British Journal of Pharmacology* 129(2), pp. 388-394.

Jorg, M. et al. 2014. The dopamine D2 and adenosine A2A receptors: past, present and future trends for the treatment of Parkinson's disease. *Current medicinal chemistry* 21(27), pp. 3188-3210.

Jørgensen, N. R. et al. 2012. Single-nucleotide polymorphisms in the P2X7 receptor gene are associated with post-menopausal bone loss and vertebral fractures. *European Journal of Human Genetics* 20(6), p. 675.

Kaczanowski, S. and Zielenkiewicz, P. 2010. Why similar protein sequences encode similar three-dimensional structures? *Theoretical Chemistry Accounts* 125(3-6), pp. 643-650.

Kaczmarek-Hájek, K. et al. 2012. Molecular and functional properties of P2X receptors—recent progress and persisting challenges. *Purinergic signalling* 8(3), pp. 375-417.

Kamerman, P. R. et al. 2015. World Health Organization (WHO) essential medicines lists: where are the drugs to treat neuropathic pain? *Pain* 156(5), p. 793.

Kaneko, H. et al. 2011. DICER1 deficit induces Alu RNA toxicity in age-related macular degeneration. *Nature* 471(7338), p. 325.

Kanneganti, T.-D. et al. 2007. Pannexin-1-mediated recognition of bacterial molecules activates the cryopyrin inflammasome independent of Toll-like receptor signaling. *Immunity* 26(4), pp. 433-443.

Kapitonov, V. and Jurka, J. 2007. Kolobok, a novel superfamily of eukaryotic DNA transposons. *Repbase Rep* 7(2), pp. 113-113.

Karasawa, A. and Kawate, T. 2016. Structural basis for subtype-specific inhibition of the P2X7 receptor. *elife* 5.

Karasawa, A. et al. 2017. The P2X7 receptor forms a dye-permeable pore independent of its intracellular domain but dependent on membrane lipid composition. *eLife* 6.

Kasuya, G. et al. 2016. Structural Insights into Divalent Cation Modulations of ATP-Gated P2X Receptor Channels. *Cell Reports* 14(4), pp. 932-944.

Kasuya, G. et al. 2017. Structural insights into the nucleotide base specificity of P2X receptors. *Scientific reports* 7: 45208.

Kaul, P. N. 1998. Drug discovery: Past, present and future. In: Kaul, P.N. et al. eds. *Progress in Drug Research*. Basel: Birkhäuser Basel, pp. 9-105.

Kawate, T. et al. 2009. Crystal structure of the ATP-gated P2X4 ion channel in the closed state. *Nature* 460(7255), pp. 592-598.

Kerur, N. et al. 2013. TLR-independent and P2X7-dependent signaling mediate Alu RNA-induced NLRP3 inflammasome activation in geographic atrophy. *Investigative ophthalmology & visual science* 54(12), pp. 7395-7401.

Keystone, E. C. et al. 2012. Clinical evaluation of the efficacy of the P2X7 purinergic receptor antagonist AZD9056 on the signs and symptoms of rheumatoid

arthritis in patients with active disease despite treatment with methotrexate or sulphasalazine. *Annals of the Rheumatic Diseases* 71(10), pp. 1630-1635.

Khadra, A. et al. 2013. Dual gating mechanism and function of P2X7 receptor channels. *Biophysical journal* 104(12), pp. 2612-2621.

Khakh, B. S. et al. 2001. International union of pharmacology. XXIV. Current status of the nomenclature and properties of P2X receptors and their subunits. *Pharmacological reviews* 53(1), pp. 107-118.

Khakh, B. S. et al. 1999. Allosteric control of gating and kinetics at P2X4receptor channels. *Journal of Neuroscience* 19(17), pp. 7289-7299.

Khoja, S. et al. 2018. Preclinical evaluation of avermectins as novel therapeutic agents for alcohol use disorders. *Psychopharmacology* 235(6), pp. 1697-1709.

Kim, M. et al. 2001. Proteomic and functional evidence for a P2X7 receptor signalling complex. *The EMBO journal* 20(22), pp. 6347-6358.

Kitchen, D. B. et al. 2004. Docking and scoring in virtual screening for drug discovery: methods and applications. *Nature reviews Drug discovery* 3(11), pp. 935-949.

Klapperstück, M. et al. 2000. Antagonism by the suramin analogue NF279 on human P2X1 and P2X7 receptors. *European journal of pharmacology* 387(3), pp. 245-252.

Kolb, H. et al. 2016. Development and Preclinical Evaluation of [18F] JNJ-64413739 as a PET Radioligand for P2X7 Receptors. *Biological Psychiatry* 41(12), pp. S187-188.

Korb, O. et al. 2009. Empirical scoring functions for advanced protein− ligand docking with PLANTS. *Journal of chemical information and modeling* 49(1), pp. 84-96.

Korb, O. et al. 2006. PLANTS: Application of ant colony optimization to structure-based drug design. In: Dorigo, M. et al. eds. *Ant Colony Optimization and Swarm Intelligence.*, Vol. 4150. Berlin, Heidelberg: Springer, pp. 247-258.

Kotnis, S. et al. 2010. Genetic and Functional Analysis of Human P2X5 Reveals a Distinct Pattern of Exon 10 Polymorphism with Predominant Expression of the Non-functional Receptor Isoform. *Molecular pharmacology* 77(6), pp. 953-960.

Koványi, B. et al. 2016. The role of P2X7 receptors in a rodent PCP-induced schizophrenia model. *Scientific reports* 6: 36680.

Krause, R. M. et al. 1998. Ivermectin: a positive allosteric effector of the α7 neuronal nicotinic acetylcholine receptor. *Molecular pharmacology* 53(2), pp. 283-294.

Kurashima, Y. et al. 2015. Pathophysiological role of extracellular purinergic mediators in the control of intestinal inflammation. *Mediators of inflammation* 2015: 427125, pp. 1-8.

Laskowski, R. A. et al. 1993. PROCHECK: a program to check the stereochemical quality of protein structures. *Journal of applied crystallography* 26(2), pp. 283-291.

Latapiat, V. et al. 2017. P2X4 receptor in silico and electrophysiological approaches reveal insights of ivermectin and zinc allosteric modulation. *Frontiers in pharmacology* 8.

Leach, A. R. 2001. *Molecular modelling: principles and applications*. Pearson education.

Letavic, M. A. et al. 2013. Synthesis and pharmacological characterization of two novel, brain penetrating P2X7 antagonists. *ACS medicinal chemistry letters* 4(4), pp. 419-422.

Lewis, C. et al. 1995. Coexpression of P2X2 and P2X3 receptor subunits can account for ATP-gated currents in sensory neurons. *Nature* 377(6548), pp. 432-435.

Li, Z. et al. 2016. X-ray crystallographic studies of the extracellular domain of the first plant ATP receptor, DORN1, and the orthologous protein from Camelina sativa. *Acta Crystallographica Section F: Structural Biology Communications* 72(10), pp. 782-787.

Lister, M. F. et al. 2007. The role of the purinergic P2X7 receptor in inflammation. *Journal of Inflammation* 4: 5, pp. 1-14.

Liu, C. et al. 2017. Effects of LncRNA BC168687 siRNA on Diabetic Neuropathic Pain Mediated by P2X7 Receptor on SGCs in DRG of Rats. *BioMed research international* 2017: 7831251, pp. 1-10.

Liu, S. et al. 2016. LncRNA NONRATT021972 siRNA regulates neuropathic pain behaviors in type 2 diabetic rats through the P2X 7 receptor in dorsal root ganglia. *Molecular brain* 9(1), p. 44.

Liu, X. et al. 2008. Identification of key residues coordinating functional inhibition of P2X7 receptors by zinc and copper. *Molecular pharmacology* 73(1), pp. 252-259.

Lord, B. et al. 2014. Pharmacology of a novel central nervous system–penetrant P2X7 antagonist JNJ-42253432. *Journal of Pharmacology and Experimental Therapeutics* 351(3), pp. 628-641.

Lovell Simon, C. et al. 2003. Structure validation by Cα geometry: ϕ,ψ and Cβ deviation. *Proteins: Structure, Function, and Bioinformatics* 50(3), pp. 437-450.

Lucae, S. et al. 2006. P2RX7, a gene coding for a purinergic ligand-gated ion channel, is associated with major depressive disorder. *Human molecular genetics* 15(16), pp. 2438-2445.

Lucattelli, M. et al. 2011. P2X7 receptor signaling in the pathogenesis of smoke-induced lung inflammation and emphysema. *American journal of respiratory cell and molecular biology* 44(3), pp. 423-429.

Lyne, P. D. 2002. Structure-based virtual screening: an overview. *Drug discovery today* 7(20), pp. 1047-1055.

Macalino, S. J. Y. et al. 2015. Role of computer-aided drug design in modern drug discovery. *Archives of pharmacal research* 38(9), pp. 1686-1701.

Mackay, L. et al. 2017. Deciphering the regulation of P2X4 receptor channel gating by ivermectin using Markov models. *PLoS computational biology* 13(7), p. e1005643.

MacKenzie, A. et al. 2001. Rapid secretion of interleukin-1ß by microvesicle shedding. *Immunity* 15(5), pp. 825-835.

Mahmood, R. et al. 1987. The interaction and photolabeling of myosin subfragment 1 with 3'(2')-O-(4-benzoyl) benzoyladenosine 5'-triphosphate. *Journal of Biological Chemistry* 262(30), pp. 14479-14486.

Mankus, C. et al. 2011. Corneal epithelium expresses a variant of P2X7 receptor in health and disease. *PLoS One* 6(12), p. e28541.

Mansoor, S. E. et al. 2016. X-ray structures define human P2X 3 receptor gating cycle and antagonist action. *Nature* 538(7623), p. 66.

Marquez-Klaka, B. et al. 2007. Identification of an intersubunit cross-link between substituted cysteine residues located in the putative ATP binding site of the P2X1 receptor. *Journal of Neuroscience* 27(6), pp. 1456-1466.

Martinon, F. et al. 2009. The inflammasomes: guardians of the body. *Annual review of immunology* 27, pp. 229-265.

Masuda, T. et al. 2014. Transcription factor IRF5 drives P2X4R+-reactive microglia gating neuropathic pain. *Nature communications* 5: 3771.

Masuda, T. et al. 2012. IRF8 is a critical transcription factor for transforming microglia into a reactive phenotype. *Cell reports* 1(4), pp. 334-340.

Matsumura, Y. et al. 2016. A novel P2X4 receptor-selective antagonist produces anti-allodynic effect in a mouse model of herpetic pain. *Scientific reports* 6: 32461.

Matsushita, K. et al. 2014. Chemokine (CC motif) receptor 5 is an important pathological regulator in the development and maintenance of neuropathic pain. *Anesthesiology: The Journal of the American Society of Anesthesiologists* 120(6), pp. 1491-1503.

McQuillin, A. et al. 2009. Case–control studies show that a non-conservative amino-acid change from a glutamine to arginine in the P2RX7 purinergic receptor

protein is associated with both bipolar-and unipolar-affective disorders. *Molecular psychiatry* 14(6), p. 614.

Menez, C. et al. 2012. Relative neurotoxicity of ivermectin and moxidectin in Mdr1ab (−/−) mice and effects on mammalian GABA (A) channel activity. *PLoS neglected tropical diseases* 6(11), p. e1883.

Michel, A. et al. 2008. Negative and positive allosteric modulators of the P2X7 receptor. *British journal of pharmacology* 153(4), pp. 737-750.

Miklavc, P. et al. 2011. Fusion-activated Ca2+ entry via vesicular P2X4 receptors promotes fusion pore opening and exocytotic content release in pneumocytes. *Proceedings of the National Academy of Sciences* 108(35), pp. 14503-14508.

Miklavc, P. et al. 2013. A new role for P2X4 receptors as modulators of lung surfactant secretion. *Frontiers in cellular neuroscience* 7: 171.

Miller, K. et al. 1998. Cibacron blue allosterically modulates the rat P2X4 receptor. *Neuropharmacology* 37(12), pp. 1579-1586.

Miras-Portugal, M. T. et al. 2015. Role of P2X7 and P2Y 2 receptors on α-secretase-dependent APP processing: Control of amyloid plaques formation "in vivo" by P2X7 receptor. *Computational and structural biotechnology journal* 13, pp. 176-181.

Monçao-Ribeiro, L. C. et al. 2014. P2X7 receptor modulates inflammatory and functional pulmonary changes induced by silica. *PLoS One* 9(10), p. e110185.

Montreekachon, P. et al. 2011. Involvement of P2X7 purinergic receptor and MEK1/2 in interleukin – 8 up – regulation by LL – 37 in human gingival fibroblasts. *Journal of periodontal research* 46(3), pp. 327-337.

Morandini, A. et al. 2014. The role of P2X7 receptor in infectious inflammatory diseases and the influence of ectonucleotidases. *Biomedical journal* 37(2), pp. 169-177.

Mulryan, K. et al. 2000. Reduced vas deferens contraction and male infertility in mice lacking P2X1 receptors. *Nature* 403(6765), pp. 86-89.

Myers, S. and Baker, A. 2001. Drug discovery—an operating model for a new era. *Nature biotechnology* 19(8), p. 727.

Nagata, K. et al. 2009. Antidepressants inhibit P2X 4 receptor function: a possible involvement in neuropathic pain relief. *Molecular pain* 5: 20.

National Health Service (NHS). 2018. *Age-related macular degeneration (AMD)* [Online]. Available at: https://http://www.nhs.uk/conditions/age-related-macular-degeneration-amd/ [Accessed: 11 April 2018]

National Institute for Health and Care Excellence (NICE). 2018. *Age-related macular degeneration: Reccomendations* [Online]. Available at:

https://http://www.nice.org.uk/guidance/ng82/chapter/Recommendations [Accessed: 11 April 2018]

Nelson, D. W. et al. 2006. Structure−Activity Relationship Studies on a Series of Novel, Substituted 1-Benzyl-5-phenyltetrazole P2X7 Antagonists. *Journal of Medicinal Chemistry* 49(12), pp. 3659-3666.

Newbolt, A. et al. 1998. Membrane topology of an ATP-gated ion channel (P2X receptor). *Journal of Biological Chemistry* 273(24), pp. 15177-15182.

Newcom, J. and Spear, K. 2015. P2X4 receptor modulating compounds.International: Sunovion Pharmaceuticals Inc.

Niño – Moreno, P. et al. 2007. P2X7 and NRAMP1/SLC11 A1 gene polymorphisms in Mexican mestizo patients with pulmonary tuberculosis. *Clinical & Experimental Immunology* 148(3), pp. 469-477.

Nörenberg, W. et al. 2012. Positive allosteric modulation by ivermectin of human but not murine P2X7 receptors. *British journal of pharmacology* 167(1), pp. 48-66.

North, R. A. 2002. Molecular Physiology of P2X Receptors. *Physiological Reviews* 82(4), pp. 1013-1067.

Ochi-Ishi, R. et al. 2014. Involvement of the chemokine CCL3 and the purinoceptor P2X7 in the spinal cord in paclitaxel-induced mechanical allodynia. *Molecular pain* 10: 53.

Ohlendorff, S. D. et al. 2007. Single nucleotide polymorphisms in the P2X7 gene are associated to fracture risk and to effect of estrogen treatment. *Pharmacogenetics and genomics* 17(7), pp. 555-567.

Ooms, F. 2000. Molecular Modeling and Computer Aided Drug Design. Examples of their Applications in Medicinal Chemistry. *Current Medicinal Chemistry* 7(2), pp. 141-158.

Oury, C. et al. 2000. A natural dominant negative P2X1 receptor due to deletion of a single amino acid residue. *Journal of Biological Chemistry* 275(30), pp. 22611-22614.

Oyanguren-Desez, O. et al. 2011. Gain-of-function of P2X7 receptor gene variants in multiple sclerosis. *Cell calcium* 50(5), pp. 468-472.

Papineni, R. V. et al. 2002. Suramin interacts with the calmodulin binding site on the ryanodine receptor, RYR1. *Journal of Biological Chemistry* 277(51), pp. 49167-49174.

Park, J.-H. et al. 2016. Potent suppressive effects of 1-piperidinylimidazole based novel P2X7 receptor antagonists on cancer cell migration and invasion. *Journal of medicinal chemistry* 59(16), pp. 7410-7430.

Pasqualetto, G. et al. 2018. The molecular determinants of small-molecule ligand binding at P2X receptors. *Frontiers in Pharmacology* 9: 58.

Pelegrin, P. and Surprenant, A. 2009. Dynamics of macrophage polarization reveal new mechanism to inhibit IL‐1β release through pyrophosphates. *The EMBO journal* 28(14), pp. 2114-2127.

Perola, E. et al. 2000. Successful virtual screening of a chemical database for farnesyltransferase inhibitor leads. *Journal of medicinal chemistry* 43(3), pp. 401-408.

Pettersen, E. F. et al. 2004. UCSF Chimera—a visualization system for exploratory research and analysis. *Journal of computational chemistry* 25(13), pp. 1605-1612.

Plenge, R. M. 2016. Disciplined approach to drug discovery and early development. *Science Translational Medicine* 8(349), pp. 349ps315-349ps315.

Potucek, Y. D. et al. 2006. Purinergic receptors modulate MAP kinases and transcription factors that control microglial inflammatory gene expression. *Neurochemistry international* 49(2), pp. 204-214.

Priel, A. and Silberberg, S. D. 2004. Mechanism of ivermectin facilitation of human P2X4 receptor channels. *The Journal of general physiology* 123(3), pp. 281-293.

Puthussery, T. and Fletcher, E. L. 2004. Synaptic localization of P2X7 receptors in the rat retina. *Journal of Comparative Neurology* 472(1), pp. 13-23.

Qureshi, O. S. et al. 2007. Regulation of P2X4 receptors by lysosomal targeting, glycan protection and exocytosis. *Journal of cell science* 120(21), pp. 3838-3849.

Radford, K. M. et al. 1997. Baculovirus expression provides direct evidence for heteromeric assembly of P2X2 and P2X3 receptors. *Journal of Neuroscience* 17(17), pp. 6529-6533.

Rarey, M. et al. 1996. A fast flexible docking method using an incremental construction algorithm. *Journal of molecular biology* 261(3), pp. 470-489.

Rassendren, F. et al. 1997. The permeabilizing ATP receptor, P2X7 cloning and expression of a human cDNA. *Journal of Biological Chemistry* 272(9), pp. 5482-5486.

Roberts, J. A. and Evans, R. J. 2004. ATP binding at human P2X1 receptors Contribution of aromatic and basic amino acids revealed using mutagenesis and partial agonists. *Journal of Biological Chemistry* 279(10), pp. 9043-9055.

Roberts, J. A. and Evans, R. J. 2006. Contribution of conserved polar glutamine, asparagine and threonine residues and glycosylation to agonist action at human P2X1 receptors for ATP. *Journal of neurochemistry* 96(3), pp. 843-852.

Roberts, J. A. et al. 2006a. Molecular properties of P2X receptors. *Pflügers Archiv* 452(5), pp. 486-500.

Roberts, V. et al. 2006b. Purinergic receptors in human placenta: evidence for functionally active P2X4, P2X7, P2Y2, and P2Y6. *American Journal of Physiology-Regulatory, Integrative and Comparative Physiology* 290(5), pp. R1374-R1386.

Roche, D. J. et al. 2016. A pilot study of the safety and initial efficacy of ivermectin for the treatment of alcohol use disorder. *Alcoholism: Clinical and Experimental Research* 40(6), pp. 1312-1320.

Rong, W. et al. 2003. Pivotal role of nucleotide P2X2 receptor subunit of the ATP-gated ion channel mediating ventilatory responses to hypoxia. *Journal of Neuroscience* 23(36), pp. 11315-11321.

Royle, S. J. et al. 2005. Non-canonical YXXGΦ endocytic motifs: recognition by AP2 and preferential utilization in P2X4 receptors. *Journal of cell science* 118(14), pp. 3073-3080.

Sadovnick, A. D. et al. 2017. Purinergic receptors P2RX4 and P2RX7 in familial multiple sclerosis. *Human mutation* 38(6), pp. 736-744.

Sakuma, S. et al. 2013. Diazepinedione derivative. Nippon Chemiphar Co Ltd.

Šali, A. and Blundell, T. L. 1993. Comparative protein modelling by satisfaction of spatial restraints. *Journal of molecular biology* 234(3), pp. 779-815.

Samways, D. S. et al. 2012. Allosteric modulation of Ca2+ flux in ligand-gated cation channel (P2X4) by actions on lateral portals. *Journal of Biological Chemistry* 287(10), pp. 7594-7602.

Sanderson, J. et al. 2014. Purines in the eye: recent evidence for the physiological and pathological role of purines in the RPE, retinal neurons, astrocytes, Müller cells, lens, trabecular meshwork, cornea and lacrimal gland. *Experimental eye research* 127, pp. 270-279.

Sanner, M. F. et al. 1996. Reduced surface: an efficient way to compute molecular surfaces. *Biopolymers* 38(3), pp. 305-320.

Saul, A. et al. 2013. Heteromeric assembly of P2X subunits. *Frontiers in cellular neuroscience* 7: 250.

Savio, L. E. B. et al. 2018. The P2X7 receptor in inflammatory diseases: Angel or demon? *Frontiers in pharmacology* 9: 52.

Schachter, J. B. et al. 1997. HEK293 human embryonic kidney cells endogenously express the P2Y1 and P2Y2 receptors. *Neuropharmacology* 36(9), pp. 1181-1187.

Schinkel, A. H. et al. 1997. Normal viability and altered pharmacokinetics in mice lacking mdr1-type (drug-transporting) P-glycoproteins. *Proceedings of the National Academy of Sciences* 94(8), pp. 4028-4033.

Schmidt, M. E. et al. 2017. Clinical qualification of [18F] JNJ-64413739, a novel candidate PET ligand for the P2X7 receptor.

Schneider, M. et al. 2017. Interaction of Purinergic P2X4 and P2X7 Receptor Subunits. *Frontiers in Pharmacology* 8: 860.

Schrödinger. 2018. *Docking and Scoring* [Online]. Available at: http://www.schrodinger.com/science-articles/docking-and-scoring [Accessed: 4 August 2018].

Serrano, A. et al. 2012. Differential expression and pharmacology of native P2X receptors in rat and primate sensory neurons. *Journal of Neuroscience* 32(34), pp. 11890-11896.

Shan, Q. et al. 2001. Ivermectin, an unconventional agonist of the glycine receptor chloride channel. *Journal of Biological Chemistry* 276(16), pp. 12556-12564.

Shelley, J. C. et al. 2007. Epik: a software program for pK a prediction and protonation state generation for drug-like molecules. *Journal of computer-aided molecular design* 21(12), pp. 681-691.

Shen, J.-B. et al. 2006. Extracellular ATP-stimulated current in wild-type and P2X4 receptor transgenic mouse ventricular myocytes: implications for a cardiac physiologic role of P2X4 receptors. *The FASEB Journal* 20(2), pp. 277-284.

Shen, J.-B. et al. 2009. Reversal of cardiac myocyte dysfunction as a unique mechanism of rescue by P2X4 receptors in cardiomyopathy. *American Journal of Physiology-Heart and Circulatory Physiology* 296(4), pp. H1089-H1095.

Silberberg, S. D. et al. 2007. Ivermectin Interaction with Transmembrane Helices Reveals Widespread Rearrangements during Opening of P2X Receptor Channels. *Neuron* 54(2), pp. 263-274.

Sim, J. and North, A. R. 2010. Amitriptyline does not block the action of ATP at human P2X4 receptor. *British journal of pharmacology* 160(1), pp. 88-92.

Söderlund, J. et al. 2011. Elevation of cerebrospinal fluid interleukin-1ß in bipolar disorder. *Journal of Psychiatry & Neuroscience* 36(2), pp. 114-118.

Song, C. M. et al. 2009. Recent advances in computer-aided drug design. *Briefings in bioinformatics* 10(5), pp. 579-591.

Sorge, R. E. et al. 2012. Genetically determined P2X7 receptor pore formation regulates variability in chronic pain sensitivity. *Nature medicine* 18(4), p. 595.

Soronen, P. et al. 2011. P2RX7 gene is associated consistently with mood disorders and predicts clinical outcome in three clinical cohorts. *American Journal of Medical Genetics Part B: Neuropsychiatric Genetics* 156(4), pp. 435-447.

Soto, F. et al. 1996. P2X4: an ATP-activated ionotropic receptor cloned from rat brain. *Proceedings of the National Academy of Sciences* 93(8), pp. 3684-3688.

Soto, F. et al. 1999. Antagonistic properties of the suramin analogue NF023 at heterologously expressed P2X receptors. *Neuropharmacology* 38(1), pp. 141-149.

Stock, T. C. et al. 2012. Efficacy and safety of CE-224,535, an antagonist of P2X7 receptor, in treatment of patients with rheumatoid arthritis inadequately controlled by methotrexate. *The Journal of rheumatology* 39(4), pp. 720-727.

Stojilkovic, S. S. and Zemkova, H. 2013. P2X receptor channels in endocrine glands. *Wiley Interdisciplinary Reviews: Membrane Transport and Signaling* 2(4), pp. 173-180.

Stokes, L. et al. 2006. Characterization of a selective and potent antagonist of human P2X7 receptors, AZ11645373. *British journal of pharmacology* 149(7), pp. 880-887.

Stokes, L. et al. 2011. A Loss-of-Function Polymorphism in the Human P2X4 Receptor Is Associated With Increased Pulse Pressure. *Hypertension* 58(6), pp. 1086-1092.

Stoop, R. et al. 1997. Different Sensitivities to pH of ATP-Induced Currents at Four Cloned P2X Receptors. *Journal of Neurophysiology* 78(4), pp. 1837-1840.

Surprenant, A. et al. 1996. The cytolytic P2Z receptor for extracellular ATP identified as a P2X receptor (P2X7). *Science* 272(5262), pp. 735-738.

Suurväli, J. et al. 2017. P2X4: A fast and sensitive purinergic receptor. *Biomedical journal* 40(5), pp. 245-256.

Swartz, T. H. et al. 2015. Purinergic receptors: key mediators of HIV-1 infection and inflammation. *Frontiers in immunology* 6: 585.

Tanaka, J. et al. 1996. Cellular distribution of the P2X4 ATP receptor mRNA in the brain and non-neuronal organs of rats. *Archives of histology and cytology* 59(5), pp. 485-490.

Tarallo, V. et al. 2012. DICER1 loss and Alu RNA induce age-related macular degeneration via the NLRP3 inflammasome and MyD88. *Cell* 149(4), pp. 847-859.

Tekin, D. et al. 2010. Polymorphism in the p2x7 gene increases susceptibility to extrapulmonary tuberculosis in Turkish children. *The Pediatric infectious disease journal* 29(8), pp. 779-782.

Tenneti, L. et al. 1998. Expression and trans-synaptic regulation of P2x4 and P2z receptors for extracellular ATP in parotid acinar cells. Effects of parasympathetic denervation. *Journal of Biological Chemistry* 273(41), pp. 26799-26808.

Tewari, M. et al. 2015. Astrocytes mediate HIV – 1 Tat – induced neuronal damage via ligand – gated ion channel P2X7R. *Journal of neurochemistry* 132(4), pp. 464-476.

Thimm, D. et al. 2015. The nucleobase adenine as a signalling molecule in the kidney. *Acta Physiologica* 213(4), pp. 808-818.

Thompson, B. A. et al. 2012. A novel role for P2X7 receptor signalling in the survival of mouse embryonic stem cells. *Cellular signalling* 24(3), pp. 770-778.

Thompson, K. E. et al. 2013. Fusion-activated cation entry (FACE) via P2X4 couples surfactant secretion and alveolar fluid transport. *The FASEB Journal* 27(4), pp. 1772-1783.

Tian, M. et al. 2014. Carbamazepine derivatives with P2X4 receptor-blocking activity. *Bioorganic & medicinal chemistry* 22(3), pp. 1077-1088.

Tomioka, A. et al. 2000. Propofol potentiates ATP-activated currents of recombinant P2X4 receptor channels expressed in human embryonic kidney 293 cells. *Neuroscience Letters* 284(3), pp. 167-170.

Torres, G. E. et al. 1998. N-Linked glycosylation is essential for the functional expression of the recombinant P2X2 receptor. *Biochemistry* 37(42), pp. 14845-14851.

Toulme, E. et al. 2010. P2X4 receptors in activated C8-B4 cells of cerebellar microglial origin. *The Journal of general physiology* 135(4), pp. 333-353.

Trautmann, A. 2009. Extracellular ATP in the Immune System: More Than Just a "Danger Signal". *Science Signaling* 2(56), p. pe6.

Traxler, P. and Furet, P. 1999. Strategies toward the design of novel and selective protein tyrosine kinase inhibitors. *Pharmacology & therapeutics* 82(2-3), pp. 195-206.

Treede, R.-D. et al. 2015. A classification of chronic pain for ICD-11. *Pain* 156(6), p. 1003.

Trist, I. M. L. et al. 2018. Application of Molecular Modelling to Speed-up the Lead Discovery Process.*Computational Tools for Chemical Biology*. The Royal Society of Chemistry, pp. 281-316.

Tsuda, M. et al. 2003. P2X4 receptors induced in spinal microglia gate tactile allodynia after nerve injury. *Nature* 424(6950), pp. 778-783.

Tsuda, M. et al. 2008. Fibronectin/integrin system is involved in P2X4 receptor upregulation in the spinal cord and neuropathic pain after nerve injury. *Glia* 56(5), pp. 579-585.

Turner, S. A. et al. 2005. Parenteral administration of ivermectin in a patient with disseminated strongyloidiasis. *The American journal of tropical medicine and hygiene* 73(5), pp. 911-914.

Tvrdonova, V. et al. 2014. Identification of functionally important residues of the rat P2X4 receptor by alanine scanning mutagenesis of the dorsal fin and left flipper domains. *PloS one* 9(11): e112902.

Ullmann, H. et al. 2005. Synthesis and structure− activity relationships of suramin-derived P2Y11 receptor antagonists with nanomolar potency. *Journal of medicinal chemistry* 48(22), pp. 7040-7048.

Ulmann, L. et al. 2008. Up-regulation of P2X4 receptors in spinal microglia after peripheral nerve injury mediates BDNF release and neuropathic pain. *Journal of Neuroscience* 28(44), pp. 11263-11268.

Ursu, D. et al. 2014. Gain and loss of function of P2X 7 receptors: mechanisms, pharmacology and relevance to diabetic neuropathic pain. *Molecular pain* 10: 37.

Van Hecke, O. et al. 2014. Neuropathic pain in the general population: a systematic review of epidemiological studies. *Pain* 155(4), pp. 654-662.

Varley, I. et al. 2016. Functional polymorphisms in the P2X7 receptor gene are associated with stress fracture injury. *Purinergic signalling* 12(1), pp. 103-113.

Vavra, V. et al. 2011. Facilitation of glutamate and GABA release by P2X receptor activation in supraoptic neurons from freshly isolated rat brain slices. *Neuroscience* 188, pp. 1-12.

Vial, C. and Evans, R. J. 2002. P2X1 receptor-deficient mice establish the native P2X receptor and a P2Y6-like receptor in arteries. *Molecular pharmacology* 62(6), pp. 1438-1445.

Virginio, C. et al. 1999. Kinetics of cell lysis, dye uptake and permeability changes in cells expressing the rat P2X7 receptor. *The Journal of physiology* 519(2), pp. 335-346.

Virginio, C. et al. 1998. Trinitrophenyl-Substituted Nucleotides Are Potent Antagonists Selective for P2X1, P2X3, and Heteromeric P2X2/3 Receptors. *Molecular Pharmacology* 53(6), pp. 969-973.

Wang, J. et al. 2018. Druggable negative allosteric site of P2X3 receptors. *Proceedings of the National Academy of Sciences* 115(19), pp. 4939-4944.

Wang, L. et al. 2004. P2 receptor mRNA expression profiles in human lymphocytes, monocytes and CD34+ stem and progenitor cells. *BMC immunology* 5: 16.

Wang, L. et al. 2002. P2 receptor expression profiles in human vascular smooth muscle and endothelial cells. *Journal of cardiovascular pharmacology* 40(6), pp. 841-853.

Wang, M. et al. 2017a. Synthesis and preliminary biological evaluation of radiolabeled 5-BDBD analogs as new candidate PET radioligands for P2X4 receptor. *Bioorganic & medicinal chemistry* 25(14), pp. 3835-3844.

Wang, X. et al. 2013. Target essentiality and centrality characterize drug side effects. *PLoS computational biology* 9(7), p. e1003119.

Wang, X. H. et al. 2017b. Inhibiting purinergic P2X7 receptors with the antagonist brilliant blue G is neuroprotective in an intranigral lipopolysaccharide animal model of Parkinson's disease. *Molecular medicine reports* 15(2), pp. 768-776.

Ward, W. H. et al. 1994. Epidermal growth factor receptor tyrosine kinase: investigation of catalytic mechanism, structure-based searching and discovery of a potent inhibitor. *Biochemical pharmacology* 48(4), pp. 659-666.

Weinhold, K. et al. 2010. Interaction and interrelation of P2X7 and P2X4 receptor complexes in mouse lung epithelial cells. *Cellular and molecular life sciences* 67(15), pp. 2631-2642.

Wesselius, A. et al. 2013a. Association of P2X7 receptor polymorphisms with bone mineral density and osteoporosis risk in a cohort of Dutch fracture patients. *Osteoporosis International* 24(4), pp. 1235-1246.

Wesselius, A. et al. 2013b. Non-synonymous polymorphisms in the P2RX4 are related to bone mineral density and osteoporosis risk in a cohort of Dutch fracture patients. *Purinergic signalling* 9(1), pp. 123-130.

Wildman, S. S. et al. 1999. Selectivity of diadenosine polyphosphates for rat P2X receptor subunits. *European Journal of Pharmacology* 367(1), pp. 119-123.

Wiley, J. S. et al. 1993. The ATP4− receptor-operated channel (P2Z class) of human lymphocytes allows Ba2+ and ethidium+ uptake: inhibition of fluxes by suramin. *Archives of biochemistry and biophysics* 305(1), pp. 54-60.

Wilkinson, W. J. et al. 2009. Carbon monoxide is a rapid modulator of recombinant and native P2X2 ligand – gated ion channels. *British journal of pharmacology* 158(3), pp. 862-871.

Wilkinson, W. J. and Kemp, P. J. 2011. The carbon monoxide donor, CORM-2, is an antagonist of ATP-gated, human P2X4 receptors. *Purinergic signalling* 7(1), pp. 57-64.

Williams, D. and Lemke, T. 2002. Overview: Drug Design and Development: A Perspective. *Foye's Principles of Medicinal Chemistry; Troy, D., Ed., Lippincott Williams & Wilkins, New York*, pp. 12-36.

Williams, N. and Coleman, P. 1982. Exploring the adenine nucleotide binding sites on mitochondrial F1-ATPase with a new photoaffinity probe, 3'-O-(4-benzoyl) benzoyl adenosine 5'-triphosphate. *Journal of Biological Chemistry* 257(6), pp. 2834-2841.

Wilson, H. et al. 2007. P2X receptor characterization and IL – 1/IL – 1Ra release from human endothelial cells. *British journal of pharmacology* 151(1), pp. 96-108.

World Health Organization (WHO). 2017. *Cardiovascular Diseases (CVDs)* [Online]. WHO. Available at: http://www.who.int/mediacentre/factsheets/fs317/en/ [Accessed: 2018].

World Health Organization (WHO). 2018. *Causes of blindness and visual impairment* [Online]. Available at: http://www.who.int/blindness/causes/en/ [Accessed: 11 April 2018

Wyatt, L. R. et al. 2013. Sociocommunicative and sensorimotor impairments in male P2X4-deficient mice. *Neuropsychopharmacology* 38(10), p. 1993.

Xiao, J. et al. 2009. Lack of association between polymorphisms in the P2X7gene and tuberculosis in a Chinese Han population. *FEMS Immunology & Medical Microbiology* 55(1), pp. 107-111.

Xiong, K. et al. 2000. Inhibition by ethanol of rat P2X4 receptors expressed in Xenopus oocytes. *British Journal of Pharmacology* 130(6), pp. 1394-1398.

Xu, J. et al. 2014. Imaging P2X4 receptor subcellular distribution, trafficking, and regulation using P2X4-pHluorin. *The Journal of general physiology* 144(1), pp. 81-104.

Yamamoto, K. et al. 2000a. Fluid shear stress activates Ca2+ influx into human endothelial cells via P2X4 purinoceptors. *Circulation Research* 87(5), pp. 385-391.

Yamamoto, K. et al. 2000b. P2X4 receptors mediate ATP-induced calcium influx in human vascular endothelial cells. *American Journal of Physiology-Heart and Circulatory Physiology* 279(1), pp. H285-H292.

Yamamoto, K. et al. 2006. Impaired flow-dependent control of vascular tone and remodeling in P2X4-deficient mice. *Nature medicine* 12(1), pp. 133-137.

Yamashita, T. et al. 2016. Duloxetine inhibits microglial P2X4 receptor function and alleviates neuropathic pain after peripheral nerve injury. *PloS one* 11(10), p. e0165189.

Yan, D. et al. 2013. Mutation of the ATP-gated P2X(2) receptor leads to progressive hearing loss and increased susceptibility to noise. *Proceedings of the National Academy of Sciences of the United States of America* 110(6), pp. 2228-2233.

Yan, Z. et al. 2010. Experimental characterization and mathematical modeling of P2X7 receptor channel gating. *Journal of Neuroscience* 30(42), pp. 14213-14224.

Yan, Z. et al. 2011. Calcium-dependent block of P2X7 receptor channel function is allosteric. *The Journal of general physiology* 138(4), pp. 437-452.

Young, M. T. 2010. P2X receptors: dawn of the post-structure era. *Trends in biochemical sciences* 35(2), pp. 83-90.

Young, M. T. et al. 2006. Identification of Thr283 as a key determinant of P2X7 receptor function. *British journal of pharmacology* 149(3), pp. 261-268.

Young, M. T. et al. 2007. Amino acid residues in the P2X7 receptor that mediate differential sensitivity to ATP and BzATP. *Molecular pharmacology* 71(1), pp. 92-100.

Zemkova, H. et al. 2014. Allosteric modulation of ligand gated ion channels by ivermectin. *Physiological research* 63(Suppl. 1), pp. S215-S224.

Zhao, J. et al. 2013. P2X7 blockade attenuates murine lupus nephritis by inhibiting activation of the NLRP3/ASC/caspase 1 pathway. *Arthritis & Rheumatology* 65(12), pp. 3176-3185.

Zhao, Y. et al. 2015. Vascular nitric oxide: Beyond eNOS. *Journal of pharmacological sciences* 129(2), pp. 83-94.

Zheng, W. et al. 2013. Phenotypic screens as a renewed approach for drug discovery. *Drug discovery today* 18(21-22), pp. 1067-1073.

Zheng, X. et al. 2017. Genetic polymorphisms of the P2X7 gene associated with susceptibility to and prognosis of pulmonary tuberculosis. *Infection, Genetics and Evolution* 53, pp. 24-29.

Zhu, B. et al. 2017. Identification and characterization of related substances in EVT-401 by hyphenated LC–MS techniques. *Journal of Pharmaceutical Analysis* 7(4), pp. 223-230.

APPENDIX 1:
Generation of P2X4-expressing stable cell lines

A1.1 Human P2X4 stable cell line (G34)

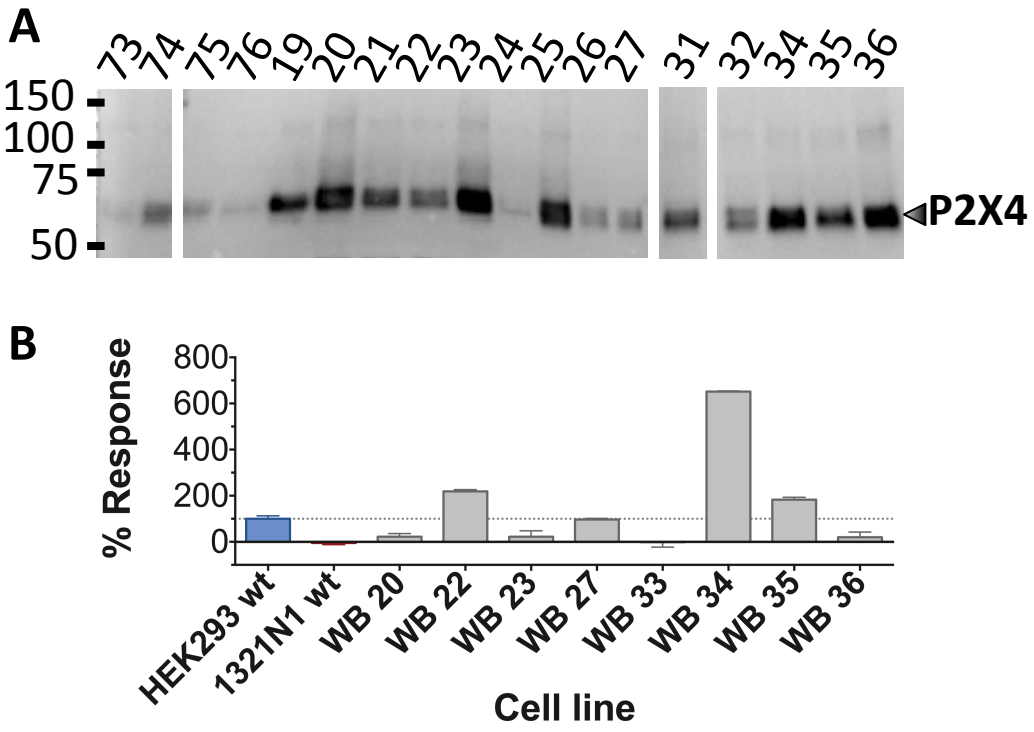

Figure A-1: A. Immunoblot of 1321N1 stable cell line clones expressing human P2X4 receptor detected with anti-P2X4 antibody. Cell transfected with 1 µg DNA and grown with G418 from single cell colonies. Cells were lysed from confluent 6-wells plates. Samples from each clone were resolved by SDS-PAGE and blotted with polyclonal anti-P2X4 (1:2000 dilution) followed by HRP-conjugated anti-rabbit IgG. B. Functional assessment of the clones after antibiotic selection. 100 µM ATP was used to elicit responses measured via calcium influx assay.

A1.2 Rat P2X4 stable cell line (RML2)

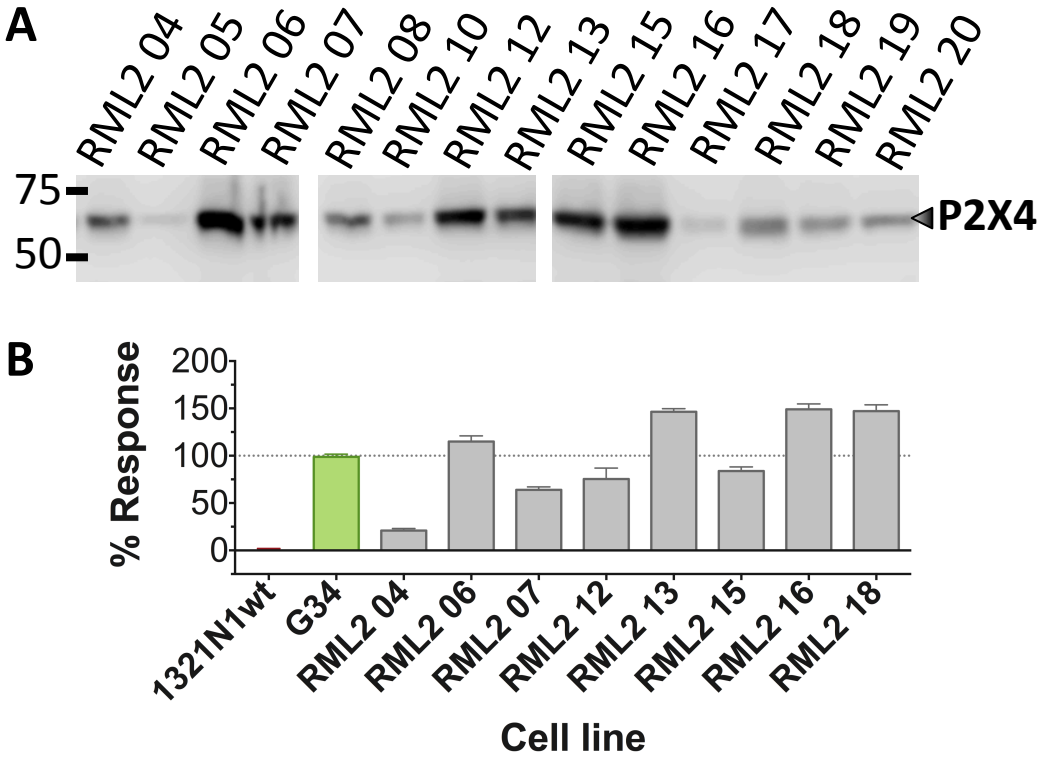

Figure A-2: Expression and functional characterization of rat P2X4 receptor in clones of 1321N1 post-selection. Rat P2X4 construct was gifted by Murriel-Legnardo (construct named RML2 hereafter). Clones were transfected with 1µg RML2, selected with G418 and single foci were isolated and expanded. 28 clones were checked for wild-type rat P2X4 expression with 26 clones. (**A**) Following transfection with 1µg DNA (RML2 plasmid), single-cell colonies were grown in presence of G418. Cells aliquot from each colony were lysed and samples with 4 µg of total protein were resolved by SDS-PAGE and immuno-blotted with polyclonal anti-P2X4 (1:2000 dilution). G34, the stable cell line expressing human P2X4, was used as positive control. Expression levels were notably variable across the clones. 8 of the clones with high expression levels were assessed for functionality (**B**). Clone 13 (name hereafter 'RML2 13') showed a pronounced response to 100µM ATP in the calcium influx assay and was chosen for further characterization. Not all the assessed clones were included in the present figure.

A1.3 Rat P2X4 T312I (RTI 13) and human P2X4 I312T (HIT 08) cell lines

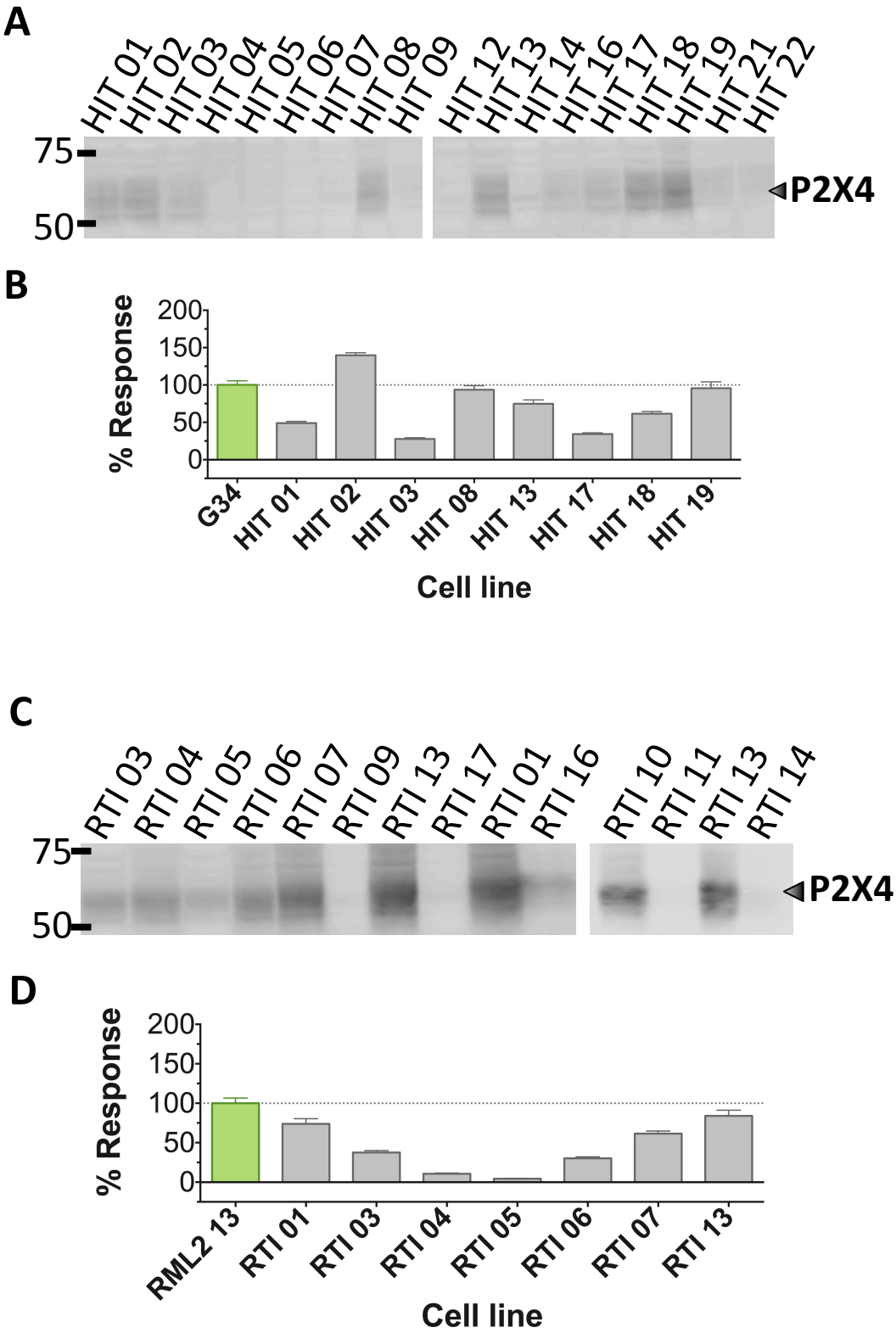

Figure A-3: Expression and functionality of 1321N1 cell expressing human P2X4 Ile-312 to Thr (A, B) and rat P2X4 Thr-312 to Ile (C, D) receptors. The

DNA constructs of human P2X4 I312T mutant and rat P2X4 T312I were generated by Dr Mark T. Young using Quikchange according to the supplier protocol (A), (C) Immunoblot showing expression level of human and rat P2X4 mutants in single-cell colonies. Transfection with 1µg DNA was followed by selection with G418. Samples from each colony were lysed and aliquots containing 4.2 µg of total protein were resolved by SDS-PAGE and immunoblotted with polyclonal anti-P2X4 (1:2000 dilution) followed by treatment with anti-rabbit HRP conjugated secondary antibody detected by chemilunminescence method. Not all the assessed clones were included in the present figure. (B), (D) ATP response (at 100 µM concentration) of selected clones. Stable cell lines expressing human P2X4 wild-type (G34) and rat P2X4 wild-type (RML2 13) were taken as positive reference (data normalized to the positive control). Sequencing of the genomic DNA extracted from of RTI 13 and HIT 08 confirmed the presence of the correct mutation in each corresponding stable cell line.

APPENDIX 2:
BX-430 inhibition at rP2X4 WT, rP2X4 T312I, hP2X4 WT and hP2X4 I312T (independent experiments)

A2.1 BX-430 inhibitory effect at human P2X4 WT

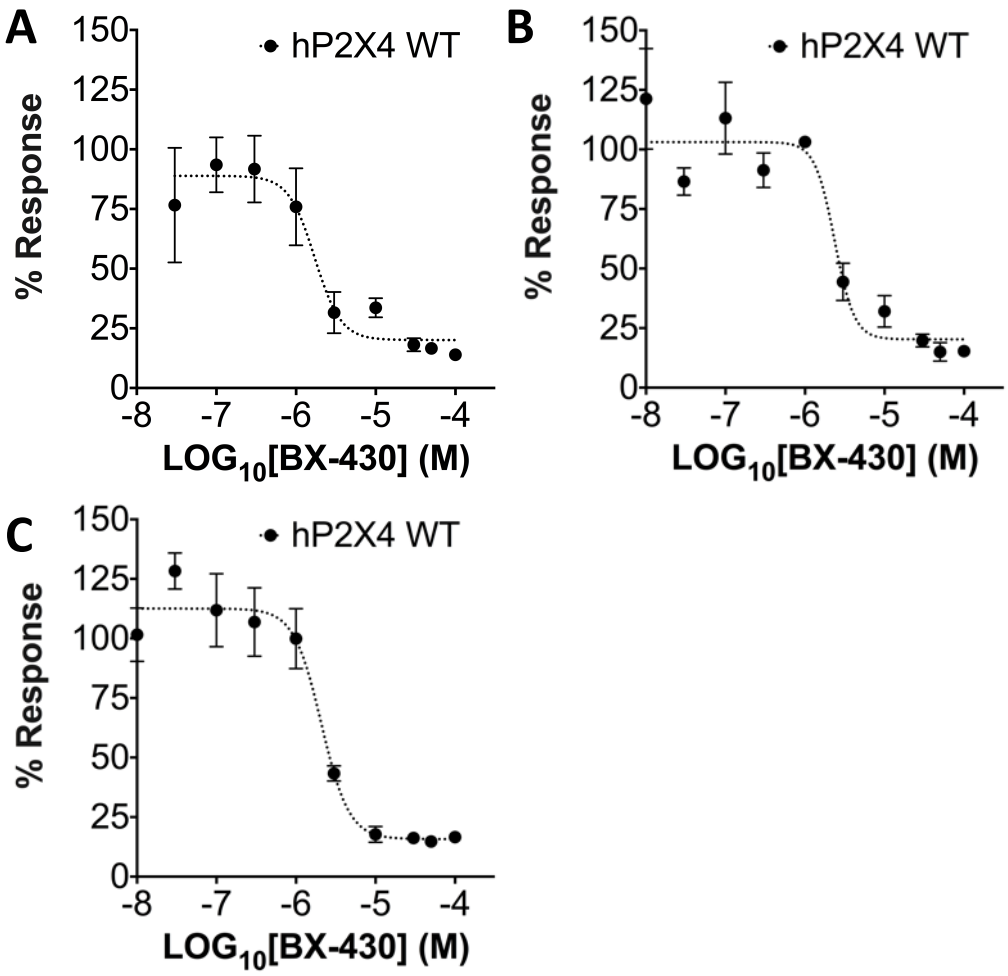

	IC_{50} (µM)	$LogIC_{50}$	Hill Coeficient
Curve-fit experiment A	1.7 (n=2-4)	-5.765	-2.641
Curve-fit experiment B	2.4 (n=4-5)	-5.627	-3.521
Curve-fit experiment C	2.1 (n=3-5)	-5.681	-2.498

Figure A-4: BX-430 inhibitory effect at human P2X4 WT. An inhibition curve was fit for each independent experiment.

A2.2 BX-430 inhibitory effect at human P2X4 I312T

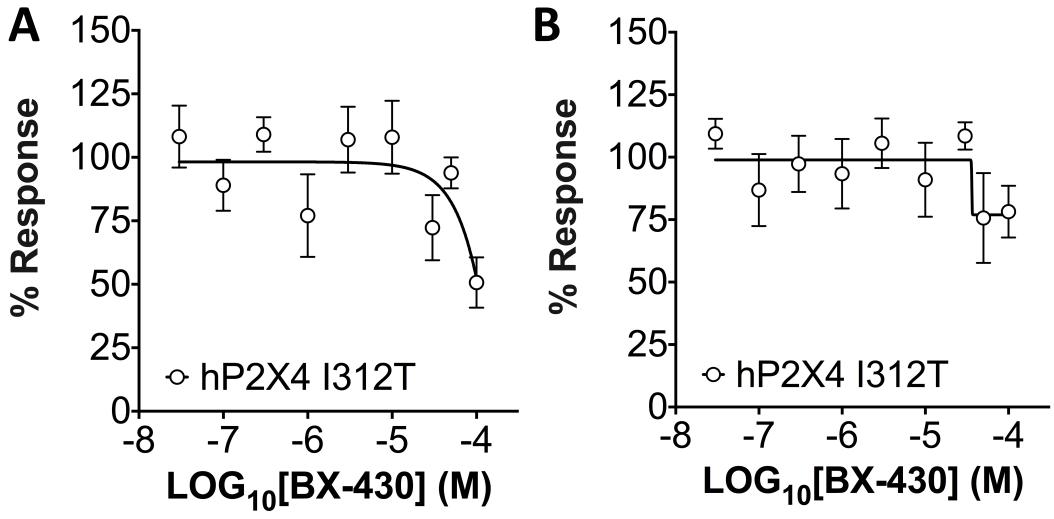

	IC_{50} (μM)	$LogIC_{50}$	Hill Coeficient
Curve-fit experiment A	(Interrupted curve) (n=4-5)	-	-
Curve-fit experiment B	~41 (Ambiguous fit) (n=4-5)	~-4.387	~-2060

Figure A-5: BX-430 inhibitory effect at human P2X4 I312T. An inhibition curve was fit for each independent experiment.

A2.3 BX-430 inhibitory effect at rat P2X4 WT

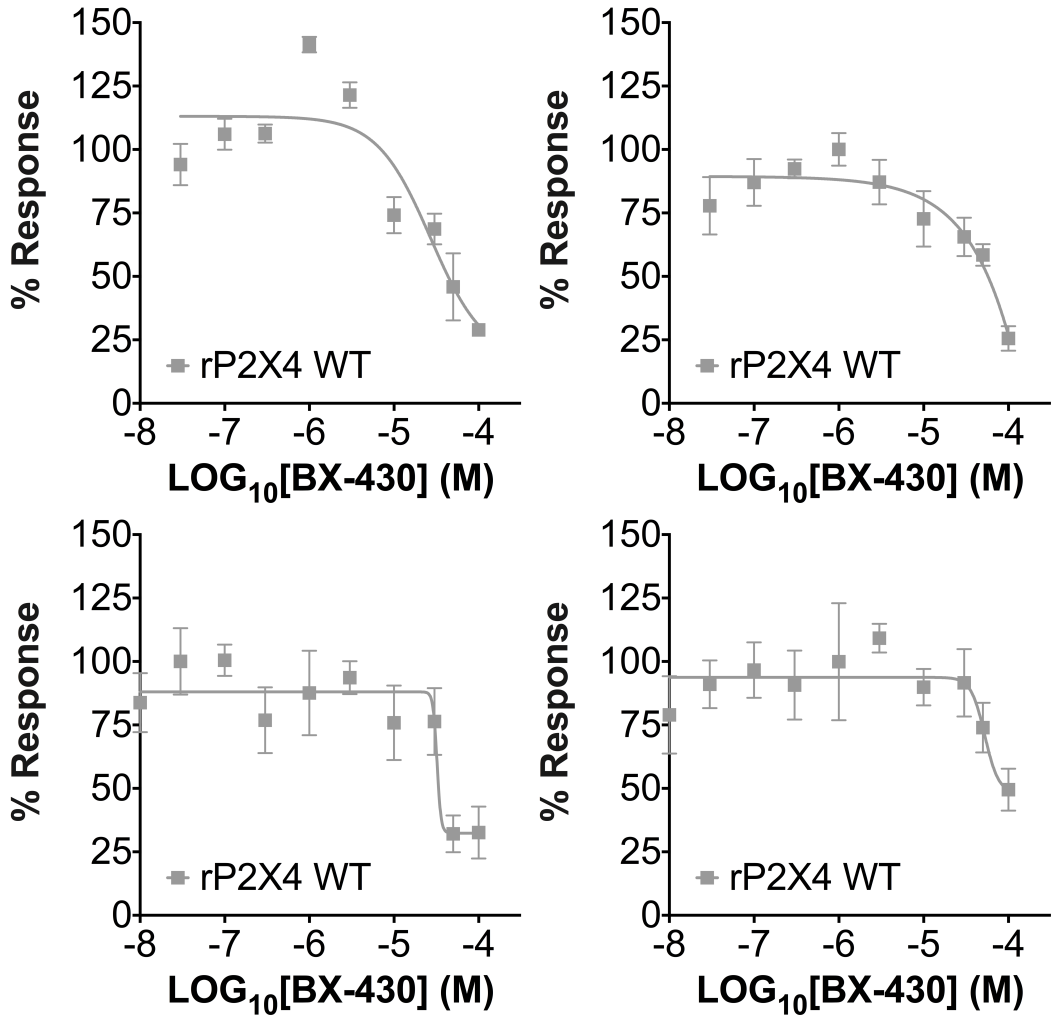

	IC_{50} (μM)	$LogIC_{50}$	Hill Coeficient
Curve-fit experiment A	27.1 (n=4)	-4.567	-1.369
Curve-fit experiment B	~230 (n=3-4) (Ambiguous fit)	~-1.637	~-0.8433
Curve-fit experiment C	~32 (n=3-4) (Ambiguous fit)	-4.492	-18.54
Curve-fit experiment D	52.6 (n=5)	-4.279	-5.315

Figure A-6: BX-430 inhibitory effect at rat P2X4 WT. An inhibition curve was fit for each independent experiment.

A2.4 BX-430 inhibitory effect at rat P2X4 T312I

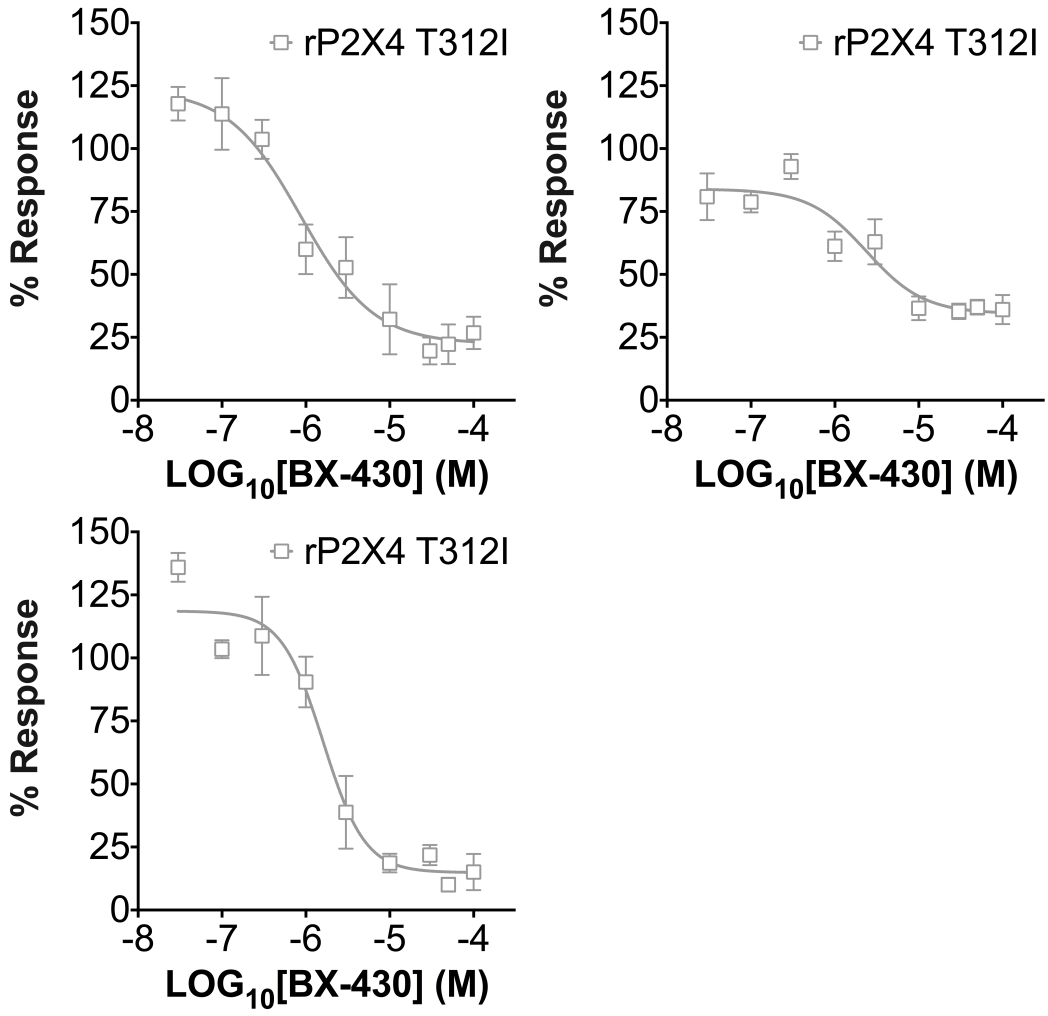

	IC_{50} (µM)	$LogIC_{50}$	Hill Coeficient
Curve-fit experiment A	0.88 (n=4)	-6.056	-1.004
Curve-fit experiment B	2.38 (n=4-5)	-5.623	-1.266
Curve-fit experiment C	1.6 (n=4-5)	-5.794	-1.744

Figure A-7: BX-430 inhibitory effect at rat P2X4 T312I. An inhibition curve was fit for each independent experiment.

APPENDIX 3:
Generation of P2X7-expressing stable cell lines

A3.1 Human P2X7 cell lines (WB50)

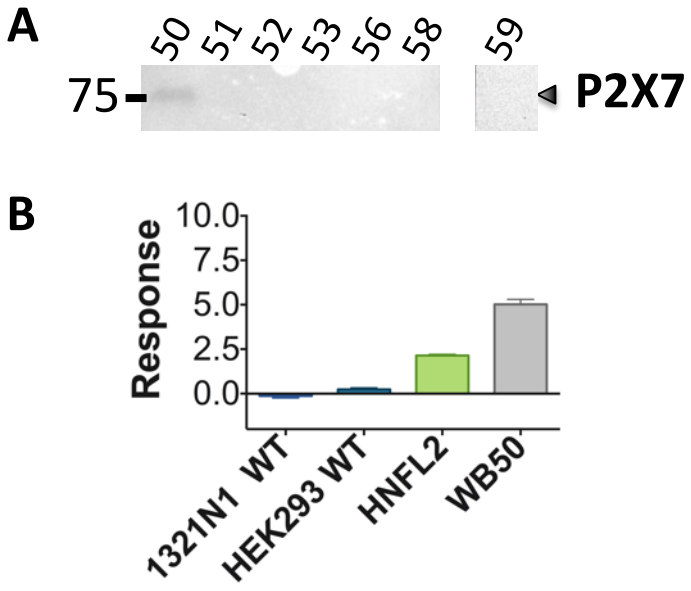

Figure A-8: Expression and functional assessment of human P2X7-expressing clones (1321N1 cells). **A**. Immunoblot of clones stably transfected with human P2X7 receptor and detected with anti-P2X7 antibody. Stable cells from single cell colonies were obtained through transfected with 1 μg DNA and selected with G418. Clones were grown to confluence and subsequently lysed. Samples were blotted with polyclonal anti-P2X7 (1:2000 dilution) followed by HRP-conjugated anti-rabbit IgG. **B**. ATP-dependent YO-PRO dye uptake in for clone WB50, employed in all the experiments described in **Chapter 5**. HNFL2, a mouse P2X7 (M283) stable cell line, was used as positive control while 1321N1 WT and HEK293 WT as negative controls.

A3.2 Human P2X7 cell lines (WB50)

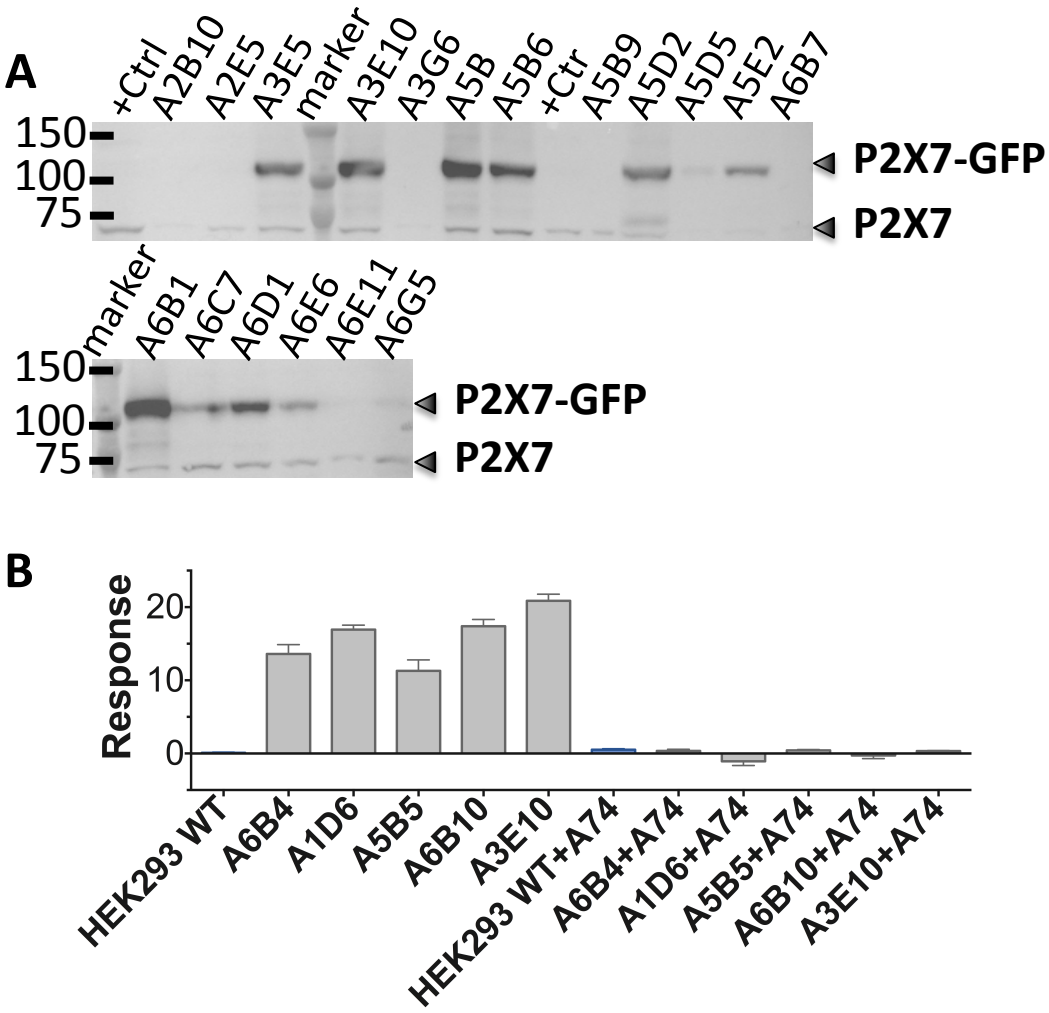

Figure A-9: Expression and functional assessment of HEK293 stable cell line clones expressing rat P2X7-GFP. A. **Immunoblot of HEK-293 stable clones expressing rat P2X7-GFP receptor detected with anti-P2X7 antibody.** Stable cells from single cell colonies were obtained through transfected with 1 μg DNA and selected with G418 in presence of 0.1 μM A740003. Clones were grown to confluency in 6-wells plates, then lysed. Samples were blotted with polyclonal anti-P2X7 (1:2000 dilution) followed by HRP-conjugated anti-rabbit IgG. **B**. ATP-dependent YO-PRO dye uptake in 5 clones incubated with +/- 0.1 μM A740003 and and stimulated with 300 μM ATP. Clone A3E10 was selected and use for all the subsequent experiments reported in **Chapter 5**.

APPENDIX 4:
Publications

1. Pasqualetto, G. et al. 2018. The molecular determinants of small-molecule ligand binding at P2X receptors. Frontiers in Pharmacology 9: 58.